



**HAL**  
open science

# Réalisation d'électrodes souples pour batteries lithium-ion par procédé d'impression

Oussama El Baradai

► **To cite this version:**

Oussama El Baradai. Réalisation d'électrodes souples pour batteries lithium-ion par procédé d'impression. Other. Université de Grenoble, 2014. English. NNT : 2014GRENI036 . tel-01348853

**HAL Id: tel-01348853**

**<https://theses.hal.science/tel-01348853>**

Submitted on 26 Jul 2016

**HAL** is a multi-disciplinary open access archive for the deposit and dissemination of scientific research documents, whether they are published or not. The documents may come from teaching and research institutions in France or abroad, or from public or private research centers.

L'archive ouverte pluridisciplinaire **HAL**, est destinée au dépôt et à la diffusion de documents scientifiques de niveau recherche, publiés ou non, émanant des établissements d'enseignement et de recherche français ou étrangers, des laboratoires publics ou privés.

## THÈSE

Pour obtenir le grade de

## DOCTEUR DE L'UNIVERSITÉ DE GRENOBLE

Spécialité : **Mécanique des fluides, Procédés, Énergétique**

Arrêté ministériel : 7 août 2006

Présentée par

**Oussama El Baradai**

Thèse dirigée par **Didier Chaussy**  
codirigée par **Yann Bultel et Davide Beneventi**

préparée au sein du **Laboratoire de Génie des Procédés  
Papetiers (LGP2)**  
dans l'**École Doctorale Ingénierie - Matériaux Mécanique  
Énergétique Environnement Procédés Production (I-MEP2)**

## Elaboration of flexible lithium - ion electrodes by printing process

## Réalisation d'électrodes souples pour batteries lithium-ion par procédé d'impression

Thèse soutenue publiquement le **24 Avril 2014**,  
devant le jury composé de :

**Mme Christine VAUTRIN-UI**

Professeur, C.R.M.D. (Orléans) : Rapporteur

**Mr Christophe PIJOLAT**

Professeur, SPIN (St Etienne) : Rapporteur

**Mr Dominique GUYOMARD**

Professeur, IMN (Nantes) : Président

**Mr Yann BULTEL**

Professeur, LEPMI (Grenoble) : Membre

**Mr Davide BENEVENTI**

Chargé de recherche HDR CNRS, LGP2 (Grenoble) : Membre

**Mr Didier CHAUSSY**

Professeur LGP2 (Grenoble) : Membre





# Table of contents

<b>Introduction</b> .....	1
<b>1. Flexible Lithium ion batteries: state of the art</b> .....	7
1.1 Batteries .....	7
1.1.1 Electrochemical principles .....	7
1.1.2 Classification of cells and batteries .....	10
1.2 Market battery.....	12
1.2.2 Design and manufacturing batteries .....	16
1.2.3 Design and manufacturing of Li - ion batteries.....	17
1.3 Lithium - ion batteries (LiBs) .....	22
1.3.1 Electrodes .....	24
1.3.2 Separator.....	26
1.3.3 Electrolyte .....	28
1.3.4 Solid electrolyte interface (SEI) .....	30
1.3.5 Alternative electrodes elaboration process for low cost and large area .....	33
1.3.6 Printed elaboration process .....	33
1.3.7 Printed primary batteries .....	37
1.3.8 Flexible secondary batteries .....	43
1.3.9 Thin and printed flexible Lithium - ion batteries .....	45
<b>2. Experimental</b> .....	60
2.1 Materials .....	60
2.1.1 Cellulose based materials .....	60
2.1.2 Electrodes materials .....	61
2.1.3 Substrates and other materials.....	62
2.2 Ink manufacturing.....	63
2.2.1 Ink formulation strategy .....	63
2.2.2 Rheological characterization protocol.....	67

2.3	Printing electrodes .....	69
2.3.1	Screen printing process .....	69
2.3.2	Characterization of the electrodes .....	72
2.4	Assembling electrodes .....	76
2.4.1	Front / back assembling design .....	76
2.4.2	Stack assembling design.....	76
2.5	Electrochemical characterization.....	77
2.5.1	Galvanostatic measurements .....	78
2.5.2	Cyclic voltammetry measurements .....	78
<b>3.</b>	<b>Development and characterization of printed anode .....</b>	<b>82</b>
3.1	Ink formulation .....	82
3.1.1	Rheology characterization.....	83
3.2	Electrode characterization .....	91
3.2.1	Physical characterization.....	91
3.2.2	Electrochemical characterization .....	95
3.2.3	Influence of inactive components .....	100
3.3	Calendering study.....	101
3.3.1	Physical characterization.....	101
3.3.2	Electrochemical characterization .....	104
3.3.3	Optimization of SEI layer .....	106
3.4	Conclusion.....	108
<b>4.</b>	<b>Development and characterization of printed cathode.....</b>	<b>112</b>
4.1	Ink formulation .....	112
4.1.1	Rheology characterization.....	114
4.2	Electrode characterizations.....	121
4.2.1	Physical characterizations .....	121
4.2.2	Electrochemical characterization .....	125
4.2.3	Calendering study.....	131

4.3	Conclusion.....	134
<b>5.</b>	<b>Development and characterization of full cell.....</b>	<b>137</b>
5.1	Cell assembling strategy.....	137
5.1.1	front / back (recto / verso) assembling strategy.....	138
5.1.2	Influence of packaging strategy.....	140
5.1.3	Physical characterization.....	144
5.1.4	Electrochemical characterization.....	148
5.2	Comparative study.....	151
5.2.1	Influence of testing strategy.....	151
5.2.2	Calendering study.....	152
5.2.3	Influence of substrate.....	153
5.3	Conclusion.....	157
	<b>General conclusion.....</b>	<b>161</b>
	<b>References.....</b>	<b>163</b>
	<b>French extended abstract</b>	

# List of abbreviations

AFM = Atomic force microscopy

CB = Carbon black

CNT = Carbon nano tube

DEC = Diethylen carbonate

DMC = Dimethyl carbonate

EC = Ethylen carbonate

EMC = Ethyl methyl carbonate

FB = Cellulose fibers

FESEM = Field effect scanning electron microscopy

GED = Gravimetric energy density

GP = Graphite

GPE = Gelled polymer electrolyte

LCO = Lithium cobaltum oxide

LFP = Lithium iron phosphate

LIB = Lithium ion batteries

LNCMO = Lithiated metal oxide

LTO = Lithium titanium oxide

LVR = Linear viscoelastic region

MFC = Microfibrillated cellulose

NCA = Nickel cobaltum oxide

NMC = Nickel manganese oxide

NMP = N-methylpyrrolidone

OCV = Open circuit voltage

PAA = Polyacrylic acid

PAC = Polyvinyl alcohol/cellulose

PC = Propylene carbonate

PE = Polyethylene

PEDOT = Polyethylene dioxythiophene

PEO = Polyethylene oxide

PP = Polypropylene

PPO = Poly(p-phenylene oxide)

PVA = Polyvinyl alcohol

PVdF = Polyvinylidene fluoride

RFID = Radio frequency identification

SED = Surface energy density

SEI = Solid electrolyte interface

SEM = Scanning electron microscopy

SPE = Pure solid polymer

SS = Stainless steel

VED = Volumetric energy density

# **Introduction**



# Introduction

The present energy economy based on fossil fuels encounters serious difficulties due to a series of factors, including the continuous increase in the demand for oil and the depletion of non – renewable resources. Another aspect is associated with CO<sub>2</sub> emissions, which have increased with a dramatic jump in the last 30 years, this resulting in a rise global temperature with associated series of dramatic climate changes. The urgency for energy renewal requires the use of clean energy sources. Accordingly, investments for the exploitations of renewable energy resources are increasing worldwide with particular attention to wind and solar power energy plants (REPs). The intermittency of these resources requires high efficiency storage systems. Electrochemical energy production is an alternative energy power sources as long as this energy consumption is designated to be more sustainable and environmentally friendly. Electrochemical systems such as batteries, fuel cells and super capacitors that can efficiently store and deliver energy on demand are playing a crucial role in this field.

Batteries are portable devices capable of delivering the stored chemical energy as electrical energy with high conversion and without gaseous emission. Moreover batteries offer the most promising option to power efficiently hybrid vehicles (HEVs) and electric vehicles (EVs). In this scenario, particularly appealing are rechargeable batteries benefiting from high specific energy, high rate capability, high safety and low cost. Promising candidates are Li - ion batteries (LiBs) that today exceed at least any competing technology thanks to the high value of energy density. LiBs are the power sources of the choice for the portable electronic market, accounting for more than 63% of worldwide sales values in portable batteries.

Despite the good electrochemical performances of commercial Li-ion batteries, their massive diffusion (driven by the ever increasing demand of low-cost energy storage systems) and sustainable use is still limited by three main factors:

- Reduction of the production and the overall device cost,
- Identification of environmentally friendly materials and production processes
- Development of devices those are easily up-scalable and recyclable.

In this scenario, the use of low-cost, bio-sourced and water-processable cellulosic materials for the production of Li-ion cells seems to be one way to solve these problems. For this reason paper has also recently been considered as a potential substrate for low-cost flexible electronics.

Paper is by far the cheapest and the most widely used flexible substrate in daily life. The price of paper is substantially lower than that of plastic substrates such as polyethylene terephthalate and polyimide. In addition, paper is also environmentally friendly, since it is recyclable and made of renewable raw materials. Employing printing technologies for the manufacturing of such power supplies promise cheap mass production processes, whilst keeping highest flexibility for the product designers. In the classic production processes, for conventional batteries, typically pick-and-place techniques are employed which require significant tooling costs for product change-over. While printing technologies with their cost – efficient and mass production techniques allow a low-cost and large area manufacturing

The objectives of this project can be summarized in three points:

- i) The substitution of conventional synthetic binders used in lithium ion batteries by biosourced polymers (i.e. cellulose and derivatives).
- ii) The formulation of water based slurries (inks) containing active materials processable with conventional printing devices.
- ii) The fabrication of flexible battery by deposition of active materials on paper by using printing processes.

The present manuscript is therefore organized in five chapters:

**Chapter 1:** a literature review emphasizes the interest of the project and introduces a brief overview of batteries and lithium-ion batteries. Secondly an overview focused about Lithium-ion batteries in terms of materials, functioning, manufacturing is presented. Finally one exhaustive part is dedicated to describe formulation process of conductive inks and different manufacturing process to produce lithium-ion batteries.

**Chapter 2:** resumes the materials and methods used during the experimental work. The Raw materials are schematically outlined. Moreover, the principal characterization and printing manufacturing techniques are described. In addition electrode preparation, cell assembly and electrochemical testing techniques are also detailed.

The following chapters are dedicated to the analysis and interpretation of the results. Each chapter is focused on the development and characterization of one aspect of the battery. Third chapter is focused on the anode, fourth chapter on the cathode and the fifth chapter on the full cell.

**Chapter 3:** the manufacturing of the anode electrode is presented. Rheological results are presented for formulated inks, by showing the influence of different components. Different

rheological experiments are carried out by performing oscillation and thixotropy tests in order to understand the structure of the ink and the impact of binding components to the rheological response of inks. After printing, physical and electrochemical characterization of printed anode is presented by showing main results. The last part is focused on different strategies chosen to enhance electrode's performance. More precisely a calendering strategy and the introduction of additive components are investigated.

**Chapter 4:** Screen printed cathode electrodes are manufactured. Inks are formulated by using as binding and reinforcing cellulose derivatives and a conductive agent is added in order to insure a good electronic conductivity. Rheological studies are performed in order to find the suitable properties for the screen printed process and to investigate the influence of components. Physical and electrochemical characterization of printed electrodes are presented and discussed and a calendering study is proposed to enhance properties. Finally a conclusion resumes main results obtained in this work in terms of rheological, physical and electrochemical properties.

**Chapter 5:** This chapter is focused on printing and characterization of a full printed cell. Firstly a presentation of different assembling strategies is proposed by underlining the advantages and disadvantages. A part is dedicated to expose our assembling strategy based on front / reverse printing approach. Physical and electrochemical experiments are performed and results are analysed in comparison with other full cells obtained by conventional assembling techniques. Moreover key parameters are identified as porosity, thickness and grammage of separators that affect performances of the full cell.

A general conclusion resumes main results and points out new techniques employed during this work. A part is dedicated to suggest some perspective lines in order to enhance and pursuit this work.



**Flexible Lithium-ion  
batteries:  
state of the art**



# 1. Flexible Lithium ion batteries: state of the art

## 1.1 Batteries

### 1.1.1 Electrochemical principles

Systems for electrochemical energy storage and conversion include batteries, fuel cells, and electrochemical capacitors (ECs). Although the energy storage and conversion mechanisms are different, there are “electrochemical similarities” of these three systems. All of them consist of two electrodes in contact with an electrolyte solution as showed in Figure 1.1

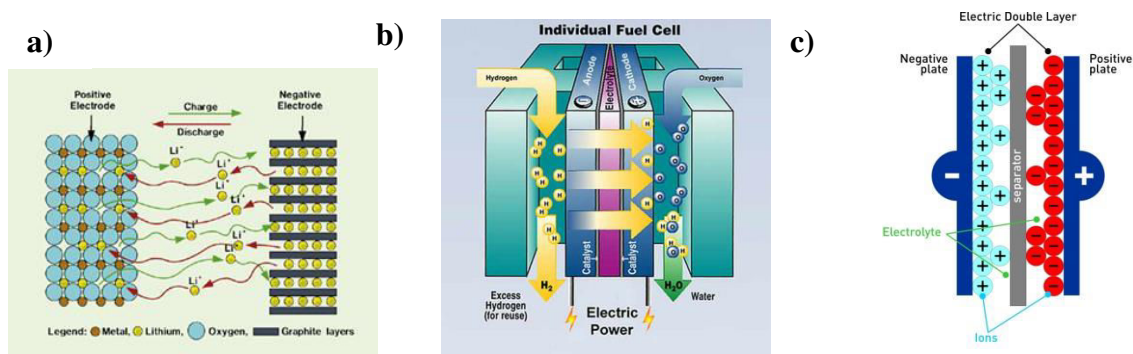


Figure 1.1.a) Lithium ion battery b) Fuel cell c) Capacitor scheme [1-2-3]

Batteries and fuel cells are electrochemical devices which convert chemical energy into electrical energy by electrochemical oxidation and reduction reactions, which occur at the electrodes. All systems consist of an anode where oxidation takes place during discharge, a cathode where reduction takes place, and an electrolyte which conducts the electrons within the cell [4]. The difference between batteries and fuel cells is related to the locations of energy storage and conversion. Batteries are closed systems, with the anode and cathode being the charge-transfer medium and taking an active role in the redox reaction as “active masses”. In other words, energy storage and conversion occur in the same compartment. Fuel cells are open systems where the anode and cathode are just charge-transfer media and the active masses undergoing the redox reaction are delivered from outside the cell, either from the environment, for example, oxygen from air. In electrochemical capacitors (or super capacitors), energy may not be delivered via redox reactions and, thus the use of the terms

anode and cathode may not be appropriate but are in common usage. Ions at the electrolyte / electrode interface, so-called electrical double layers (EDLs) are formed and released, which results in a parallel movement of electrons in the external wire that is in the delivering process. In comparison to super capacitors and fuel cells, batteries have found by far the most application market and they have an established market position.

The terms “specific energy” [expressed in watt-hours per kilogram (Wh/kg)] and “energy density” [in watt-hours per liter (Wh/L)] are used to compare the energy contents of a system, whereas the rate capability is expressed as “specific power” (in W/kg) and “power density” (in W/L). Alternatively, the attributes “gravimetric” (per kilogram) and “volumetric” (per liter) are used. To compare the power and energy capabilities, a representation known as the Ragone plot or diagram has been developed. A simplified Ragone plot (Figure 1.2) shows that fuel cells can be considered to be high-energy systems, while super capacitors are considered to be high-power systems. Batteries have intermediate power and energy characteristics.

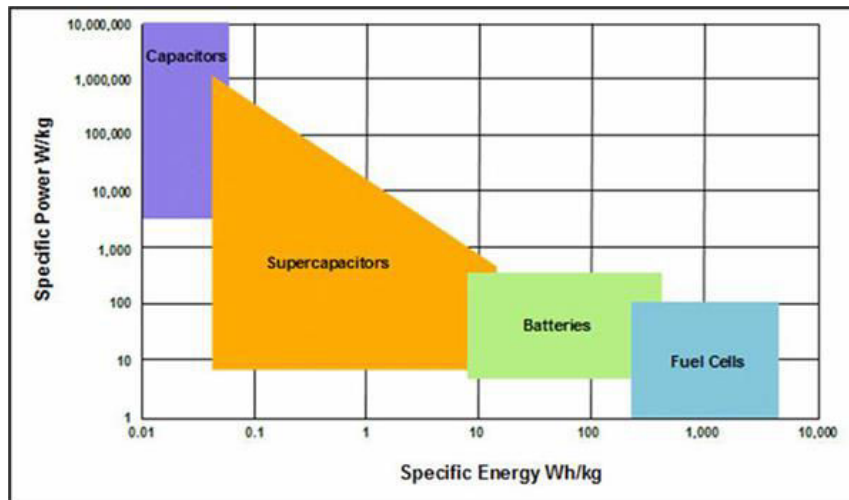


Figure 1.2. Ragone Plot of electrochemical storage devices [5]

## Battery electrochemical principles

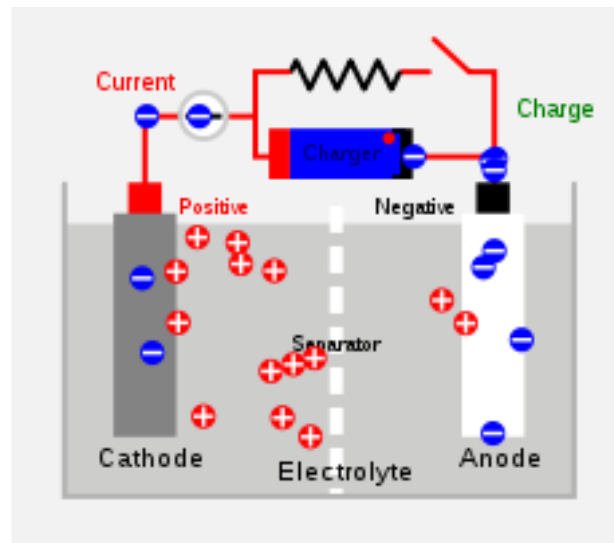


Figure 1.3. Battery principle scheme [6]

A battery is a device that converts the chemical energy contained in its active materials directly into electric energy by means of an electrochemical oxidation-reduction (redox) reaction as illustrated in Figure 1.3. In the case of a rechargeable system, the battery is recharged by a reversal of the process. This type of reaction involves the transfer of electrons from one material to another through an electric circuit [7].

While the term “battery” is often used, the basic electrochemical unit being referred to is the “cell.” A battery consists of one or more of these cells, connected in series or parallel, or both, depending on the desired output voltage and capacity.

The cell consists of three major components:

- 1. The anode or negative electrode:** It is the reducing or fuel electrode which gives up electrons to the external circuit and is oxidized during the electrochemical reaction.
- 2. The cathode or positive electrode** the oxidizing electrode which accepts electrons from the external circuit and is reduced during the electrochemical reaction.
- 3. The electrolyte** the ionic conductor which provides the medium for transfer of charge, as ions, inside the cell between the anode and cathode. The electrolyte is typically a liquid, such as water or other solvents, with dissolved salts, acids, or alkalis to impart ionic conductivity.

Some batteries use solid electrolytes, which are ionic conductors at the operating temperature of the cell.

The operation of a cell during discharge and charge are also shown schematically in Figure 1.4.

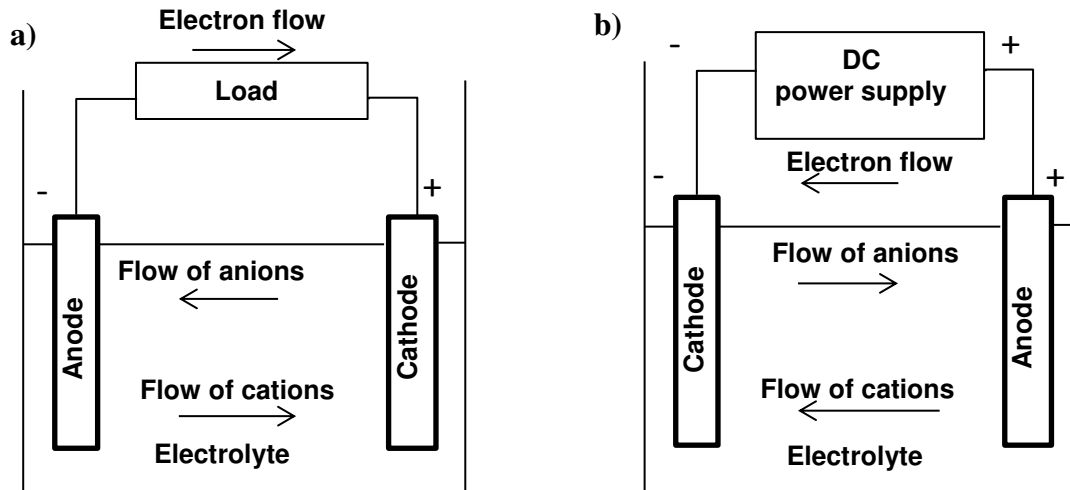


Figure 1.4. Charge - discharge principle reactions: a) Discharge electrochemical operations b) Charge electrochemical operations [7].

During the discharge, when the cell is connected to an external load, electrons flow from the anode, which is oxidized, through the external load to the cathode, where the electrons are accepted and the cathode material is reduced. The electric circuit is completed in the electrolyte by the flow of anions (negative ions) and cations (positive ions) to the anode and cathode, respectively.

During the recharge of a rechargeable or storage cell, the current flow is reversed and oxidation takes place at the positive electrode and reduction at the negative electrode, as shown in figure 1.4.b.

### 1.1.2 Classification of cells and batteries

Electrochemical cells and batteries are identified as primary (non rechargeable) or secondary (rechargeable), depending on their capability of being electrically recharged. Within this classification, other classifications are used to identify particular structures or designs.

## **Primary cells or batteries**

These batteries are not capable of being easily or effectively recharged electrically and hence, are discharged once and discarded. The primary battery is a convenient, usually inexpensive, lightweight source of packaged power for electric devices, lighting, photographic equipment, toys, memory backup, and a host of other applications, giving freedom from utility power. The general advantages of primary batteries are a good shelf life, a high energy density at low to moderate discharge rates, and an ease of use. Although large high capacity primary batteries are used in military applications, signaling, standby power, and so on, the vast majority of primary batteries are the familiar single cell cylindrical and flat button batteries or multicell batteries that use these component cells.

## **Secondary or Rechargeable Cells or Batteries**

These batteries can be recharged electrically, after discharge, to their original condition by promoting charge reaction. They are storage devices for electric energy and are known also as “storage batteries” or “accumulators.” The applications of secondary batteries can be divided in two main categories:

**1. Energy storage application:** in which the secondary battery is used as an energy-storage device, generally being electrically connected and charged by a prime energy source and delivering its energy to the load on demand. Examples are automotive and aircraft systems, emergency no-fail and standby (UPS) power sources, hybrid electric vehicles and stationary energy storage (SES) systems for electric utility load leveling.

**2. Discharged applications:** in which the secondary battery is used or discharged essentially as a primary battery, but recharged after use rather than being discarded. Secondary batteries are used in this manner as, for example, in portable consumer electronics, power tools, electric vehicles, etc., for cost savings, and in applications requiring power density beyond the capability of primary batteries.

Secondary batteries are characterized (in addition to their ability to be recharged) by a high power density, high discharge rate, flat discharge curves, and good low-temperature performance.

Their energy densities are generally lower than those of primary batteries. Their charge retention also is poorer than that of most primary batteries, although the capacity of the secondary battery can be restored by recharging. Some batteries, known as “mechanically rechargeable types,” are “recharged” by replacement of the discharged or depleted electrode, usually the metal anode, with a fresh one

## 1.2 Market battery

The market for batteries is directly related to the applications they serve, such as automobiles, cellular phones, notebook computers, and other portable electronic devices. The growth in any particular segment follows closely the introduction of new devices powered by batteries. The introduction of new materials with higher performance parameters gives the various designers freedom to incorporate new functionalities.

The total battery market, including large batteries for automobiles and small device batteries, has grown from \$ 50 billion in 2006 to about \$ 71 billion in 2008 with the Europe part representing about 20%, USA 24 %, East Asia 40% and the rest of world 16%. Nowadays this division with East Asia is increased and it will maintain the same trend next years [8].

The small device battery market will grow very rapidly due to a rapid increase in the number of small electronic and electrical devices. However this will be offset by the increased functionality and the life before recharge of this product being extended. On the other hand hybrid and pure electric vehicles will become always more popular and these call for more sophisticated and more expensive batteries. In 2009 market battery attained about 61.2 \$ billion and a growth trend of 144 % with almost 150 \$ billion in 2019 is estimated as shown in Table 1.1.

Table 1.1. Battery market growth from 2009 to 2019[8]

	<b>2009</b>	<b>2019</b>	<b>Growth</b>
	\$ billion	\$ billion	%
For small devices	36.2	93.6	159
Other	25	56	124
Total	61.2	149.6	144

The market split between types of battery is shown below for 2009 in Table 1.2. In 2019 a very different picture will emerge as showed in Figure 1.5.b with new large sectors, such as

laminar and printing batteries becoming more and more considerable by taking 15.7% of market.

Table 1.2. Battery market in terms of devices type [8]

Type	Number million	\$ billion
Coin cell	30000	1,5
Standard cylindrical	36000	18,0
Special shapes for laptops, mobile phones etc.	4300	11,0
Other	5700	5,7
TOTAL	76000	36,2

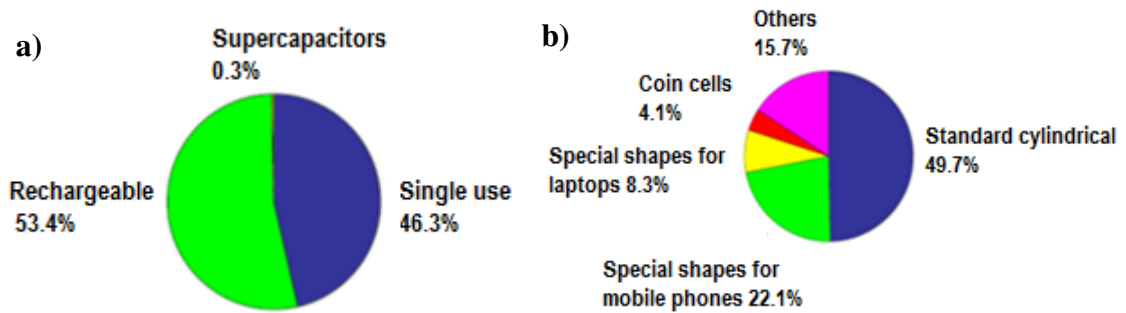


Figure 1.5. Global battery market pie-graph: a) Split storage devices market in 2009 [8], b) Split of small devices battery market in 2019.

By value, rechargeable batteries retain their dominance in portable devices followed by single use batteries and supercapacitors. Other forms of energy storage such as fuel cells at the moment don't find their place in the market as shown in Figure 1.5.b.

### Lithium - ion battery market

Lithium - ion batteries (LIBs) were commercially developed in the 1990's. Since then, the market for lithium ion battery has grown to \$11 billion in 2010 and it is expected to reach \$ 43 billion by 2020. The sales of lithium - ion cells are shown in figure 1.6. The slower growth period, around 2000, occurred when cell production in China and Korea began to ramp up. The cell producers accomplished the performance improvements through engineering improvements in cell design, new carbon materials for anode and automated high speed production to reduce the cost. The major cell manufacturers are listed in Table 1.3. There are

no major lithium - ion manufacturers in the United States or in Europe. Even though they constitute large markets for devices powered by Li ion batteries [9].

Table 1.3. Major cell manufacturers in the world [10]

<b>Manufacturer</b>	<b>Percentage of total</b> %
Sanyo	27,50
Sony	13,30
Samsung	10,88
Matsuchita	10,07

Due to the high value of the energy content, LIBs have triggered the growth of the market of electronic small devices such as mobile phones, lap – top computers etc. In addition LIBs are today produced by billions of units per year as shown in Figure 1.6.

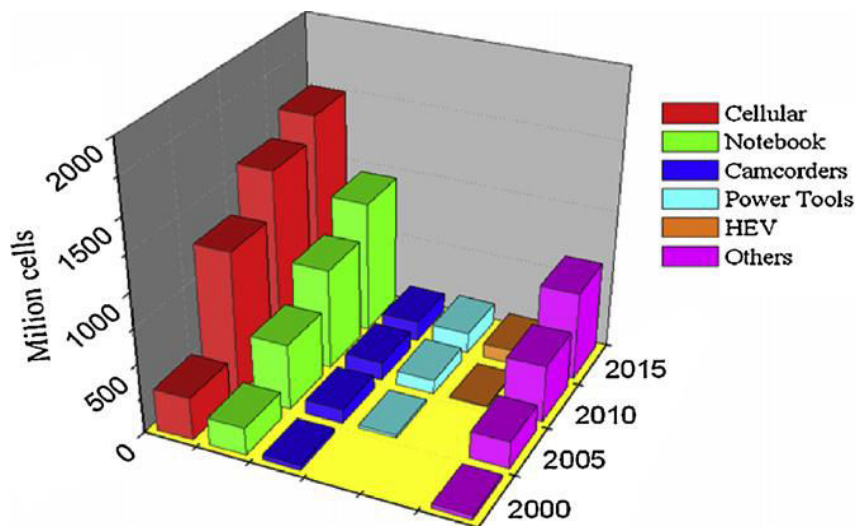


Figure 1.6. LiBs market [11]

Starting in 2004 a shift in the market application began to occur, as showed in Figure 1.7 in one segment basically they drive to increase capacity and performance for the competitive notebook and cellular phone applications. This requires the development and introduction of higher capacity, higher performance anode and cathode materials. In the same line, new anode materials have been developed based on nanostructured lithium alloy anodes.

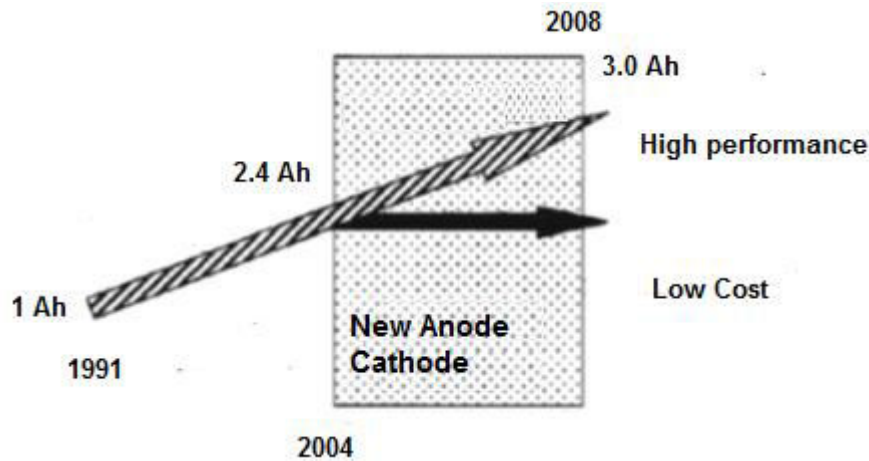


Figure 1.7. Split development in LIB market [12]

### **Thin and Printed battery market**

Another type of batteries emerged in the global battery market and became more and more important: printed and thin film batteries. All these types of batteries are widely used for large area flexible electronic applications. In addition these batteries have major advantages in such application as smart card for smart packaging sector. The radio frequency identification (RFID) market is another sector which seems to have the potential as a very high volume application for printable batteries. Figure 1.8 shows how thin and printed batteries will have an increment trend of almost 600 % in 2019 compared to 2014 incomes.

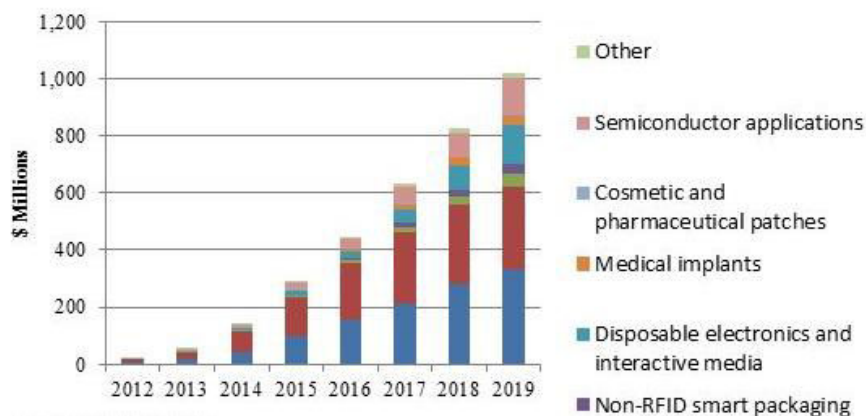


Figure 1.8. Thin film and printed battery market evolution [8]

### **1.2.2 Design and manufacturing batteries**

Proper design of the battery is important to assure optimum, reliable, and safe operation. It is important to point out that the performance of a cell in a battery can be significantly different from that of an individual cell depending on the particular environment of that cell in the battery. Such factors as the cell uniformity, number of cells, series or parallel connections, battery case material and design, can affect the performance of the battery. Other conditions, such as discharge and charge current and temperature, can also determine the good response of the battery. The problem is usually affected by conditions of use, such as high-rate charging and discharging, operation, and extreme temperatures and other conditions which tend to increase the variability of the cells within the battery. Another factor that must be considered, particularly with newly developing battery technologies, is the difficulty of scaling up laboratory data based on smaller individual batteries to multicells batteries using larger cells manufactured on a production line [13].

The following constructional features also should be considered in the design and fabrication of batteries:

#### **1. Intercell connections**

Welding of conductive tabs between cells is the preferred method of intercell connection for most of battery systems. Resistance spot welding is the welding method of choice. Care must be taken to ensure a proper weld without burning through the cell container. Excessive welding temperatures could also result in damage to the internal cell components. Typically two electrodes made of a copper alloy are embedded. A current path is established between the electrodes. Melting and fusion occur at the interface of the tab and the cell due to resistance heating [13]. In all instances at least two weld spot should be made at each connection joint. The last preferred method of battery connections is the use of pressure contacts. This type of connection can be affected by corrosion at the contact points.

#### **2. Encapsulation of cells**

Most applications require that the cells within the battery be rigidly fixed in position. In many instances this involves the encapsulation of the cells with epoxy, foams, tar, or other suitable potting materials. Care must be taken to prevent the potting material from blocking the vent

mechanism of the cells. A common technique is to orient the cell vents in the same direction and encapsulate the battery to a level below the vent.

### **3. Packaging configuration and materials**

Careful design of the case should include the following points:

1. Materials must be compatible with the cell chemistry chosen.
2. Flam - retardant materials may be used to comply with end use requirements.
3. Adequate battery venting must allow for the release of vented cell gases. In sealed batteries this requires the use of a pressure relief valve or breather mechanism
4. The design must provide for effective dissipation of heat to limit the temperature rise use and especially during charge [13].

### **4. Terminals and contact materials**

Terminal material must be compatible with the environment of the battery contents as well as the surroundings. Non corrosive materials should be selected. For example Nickel-cadmium batteries use solid nickel contacts to minimize corrosion at the terminal contact [13].

### **1.2.3 Design and manufacturing of Li - ion batteries**

The lithium battery is a high energy system and must be treated with care. Electrical, mechanical and thermal abuse can initiate thermal runaway conditions that can cause the cell to self destruct. The internal designs for the Li - ion cell must result in uniform current density across, and through, the electrode structures. Large surface area electrodes are employed to give the cells high rate performance. The pore structure and the combination of conductive agent (such as carbon) give good contact to all the particles of the active material. High contact is essential between the active materials, the conductive carbon and the current collector, for full utilization of the active materials and for good efficiency during high rate performance. A binder, usually a polymer such as polyvinylidene fluoride (PVdF), is used to hold the electrode structure together and bond it to the current collector. The binder needs some flexibility to accommodate the volume changes that occur in the active materials during charge and discharge. Additives to the coating slurry may improve contact of the active mass to the current collectors. The collector foils may be coated with a conductive carbon paint that

## Flexible lithium - ion batteries: State of the art

protects surfaces from corrosion and to improve the contact of the active mass to the current collector. Figure 1.9 depicts a generalized flow chart for the assembly process.

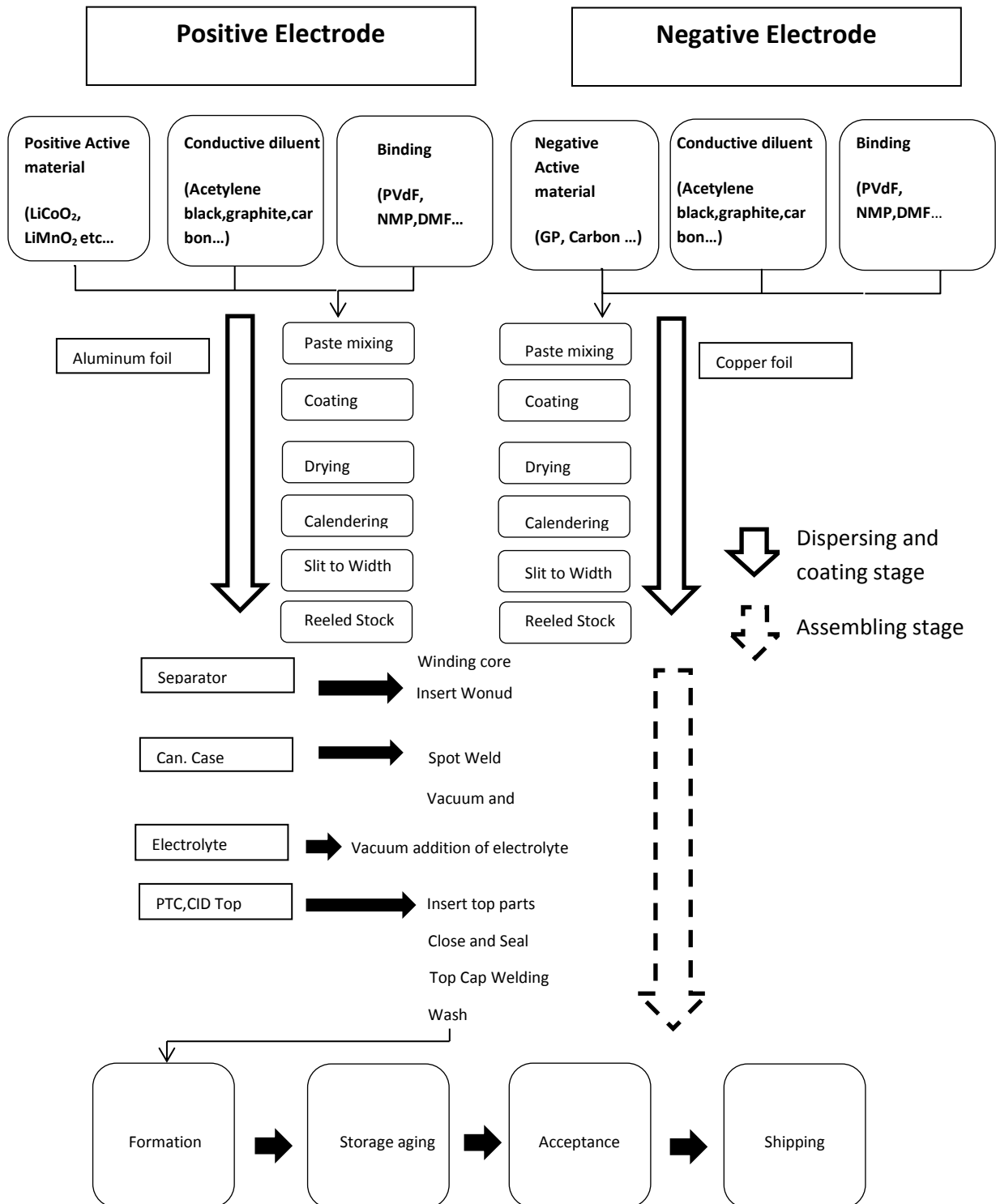


Figure 1.9. Process outline for Lithium – ion cell fabrication [14]

### Coating electrode process

The coating process is a critical element in ensuring a high capacity and high reliability product. The initial steps in the preparation of the active mass determine the outcome. Figure 1.10 illustrates a schematic electrode coating operation. Cohen and Guttoff [15] describe a methodology to arrive at the best coating technique, based on the rheology of the coating slurry. Common types of coaters include extrusion, reverse roll coating and knife over all or doctor blade methods. Coated foils pass through an oven to evaporate the solvent and leave a precise amount of active mass on the foil. Many coating solvents are classed as hazardous and cannot be released in atmosphere. As a cost saving measure, the solvent is generally recovered for reuse in the process.

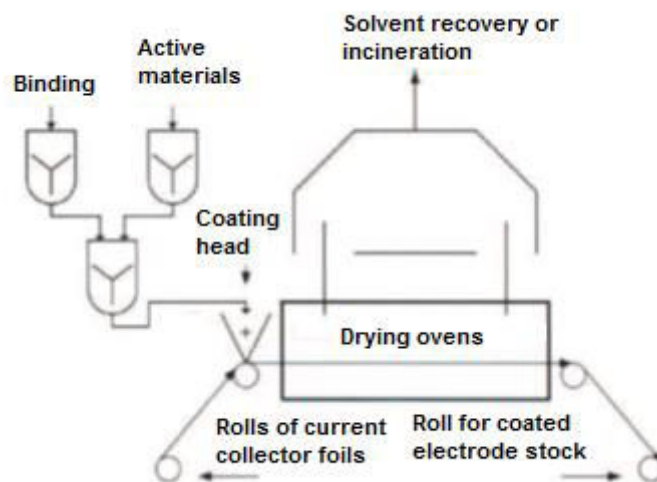


Figure 1.10. Coating process for anode and cathode electrodes [14]

The coating operations begin by mixing the active materials, polymer binder and conductive diluent. The objective of the dry blend is to coat the nonconductive particles of the active material with a thin film of the conductive carbon. This coating provides electrical contact to the current collector for full utilization of all the particles in the mix. The polymer is dissolved in the coating solvent in a separate container. The dry mix blend and the solvent solution are then combined to form slurry as described in Figure 1.10. An intensive mixing procedure is used to dry the blend of the non-conducting active materials and the carbon before adding the coating solvent and binder. The solvent addition is used to adjust the viscosity of the slurry for

the coating operation. Generally PVdF is the binder of choice and the solvent is N-methylpyrrolidone (NMP). The slurry for the mixing operations is placed in sealed container which serves as the reservoir and transfer medium for the coating operations. Precise amounts of coating slurry are pumped from the storage container with a gear pump, in order to avoid any entrainment of air in the fluid going to the coating head [16]. After coating, the rolls are calendered to produce a precision thickness, and then cut for the specific cell design. Two or three passes through the calender may be required to arrive at the desired thickness. The final thickness control is essential for the winding step in the assembly process so that the electrode coil has the proper dimension. The uniformity of the coating thickness and composition is critical to good performance as well as in the subsequent cell assembly processes. It is possible to coat both sides simultaneously, but this is not done in practice, as it requires exceptionally good process control. Usually the electrode stock is passed through the coating operation twice to coat each side of the current collector foil. The coated foils are then calendered to compact the coated layer. Two passes provide better control of pore size and thickness in the final product. The electrode foils are then slit to size for the cell assembly.

### **Cell assembling process**

Most lithium - ion cells, both cylindrical and prismatic, use the wound core construction. The strips have the required loading of active material, length, width and thickness to match cell designs. The coating operation produces interrupted coating to match the length of the cell. The winding machines are designated to operate automatically using strips of anode, cathode and separator. The operation starts by welding the tabs onto the uncoated section of the foils. The winding machine then cuts the strip to the proper length and winds the combination anode - cathode - separator into a tight coil or bobbin. As the wound core increases in diameter, the winding machine automatically compensates to maintain constant tensions as the coil increases in diameter for close tolerance on the diameter. Any irregularity leads to a gap between the separator and electrode, which may cause malfunctions, shortened cycle life. The winding operations are complex and require a high level of precision and automatic control. Figure 1.11 illustrates a typical production process for cylindrical cells. The winding operation uses reels of anode and cathode from the coating, calendering and slitting operations. The process for fabricating prismatic cell is very similar as shown in Figure 1.12.

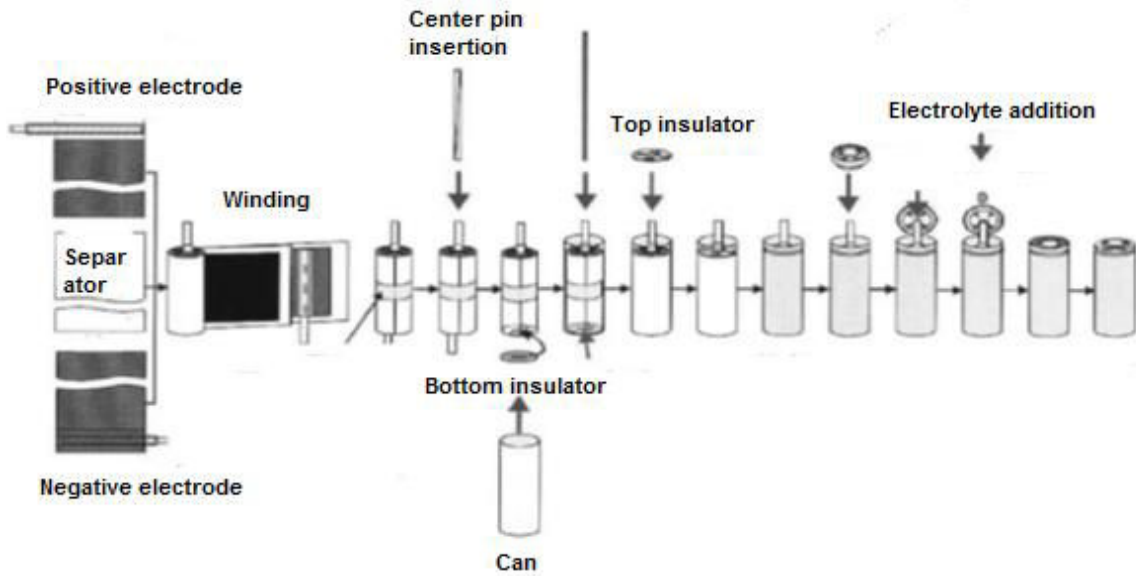


Figure 1.11. Cylindrical cell assembling process [16]

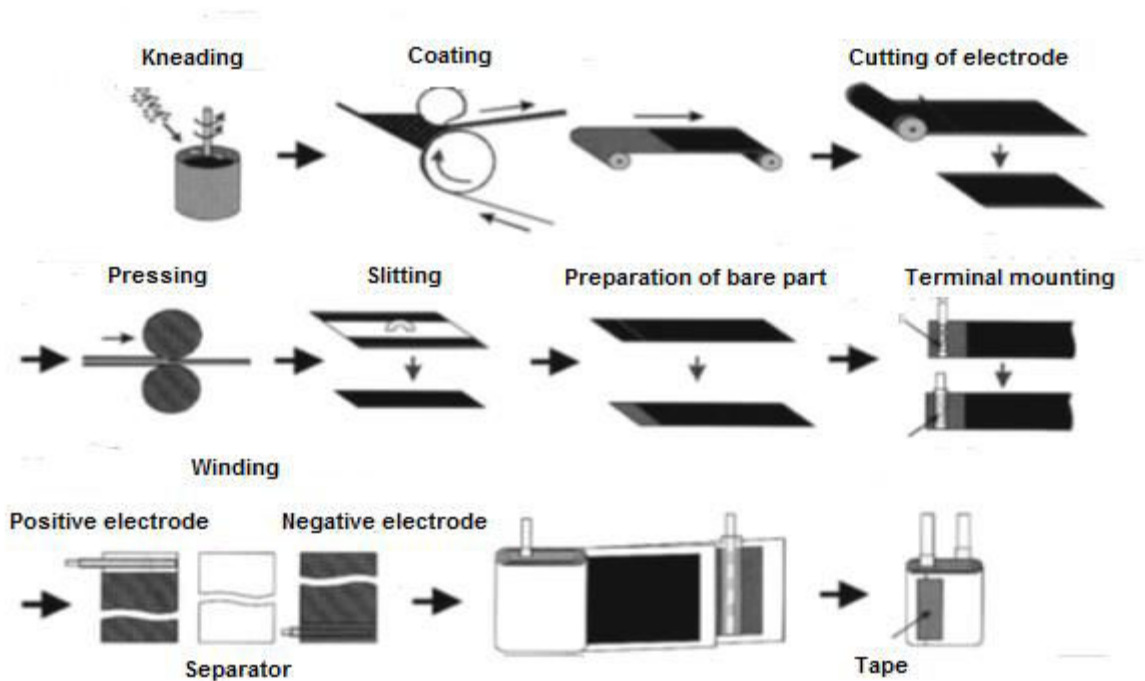


Figure 1.12. Prismatic cell assembling process [16]

After winding the coil is checked for internal shorts before being inserted into the can. The bobbin, with a typical design called “jelly roll”, is inserted into the can so that the can provides constant pressure to hold the anode and cathode close together, and eliminate any voids between them. Unless all operations are carried out in a dry room or dry box. The

adsorbed water in the active material must be removed by heat and vacuum before the electrolyte filling process.

Electrolyte is inserted into the cell by a precision pump and vacuum filled to ensure that the electrolyte permeates and completely fills the available porosity. The electrolyte amount is generally tailored by trial and error method. After filling the cell with electrolyte, the cell is sealed by controlled compression of a polymer gasket placed between the cell can and the top plate. A safety device is contained in the cell top plate to prevent dangerous temperature and pressure from developing internal to the cell [16]

### 1.3 Lithium - ion batteries (LiBs)

The motivation for using a battery technology based on lithium metal relied on the fact that lithium is the most electronegative (-3.04 V versus standard hydrogen electrode) as well as the lightest metal (equivalent weight  $M = 6.94 \text{ g/mol}^{-1}$  and specific gravity  $\rho = 0.53 \text{ g.cm}^{-3}$ ), thus facilitating the design of storage systems with high energy density. Figure 1.13 shows the schematic illustration of the discharge and charge process of lithium rechargeable battery.

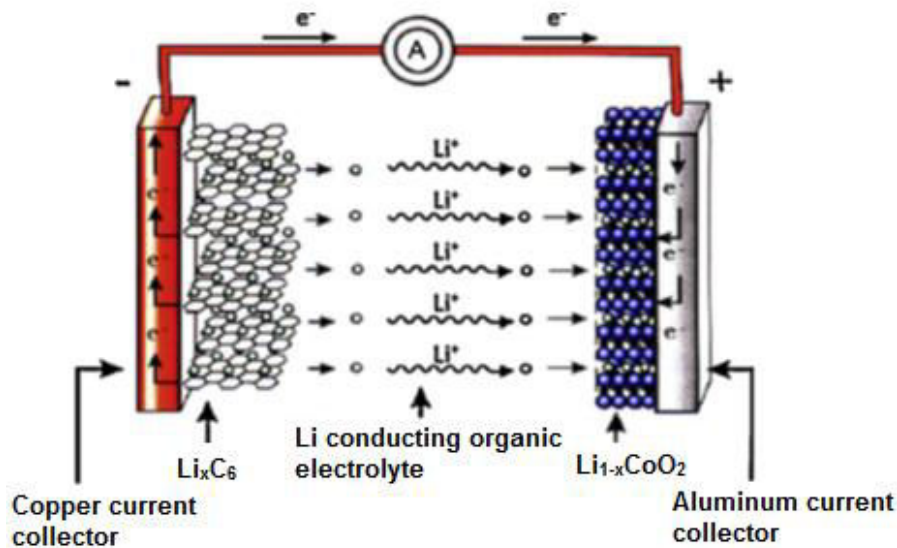
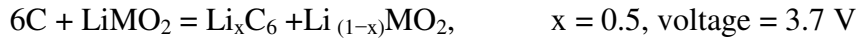


Figure 1.13. Lithium - ion battery function scheme during discharge [14]

In its most conventional structure a lithium ion battery contains a graphite anode (C), a cathode formed by a lithium metal oxide (LiMO<sub>2</sub>) and an electrolyte consisting of lithium salt in a mixed organic solvent imbedded in a separator felt. These batteries operate on a process:



involving the reversible extraction and insertion of lithium ions between the two electrodes with a concomitant removal and addition of electrons.

Among the various existing technologies, LiBs, because of their high energy density and design flexibility, outperform other systems, accounting for 63% of worldwide sales values in portable batteries. The share of worldwide sales for nickel – cadmium (Ni-Cd) and Nickel – metal hydride (NiMH) batteries is 23 % and 14% respectively. Ni-Cd batteries remain the most suitable technologies for high power applications (for example power tools) [17]. Figure 1.14 compares different rechargeable battery technology.

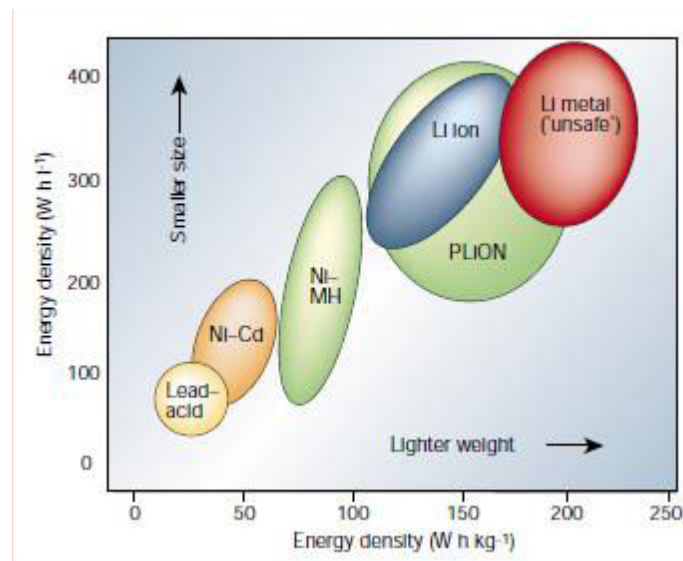


Figure 1.14. Comparison of the different battery technologies in terms of volumetric and gravimetric energy density [17]

### 1.3.1 Electrodes

Many studies of lithium ion batteries have been focused on improving electrochemical performances of electrode materials and lowering the cost. The nature of the active material is of primary importance to the resulting cell energy density. The main features of the active material which determine cell energy are the number of electrons they can store per unit volume or weight (volumetric capacity or specific capacity) and the electrochemical potential they can produce.

#### **Positive Active materials**

The choice of the active material depends on different factors. For lithium ion batteries, because of carbon negative electrode is not lithiated (no lithium ions), the positive one acts as a source of lithium, thus requiring use of lithium based intercalation compounds stable in air to facilitate the cell assembly.  $\text{LiCoO}_2$  is most used in commercial Lithium - ion batteries with a deintercalating and intercalating lithium process around 4V. Safety reason has limited  $\text{LiCoO}_2$  commercial production.[17]

Several routes were investigated to overcome these safety issues:

1. **Stabilization of the layered structural framework by a cationic substitute:** A series of lithium nickel manganese oxide (NMC) was proposed in literature. One example is  $\text{Li}(\text{Ni}_{1/3}\text{Co}_{1/3}\text{Mn}_{1/3})\text{O}_2$ . Yabuchi et al. [18] reported a reversible capacity of about 200 mAh/g in a range voltage between 2.5 and 4.6 V. Other authors report electrochemically properties of structures based on lithium, nickel, cobalt and aluminum oxides (NCA) where aluminum has been used for partial replacement of cobalt in order to improve electrochemical performances. Ju et al. [19] reported a  $\text{Li}(\text{Ni}_{0.8}\text{Co}_{0.15}\text{Al}_{0.05})\text{O}_2$  structure with a specific capacity of 190 mAh/g at a current rate of 0.1C.
2. **Synthesis of polyanionic structures with M-O-X bonds:** where by changing the nature of X element redox potential can be tuned. For example  $\text{LiFePO}_4$  can presently be used at 90% of its theoretical capacity (170 mAh/g) and thus is a serious candidate for the next generation of Li -ion cells.

## Negative active materials

As a result of numerous chemical modifications, carbon negative electrodes display electrochemical performances that are improving continuously [20]. Reversible capacity of around 400 mAh/g is now being reached, compared with a practical value of 350 mAh/g for graphite. In parallel research efforts are focused on searching carbon alternatives in the hope of finding materials with larger capacities and slightly more positive intercalation voltages compared to  $\text{Li}/\text{Li}^+$ . Lithium alloys (Li alloys) are one example. While attractive in terms of gravimetric capacity, Li alloys suffer from cyclability resulting from large lithium driven volume swings (up to 270%), which cause disintegration and hence a loss of electrical contacts between particles. Thackeray et al. [21] developed selecting alloys that show a strong structural relationship to their lithiated products. This alloys provided reversible capacity between 250 and 300 mAh/g. One drawback of these electrodes is their poor cyclability, particularly upon the initial cycle. Tin based materials have been extensively studied as substitute for graphite [22]. Metallic tin has a large theoretical capacity (992 mAh/g) that is much better than graphite (372 mAh/g). The crucial drawback in the use of tin alloys is the huge volume change during charge and discharge reactions ( $> 300\%$ ) that leads to mechanical strain and thus to pulverization and fade of capacity of the electrode [23].

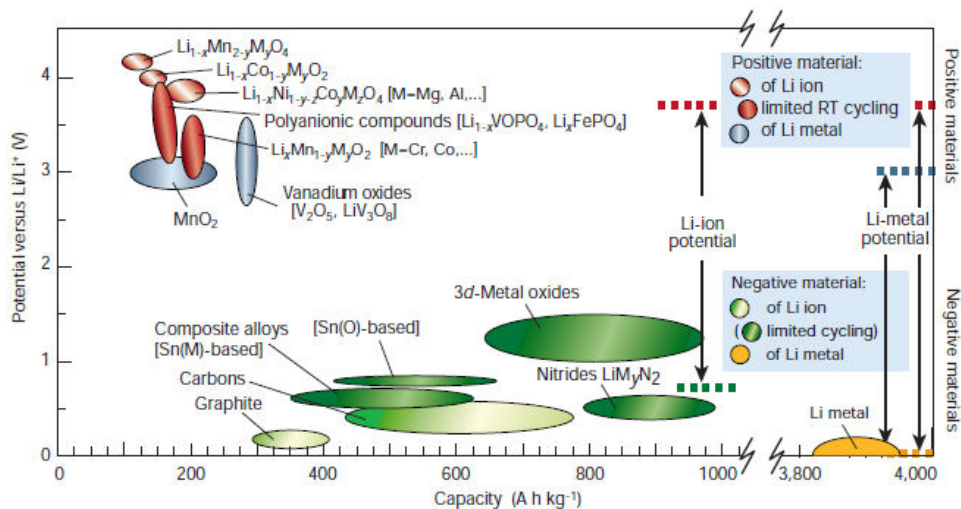


Figure 1.15. Performance of cathode and anode for secondary batteries [17]

Figure 1.15 shows voltage versus capacity for positive and negative electrodes. The difference

in capacity between Li metal and other negative materials is evident. For this reason, there is still great interest in solving the problem of dendrite growth in Lithium based electrodes.

### 1.3.2 Separator

A separator is a porous membrane placed between electrodes of opposite polarity, permeable to ionic flow but preventing electric contact of the electrodes [24]. Owing to continuous advances in battery technology, separator functions has also become more demanding and complex. They should be very good electronic insulator and have the capability of conducting ions by either intrinsic ionic conductor or by soaking electrolyte. Their role is to minimize any processes that adversely affect electrochemical energy efficiency of the batteries. Separator for batteries can be divided in different types, depending on their physical and chemical characteristics. In most batteries, the separators are either made of nonwoven fabrics or polymer films. Batteries operate near ambient temperature use separators fabricated from organic materials such as cellulosic papers, polymers or inorganic materials as well as asbestos, glass wool and SiO<sub>2</sub>. Lithium - ion batteries with organic electrolytes mostly use microporous film based on polyolefins materials and other additives, depending on the nature of the battery (Table 1.4)

Table 1.4. Types of separator used in different secondary lithium batteries [24]

Battery system	Type of separator	Composition
Lithium ion (liquid electrolyte)	microporous	Polyolefins (PE,PP..) PVdF
Lithium ion gel polymer	microporous	Polyolefins (PE,PP..) coated with PVdF or other gelling agents
Lithium polymer	microporous	Poly(ethylene oxide) with lithium salt

### Lithium - ion separator batteries

Since introduction of Li - ion batteries in 1990's, various studies on separators have been done because of LiBs require different separators compared with separators for conventional batteries. Microporous separators using polyolefin have been developed and extensively used. They have been found to be compatible with the cell chemistry and can be cycled for

several hundred cycles without significant degradation in chemical or physical properties. Microporous membrane in use are thin ( $< 30 \mu\text{m}$ ) and are made of polyethylene (PE), polypropylene (PP) or laminates of polyethylene and polypropylene. Non woven materials have also been developed for lithium ion cells but have not completely accepted, in part due to the difficulty to obtain a thin material with good uniformity and high strength [24]. Manufacturing process can be realized in two ways; dry and wet processes. Both usually employed one or more orientation steps to impart porosity or increase tensile strength. Figure 1.16 shows surface images of commercial separators taken by SEM instrument and table 1.5 resumes main properties of commercial separators for LIB.

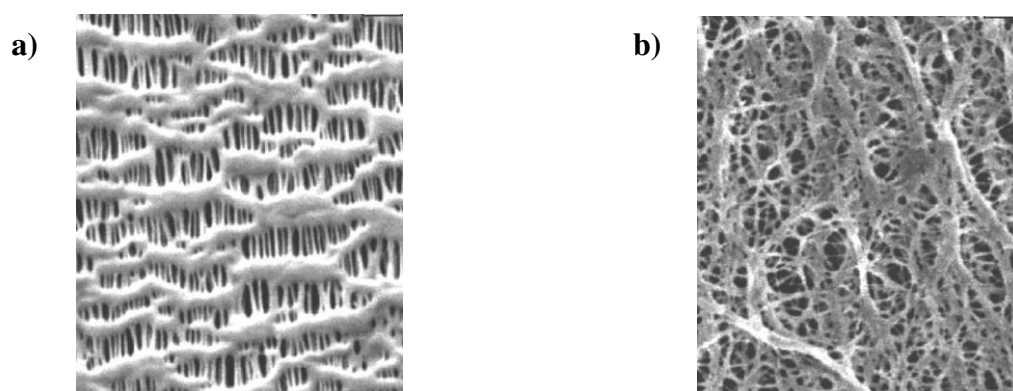


Figure 1.16. Microstructure of the microporous polyolefin membranes made by a) dry process and b) wet process [24]

Table 1.5. Typical properties of commercial microporous membrane [24]

Separator properties	Celgard <sup>®</sup>			Asahi Hipore <sup>®</sup>	Tonen Setela <sup>®</sup>
	2730	2400	2320		
Structure	Single layer	Single layer	Trilayer	Single layer	Single layer
Composition	PE	PP	PP/PE/PP	PE	PE
Thickness ( $\mu\text{m}$ )	20	25	20	25	25
Air permeability (s/10ml)	22	24	20	21	26
Ionic resistivity ( $\Omega \text{cm}^2$ )*	2.23	2.55	1.36	2.66	2.56
Porosity	43	40	42	40	41
Melting temperature ( $^{\circ}\text{C}$ )	135	165	135/165	138	137

\* In 1 M LiPF<sub>6</sub> EC:EMC (30:70 by volume)

### 1.3.3 Electrolyte

Because electrolytes interact closely with electrodes, during the operation of charge and discharge, their effect on cell performances has been thoroughly studied during these years.

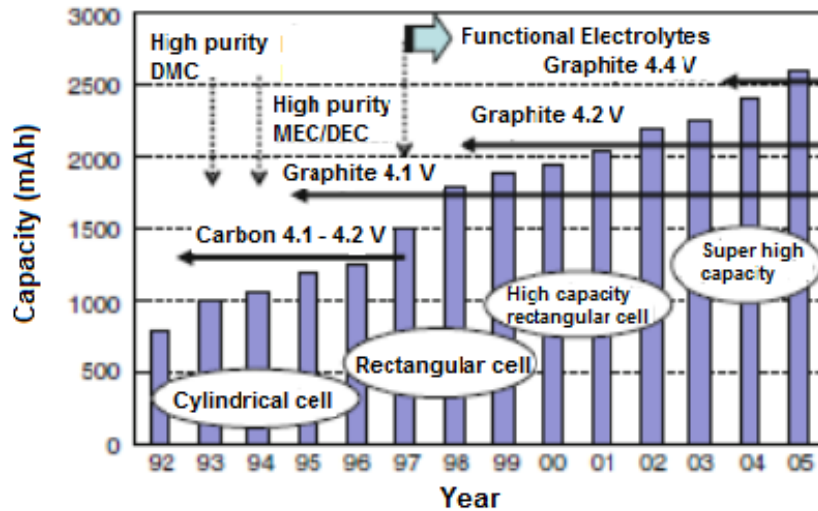


Figure 1.17. Relation between batteries and electrolytes evolution [25]

As shown in Figure 1.17 the invention of electrolytes, more and more adjusted for lithium - ion batteries requirements, made possible the use of high performance graphite, resulting in increase of charging voltage.

Table 1.6 compares ionic conduction in polymer electrolytes and liquid electrolytes.

Table 1.6. Behavior of polymer and liquid electrolytes as function of environment and phenomena involved [26]

Phenomenon/environment	Electrolyte behavior	
	Polymer	Liquid
Matrix	Flexible	Mobile
Position of ion sites	Change as chains flex	None
Solution	Yes	Yes
Solvation	By matrix : roll on mechanism	Forms mobile solvated ions
Participation of charged ion clusters	Often yes	Usually no, except in molten salts

## Liquid electrolyte

Most compositions of lithium electrolytes are based on solutions of one or more lithium salts in mixture of two or more solvents as showed in Table 1.7.

Table 1.7. Organic carbonates and esters properties as electrolyte solvents in terms of molecular weight ( $M_w$ ), melting temperature ( $T_m$ ), boiling temperature ( $T_b$ ), viscosity ( $\eta$ ) and density ( $d$ ) inspired by [27].

<b>Solvent</b>	<b>Mw</b>	<b>T<sub>m</sub> (°C)</b>	<b>T<sub>b</sub> (°C)</b>	<b><math>\eta</math> (cP) 25°C</b>	<b>d (g cm<sup>-3</sup>)</b>
EC	88	36.4	248	1.90 (40 °C)	1.321
PC	102	-45.8	242	2,53	1.200
DMC	90	4.6	240	0.59 (20 °C)	1.063
DEC	118	-74.3	91	0.75	0.969
EMC	104	-53	126	0.65	1.001

## Solvent

The ideal electrolyte solvent should meet minimal criteria: 1) it should be able to dissolve salts to sufficient concentration that means a high dielectric constant. 2) It should have low viscosity to facilitate ions transport. 3) It should remain inert to all cell components and be safe, nontoxic and economic.

During the years, studies have been focused on different solvent families, (propylene carbonate [28], ethers [29-30-31]) without finding optimum compromise due to capacity fading [32-33-34]; poor capacity retention [35-36-37] respectively. Even if Scrosati et al. had already demonstrated that ethylene carbonate (EC) based electrolyte showed improvements in bulk ion conductivity and in interfacial properties, the real breakthrough in LiBs occurred in 1994 when Tarascon et al. formulated a solvent based on a linear carbonates, dimethyl carbonate (DMC) with ethylene carbonate (EC) as cosolvent [38]. DMC forms homogenous mixture with EC and it remains stable on a spinel cathode surface up to 5.0 V [39–40]. This formulation was quickly adopted by the researchers and manufacturers [41-42].

## Lithium salts

The available choice of lithium salts for electrolyte application is limited. Dudley et al. [43] described over 150 electrolyte solvents composition but only 5 lithium salts (Table 1.8).

Because of the small ionic radius, most simple salts of lithium didn't find minimum solubility requirement in low dielectric media.

Table 1.8. Main properties of typical salts used in lithium ion batteries solvents in terms of molecular weight ( $M_w$ ), melting temperature ( $T_m$ ), and conductivity ( $\sigma$ ) [25]

Salt	Mw	Tm (°C)	$\sigma$ (mScm <sup>-1</sup> ) 1M 25°C	
			In PC	In EC/DMC
LiBF <sub>4</sub>	93.9	293	3.4	4.9
LiPF <sub>6</sub>	151.9	200	5.8	10.7
LiAsF <sub>6</sub>	195.9	340	5.7	11.1
LiClO <sub>4</sub>	106.4	236	5.6	8.4

Lithium hexafluoro phosphate LiPF<sub>6</sub> is the most commercialized salts thanks to combinations of properties. In non aqueous solvents based on mixed alkyl carbonates, LiPF<sub>6</sub> remains one of the most conducting salts. This high conductivity results in an excellent compromise between its ionic mobility and dissociation constant.

### 1.3.4 Solid electrolyte interface (SEI)

When battery operates, electrolyte solvent can affect process for graphitic anode. Solvents decompose reductively on the carbonaceous anode and the decomposition product forms a protective film. When the surface is covered, the film prevents further decomposition. This layer is an ionic conductor but an electronic insulator. This film is named 'solid electrolyte interface' (SEI). SEI determines safety power capability and cycle life of battery [44-45]. Different studies highlight the composition of the SEI layer. Close to the electrode surface emerges an inorganic matrix consisting mainly of LiF and Li<sub>2</sub>CO<sub>3</sub>, while out the electrode surface a porous organic or polymer layer extending out of the electrode surface [46]. The nature of the electrode plays an important role on the solvent decomposition mechanism [47]. SEI thickness can range from 20 to several hundred Angstroms. Large crystals of LiF have been also found in this matrix [48] as shown in Figure 1.18.

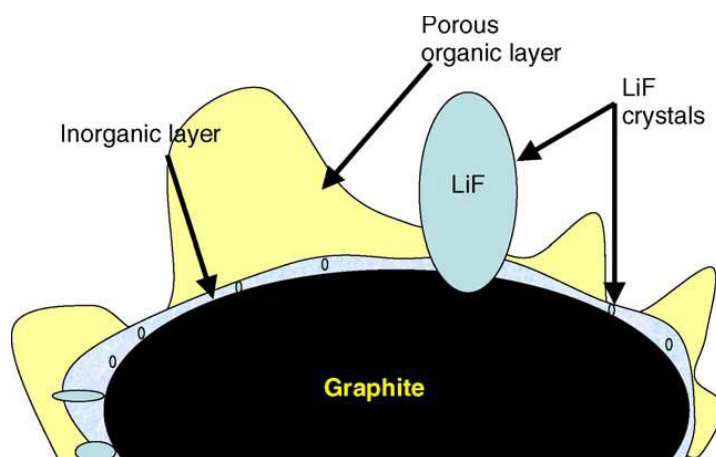


Figure 1.18. SEI formation process onto a graphite particle with formation of LiF crystals close to the surface and porous organic layer out of the surface. [44]

## Solid electrolyte

Solid state ionics have been discovered more than 150 years ago (Faraday reported the transport of silver ions through silver sulfide in 1834) but they become a very attractive domain in the last 40 years [49-50]. A chronology of various types of solid electrolytes developed since 1950 is showed in Table 1.9.

Table 1.9. Chronology of solid electrolyte cells since 1950 to 1999 in terms of conductivity [50]

Date	Electrolyte	Log ( $\sigma$ )Scm <sup>-1</sup>	Typical cell system
1950-1960	AgI	-5	Ag/V <sub>2</sub> O <sub>3</sub>
1965-1975	Na $\beta$ -alumina	-1,5	Na-Hg/I <sub>2</sub> PC
1980-1986	Li <sub>0,36</sub> I <sub>0,14</sub> O <sub>0,007</sub> P <sub>0,11</sub> S <sub>0,38</sub>	-3,3	Li/TiS <sub>2</sub>
1985-1992	Plasticized (Gel) SPE	-3	Li/V <sub>6</sub> O <sub>13</sub>
1995-1999	LiPON	-5,6	Li/LiMn <sub>2</sub> O <sub>4</sub>

Different kinds of materials have been explored to enhance ionic conductivity in solid state materials. These materials have ranged by Tatsuminago et al. [51] in different categories: 1) sulfide solid electrolytes (amorphous and crystalline) with a conductivity of 10<sup>-3</sup> Scm<sup>-1</sup>[52-53], 2) crystalline oxide solid electrolyte with a conductivity ranging between 10<sup>-5</sup> and 10<sup>-4</sup> Scm<sup>-1</sup> [54-55], 3) amorphous oxide solid electrolytes with poor ionic conductivity such as LiPON electrolyte with a ionic conductivity of 3.3 10<sup>-6</sup> Scm<sup>-1</sup>[56]. Even though poor ionic conduction of solid electrolytes it is possible to make electronic devices by using solid

electrolyte. This is a result of a manufacturing ability to form very thin film and polymeric gel electrolytes as thin film which maximize interfacial contact area between the elements of the cell. Thus the ohmic impedance contribution can be reduced.

### **Gel – polymer electrolyte**

The development of polymer electrolytes has been in progress in the last years. With the use of polymer electrolytes in lithium batteries, high specific energy, safe operation and low cost of fabrication can be expected. At present various research units are involved in developing polymer lithium batteries. For example the PolyPlus Battery<sup>®</sup> is developing room temperature lithium polymer battery which would have specific energy as high as 500 Wh/kg [57]. Purposes to develop polymer electrolytes for lithium ion batteries are different: 1) suppression of dendrite growth developing during charging periods in liquid electrolytes. 2) Enhanced endurance to varying electrode volume. This feature enable the construction of batteries in which polymer conforms volume changes that occur during charge - discharge cycling. 3) Reduced reactivity with liquid electrolyte. 4) Better shape flexibility and manufacturing integrity.

Nowadays, several types of polymer electrolytes have been developed. Table 1.10 lists some polymers used as hosts for polymer electrolytes [58].

Table 1.10. Physical properties of polymers used as hosts for polymer electrolyte [58]

<b>Polymer host</b>	<b>Glass transition temperature (T<sub>g</sub>)</b>	<b>Melting point T<sub>m</sub> (°C)</b>
Poly(ethylene oxide)	-64	65
Poly(propylene oxide)	-60	-
Poly(dimethylsiloxane)	-127	-40
Poly(methyl methacrylate)	105	-
Poly(vinylidene fluoride)	-40	171

Alagmir et al. [59] group all polymers systems in two categories: pure solid polymer (SPE) and gelled polymer electrolyte systems (GPE).

SPEs are composed of lithium salts (table 2.5) dissolved in high molecular weight polyether hosts (e.g. PEO and PPO) which act as solid solvents. They are generally manufactured in thin film configuration by using solvent evaporation process techniques.

GPEs are characterized by a higher ambient ionic conductivity but poorer mechanism properties. They are obtained by incorporating a larger quantity of liquid solvent to a polymer matrix capable of forming a stable gel with the polymer host structure. Owing to their unique hybrid structure, neither liquid nor solid, GPEs exhibits simultaneously cohesive property of solids and diffusive transport properties of liquid. Generally gel polymers matrix is obtained by a chemical or physical cross linking process. Nair et al. [60-61] proposed a methachrylic based thermo-set gel-polymer electrolyte prepared by free radical photopolymerisation (UV-curing). This preparation process is reliable and rapid. The obtained membrane showed good behaviour in terms of ionic conductivity, interfacial stability with Li-metal electrode and cyclability.

### **1.3.5 Alternative electrodes elaboration process for low cost and large area**

Although lithium - ion batteries are compact and volumetrically efficient, the “jellyroll” strategy design limits batteries shapes in rectangular and cylindrical which constraint the factor form of devices. Recent efforts have been done by researchers to overcome this constraint towards development of unconventional battery design that can be accommodated in a device without affecting their form factors [62]. These devices can be paper-thin, lightweight and manufactured by low cost processes as described in following sections.

### **1.3.6 Printed elaboration process**

In printed electronic, several printing techniques have been used with promising results in terms of reproducibility and printing quality. The majority of the work has involved, up to now, ink – jet, screen printing and flexography technologies and recently paintable technique deposition [63]. Figure 1.19 illustrates the schematic representation of each printing process and table 1.11 describes main properties of printing processes.

Table 1.11. Main printing techniques and their properties [63]

Printing process	Printing principle	Drying	Dynamic viscosity (Pa s)	Comments
Offset	Ink splitting	Absorption	40-100	High print quality
Gravure	Ink splitting	Evaporation of solvents	0.05-0.02	Thick printed layer
Flexography	Ink splitting	Evaporation of solvents	0.05-0.5	Medium quality
Inkjet	Pressure impulse	Evaporation/absorption	1-30	Thick printed layer
Screen printing	Pressing ink	Dependent on ink type	Dependent on the mesh width	Slow drying

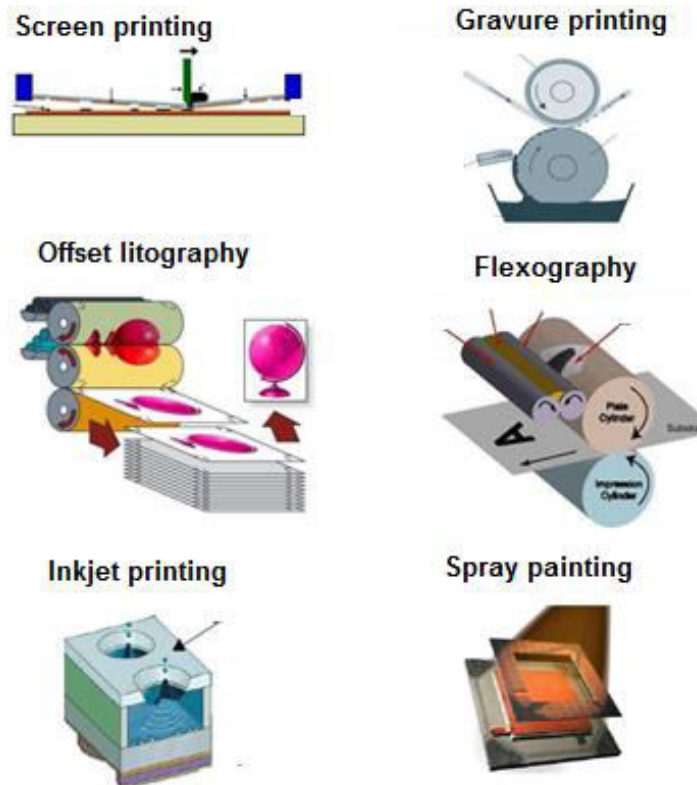


Figure 1.19. Main Printable and spray deposition techniques

### **Screen printing process**

Figure 1.20 illustrates screen printing process. Ink is transferred to the substrate through a stencil or a textile mesh supported by synthetic fibres or metal stretched tightly on a frame. During printing process, a squeegee moves the paste across the screen. This action causes a decrease in the viscosity of the paste and allows transfer of ink through the patterned area. One time squeegee passed, the screen peels off and the paste viscosity returns to initial value before squeegee deformation.

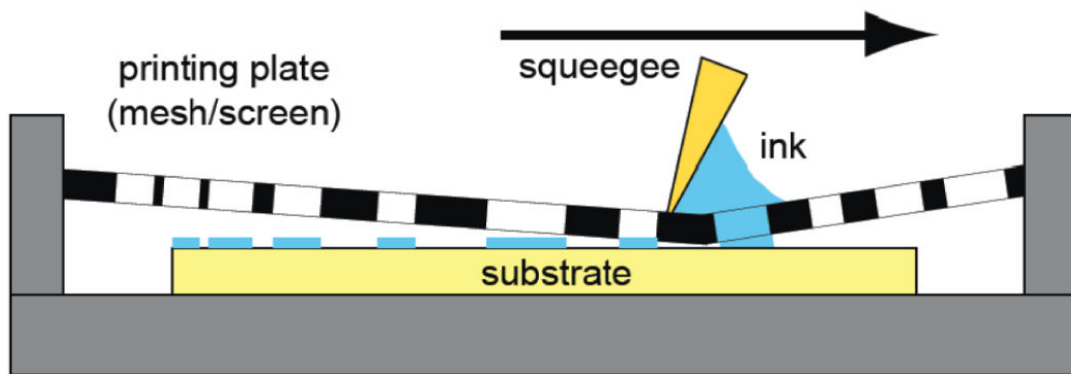


Figure 1.20. Screen printing process outline [63]

Different parameters affect quality of screen printed motifs [64]:

**Viscosity of the ink:** Screen printed process requires a precise range of viscosity to insure a good printed. In order to have a properly transfer, ink has to present a pseudoplastic rheological behaviour with a decrement of viscosity when shear stress or shear rate increases. Thixotropic behaviour is also crucial to avoid some characteristic printed defects as slumping effect.

**Squeegee pressure:** Squeegee is generally made in polyurethane that normally has a square cross section and it is mounted on a 45 ° angle to insure contact between sharp edge and screen. The squeegee hardness is an important factor. A too soft squeegee would push the past out of screen pattern and on the other hand a too hard squeegee would not accommodate the roughness of substrate and paste would not transfer uniformly.

**Squeegee speed:** Squeegee speed determines amount of ink deposited on substrate. It depends on ink thixotropy behaviour.

**Snap-off distance:** Snap – off distance determines the upward movement of the screen when the squeegee passes by. The applied force lowers the ink viscosity and allows it to release from the wire gauze. A little snap – off distance would not allow release of ink from the screen. Contrary a high snap – off distance would lead a higher pressure of squeegee on the screen to release ink. This would decrease the tension of the screen and hence its lifetime.

**Emulsion thickness:** During screen fabrication an organic emulsion layer is spread over the entire mesh surface filling open areas. The emulsion thickness affects the height of the deposited ink. A SEM image of emulsion thickness is showed in Figure 1.21.

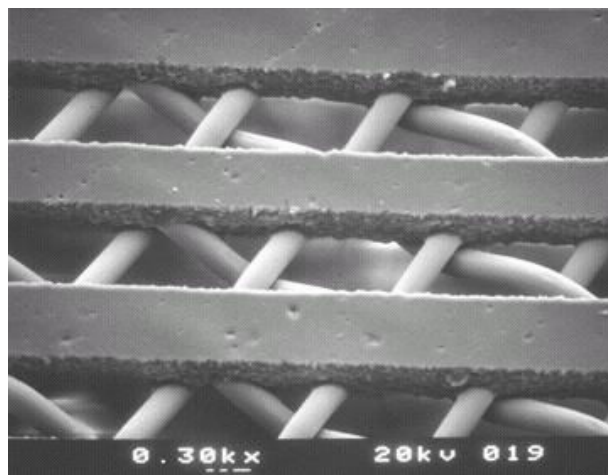


Figure 1.21. SEM image of emulsion and mesh thickness [64]

**Mesh opening:** Mesh opening affects the flowing of the ink through the screen mesh. When open area increases screen capability enhances.

### 1.3.7 Printed primary batteries

#### Screen printed primary batteries

In the last ten years, thin film for primary batteries has been explored due to a large area per electrode volume and shorter diffusion path [65–66]. However the process of producing thin film electrode is quite expensive. A concrete alternative has been found in screen printing process which is a relatively cost-effective process for the construction of geometrically well defined and highly reproducible structures [67]. Printing technique leads to the potential development of primary and secondary batteries. An example is the experience performed by George et al. [68] for developing a zinc alkaline battery system. Zinc containing anodes and manganese dioxide cathodes were printed onto silver current collectors and assembled into cells using separator paper and potassium hydroxide electrolyte as showed in Figure 1.22.

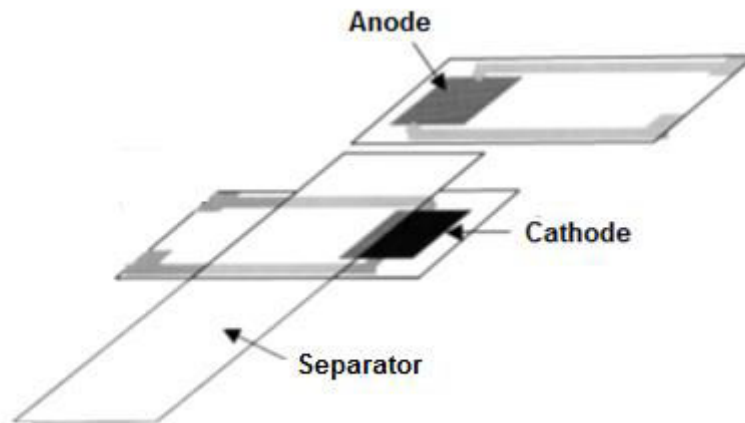


Figure 1.22. Fabrication strategy of full battery [68]

The fabricated prototype shows good results discharged at a rate of  $1 \text{ mA/cm}^2$  when high content of graphite is used (around 90% of theoretical capacity). Nevertheless one drawback is the packaging method that doesn't prevent a possible leakage of electrolyte and creep age. Another example has been reported by Wendler et al. [69] they developed a Zinc / Manganese Dioxide cell (Figure 1.23.a) where all components have been screen printed thanks to the formulation of separator and electrolyte paste developed by authors. To avoid leakage effect, Wendler and coworkers developed a sealing technology.

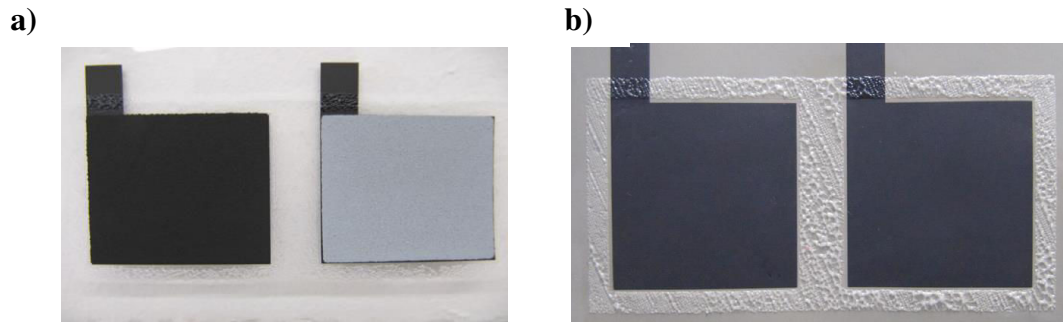


Figure 1.23. a) Zinc/Manganese-Dioxide electrodes with suitable print quality, b) surrounded by the sealant [69]

They printed sealing polymer all around the collectors and across the collector leads out (Figure 1.23.b), then the sealing polymer is activated by heat and the cell is thereby closed. Results showed a capacity of 20 mAh for a charging current of 1 mA. Hilder et al. [70] printed a paper battery based on zinc carbon polymer composite for anode electrode and polyethylene dioxythiophene (PEDOT) cathode (Figure 1.24). The performances are lower with an open circuit voltage of 1.2 V and a discharge capacity of  $0.5 \text{ mAh cm}^{-2}$ . Gaikwad et al. [71] printed a Zn /  $\text{MnO}_2$  cell system in a mesh embedded structure that acts as support and reduces the stress of electroactive materials during mechanical bending. This battery shows good performance in comparison to commercial available Zn /  $\text{MnO}_2$ . As shown in Figure 1.25 discharge profile improved after bending due to the compression of the battery, which leads to better interfacial contacts between electrodes.

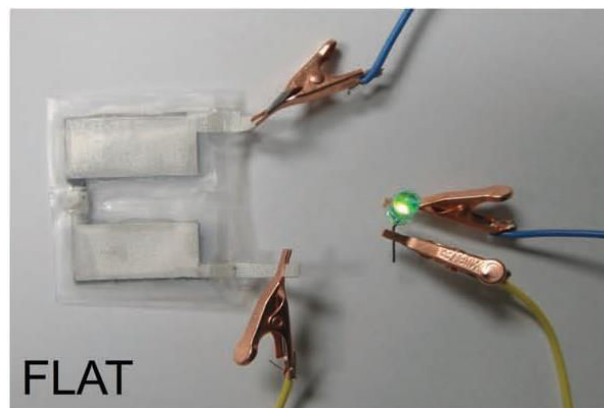


Figure 1.24. Demonstration of two flexible cells connected in series to power a green LED.

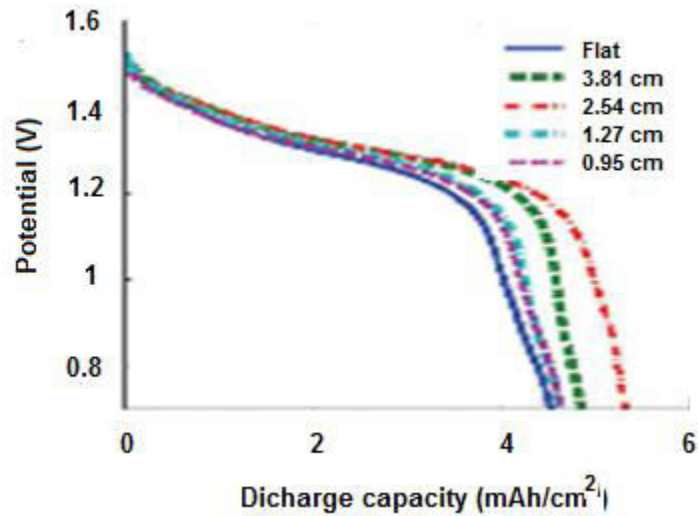


Figure 1.25. Discharge profile of the flexible battery when flexed to different radii of curvature while discharging. Discharge experiments were carried out at 1 mA [71].

Primary printed thin films are not the best solution for electronic devices. A challenge is the low potential of primary printed cell (1.4 V), which alone does not meet the typically higher potential requirement for printed electronic devices as well as thin film transistor (30V). Gaikwad et al. [72] printed a series connected array of alkaline cells with sufficient energy and power to drive a printed circuit. In this study, ten cells of Zn / MnO<sub>2</sub> have been printed on a commercially based cellulose membrane (Figure 1.26).

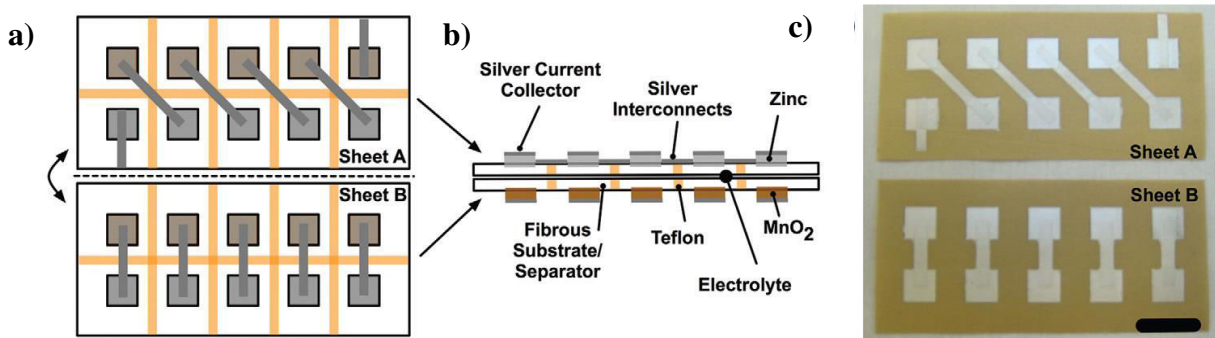


Figure 1.26. a) Diagram of 10 Zn-MnO<sub>2</sub> cells, printed on a fibrous substrate, (b) Diagram of the cross-section of the battery with sheets A and B stacked together. (c) Optical image of sheets A and B after printing the zinc/MnO<sub>2</sub> electrodes and the silver current collector and interconnects [72]

The measured initial open circuit voltage (OCV) of the battery pack is 14 V, while the OCV of each individual cell is approximately 1.4 V. Figure 1.27 shows the discharge profile of the battery pack through a 100 k $\Omega$  resistor. With this load, the potential of the battery drops to 10 V after 7.5 h, corresponding to a capacity of 0.8 mAh.

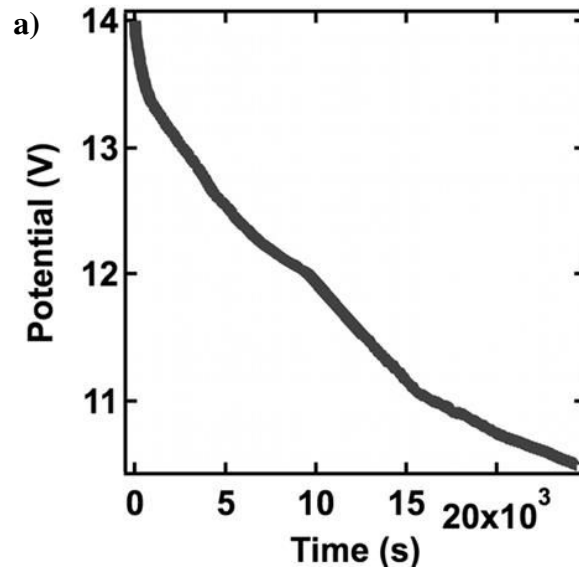


Figure 1.27. Discharge profile of the battery pack [72]

Another system particularly attractive for printing because of the high energy and air stability is silver / zinc battery system [73]. Despite the high price of silver, the low material consumption for printed batteries make the processing / cost dominant. As result printed silver zinc batteries are a good candidate to electrochemical system. Braam et al. [74] reported the development of a primary, planar two dimensional printed silver zinc battery (Figure 1.28).

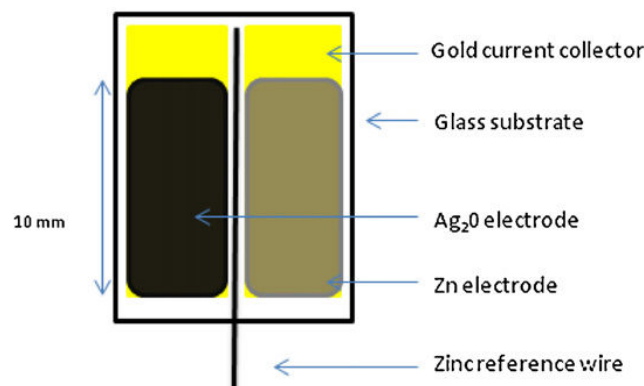


Figure 1.28. Schematic layout of Ag/Zn printed battery

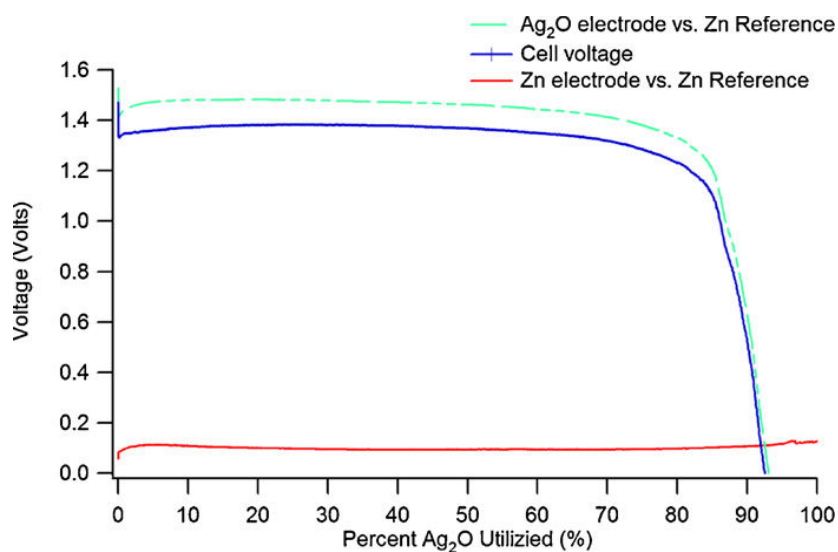


Figure 1.29. Discharge characteristic function of %  $\text{Ag}_2\text{O}$  at  $C/2$  rate (1.408 mA) [74]

The fabricated batteries show a high energy density of  $4.1 \text{ mWh cm}^{-2}$  and a capacity of 1.4 mAh at  $C/2$  rate. Different binders have been compared and with 1% polyvinyl alcohol (PVA) the highest  $\text{Ag}_2\text{O}$  and Zn active material utilization were achieved as shown in Figure 1.29. Table 1.12 lists components and performances of flexible primary batteries and summarizes the fabrication techniques.

Table 1.12. Lists of components and performances of 1<sup>st</sup> batteries

Type Anode/Cathode	Manuf. process	Substrate	Size ( $\text{cm}^2$ )	Electrolyte	Thickness ( $\mu\text{m}$ )	Capacity	Reference
Zn/MnO <sub>2</sub>	Screen printed	Silver	1x1	KZn	324	3-4 mAh at $1 \text{ mA cm}^2$	[68]
Zn/MnO <sub>2</sub>	Paint spray	-	2x2	KZn	600	20 mAh	[69]
Zn/PEDOT	Screen printed	Paper	1x2	LiCl/LiOH	-	1 mAh	[70]
Zn/MnO <sub>2</sub>	Screen printed	Nylon	3.2	PAA based GPE	215	5.6 mAh at 0.5mA	[71]
Zn/MnO <sub>2</sub>	Screen printed	PAC	1x1	KOH	60	0.8 mAh	[72]
Zn/AgO <sub>2</sub>	Screen printed	Au collect.	0.2x1	KOH	$\approx 500$	1.4 mAh at $C/2$	[73]

**Commercial primary printed batteries**

Thin printed batteries based on zinc chemistry are already in the market (Figure 1.30). They are manufactured on different substrates with different electrolytes and binders. Performances have been described in terms of peak current, capacity and operate temperature range in the Table 1.13.



Figure 1.30. Commercial primary printed batteries

Table 1.13. Main properties and characteristics of commercial batteries [8]

Company	Voltage	Chemical System	Thickness	Capacity
	V		µm	mAh
<b>Power paper<sup>®</sup></b>	1.5	Zn/MnO <sub>2</sub>	600	15
<b>Solicore<sup>®</sup></b>	3	Li/MnO <sub>2</sub>	600	10-14
<b>Blue Spark<sup>®</sup></b>	1.5	ZnMnO <sub>2</sub>	370	21-25
<b>Enfucell<sup>®</sup></b>	1.5	Zn/MnO <sub>2</sub>	700	18

### 1.3.8 Flexible secondary batteries

Ferreira et al. [75] have fabricated batteries using commercial paper as separator and physical support of thin film electrodes. They built different structures such as Cu/paper/Al structure that leads to batteries with open circuit voltage ranging between 0.5 and 1.1 V (figure 1.31).

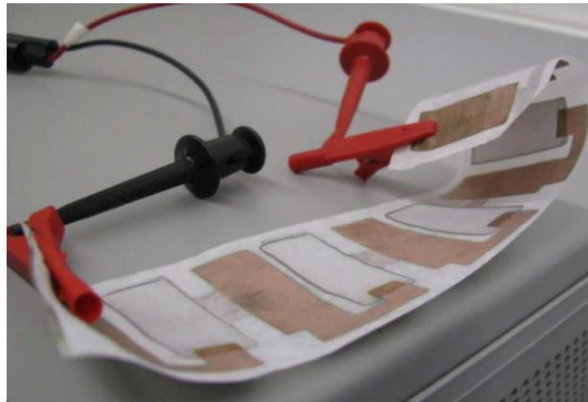


Figure 1.31. a) Structure Cu/paper/Al of the flexible batteries

The batteries show stable performance after being tested by more than 115 hours under standard atmospheric conditions and it seems that battery exhibits a fuel cell character because of performances are affected by relative humidity content. The battery is self rechargeable when exposed to relative humidity above 40%. According to the authors each element is able to supply a power ranging between  $75 \text{ nW/cm}^2$  and  $350 \mu\text{W/cm}^2$

Wendler et al. [69] reported a screen printed process to fabricate rechargeable batteries based on Nickel / Metal-hydride couple with a nominal voltage of 1.2V. Batteries have been fabricated in a coplanar configuration as shown in Figure 1.32.a. Performances have been tested in a long term charging and discharging cyclization and a capacity of 16 mAh was founded for a current rate of 1 mA (Figure 1.32.b)

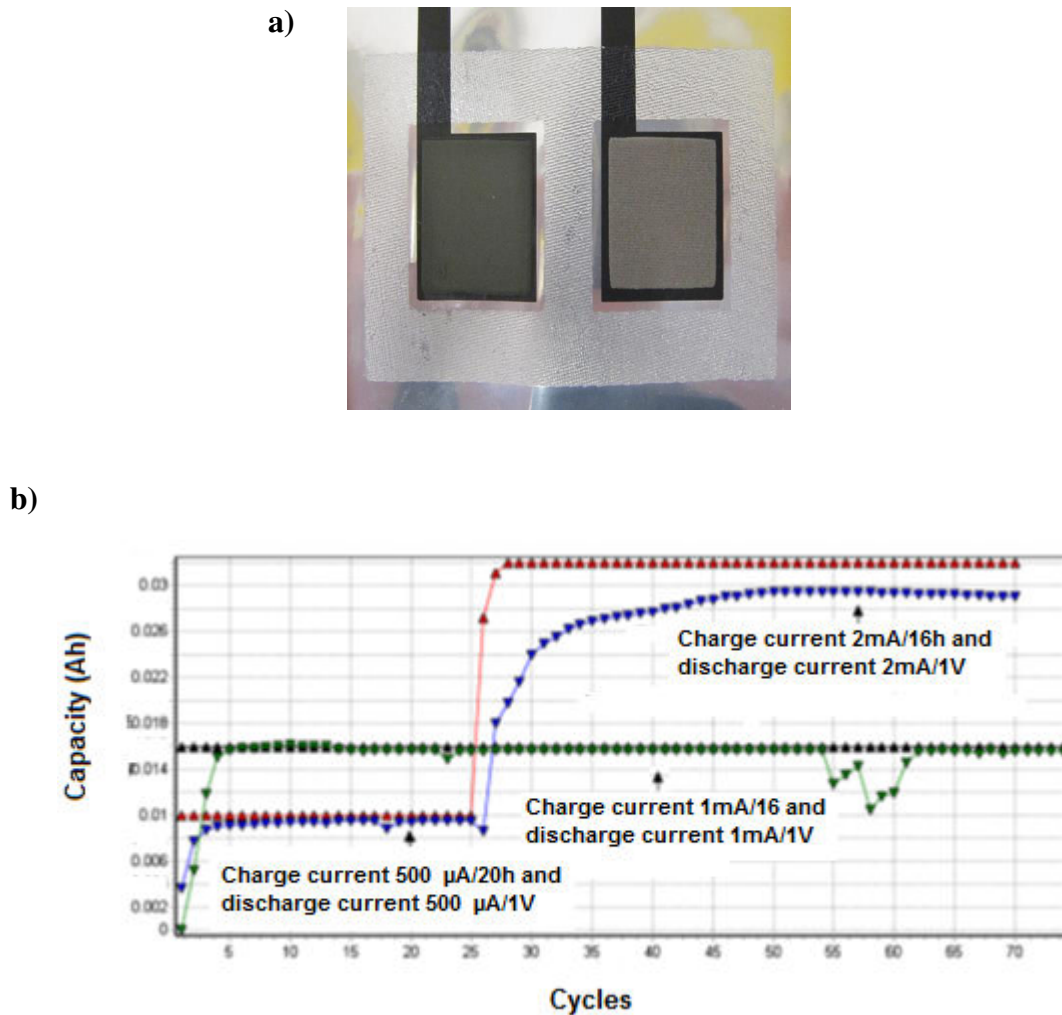


Figure 1.32. a) Surface NiMH-Electrodes with suitable print quality, surrounded by the sealant b) Capacities of printed NiMH cells during long-term cyclization. One cell is discharged with 1 mA (green curve), whereas for the other one the current was increased starting at 26<sup>th</sup> cycle from 0.5 to 2 mA [69]

An ink-jet printing process was used by Zhao et al. [76] to fabricate a thin film of SnO<sub>2</sub> anode for lithium-ion batteries. More recently efforts have been done to use SnO<sub>2</sub> as anode for lithium-ion batteries because of its high gravimetric capacity and volumetric capacity (about four times that of graphite) [77-78-79]. Different techniques have been reported in literature [80-81-82] but these methods present several drawbacks [83-84-85] related to cost process [86-87] and thermal effect due to annealing process [88-89]. These drawbacks boost research to extensive and large scale process as well as printing techniques. A stable colloidal ink was

prepared with SnO<sub>2</sub> nanoparticles, acetylene black (AB) and polymer dispersant. The prepared ink was printed by ink jet process onto a commercial copper foil. SEM images show uniform distribution of SnO<sub>2</sub> thin film electrodes with a thickness layer of 770 - 780 nm as shown in Figure 1.33.a. High initial discharge capacity about 812 mAh/g was observed at a constant discharge current density of 33 $\mu$ Acm<sup>-2</sup> (Figure 1.33.b).

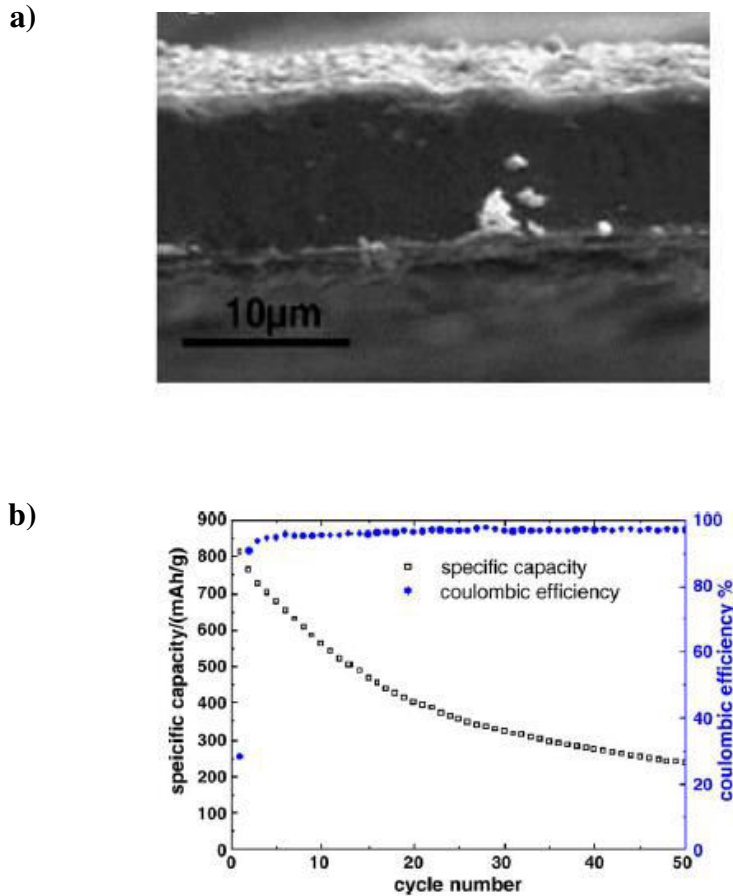


Figure 1.33. a) SEM image before charge–discharge; b) Discharge capacity and coulombic efficiency of as-printed thin film SnO<sub>2</sub> electrode as a function of cycle number [76]

### 1.3.9 Thin and printed flexible lithium - ion batteries

Among the three best rechargeable cell systems, nickel cadmium (Ni-Cd), nickel metal hydride (Ni-MH) and lithium ion (Li-ion), the rechargeable lithium technologies offer best performances. For this reason rechargeable lithium –ion batteries have become one interesting candidate to be manufactured within the tool set of printed and deposition techniques for

matters of both safety, cost efficiency, versatility and energy density. Different deposition techniques have been used by researchers to manufacture flexible batteries.

### Deposition techniques

Liangbing et al. [90] reports a new structure of thin and flexible batteries using paper as separators and free-standing carbon nanotube thin films as both current collectors. The current collectors and battery materials are integrated onto a single sheet of paper through a lamination process as reported in Figure 1.34.

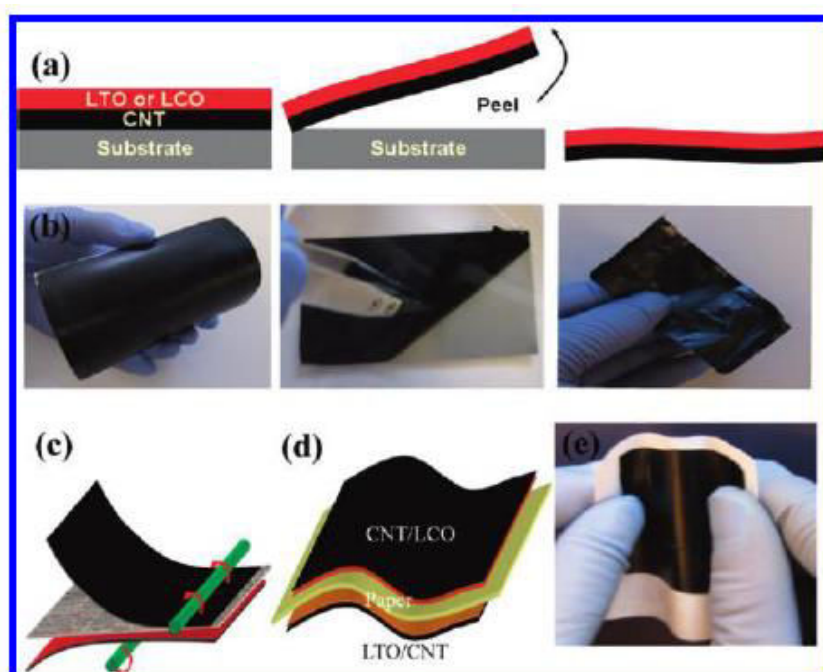


Figure 1.34. a) Schematic of fabrication process for free-standing LCO/CNT or LTO/CNT double layer thin films. b) LTO/CNT double layer film coated on SS substrate Schematic of the lamination process c) Schematic of the lamination process: the freestanding film is laminated on paper with a rod and a thin layer of wet PVdF on paper. d) Schematic of the final paper Li-ion battery device structure, with both LCO/CNT and LTO/CNT laminated on both sides of the paper substrate. e) Picture of the Li-ion paper battery before encapsulation for measurement [90]

The paper functions as both a mechanical substrate and separator membrane with lower impedance than commercial separators. After packaging, the rechargeable Li-ion paper battery, exhibits robust mechanical flexibility and a high energy density ( $108 \text{ mWhg}^{-1}$ ). Another viable technique for large area fabrications of lithium ion batteries is painting technique. Sing et al. [91] proposed a full painted battery by adopting a spray technique

(figure 1.35.a). All components have been formulated in a liquid dispersion which can be sequentially coated on substrates to achieve the multilayer battery configuration. Authors chose lithium cobalt oxide and lithium titanium oxide as positive and negative electrode respectively to reach nominal voltage of 2.5 V.

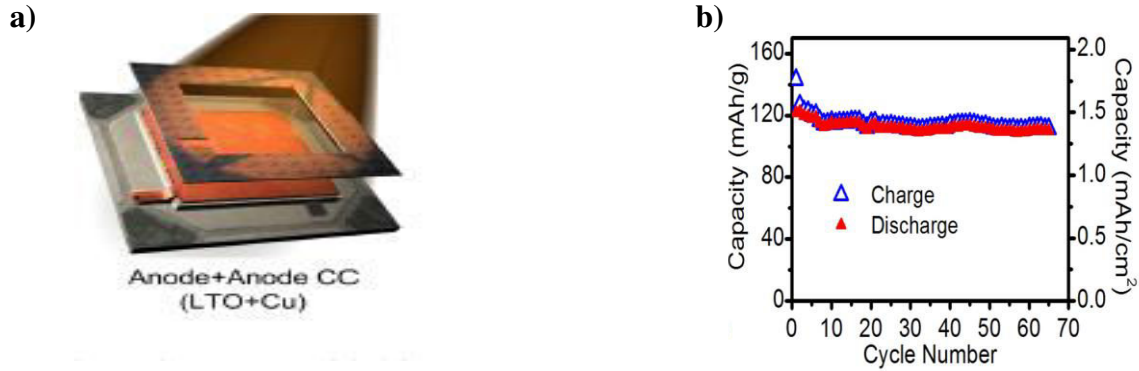


Figure 1.35. Paintable battery concept. a) Simplified view of a conventional Li-ion battery, a multilayer device assembled by tightly wound 'jellyroll' sandwich of anode-separator-cathode layers. b) Characterization of spray painted Li-ion cells [91]

Li-ion painted cell showed plateau potential and discharge capacity of 120 mAh/g at a rate of C/8. The cell retained 90% of its capacity after 60 cycles with > 98 % columbic efficiency (figure 1.35.b). Recently another breakthrough in lithium ion batteries manufacturing research occurred with the introduction of three dimensions (3D) printing machine. Sun et al. [92] print a 3D lithium ion microbatteries composed high-aspect ratio anode and cathode micro-arrays on a sub millimeter scale. Inks with suitable rheological properties have been printed onto a glass substrate by deposition of ink through 30  $\mu\text{m}$  cylindrical nozzles. After printing  $\text{Li}_4\text{Ti}_5\text{O}_{12}$  and  $\text{LiFePO}_4$  microelectrodes arrays are heated to 600°C to promote nanoparticle sintering and packaged in a thin walled polymer cage (Figure 1.36).

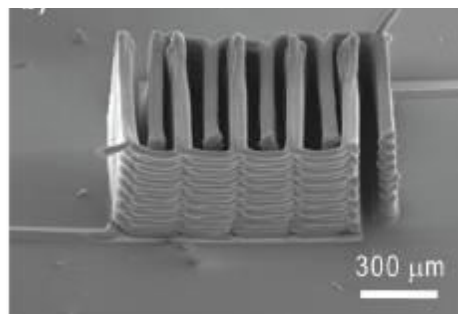


Figure 1.36. SEM images of LTO and LFP architecture [92]

The microbattery delivers  $1.5 \text{ mAh cm}^{-2}$  at a stable working voltage of  $1.8 \text{ V}$  when discharged below  $5\text{C}$ , minimum decay in capacity occurred up to 30 cycles. Using this chemistry Sun et al. demonstrated the feasibility of 3D lithium-ion batteries with a power density of  $2.7 \text{ mWcm}^{-2}$ .

### Screen printed technique

In literature screen printed process has been used to overcome constraints in  $\text{LiCoO}_2$  manufacturing for electrodes [93], related to stress control and high electrical resistivity [94]. Tae Lee et al. [95] reported an electrochemical study of  $\text{LiCoO}_2$  prepared by screen printing. Zr incorporated  $\text{LiCoO}_2$  fine powder was prepared by a sol gel method and consequently deposited by screen printing technique on platinum current collector. A crack free film was obtained with uniform thickness. Silver powders were added in order to enhance the electrical conductivity. The film exhibited a stable cycle performance charge – discharge, efficiency is improved by Ag addition to film and decreasing film thickness. A full layer composed of Zr- $\text{LiCoO}_2$  film / Fe-Si anode multilayer was examined. The cycle performances shows a constant capacity of  $250 \mu\text{Ah/cm}^2$  for at least 50 cycles with a coulombic efficiency of about 90% as showed in figure 1.37.

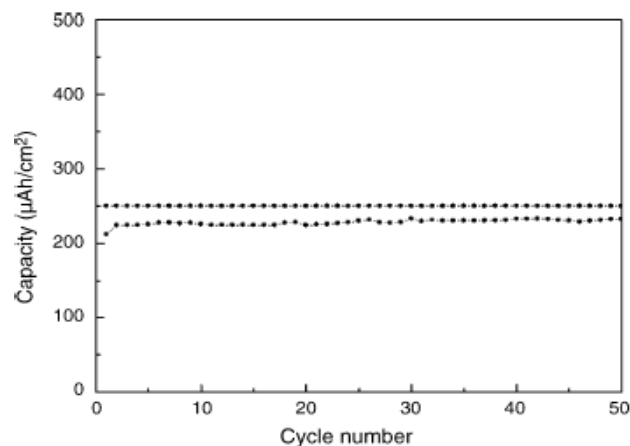


Figure 1.37. a) Cycling performance for Fe-Si multilayer film/Ag-added Zr- $\text{LiCoO}_2$  cell [95]

Park et al.[96] fabricated a  $\text{LiCoO}_2$  film with a thickness of  $6 \mu\text{m}$  by screen printing. The film was printed onto a Platinum current collector and discharged by applying the constant current in the potential range from 3.0 to 4.2 V with various current rates. Figure 1.38 shows discharge profile with various carbon black conducting agent additions. The discharge capacity decreases as the amount of carbon black increased with a maximum discharge capacity of  $46 \mu\text{Ahcm}^{-2}$  at 1% of carbon black content.

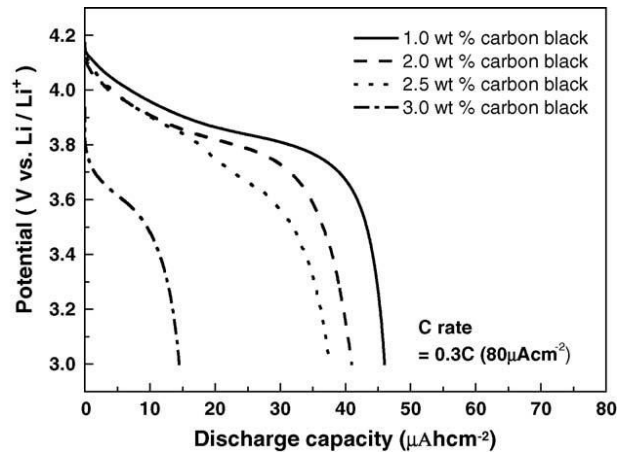


Figure 1.38. Initial discharge curves of printed  $\text{LiCoO}_2$  films depending on the amount of carbon coated at a rate of  $80 \mu\text{Acm}^{-2}$  between 3.0 and 4.2V (vs.  $\text{Li/Li}^+$ ) [96].

In another experience Park et al. [97] manufacture a thin film battery with a structure  $\text{Li/LiPON/LiCoO}_2$  where LiPON represents the solid electrolyte Lithium phosphorous oxynitride. The highest discharge capacity had a small value around  $7 \mu\text{Ah cm}^{-2}$  at a rate of  $10 \mu\text{A cm}^{-2}$ . According to authors solid electrolyte, compared to liquid electrolyte reduces contact area between active materials and electrolyte leading to large ohmic drop and a small electrical cell capacity. Geyer et al. [98] reported an integrated manufacturing approach for a lithium thin film based battery by a screen printing process. Lithiated metal oxide and graphite were used as positive and negative electrode respectively. The inks were printed onto aluminum (Figure 1.39.a) and copper substrates (Figure 1.39.b) and characterized in terms of sheet resistance and layer thickness. In the case of positive electrode the average sheet resistance was between  $1.9 \Omega/\text{cm}^2$  and  $2.2 \Omega/\text{cm}^2$ . Negative electrodes reached values between  $0.7 \Omega/\text{cm}^2$  and  $0.9 \Omega/\text{cm}^2$ .

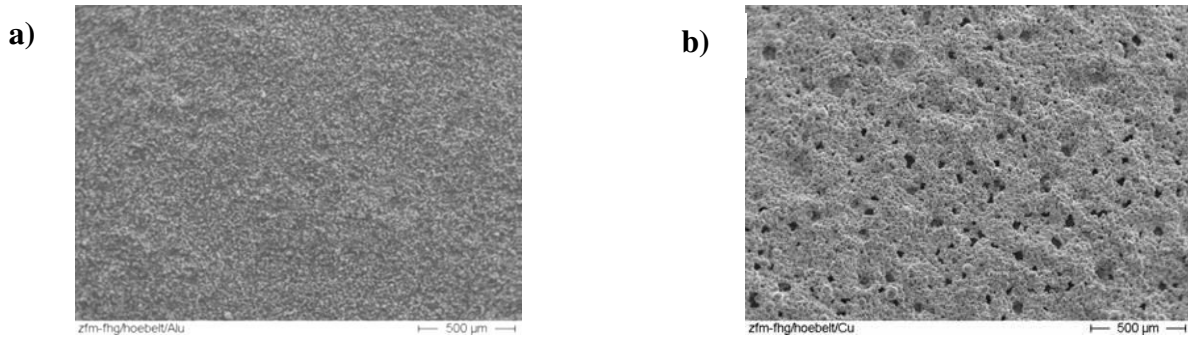


Figure 1.39. Typical scanning electron microscope images of screen printed positive a) and negative ink b) in a 1:50 magnification [97]

A correlation between sheet resistance and layer thickness of the electrode has been measured. Larger layer thicknesses lead to a decreasing sheet resistance for both electrodes. Rouault et al. [99] printed a lithium ion film battery based on a lamellar lithiated metal oxide ( $\text{LiNi}_{1/3}\text{Mn}_{1/3}\text{Co}_{1/3}\text{O}_2$ ) and graphite active material printed directly on Al and Cu foil collectors as showed in Figure 1.40.a. The screen printed batteries exhibit a practical capacity ranging between 57.6 mAh and 64.0 mAh, thus between 80 to 90 % of expected nominal capacity.

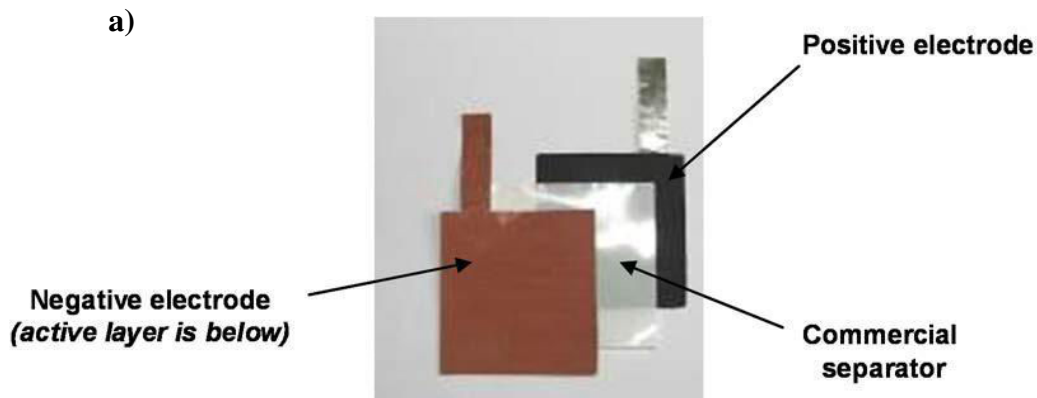


Figure 1.40. Core of the FACESS battery positioned as in the soft packaging. Positive and negative electrodes printed on Al and Cu foil respectively [99]

Otha et al. [100] reported the fabrication of all solid state lithium ion battery totally constructed by a screen printing process.  $\text{LiCoO}_2$  was used as positive cathode and an ionic conductor  $\text{Li}_3\text{BO}_3$  was hosted within the cathode layer. Lithium metal anode was deposited by

a vacuum deposition process. The electrolyte chosen by Othman et al. is a solid electrolyte based on  $\text{Li}_7\text{La}_3\text{Zr}_2\text{O}_{12}$  doped with Nb. Figure 1.41.a shows a cross section image of interface between printed cathode and solid electrolyte. The thickness of the cathode layer is about  $10\ \mu\text{m}$ . The all solid state lithium ion battery exhibited a good charge discharge capacities and lower interfacial resistance between electrodes. Figure 1.41.b shows charge / discharge curves up to the 5<sup>th</sup> cycle at a density current of  $10\ \mu\text{Acm}^{-2}$ . The discharge capacity was  $85\ \text{mAhg}^{-1}$  with a coulombic efficiency of 100% after the 2<sup>nd</sup> cycle. Discharge capacity between the 1<sup>st</sup> and 5<sup>th</sup> cycle was always the same, which confirms the stable cycle performances of battery.

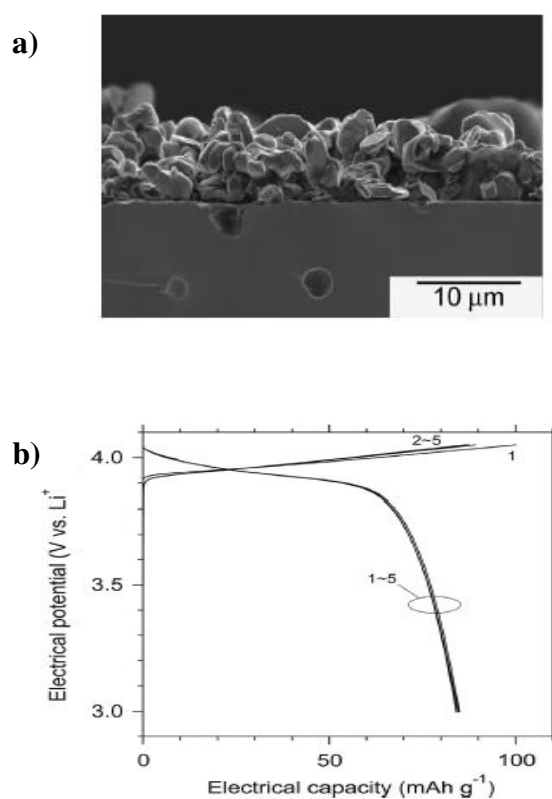


Figure 1.41.a) Cross-sectional SEM images of the interface between the positive electrode layer and the solid electrolyte.b) Charge discharge curves for the all-solid-state lithium ion battery [100].

Table 1.14 lists components and performances of flexible Lithium ion batteries and summarize the fabrication techniques previously described.

Table 1.14. Main components and performances of LiBs in literature

Type Anode/Cathode	Manuf. Process.	Substrate	Size cm <sup>2</sup>	Binder	Capacity	Reference
LTO/LCO	Laminate	Paper	-	PVdF	147 mAh at C/5	[89]
LTO/LCO	Paint spray	PET	5X5	PVdF	120 mAh at C/8	[91]
LTO/LFP	3D printed	Gold collect.	0.96 mm X 0.8 mm	Cellulose	1.5 mAh at C	[92]
Fe-Si/LCO	Screen printed	Pt collect.	-	-	250 $\mu\text{Ahcm}^{-2}$	[95]
Li/LCO	Screen printed	Pt collect.	-	Ethylcellulose	85 mAh/g at 10 $\mu\text{Ahcm}^{-2}$	[97]
GP/LCO	Screen printed	Al/Cu collect.	-	-	-	[98]
GP/LNCMO	Screen printed	Al/Cu collect.	5.5X5.5	PVdF	57-64 mAh	[99]
Li/LCO	Screen printed	Solid electr.	-	Ethyl cellulose	85 $\mu\text{Ahg}^{-1}$ at 10 $\mu\text{Ahcm}^{-2}$	[100]

### Commercial thin-printed lithium ion batteries

Commercial printed lithium batteries appeared in market in the last years with a capacity ranging between 200  $\mu\text{Ah}$  and 5Ah. Figure 1.42 and Table 1.15 summarize the main printed lithium batteries and their principal characteristics.



Figure 1.42. Commercial thin printed LiBs

Table 1.15. Main components and performances of commercial LIBs [8]

Company	Voltage	Chemical System	Thickness	Capacity
	V		$\mu\text{m}$	mAh
Cymbet corp. <sup>®</sup>	3.6	Lithium ion	5	1 mA/cm <sup>2</sup>
Front edge technology <sup>®</sup>	3	Lithium/LiCoO <sub>2</sub> Evaporation	50-300	1
Infinite power sources <sup>®</sup>	1,5	X/LiCoO <sub>2</sub>	110	0.7

### Other Li-ion manufacturing techniques

Jabbour et al. [101-102-103] proposed a papermaking approach to the production of flexible self-standing cellulose based electrodes and separators by means of a water-based filtration process. Cellulose based anodes and cathodes were prepared by filtration of aqueous slurry containing the active material (LiFePO<sub>4</sub> and graphite (GP) for the positive and negative electrode respectively) cellulose binding (refining fibres and carboxymethylcellulose). A conductive agent (carbon black) was added to cathode electrodes in order to enhance electronic conductivity. The filtration process is described in Figure 1.43.

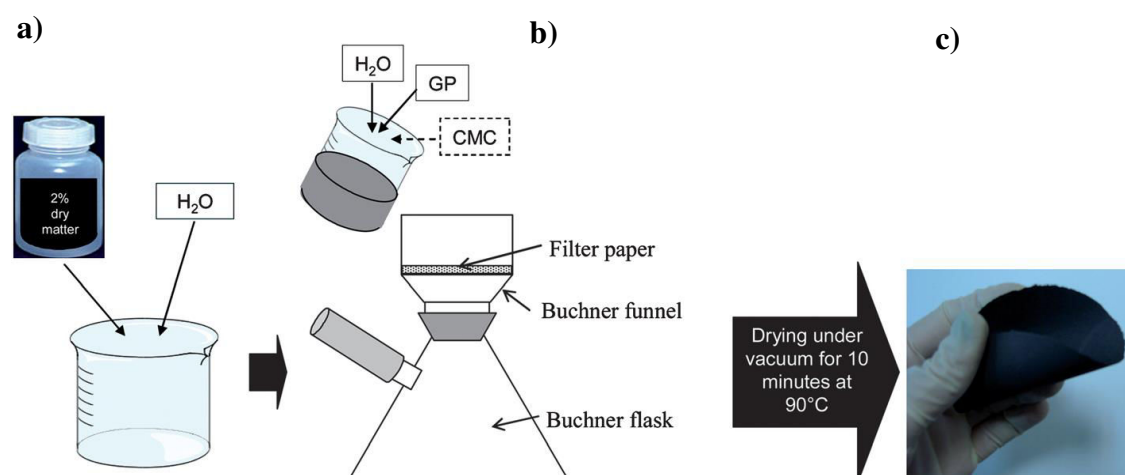


Figure 1.43. Paper-negative electrode preparation. (a) Electrode forming slurry preparation, (b) forming slurry filtration and (c) paper-electrode after drying under vacuum for 10 min at 90 °C [101].

FESEM images in Figure 1.44 show that, in the presence of intensive beaten fibers, structure of the electrode changes radically. When unbeaten fibers are used as binding, electrode is composed of fibers network coated by graphite particles (Figure 1.44.a) whereas, after intensive beating, microfibrilles appear (Figure 1.44.b) and form an additional web like network around graphite particles.

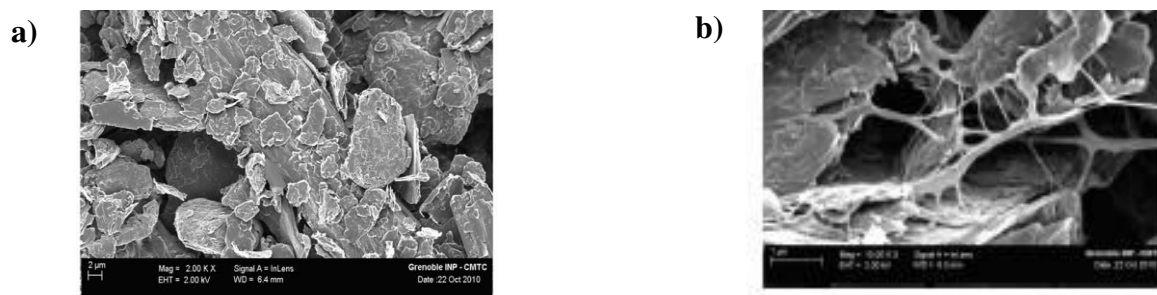


Figure 1.44. FESEM images of the surface of the anodes before (a) and after (b) intensive beating [101]

Graphite electrodes showed a capacity of  $300/350 \text{ mAhg}^{-1}$  at a current rate of  $C/10$  for 20 cycles. Electrodes were tested at different current rates ranging between  $C/10$  and  $C$  with a decrease in capacity until approximately  $250 \text{ mAhg}^{-1}$  at  $C$ . The addition of CMC in the slurry formula improves electrochemical performance as showed in Figure 1.45. The electrochemical performance of the cathode showed that specific capacity was slightly affected by the increase of the test current and a capacity drop of about  $5 \text{ mAhg}^{-1}$  was observed when increasing the current from  $C/10$  to  $C$ . Reducing the  $C$  rate doesn't affect specific capacity; in fact cathode showed a specific capacity of about  $110 \text{ mAhg}^{-1}$  after 130 cycles.

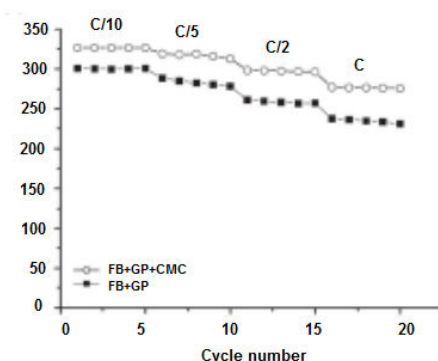


Figure 1.45. CMC influence on discharge performance anode at different current rate [101]

A complete lithium ion paper cell was also assembled using a stack of three paper separators. Before the assembling process electrodes were activated in cells with lithium metal as counter electrode at room temperature at 0.1mA and 0.2 mA current regimes for the cathode and the anode respectively. The full paper cell exhibits a capacity of about 100 mAhg<sup>-1</sup> and a highly stable cycling performance, up to 200cycles (Figure 1.46).

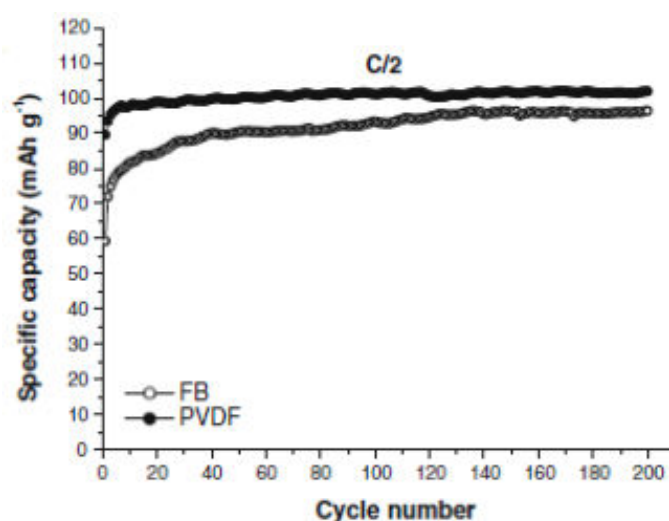


Figure 1.46. Specific discharge capacity of the LiFePO<sub>4</sub>/CB/FB paper-cathode and a LiFePO<sub>4</sub>/CB/PVdF cathode at C/2current rate [101]

Another example of filtration technique to manufacture flexible lithium ion batteries was reported by Leijonmark et al. [104]. Nano-fibrillated cellulose was used both as binder material and as separator. The battery paper was made by a manufacturing process that consists in sequential filtration of water dispersions containing battery components. The resulting paper structure has a thickness of 250 μm (Figure 1.47. a) with good capacities of 146 mAh g<sup>-1</sup> at C/10 and 101 mAh g<sup>-1</sup> at 1 C. Figure 1.47. b shows the evolution of capacity in function of dry temperature. At 170 °C cycling properties were improved

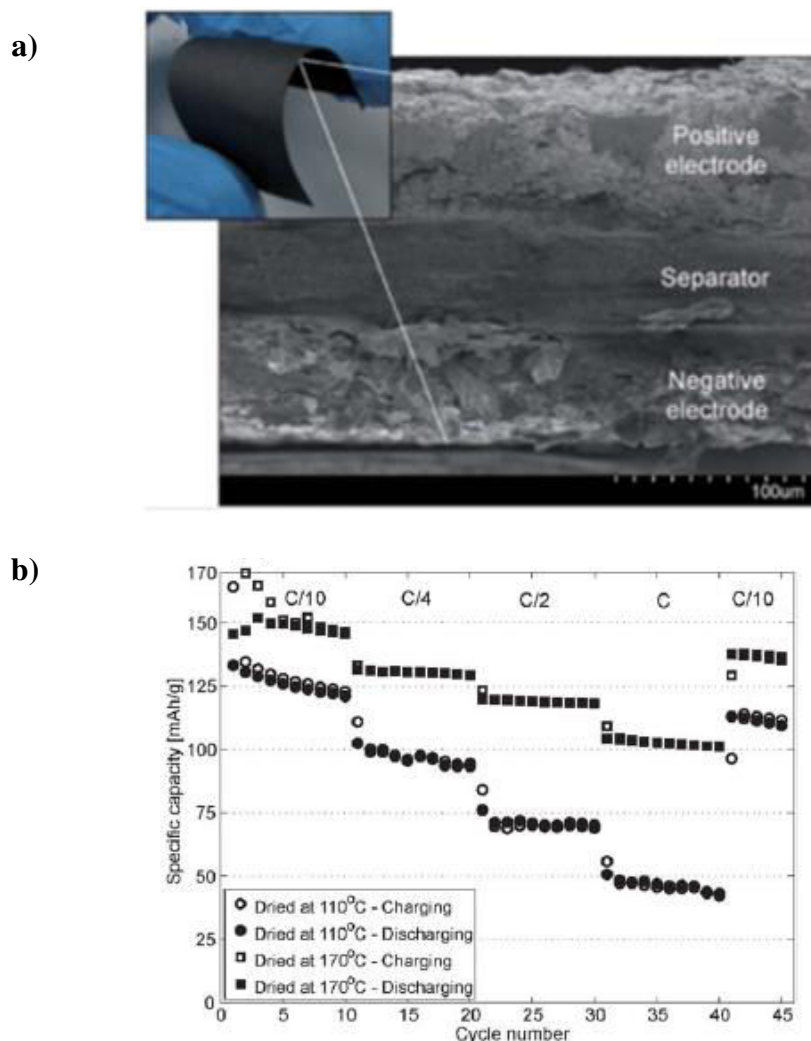


Figure 1.47. a) SEM image of a paper battery cross-section. b) Electrochemical results for paper battery cells dried at 110 °C and 170°C [104]

This effect is likely caused by parasitic side reactions with residual water contained in electrodes. Scrosati [105] reported the fabrication of a paper thin and flexible energy device by combining nanoporous cellulose and carbon nanotubes, performed by Pulickel and coworkers [106]. The battery consists in a thin evaporated lithium metal layer as anode and a carbon nanotube-cellulose composite solved in a room temperature ionic liquid. 1 M  $\text{LiPF}_6$  in EC/DEC was used as electrolyte. A large reversible capacity of about  $430 \text{ mAhg}^{-1}$  was observed during the first charge and discharge cycle at a constant rate of 10 mA/g. The capacity of 110 mAh/g was measured for cycle up to 1<sup>st</sup>. The composite paper has flexible properties. It can be rolled up, twisted or bent.



---

# Experimental



---

## 2. Experimental

### 2.1 Materials

A brief description of the experimental techniques employed for the preparation and characterization of the Li-ion cell components are here resumed. All the reported procedures were performed at room temperature ( $\sim 25^{\circ}\text{C}$ ) if not otherwise specified.

#### 2.1.1 Cellulose based materials

##### Microfibrillated cellulose (MFC)

Different methods are typically used to obtain desired MFC properties. They are isolated from cellulosic sources by mechanical shearing and impact forces or alternatively by chemical treatments (Figure 2.1.a). Through their high aspect ratio ranging between 100 and 150 [107], MFCs present a high networking tendency and water retention capacity.

##### MFCs manufacturing protocol

MFCs used in this work were provided by the FCBA (Pôle Nouveaux Matériaux, Grenoble, France) from bleached Domsjö wood pulp. The pulp was first dispersed in water and then subjected to a pretreatment step with an endo-glucanase (cellulase) enzyme, during 2h at  $50^{\circ}\text{C}$ . Subsequently, the pretreated pulp (2% w/v) was disintegrated by a homogenization process using a microfluidizer processor (Microfluidics, model M-110 EH-30), equipped with 400 and 200  $\mu\text{m}$  diameter chambers (cycles were varied in order to optimize the (fibrillation process)). The obtained suspension of fibrils was translucent (Figure 2.1.b) and the measured dry solid content was about 2% w/w. Atomic force microscopy (AFM) displayed a diameter value for MFCs lower than 200 nm and several micrometers of length (Figure 2.1.c)

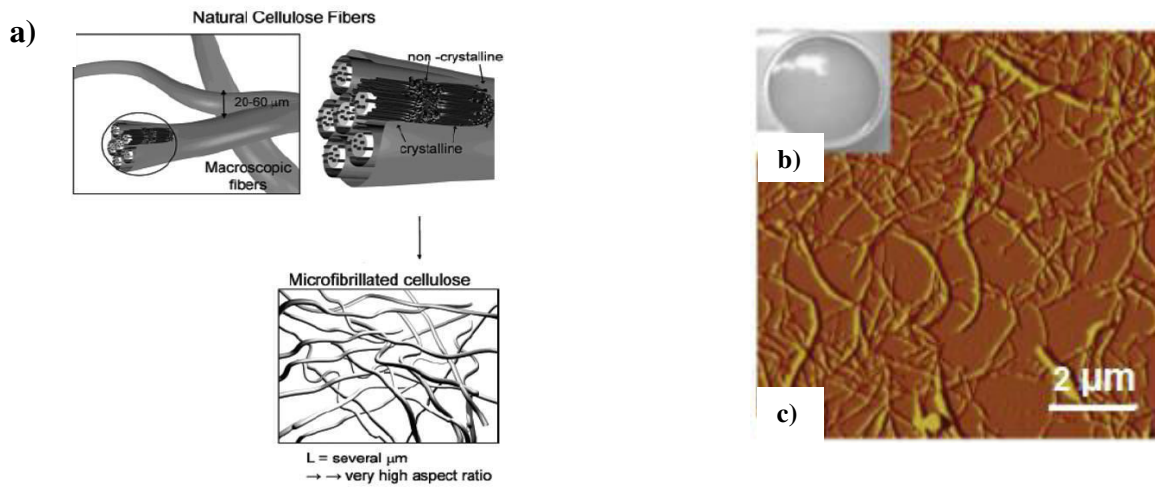


Figure 2.1. a) Representation nanoscale MFC from a cellulose fiber macroscale [107]. b) Image of MFC suspension. c) AFM image of MFC suspension dried on mica surface [108].

## 2.1.2 Electrodes materials

### Graphite based negative electrode (GP)

Graphite is the most used material as anode in LIBs technology because of low price [109]. SLP 10 Timcal<sup>®</sup> graphite with a potatoes shape ( Figure 2.2) was selected as negative electrode. The following table resumes main properties of this type of graphite (Table 2.1).

Table 2.1. Main parameters TIMCAL<sup>®</sup> SLP10

<b>TIMREX<sup>®</sup> SLP10</b>		
<b>Scott density</b>	$g/cm^3$	0.10
<b>BET surface area</b>	$m^2/g$	12
<b>D<sub>90</sub> particle size</b>	$\mu m$	12.5

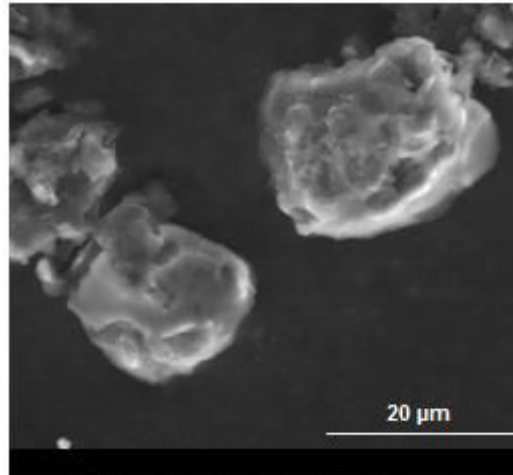


Figure 2.2. MEB image of graphite particle.

### **Phosphate based positive material (LFP)**

LiFePO<sub>4</sub> has been selected as positive electrode mainly because of its better environmental compatibility compared to other classical positive electrodes for LiBs. Other advantages of LFP are its flat voltage profile and low material cost [110]. LFP was provided by Prayon<sup>®</sup> and its measured particle size diameter D<sub>90</sub> of 10 μm.

### **2.1.3 Substrates and other materials**

In this work two different cellulosic based substrates were used as substrates. The main difference between two substrates is the grammage. The characteristics are listed in the Table 2.2.

Table 2.2. Main characteristics of cellulosic based substrates

		<b>High grammage substrate</b>	<b>Low grammage substrate</b>
Thickness	μm	142±2	78±2
Grammage	g/m <sup>2</sup>	120	23
Porosity	%	47±1	80
Roughness (S <sub>a</sub> )	μm	4.1±1,5	-
Air permeability	cm <sup>3</sup> /cm <sup>2</sup> min	417	4100

**Carboxy methylcellulose (CMC)** provided by Aldrich<sup>®</sup> was used as **binder and dispersing agent** in this work in order to prepare aqueous based ink. It exhibits an average molecular weight of  $90000 \text{ g mol}^{-1}$  and a degree of substitution (DS) of 0.7. CMC plays a key role as a thickening agent preventing graphite particles from settling out during processing. The CMC based negative electrodes exhibited an improved charge discharge efficiency and rate capability compared to conventional electrodes fabricating by non aqueous processing [111].

As **electrolyte** two different systems were employed:

\_ **1 M LiPF<sub>6</sub>** salt was used in a 1:1:3 volume mixture of ethylene **carbonate (EC)**, **propylene carbonate (PC)** and **dimethylcarbonate (DMC)** provided by Purolyte<sup>®</sup> .

\_ **1 M LiPF<sub>6</sub>** salt in a 1:1 volume mixture of **ethylene carbonate (EC)** and **dimethylcarbonate (DMC)** provided by Novolyte<sup>®</sup> technologies .

**Mono-fluoroethylene carbonate (<sup>1</sup>FEC)** provided by Aldrich<sup>®</sup> were also used as **additive components** to enhance electrodes cycling performances.

**Lithium foil** with a thickness of 19 mm was employed as **counter** (galvanostatic measurements) **and reference** (voltammetry measurements) **electrode**. Lithium was provided by Alpha Aesar<sup>®</sup>.

**Aluminum (Al)** and **Copper (Cu)** based **grids** were used as **current collectors** for the cathode and anode electrode respectively. Both they were provided by Dexmet<sup>®</sup>.

## 2.2 Ink manufacturing

### 2.2.1 Ink formulation strategy

Inks formulation were performed by following the outline presented in Figure 2.3. A first step of dispersion is performed after addition of binding and additives in order to avoid agglomerations phenomenon. After the introduction of the active material a high dispersion stage is carried out by means of a high disperser provided by VMA<sup>®</sup> (Figure 2.4.a) , followed by a homogenizing process performed by means of a 3 roll mill provided by EXACT<sup>®</sup> (Figure 2.4.b).

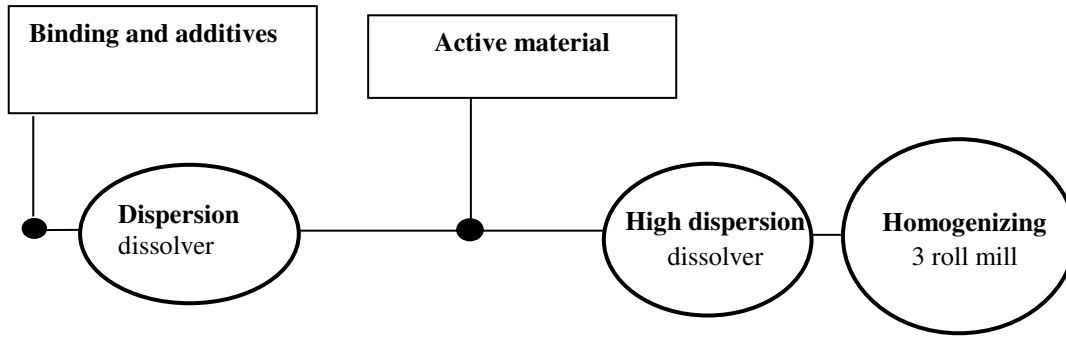


Figure 2.3 Manufacturing ink outline



Figure 2.4. a) High disperser equipment. b) three roll mill equipment

### **Formulation protocol for negative electrode**

The formulation process is illustrated in Figure 2.5. Firstly CMC polymeric dispersant was added in distilled water solvent. The obtained mixture was dispersed by means of mechanical stirrer at a rotation rate of 500 rpm for 5 minutes. Secondly, mixture is gently mixed at 100 rpm and MFC binder is progressively added. Another mixing step at 500 rpm is necessary to insure good dispersion of prepared mixture. Finally graphite active particles are added at 100 rpm and the prepared ink is further stirred at 500 rpm for 10 minutes. Two steps of high dispersion and homogenisation are necessary to obtain a stable ink. Firstly ink is homogenized by means of three roll mills equipment. In a second moment roll milled ink is dispersed at 3000 rpm for 5 minutes by using high speed disperser mixers.

## Experimental

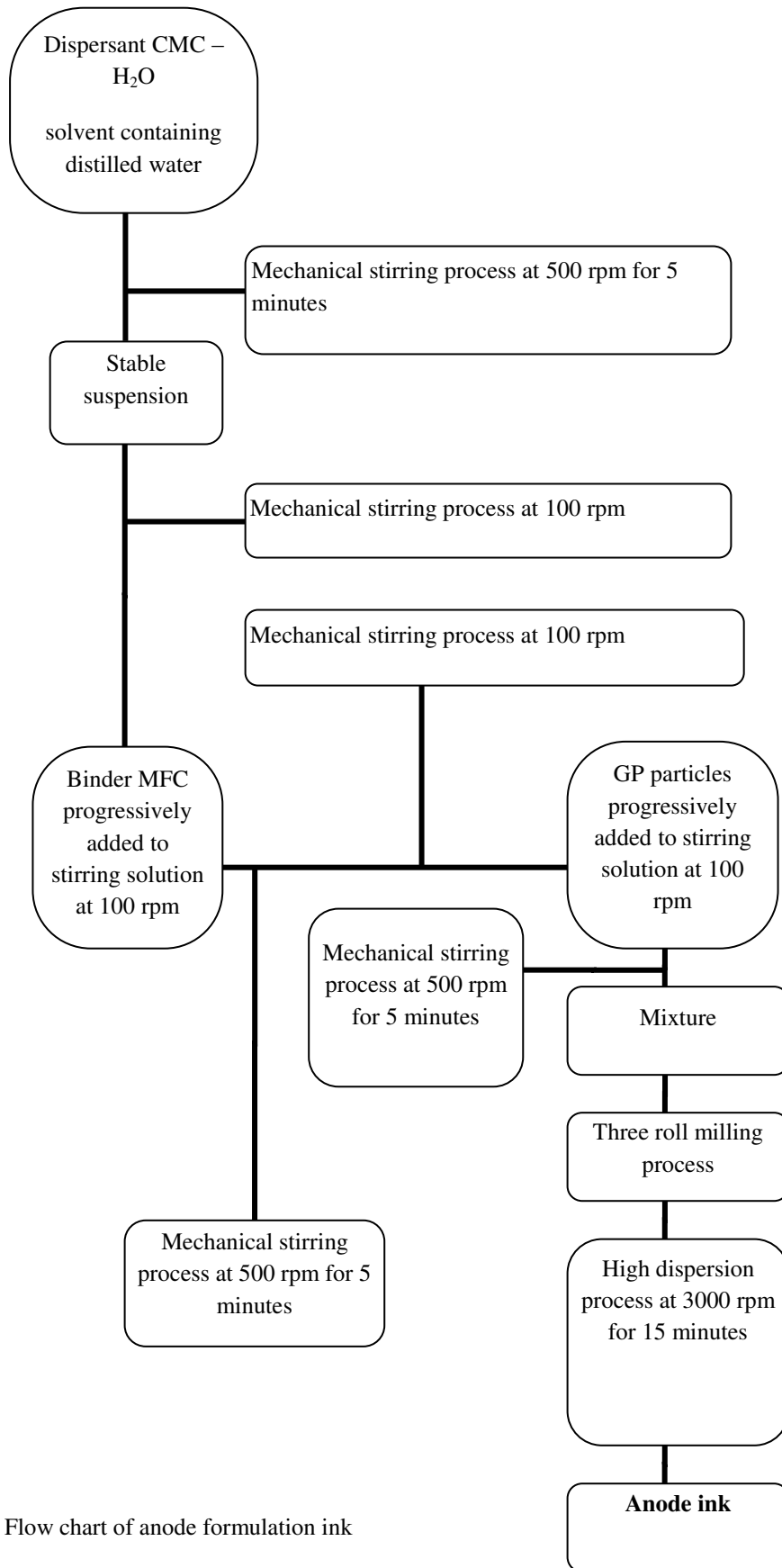


Figure 2.5. Flow chart of anode formulation ink

**Formulation protocol for positive electrode**

CMC and MFC were added in distilled water as first step as well as for anode formulation protocol. As second step CB conducting agent is added progressively to the CMC – MFC mixture and mixed at 500 rpm for 5 minutes. Finally LFP powder is added to the suspension and the system is stirred for 10 minutes at 500 rpm. In order to obtain a stable ink, a high dispersion stage is performed at 3000 rpm for 15 minutes. Figure 2.6 illustrates formulation process.

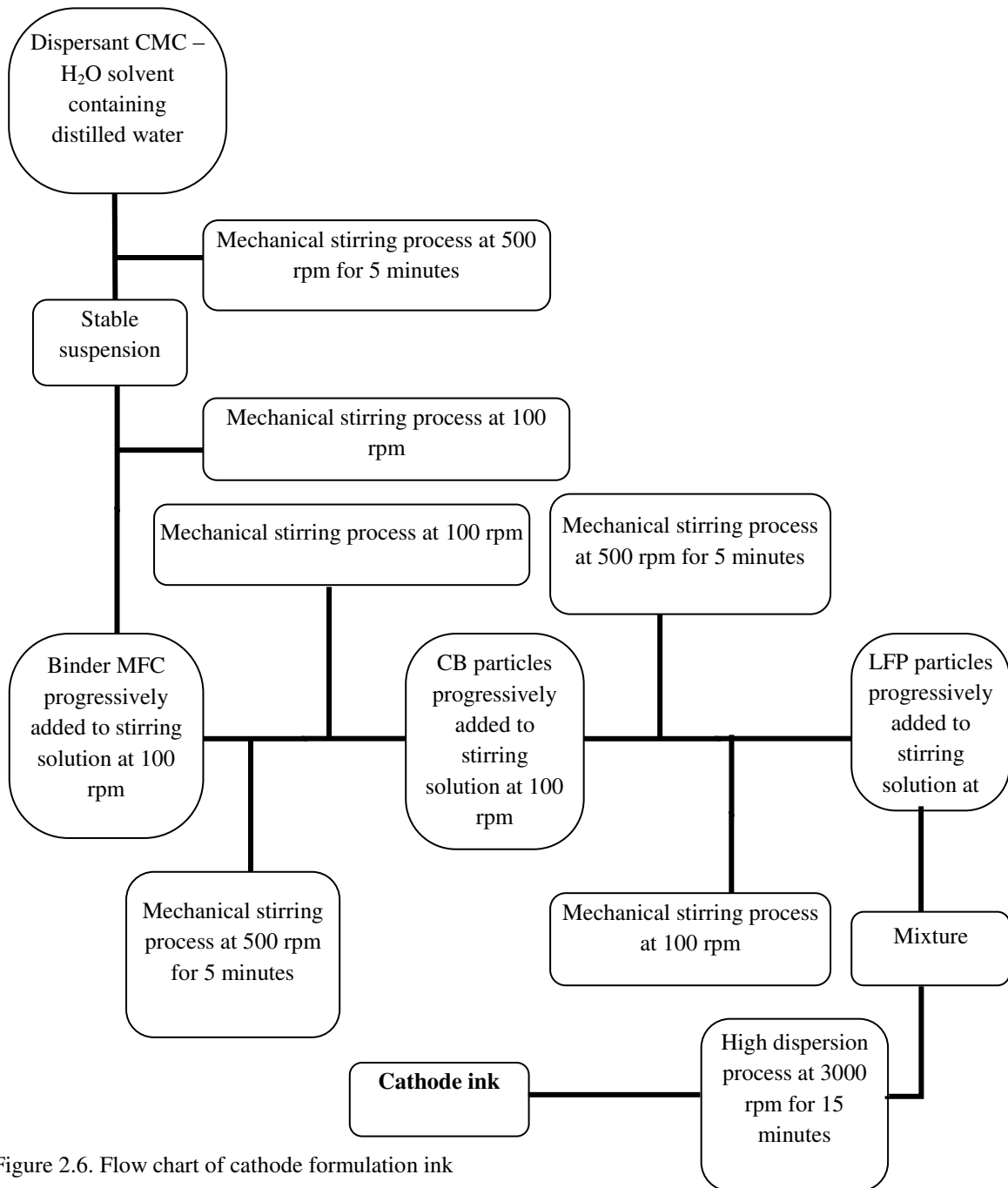


Figure 2.6. Flow chart of cathode formulation ink

### 2.2.2 Rheological characterization protocol

Rheological properties of inks were measured with a MCR 301 rotational rheometer developed by Anton Paar<sup>®</sup>. All measurements were performed at  $25 \pm 1$  °C. A parallel - plate geometry with a plate diameter of 2.5 cm was chosen to realise all experiments and a gap of 1 mm between the two plates as showed in Figure 2.7.

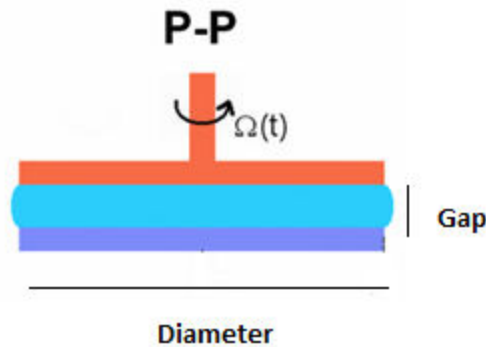


Figure 2.7. Plane- plane geometry

#### Steady shear protocol measurement

The steady shear viscosity was measured using a steady state test. Samples were initially pre-sheared at  $0.1 \text{ s}^{-1}$  to disperse components. Secondly an equilibrate step of 60 seconds was performed before measuring viscosity to avoid an ink breakdown structure. Viscosity and shear stress inks were characterized by measuring rheological properties in a shear rate ramp ranging from  $0.01$  to  $1000 \text{ s}^{-1}$ .  $1000 \text{ s}^{-1}$  was selected as maximum shear rate cause is the highest value reached during screen printing process [112-113]. Table 2.3 illustrates steady shear rheological protocol.

Table 2.3. Steady shear protocol measurement

	Steady shear protocol			
	Step			
	1	2	3	4
<b>Shear rate (<math>\text{s}^{-1}</math>)</b>	0.1	-	0.1-1000	1000-0.1
<b>Time (s)</b>	60	60	600	600

## Viscoelastic measurement

Before performing viscoelastic measurement, linear viscoelastic region (LVR) was determined by an oscillating stress sweep test. This test is mandatory to evaluate relationship between molecular structure and rheological properties. In this region viscoelastic properties are independent of stress or strain imposed levels. To determine LVR increasing stress ramp over a range of 1 to  $10^4$  Pa stress was applied at a constant frequency of 2 Hz. The point which dynamic energy deviates more than 10 % from a plateau value indicates a transition from linear to viscoelastic regime [114].

Viscoelastic measurements were performed to characterize the viscoelastic properties of the ink and the particle network strength. The evolution of complex modulus  $G^*$  was analyzed by ranging frequency from 0.1 to 100 rad/s at a fixed shear stress of 1 Pa.

## Thixotropy test protocol

Thixotropy test was performed to evaluate recovery structure of ink after a high rate imposed. As showed in Figure 2.8. The test consists of applying a constant shear rate for a determined time (I) and immediately a high shear rate is imposed for 5 minutes to insure the complete break down of the structure of ink (II). Finally a low shear rate is applied until stabilization of ink structure (III).

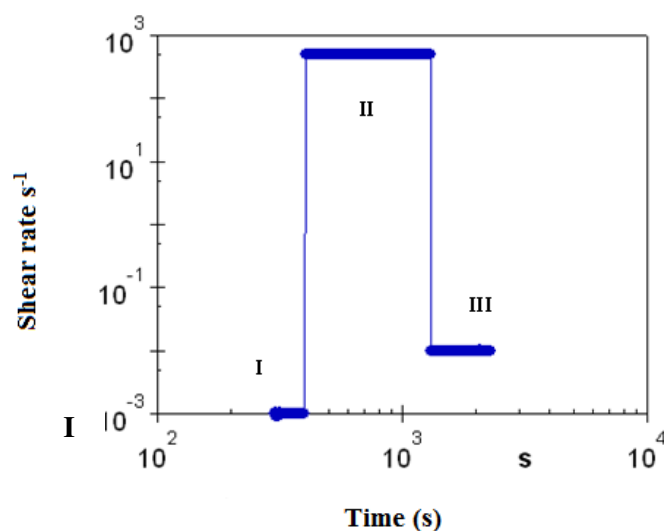


Figure 2.8. Shear profile used for thixotropy test

## 2.3 Printing electrodes

### 2.3.1 Screen printing process

#### Screen pattern

Screen printing of anode and cathode inks were performed by using a screen manufactured by STV<sup>®</sup>.

The screen is characterized by two different patterns. The first one is composed by two lines with different width as showed in Figure 2.9.a. The second one is composed by a square (Figure 2.9.b). These two patterns were selected in order to perform two different assembling strategies.

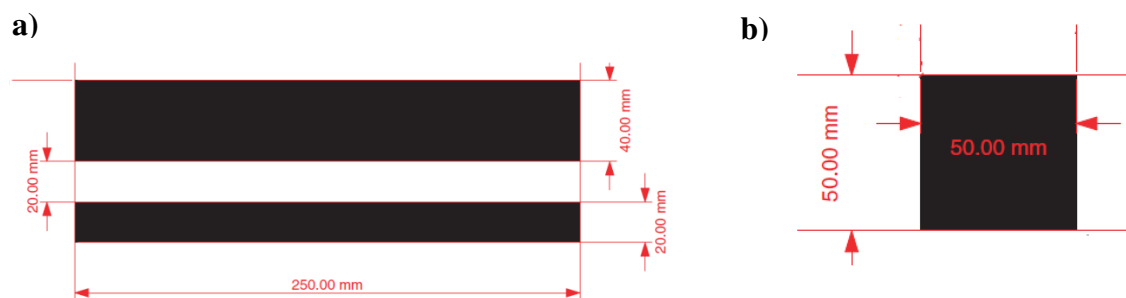


Figure 2.9.a) line pattern b) square pattern

#### Screen mesh

Polyamide Nylon mesh was selected because of its high flexibility and good emulsion adhesion properties. These characteristics allow printing on different substrates with different roughness. Different parameters can affect printing quality. Printing resolution is dependent on mesh count. Concerning mesh opening it should be at least three times larger than mean particle size used for ink formulation [115].

An optical image of mesh is presented in Figure 2.10.

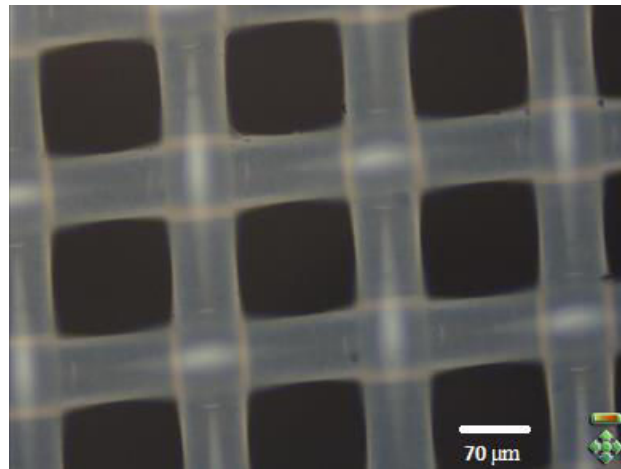


Figure 2.10. Optical image of screen mesh

Percentage open area can be calculated using the following equation [115]:

$$\% \text{ Opening area} = (1 - \text{mesh count} * \text{thread diameter})^2 * 100 \quad (\text{Equation 2.1})$$

Where:

Mesh count is defined as number of wires or openings per linear inch

Thread diameter is expressed in linear inch

### **Squeegee**

A single-sided bevel squeegee was used. Made of polymer, it has 17 cm length, forms an angle of 60° with the screen and has a hardness of 70 – 75 Shore. Generally, this type of squeegee is used for glass printing [116]

### **Screen printing press**

Screen printing tests were performed with a DEK Horizon 03i automatic flatbed press. This type of press is conceived for printing on flat flexible or rigid substrates. Off contact printing allowed sharp printings without smudging. A vacuum base was also used to prevent flexible lightweight tapes from sticking to the screen. The DEK<sup>®</sup> Horizon 03i screen printing press is shown on Figure 2.11.



Figure 2.11. Screen printing press used in this work

Table 2.4 lists parameters and characteristics of screen printing process

Table 2.4. Main parameters screen printing process

<b>Screen printing parameters</b>		
Mesh material		Polyamide Nylon
Snap off distance	mm	1
Squeegee speed	mm/s	125
Squeegee force	kg	5
Emulsion thickness	$\mu\text{m}$	110
Thread diameter	$\mu\text{m}$	70
Mesh	Threads/inch	208
Open area	%	40

## 2.3.2 Characterization of the electrodes

### Thickness and grammage measurements

The thickness of the electrodes was measured using a mechanical gauge (Adamel Lhomargy<sup>®</sup>) with a precision of 1 μm. Grammage and porosity of electrodes were evaluated with the following equations:

$$G = m^* / s \quad \text{(Equation 2.2)}$$

$$\% \text{ Porosity} = 1 - \left( \frac{\text{void volume}}{\text{bulk volume}} \right) * 100 \quad \text{(Equation 2.3)}$$

Where

$m^*$  = mass of the dry sample

$s$  = surface of the sample

### Electrical test

Electronic conductivity was measured using a four – probe system (Jandel Universal Probe<sup>®</sup>) connected to a current generator which provides current ranging from  $1 \cdot 10^{-9}$  to  $99 \cdot 10^{-3}$  A. Four probe configuration avoids perturbation in potential measurements due to wires resistance. As showed in Figure 2.12 two external probes impose a current and the two internal probes measure corresponding potential. Sheet resistance ( $R_s$ ) expressed in ( $\Omega * \square$ ) is defined as:

$$R_s = k * V/I \quad \text{(Equation 2.4)}$$

where

## Experimental

$k$  = constant depending on the geometry, in our case  $k = 4.532$

$V$  = measured potential expressed in Volt

$I$  = current expressed in Ampere

Electrical conductivity ( $\sigma$ ) expressed in (S/m) is thus calculated as

$$\sigma = 1 / (R_s * d) \quad \text{(Equation 2.5)}$$

where  $d$  represents the thickness of the printed layer expressed in meter

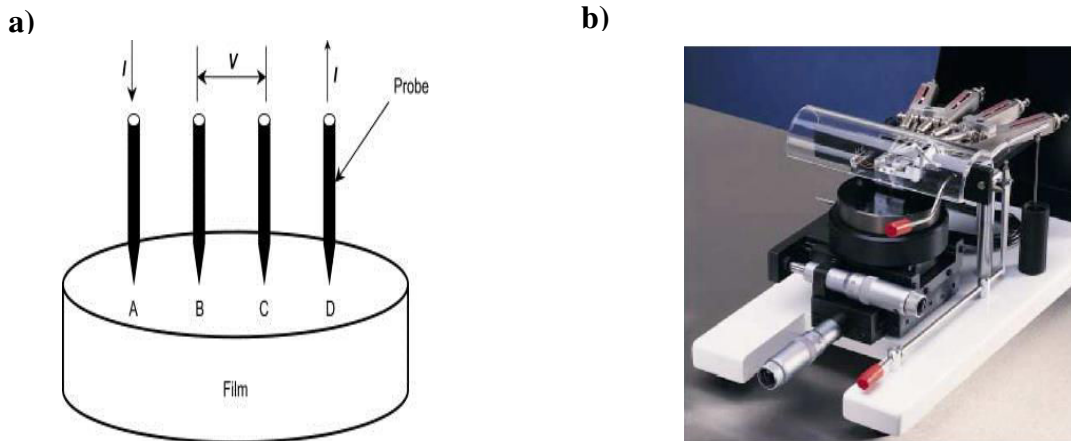


Figure 2.12. a) Four probes configuration. b) Four probe system used in this work [117]

### Peeling test

The evaluation of the adhesive performance of the ink was evaluated by means of a peel tester equipment provided by Twing Albert<sup>®</sup> (Figure 2.13.a) [118]. The equipment employed in this work allows to quantify the force required to remove a pressure sensitive tape from a test panel at an angle of 180° degrees and at a standard rate of 5 min/s. As reported in Figure 2.13.b specified parameters are the film thickness  $h$ , film width  $b$ , peel force  $P_f$ , the angle of peel between the film and the substrate  $\theta$ , the length of the peeled portion of film  $c$ , the elastic

modulus of the film E and the incremental length of the film to be peeled  $\Delta c$ . This configuration can be modelled with a linearly elastic, extensible adhesive film with constant width and thickness problem [118].

a)



b)

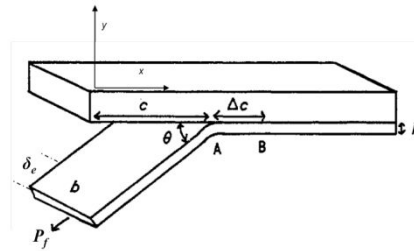


Figure 2.13. a) Picture of peel tester. b) Schematic of the peel test for a linearly elastic, extensible adhesive tape [119]

An energy balance of the process of peeling film through the length  $\Delta c$  shows that the work done by the peel force is equal to the change of the stored internal energy. If the film is assumed to be inextensible the adhesion energy, defined as the energy required to fracture a unit area of interface, can be calculated with this simplified expression known as Rivlin equation [119].

$$G = \frac{P_f(1 - \cos \theta)}{b} \quad \text{in } 180^\circ \text{ configuration} \quad \rightarrow \quad G = \frac{2P_f}{b} \quad (\text{Equation 2.6})$$

Where  $G$  = Adhesion energy in  $\text{J/m}^2$ ,  $P_f$  = Peel force expressed in kg,  $b$  = film width expressed in m

### Topography images and roughness measurements

Topography images and roughness measurements were measured by an Alicona infinite focus<sup>®</sup> optic microscope. Its operating principle combines the small depth of focus of an optical system with vertical scanning to obtain a 3D topography image [120]. Image 3D reconstruction was realised with x100 magnification allowing 10 nm resolution (Figure 2.14).

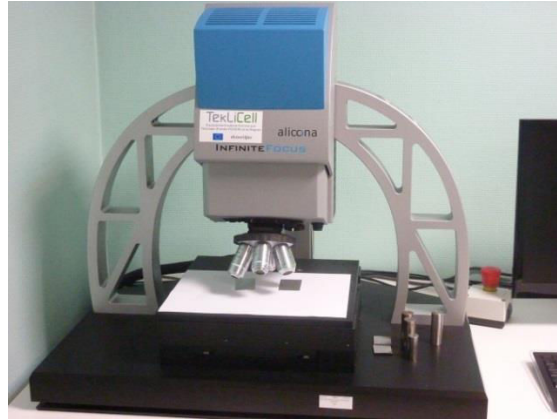


Figure 2.14. Picture of optic microscope equipment

### **Calendering test**

A calendering machine was used to enhance the surface quality and to tailor the porosity of the electrodes. The laboratory calendering machine is presented in Figure 2.15 composed of three rolls each with a 300 mm width. The metallic rolls are chromed and had a diameter of 180 cm. The elastic roll, coated with rubber has a diameter of 130 mm. The linear load can vary from  $0 \text{ kNm}^{-1}$  to  $100 \text{ kNm}^{-1}$ . The speed of the sheet is  $22.5 \text{ m min}^{-1}$ .



Figure 2.15. Laboratory calendering machine

## 2.4 Assembling electrodes

### 2.4.1 Front / back assembling design

For the fabrication of full printed battery a front / back verso configuration was selected. In this configuration electrodes are printed in each side of cellulosic substrate. Secondly current collectors were deposited onto the surface of the electrode. In the next step electrolyte was added in an inert atmosphere of an Ar filled dry glove box (Iacomex<sup>®</sup>) with a O<sub>2</sub> and H<sub>2</sub>O content < 0.1 ppm. Finally the assembled system is packaged in a bag made of plastic where vacuum and sealed process is applied to prevent from moisture or others eventual contaminations. Figure 2.16 illustrates front / back assembling design.

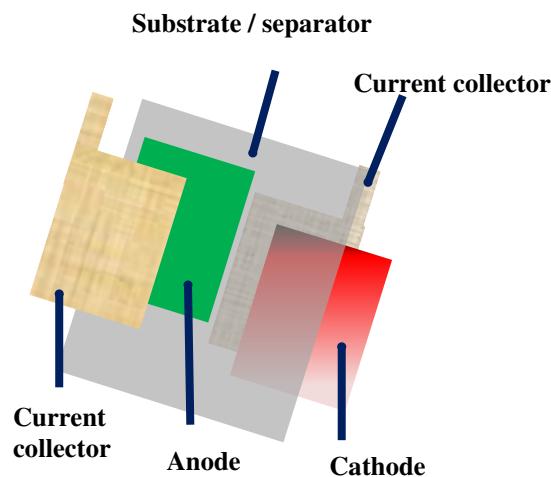


Figure 2.16. Front / reverse assembling design

### 2.4.2 Stack assembling design

In this strategy each component is printed onto different substrates. As showed in Figure 2.17 active layers are printed onto a side of the substrate. The opposite side is used as separator. All layers are then stacked to form a full cell (Figure 2.17.a). Despite numerous printed layers increase manufacturing time, this configuration allows isolation between positive and negative electrodes. A Celgard<sup>®</sup> separator can be inserted within electrode layers to enhance isolation between electrodes (Figure 2.17.b).

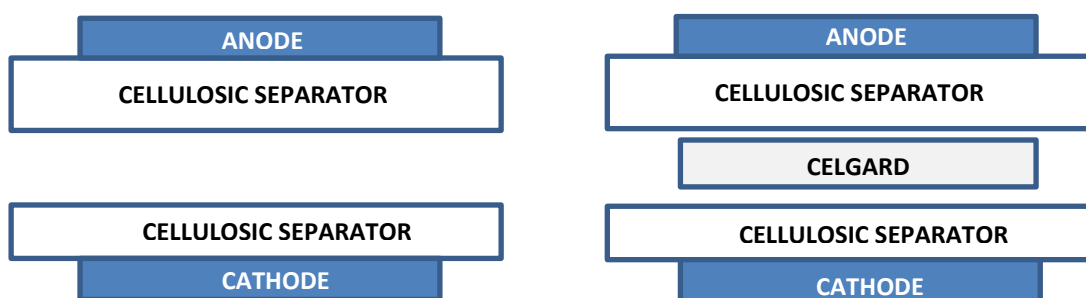


Figure 2.17. Stack layer assembling configuration. a) Cellulose separator acts as substrate for the active layer from one side and separator from the other side. b) Stack configuration with insertion of Celgard layer to enhance isolation between electrodes.

## 2.5 Electrochemical characterization

Prior to their use as components (anode, cathode or separator) in LiBs, samples were cut from printed electrodes into disks with diameter of 0.8 cm and dried at 110°C under high vacuum for 24 hours to ensure complete water removal. For electrode testing cells were assembled using a lithium foil as both the counter and the reference electrode (the latter with regards to the cyclic voltammetry measurements). A plastic separator 2500 provided by Celgard<sup>®</sup> was added to prevent contact between electrodes. A 1M LiPF<sub>6</sub> solution in a 1:3:1 mixture of EC / PC / DEC was used as liquid electrolyte. For full cell characterization a liquid electrolyte composed by 1 M LiPF<sub>6</sub> in a 1:1 EC / DMC solution was employed.

All the above reported procedures were performed in the inert atmosphere of Ar-filled dry glove box. The potential scan window for the cycling tests was fixed between 2.1 and 4.0 V and 0.02-1.2 V vs. Li/Li<sup>+</sup> for the cathode and anode respectively.

The electrochemical behavior of electrodes and the complete cells was tested in three and two electrode Teflon-made Swagelok<sup>®</sup> cells (Figure 2.18.a and 2.18.b) in terms of galvanostatic charge/discharge cycling tests and cyclic voltammetry, using a standard electrochemical instrumentation (Arbin<sup>®</sup> Testing Systems S/N 170795). All the electrochemical experiments were performed at least three times in order to have a reproducibility of the results.

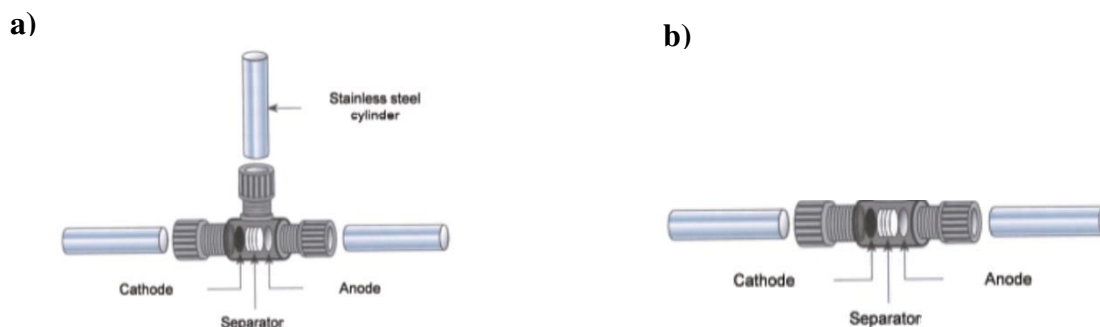


Figure 2.18. . Scheme of a) three electrode and b) two electrode test cell

### 2.5.1 Galvanostatic measurements

A direct and constant current ( $I$ ) is applied to the cell and the potential is monitored as a function of time ( $t$ ) in order to verify the potentials of the reduction/oxidation processes of the active material and the total amount of charge passed per unit mass of electrode material (i.e., the specific capacity) during complete discharge (or charge). The potential is relative to lithium as reference electrode. This technique gives information about the reversibility of the electrochemical process during cycling, the long-term cycling behavior and the rate capability, measuring the amount of charge passed through the cell in the charge and discharge of each cycle.

### 2.5.2 Cyclic voltammetry measurements

A linear scan of the potential (relative to a reference electrode) is imposed on the working electrode; then, the current flowing between the working electrode and the counter-electrode is recorded. A diagram of the current as a function of the applied potential is obtained, showing the peaks corresponding to the electrochemical processes occurring in the potential range considered. The study of such diagram allows obtaining qualitative information about the potential at which the electrochemical processes occur (by the position of the peak) and the exchanged current during the process (by the area of the peak)



---

# **Development and characterization of printed anode**



## **3. Development and characterization of printed anode**

### **Introduction**

This chapter describes the manufacturing of anode electrode. Firstly, rheological results are presented for formulated inks, by showing the influence of different components. Secondly a deeper investigation was carried out by performing oscillation and thixotropy tests in order to understand the structure of ink and the impact of binding components to the rheological response. In the second part inks were printed onto paper substrate and physical and electrochemical characterization of printed anode is presented by showing main results. The last part is focused on different strategies chosen to enhance electrode's performance. More precisely a calendering strategy and the introduction of additive components were investigated.

### **3.1 Ink formulation**

Firstly inks at different content ratio were formulated in order to find the optimal rheological range processable with selected printing process. Inks composition is expressed as sum of dry material and solvent content. Components are expressed respect to the dry solid content. Rheological measurements allow selecting 40 % wt of dry content as optimal value for selected printing process. A rheological study was performed by studying the influence of carboxymethyl (CMC) and microfibrillated (MFC) cellulose components. Owing to its electronic conductivity, graphite component (GP) was maximized to insure a good conductivity of inks. Table 3.1 shows compositions of formulated inks. As told before dry content and obviously solvent content were fixed at 40 % wt and 60 % wt respectively.

Table 3.1. Composition of optimized inks

Anode optimized formulation			
wt (%)			
GP	CMC	MFC	Graph mark
<b>97</b>	3	-	●
<b>96</b>	2.5	1.5	■
<b>97</b>	1	2	◆
<b>97</b>	2	1	▲

### 3.1.1 Rheology characterization

A steady state analysis was performed to analyze the response of ink to shear rate increment. Inks present a shear-thinning behavior and MFC content influences rheological behavior of ink in terms of apparent viscosity and shear stress (Figure 3.1 and Figure 3.2). A yield stress was observed for all formulations tested as showed in Figure 3.2. Higher concentration of MFCs result in an increase of apparent viscosity. As showed in Figure 3.1, for the whole shear rate range, no Newtonian linear region was observed. This phenomenon shows how MFCs have a strong tendency to create network structures. Despite a shear thinning behavior, for a shear rate ranging between  $60 \text{ s}^{-1}$  and  $120 \text{ s}^{-1}$ , an increase of apparent viscosity was observed for all tested inks containing MFCs. This phenomenon is likely related to the formation of a network structure due to interactions between MFCs. The same behavior was observed by Iotti et al. [121], in aqueous suspension, MFCs can interact between them thanks to their high specific surface area and their temporary bonds, as well as Van der Waals or hydrogen bonds. These interactions appear at certain shear rate values because of motion of MFCs in shear flow medium. As described by Jeffrey the motion of particles is governed by their initial orientation and their particular shape [122]. For MFCs particles, their elaborate shape becomes a predominant factor when solvent flows at shear rate close to  $100 \text{ s}^{-1}$ . At this shear rate the rotation of MFCs particle is higher enough to promote interactions between particles. According to Liu et al. [123], the influence of CMC component to the rheological behavior can be observed in the thinning behavior reported for our inks in the whole shear rate range

tested. As for polymer coils in solution, an explanation can be the disentanglement of CMC chains and the reorientation in the direction of the flow [124-125]. The consequence is the reduction of frictions between shear flow and CMC chains [126].

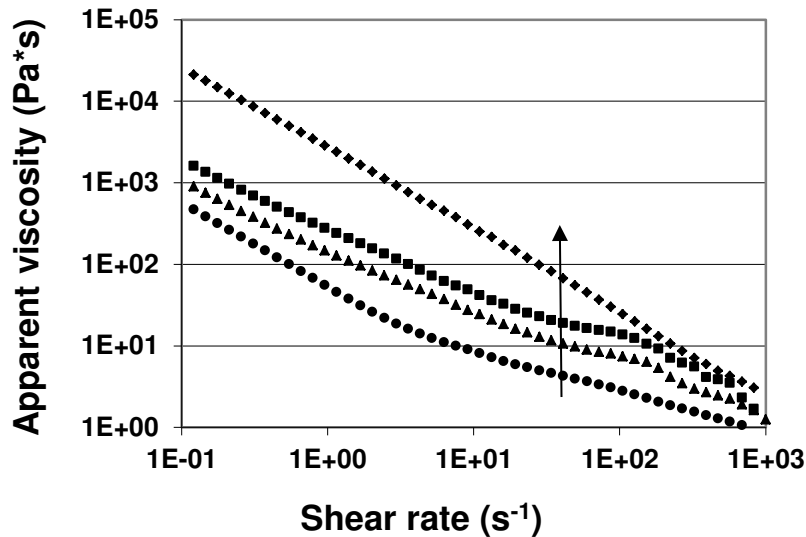


Figure 3.1. Viscosity as a function of shear rate for 0% (●), 1% (▲), 1.5% (■) and 2% (◆) MFC content

Figure 3.2. shows evolution of shear stress as a function of shear rate ranging between  $1 \text{ s}^{-1}$  and  $10 \text{ s}^{-1}$ . Inks exhibit a typical behavior with shear stress threshold. Above this shear stress inks were able to flow [127].

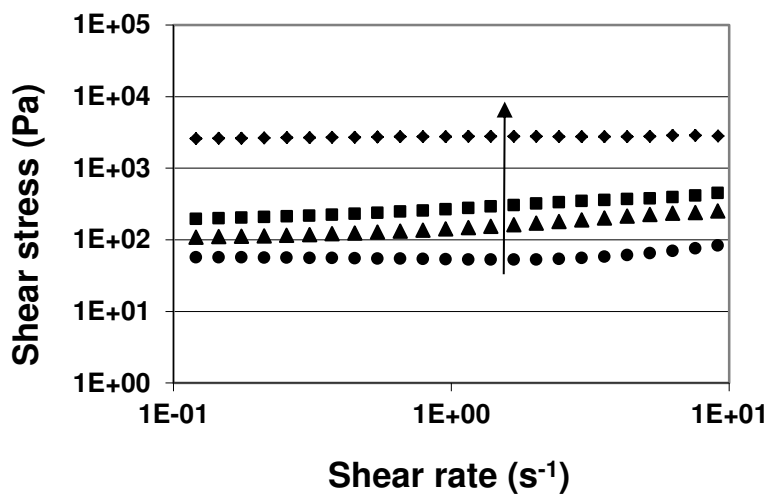


Figure 3.2. Shear stress as a function of shear rate for 0% (●), 1% (▲), 1.5% (■) and 2% (◆) MFC content

## Chapter 3: Development and characterization of printed anode

MFCs play a significant role of thickening agent as showed in Table 3.2 and Figure 3.3. A critical concentration of the system was observed corresponding to 1.5 %. Below this value, apparent viscosity and shear stress present a slight increase but one time passed this value rheological properties suddenly increase.

Table 3.2. Rheological characteristics of the formulated ink

Ink	Viscosity at $\gamma = 1 \text{ s}^{-1}$	Shear stress at $\gamma = 1 \text{ s}^{-1}$
	Pa*s	Pa
M <sub>S</sub> (GP_CMC)/ 40(97_3)	46	53
M <sub>S</sub> (GP_CMC_MFC)/ 40(97_2_1)	128	147
M <sub>S</sub> (GP_CMC_MFC)/ 40(96_2.5_1.5)	240	277
M <sub>S</sub> (GP_CMC_MFC)/ 40(97_1_2)	2396	2759

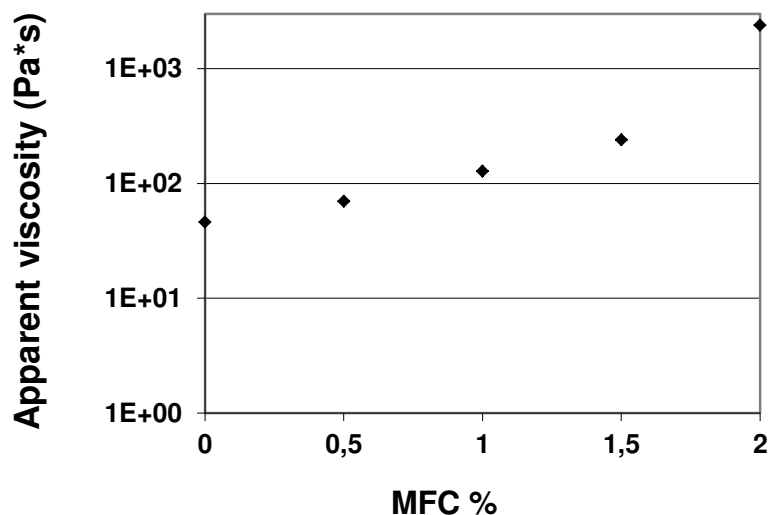


Figure 3.3. Apparent viscosity as function of MFC content

The ink containing 1 % of MFC was selected as optimized ink to print electrodes because of its viscosity is in the suitable range for screen printing technology (see table 1.11). A deeper rheological study was performed to understand its behavior. Ink was dispersed and homogenized by following experimental procedure described in chapter 2 (Paragraph 2.2.1). Figure 3.4 shows the evolution of apparent viscosity as function of shear rate. By following

## Chapter 3: Development and characterization of printed anode

the protocol described in chapter 2 (Paragraph 2.2.1), an increasing and a decreasing shear rate experiment were performed to analyze apparent viscosity behavior and to have a preliminary idea of thixotropy behavior. As showed in Figure 3.4 the experiment was carried out in two different steps. The first step consists in measuring apparent viscosity from  $10^{-1} \text{ s}^{-1}$  to  $1000 \text{ s}^{-1}$ , showed in the graph by the filled squares. Vice versa the second, represented by empty square was obtained by measuring apparent viscosity from  $1000 \text{ s}^{-1}$  to  $10^{-1} \text{ s}^{-1}$ . In “filled squares” curve, apparent viscosity decreases when shear rates increases as described in literature for shear thinning inks [122-123]. In “empty square” curves, a loop hysteresis can be observed at shear rate lower of  $10 \text{ s}^{-1}$ . For time independent experiment, rheological behavior has to be identical. As described by Ghanham et al. CMC has the ability to recover structure of ink when is allowed to rest for a long period of time, after attaining complete breakdown of thixotropy structure [128]. The same ability was reported for MFC aqueous solutions as described by Iotti et al. [121]. At low shear rate sample exhibits an increase of its viscosity until a maximum point. The existence of a critical shear rate suggests that the ink have a cohesive property and exhibits a yield stress at which ink begins to flow. This behavior is typical of screen printed inks as reported in literature for different kind of inks [129-130].

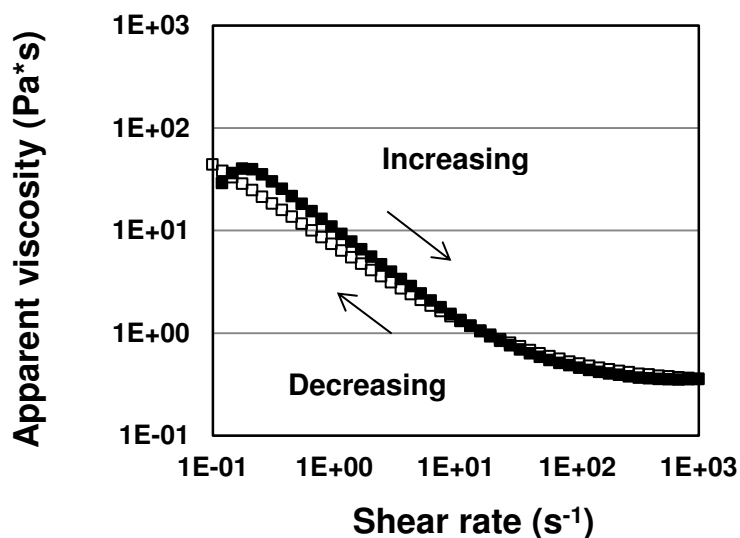


Figure 3.4. Apparent viscosity as function of shear rate for increasing shear rate (■) and decreasing shear rate (□)

A peak of shear stress is evident at critical shear rate of  $0.2 \text{ s}^{-1}$  corresponding to a yield stress of 8 Pa. Up to this value ink is able to flow by showing a pseudo plastic behavior as showed in Figure 3.5.

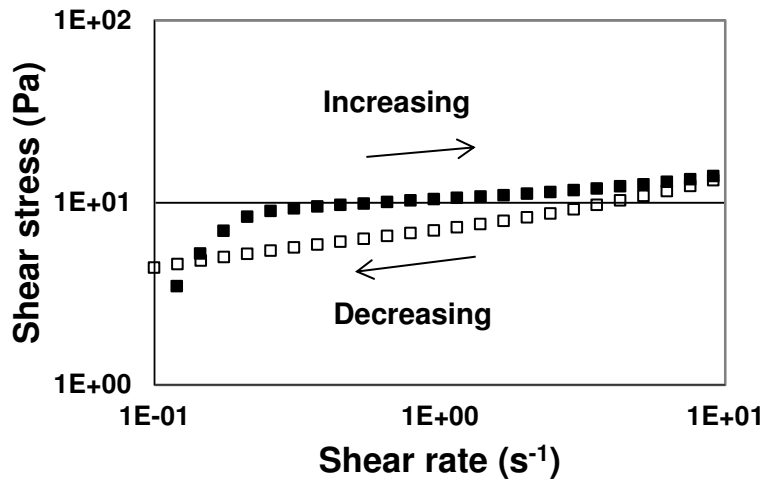


Figure 3.5. Shear stress as function of shear rate for increasing shear rate (■) and decreasing shear rate (□)

In order to extract rheological data, different mathematical models were tested to determine model giving best fit to experimental data. Best results were obtained by using four models: Carreau (x) [131], Blau model ( $\Delta$ ) [132] and Casson Steiner model ( $\diamond$ ) [133]. This models allows to extract informations relative to the cohesiveness of the ink before shearing in terms of shear stress ( $\tau_0$ ) and apparent viscosity ( $\eta_0$ ), or after complete breakdown of the structure in terms of apparent viscosity ( $\eta_\infty$ ; a) and shear stress (b). The model study was performed for shear rate ranging from  $1 \text{ s}^{-1}$  to  $1000 \text{ s}^{-1}$ , in order to consider only the flow region. As showed in Figure 3.6 tested models fit in a good way the behavior at middle and high shear rates. At lower shear rate ( $< 2 \text{ s}^{-1}$ ) a divergence between models and experimental data was observed.

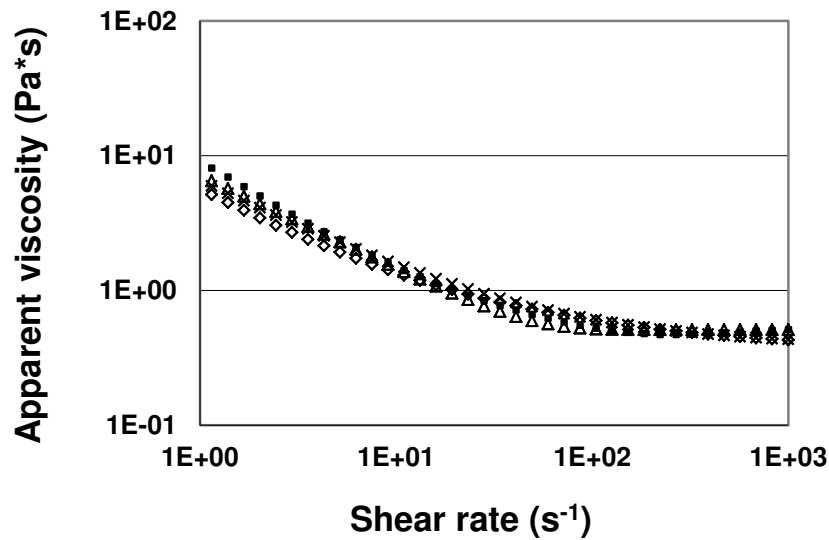


Figure 3.6. Agreement between experimental (■) and Carreau (x), Blau (Δ) and Casson Steiner (◇) model data

Table 3.3 shows the results obtained for each fit. Despite a convergence with data in Figure 3.6, the correlation ratio is low for Blau and Carreau is lower than Casson – Steiner model. In fact Casson-Steiner model seems to be the best model to fit experimental data. Actually the correlation ratio is 0.98. This model allows to quantify the stress of the ink before shearing (Casson yield stress  $\tau_0$ ) and the viscosity at high shear rates (infinite shear viscosity  $\eta_\infty$ ).

Table 3.3. Main properties extracted from Carreau (x), Carreau Gleitner (o), Blau (Δ) and Casson - Steiner (◇) models

Carreau ×			Blau Δ			Casson-Steiner ◇		
$\eta_0$	$\eta_\infty$	r	a	b	r	$\tau_0$	$\eta_\infty$	r
(Pa*s)	(Pa*s)		(Pa*s)	(s <sup>-1</sup> )		(Pa)	(Pa*s)	
44.1	0.4	0.92	0.5	44.9	0.92	3.0	0.3	0.98

### **Thixotropy study**

As defined by Barnes thixotropy is a characteristic ability of fluids with microstructure to move from a state of rest to a state of flow and viceversa [134]. The driving force for this modification is the continuous competition between build up forces due to inflow collisions and break down due to flow stresses. The term microstructure is referred to systems with flocculated particles due to alignment of fibers or molecular associations. Generally to investigate a thixotropic behavior, a study time dependent behavior experiment is performed, at a fixed shear rate, to avoid perturbations due to shear dependent phenomena. Figure 3.7 shows a thixotropy test performed following protocol described in chapter 2 (paragraph 2.2.2). The test consists of apply a low constant shear rate for a determined time and immediately after, a constant high shear rate is imposed for 5 minutes to insure the complete breakdown of ink. Finally a constant shear rate is applied until stabilization of ink structure. In this study, for the last step of the experiment, five shear rates were imposed to investigate the recover ability of the ink. The results are illustrated in Figure 3.7. To point out the recover ability of ink, only the break down and build up step of the experiment are showed. As mentioned before in steady state paragraph, ink presents a thickening behaviour at low shear rate and thinning behaviour at middle and high shear rates. This characteristic is reflected in the thixotropic property. At a shear rate lower than  $1 \text{ s}^{-1}$ , ink recovers its structure and a thinning behaviour at the first time was observed but when equilibrium is reached thickening effect is predominant. This kind of phenomenon is called “antithixotropy”. Different theories are reported in literature to explain it. If we consider the aggregation of the flocs, one interpretation could be that certain flocs can become more opened under the action of high shear rate, thus when shear rate is decreased interactions between flocs are more probable and thus apparent viscosity is higher. The same interpretation was reported by Heckroodt et al. in 1978 for clay suspensions [135] and more recently by Kanai et al. for ferric-oxide suspensions [136]. At shear rate higher than  $1 \text{ s}^{-1}$  a classical shear thinning behaviour was observed with a decrease of apparent viscosity and stabilization after a transient time.

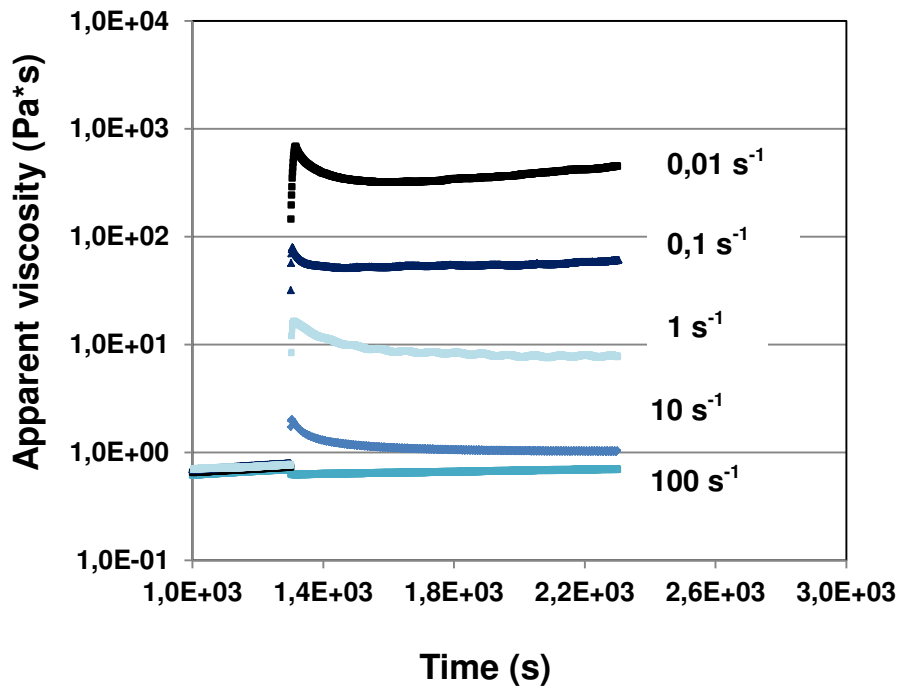


Figure 3.7. Thixotropy test as function of time

The oscillation test was performed to characterize the viscoelastic properties and the particle network strength by following protocol described in chapter 2 (Paragraph 2.2.1). To accurately evaluate the relationship between molecular structure and viscoelastic properties the experiment has to be conducted in regions where the viscoelastic properties observed are independent of imposed stress or strain level. This region is called “linear viscoelastic region” (LVR). An experiment was performed and a shear stress of 1 Pa was selected to insure a LVR. A viscoelastic experiment was performed to understand network structure between particles by studying storage modulus ( $G'$ ), represented by empty mark ( $\square$ ) and loss modulus ( $G''$ ), represented by filled mark ( $\blacksquare$ ) as function of frequency sweep.

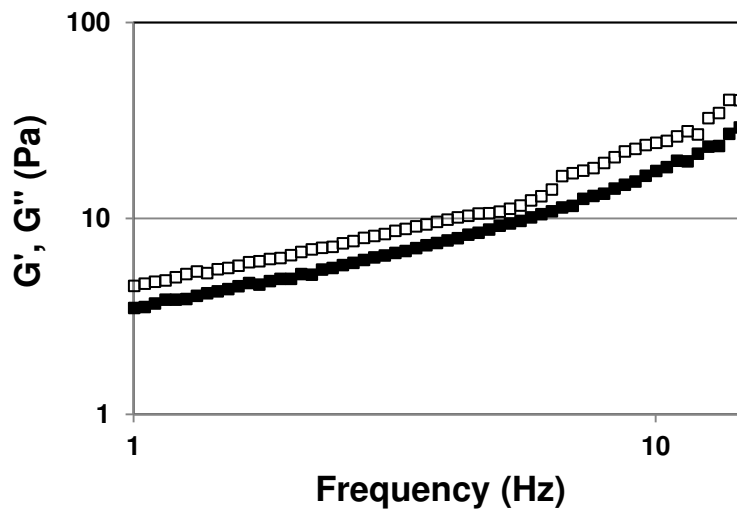


Figure 3.8. Storage ( $G'$ ;  $\square$ ) and loss modulus ( $G''$ ;  $\blacksquare$ ) as function of frequency

The graph in Figure 3.8 shows that storage modulus and loss modulus increase continuously with the frequency. This increase can be associated to a dependence of network formation with frequency. Moreover the storage modulus is always higher than loss modulus within the frequency range. This is an evidence of a structured paste where liquid like behavior are not predominant. This behavior can be associated with MFC binding role. As reported by Lowys et al. [137] and by Tandjava et al. [138] MFC suspensions exhibit a gel like behavior in a large range of frequency with  $G' > G''$ .

## 3.2 Electrode characterization

### 3.2.1 Physical characterization

Ink were printed by a screen printing process onto a cellulose substrate, selected for its good physical properties as listed in chapter 2 ( paragraph 2.1.3). Screen has a crucial role in the quality of the printed electrodes. The transfer of ink is governed by different factors such as open area and thickness of emulsion. A higher thickness of the emulsion insures a more

## Chapter 3: Development and characterization of printed anode

---

important transfer of ink [139]. As listed in Table 3.4 the screen selected has an open area of 40 % calculated by formula described in chapter 2 (paragraph 2.3.1) and the thickness of the emulsion is 110  $\mu\text{m}$ . Different squeegee forces were tested and, to avoid damages to the screen, a value of 50 N was selected. The upward movement of the screen when the squeegee passes by is governed by the snap off distance. To avoid ink transfer problems or an excessive pressure of the squeegee onto the screen, 1 mm value was selected. The number of passages of the squeegee was fixed at 1 because of the maximal transfer of ink has to be reached in 1 passage. An image of the printed electrode is showed in Figure 3.9.

Table 3.4. Parameters of screen printing process

<b>Screen printing process</b>		
Open area of screen	%	41
Emulsion thickness of screen	$\mu\text{m}$	110
Squeegee speed	mm/s	125
Squeegee force	kg	5
Snap off distance	mm	1
Number of passage		1



Figure 3.9. Graphite printed electrode.

Printed electrodes were characterized by different techniques. SEM and FESEM images were realized to analyze the micrography and the interactions between components. Cross section allowed also to evaluate coating thickness.

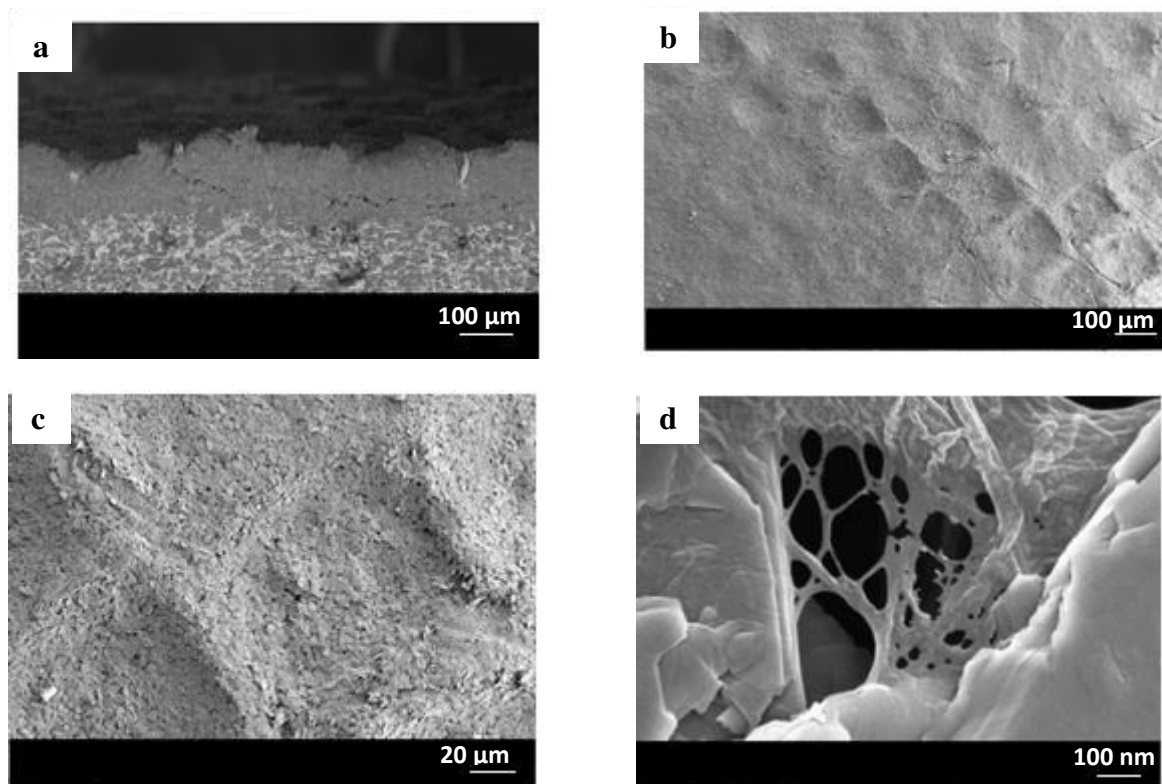


Figure 3.10. FESEM images of screen printed anode at different level of magnitude. Cross section image at 100X (a) , surface images at 300 X (b) , 5 kX(c) and 50 kX (d).

As showed in Figure 3.10.a the cross section of the electrode shows two different layers. At the bottom cellulosic separator, while at the top graphite coating. Figure 3.10.b and Figure 3.10.c show the surface of the electrode at different level of magnitude. A homogeneous surface is visible with marks of screen printing process. In Figure 3.10.d. at sub micrometric scale the binding role of MFCs is presented. MFCs act as binding by creating interactions between graphite particles with a network structure. Jabbour et al. reported a similar structure where MFCs, form a web like network around graphite platelets [101]. Strong interactions between cellulose fibers and graphite particles were described by Jeong et al.. In this case cellulose fibers surround the active material [140]. In both cases this interaction enhances mechanical properties. Physical properties of printed electrode were measured and calculated. Mains results are listed in Table 3.5.

## Chapter 3: Development and characterization of printed anode

Table 3.5. Electrode characterization in terms of coating layer, electronic conductivity, grammage, porosity and surface roughness

<b>M<sub>s</sub>(GP_CMC_MFC) / 40(97_2_1)</b>		
Coating thickness	μm	71±3
Electronic conductivity	S/m	69±19
Grammage of the coating layer	g/m <sup>2</sup>	49±2
Porosity	%	70±3
Surface Roughness (S <sub>a</sub> )	μm	11.9±0.4

As explained before, printed results are affected by screen and printing parameters. For our electrodes a coating thickness of  $71\pm 3$  μm was measured. This value is comparable with value reported in literature by Geyer et al. for anode screen printed electrode [98]. By contrast, electrical conductivity is lower. This incongruence can be due to some differences in screen or printing parameters. However measured value is higher than electronic conductivity reported for other manufacturing techniques [101]. In fact, screen printing technique allows higher deposition of ink compared with other conventional printing techniques. Calculated porosity is comparable with values obtained for screen printed electrode using conventional binding, ranging between 60% and 75% [99], by contrast surface roughness is higher. Image in Figure 3.11 illustrates surface topography. Screen pattern, due to the pressure of the screen onto the substrate, is evident at the surface of electrodes as confirmed previously by FESEM images. This particular topography affects surface roughness of electrodes. As reported by Rouault et al. [99], for graphite electrodes, printed onto copper current collector, the roughness is about 6 μm. This difference is due to the different surface roughness of substrates. Our cellulosic substrate presents a measured roughness of about 4 μm, while generally a copper current collector exhibits a surface roughness ranging between 0.2 and 0.4 μm [142-143]. .

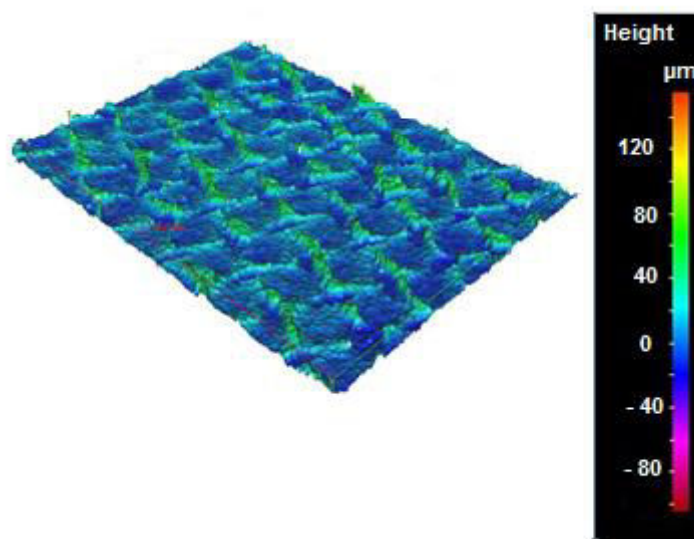


Figure 3.11. Topography image of graphite based electrode (Alicona)

### 3.2.2 Electrochemical characterization

#### Voltammetry measurements

In order to study the effect of charge and discharge on the graphite performances at first cycle and to determine reduction and oxidation peak, a voltammetry experiment was performed. A scan rate of  $0.01 \text{ mVs}^{-1}$  and a ternary electrolyte composed by  $1 \text{ M LiPF}_6$  in EC/PC/DMC (1:1:3 by wt) were chosen. The potential window was limited between 1.2 to 0.02 V to avoid lithium electroplating at low voltage and to not affect the stability of the electrode [144-145]. Metallic lithium was used as counter and reference electrodes. In Figure 3.12 voltammetry plot displays an irreversible peak reduction at 0.43 V that generally is associated to SEI layer formation of graphite particles [146]. At almost 0.16 V a second peak appears. This peak is referred to the intercalation process with formation of the compound  $\text{Li}_{1/3}\text{C}_6$  [147]. At lower potential the current increases again; it indicates the formation of a new lithium-graphite phase,  $\text{Li}_{1/2}\text{C}_6$ . The oxidation of the lithium graphite compound shows a double peak described in literature as de-intercalation of the lithium from the partially formed  $\text{Li}_{1/2}\text{C}_6$  and  $\text{Li}_{1/3}\text{C}_6$  [148] respectively.

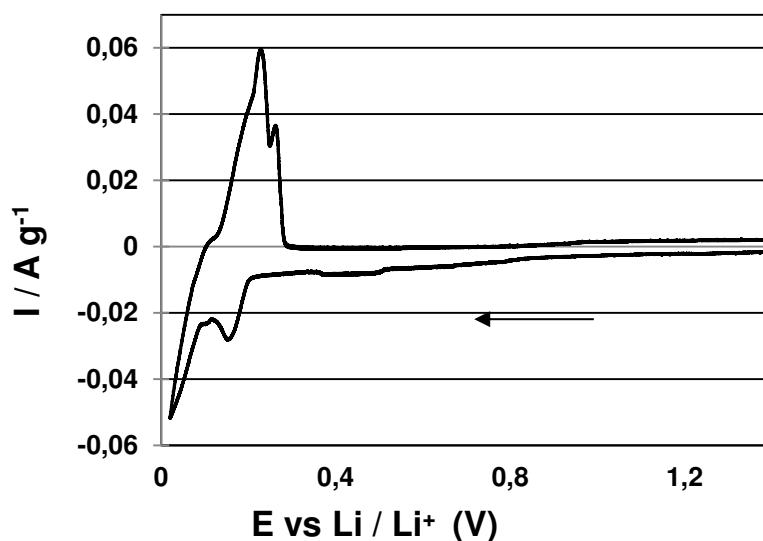


Figure 3.12. Voltammogram at  $0.01 \text{ mVs}^{-1}$  in EC/DMC/PC (1:3:1),  $1\text{M LiPF}_6$  for graphite anode.

### Galvanostatic cycling

Galvanostatic cycling was performed at different current rates between 0.02 and 1.2 V following the same assembling protocol described in chapter 2 (paragraph 2.5.1.) for voltammetry investigation. Figure 3.13 shows voltage as function of discharge and charge capacity during first cycle at open circuit voltage. When current is imposed voltage decreases rapidly from open circuit voltage of about 3.4 V until around 1V. In this potential window (3.4 V- 1 V  $\text{Li/Li}^+$ ) the electrochemical process at the interface graphite / electrolyte is associated to the reduction of an eventual water traces. In the potential window comprised between 0.7 and 1 V, SEI layer formation process is involved. As showed by charge curve, SEI layer formation is an irreversible process where charge is consumed, for this reason charge and discharge curves are not overlaid in the graph. Shift factor depends on the active material surface and on the SEI thickness. At lower potential, intercalation in graphite appeared with the formation of three lithium – graphite compounds:  $\text{Li}_{1/3}\text{C}_6$ ,  $\text{Li}_{1/2}\text{C}_6$  and  $\text{LiC}_6$  [149].

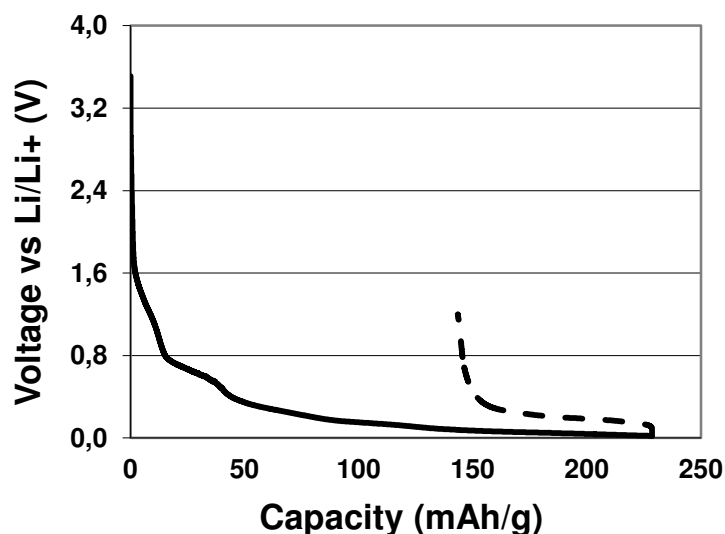


Figure 3.13. Discharge (-)/charge (--) profile at 1<sup>st</sup> cycle.

Generally chemical reactions between solvent and surface's electrode lead to the formation of a thin and homogenous SEI passivation layer. This phenomenon can be observed in a slight mismatch between charge and discharge curves at first cycle. By contrast if other processes are involved during formation of SEI layer, mismatch becomes more important. As reported by Novak et al. different phenomena can affect voltage discharge and charge profile such as exfoliation or bad interactions with some solvents [150]. In our case the difference between two curves, corresponding to a high irreversible capacity, can be associated to the elevated specific surface area of employed graphite. Some studies reported a linear relationship between irreversible capacity and specific area [151]. This phenomenon is due to the fact that SEI formation is a surface process [152]. As described in chapter 2 (paragraph 2.1.2) employed graphite exhibits a potato shape and a BET specific surface area of  $10 \text{ m}^2/\text{g}$ , which may explain the high irreversible capacity obtained. Specific capacity as function of number of cycles is presented in Figure 3.14. An initial capacity of 100 mAh/g for first 5 cycles was measured at a current rate corresponding to  $C/10$ , far from the theoretical value of graphite (372 mAh/g). An irreversible capacity of 143 mAh/g was measured at the first cycle. This value is high compared to value reported in literature, ranging from 20 and 100 mAh/g [149]. This not optimistic cycling behavior can be due to the high porosity of the electrode (70 %). Indeed, this high porosity induces a poor electronic conductivity (Table 3.5) due to the high electronic pathway. This weak electronic conductivity prevents the formation of a

homogeneous and stable SEI layer. A consequence is that only a part of the active material is involved in charge / discharge reactions. Furthermore, this high porosity induces an electronic disconnection of some graphite particles, thus only a part of the active material is involved in charge / discharge reactions, which can explain the low reversible capacity obtained.

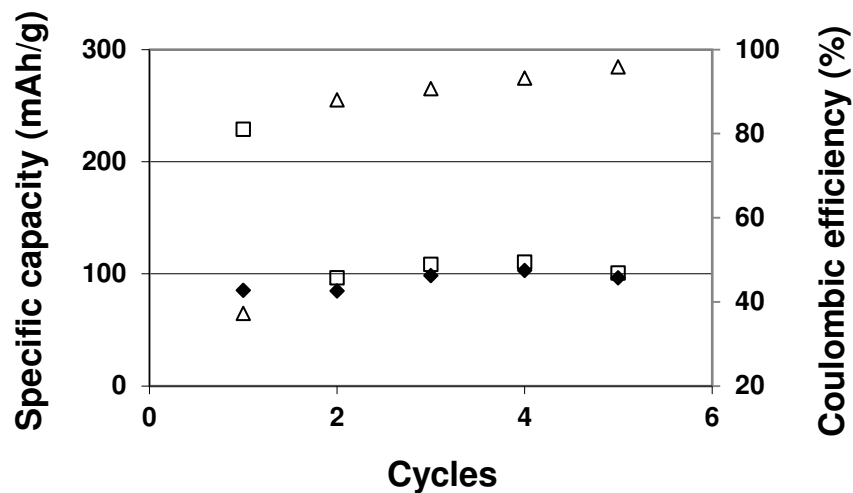


Figure 3.14. Charge (■) / discharge (□) specific capacity and coulombic efficiency (Δ) as function of cycles

Figure 3.15 shows the galvanostatic discharge and charge profiles obtained for current rates ranging between  $C/10$  and  $C$ . A continuous reduction of capacity can be observed when current rate increases. The shape of the curves reflects reversible lithium intercalation and deintercalation processes occurring at potential lower than 0.3 V [153]. The characteristic plateau due to lithium insertion and extraction is not evident at  $C$  rate higher than  $C/10$ . This phenomena is due to the high polarization of the electrode related to the high porosity (70%) and to the low electronic conductivity (69 S/m). In fact a polarization value of about 0.6 V is evident when current rate increases from  $C/10$  to  $C/5$ .

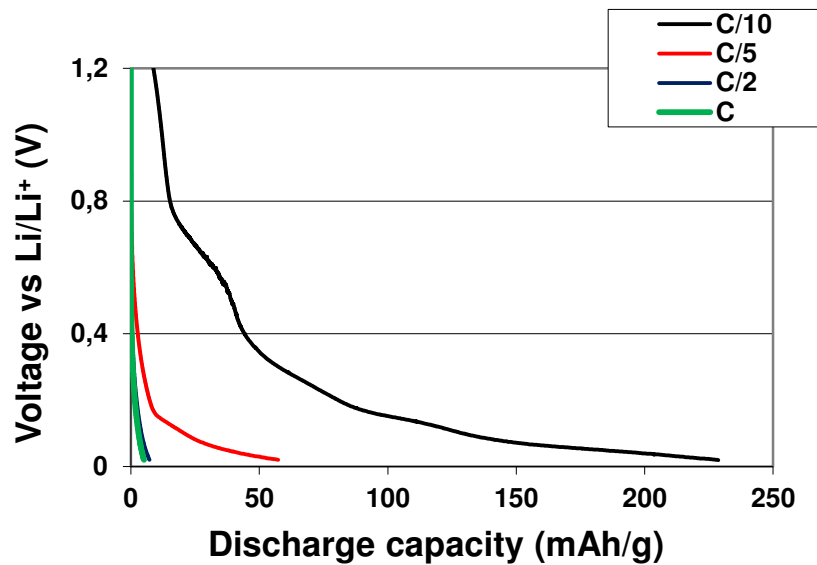


Figure 3.15. Discharge profiles at different current rates.

Figure 3.16 shows the behavior of the electrode at higher current rates. At C/5 specific capacity decreases at 57 mAh/g and remains almost stable for 10 cycles. After 15 cycles electrode were tested at C/2 for 10 cycles by obtaining a specific capacity of 25 mAh/g. Then the electrode was tested at 1 C for further 20 cycles measuring a specific capacity of 27 mAh/g. Performances are not comparable with values reported in literature because of high porosity of the electrodes (70 %) respect to conventional one (30% – 40%) and thus the high mean path of the electrons . A calendaring step is an appropriate strategy to improve electronic conductivity and to reduce the porosity of the electrodes. Moreover the addition of a conductive agent can enhance performances. As reported in literature by Yoshio et al., carbon coated graphite shows superior electrochemical performances compared with original graphite [152]. If we consider the coulombic efficiency, it rises progressively since a value of 37 % until 98 %. This could be due to the formation of SEI layer that in this case involves more cycles to obtain a stable layer or to side reactions between lithium ions and impurities adsorbed onto the surface of the electrode.

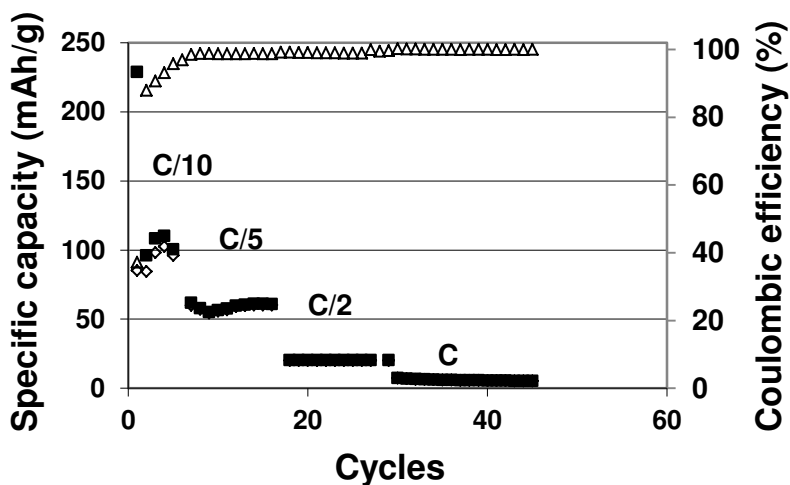


Figure 3.16. a) Specific discharge/charge and b) coulombic efficiency capacity as function of cycles

### 3.2.3 Influence of inactive components

In order to evaluate the effect of different components to the electrochemical behavior, three different inks containing MFC or CMC and both of them were formulated and printed onto cellulose substrates. The MFC based ink was deposited by blade method because of its high viscosity, by following procedures commonly used in literature [154-155]. Each ink contains the same amount of active material and inactive material with 97 % and 3% wt respectively. Figure 3.17 and table 2.6 shows the evolution of electrochemical performances, porosity and electrical conductivity as function of inactive material type. Despite porosity values are constant, CMC based sample exhibited the best performances with a capacity of 139 mAh/g. This is likely due to its better electronic conductivity (87 S/m) compared to the other two inks. In addition CMC has an important role for the stability of the ink. In fact as demonstrated by Lee et al., better dispersions of graphite particles can be obtained when CMC binding is employed, overall for CMC with low degree of substitution (DS) [156]. In fact results shows how the combination of MFC and CMC exhibits better performances compared with MFC based electrode. Despite CMC based electrode has best performance, the addition of MFC can improve mechanical properties as described by Chiappone et al. [157].

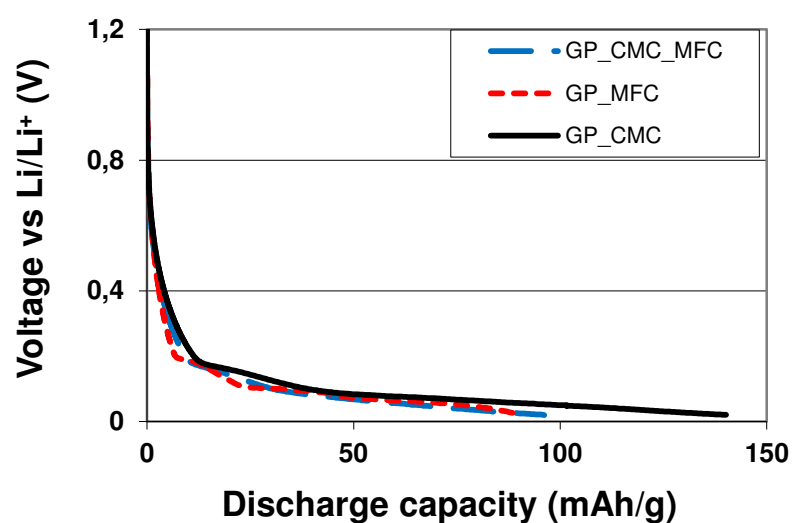


Figure 3.17. Discharge profile as function of binding components for 2<sup>nd</sup> cycle at C/10

Table 3.6. Specific capacity as function of binding components at different current rates

	Specific capacity (mAh/g)		
	C/10 mAh/g	Porosity %	Electronic conductivity Sm <sup>-1</sup>
GP_CMC	139±7	70±4	87±20
GP_MFC	86±0.6	70±3	54±15
GP_MFC_CMC	93±8	70±3	69±19

### 3.3 Calendering study

#### 3.3.1 Physical characterization

The purpose of this study was to investigate the calendering effects on the physical and electrochemical properties of graphite based negative electrode. Different electrodes were printed by following printing protocol described in paragraph 2.3.2. Electrodes were fed through the gap of a calendering machine to be compressed at four different linear loads: 1- 3

– 33 – 73 kN/m in order to obtain four different electrode densities. After being calendered, electrodes were characterized in terms of surface topography and roughness by means of multifocal microscope as described in paragraph 2.3.2. Electronic conductivity was measured by a four point probes, porosity and thickness were calculated and measured respectively as described in paragraph 2.3.2

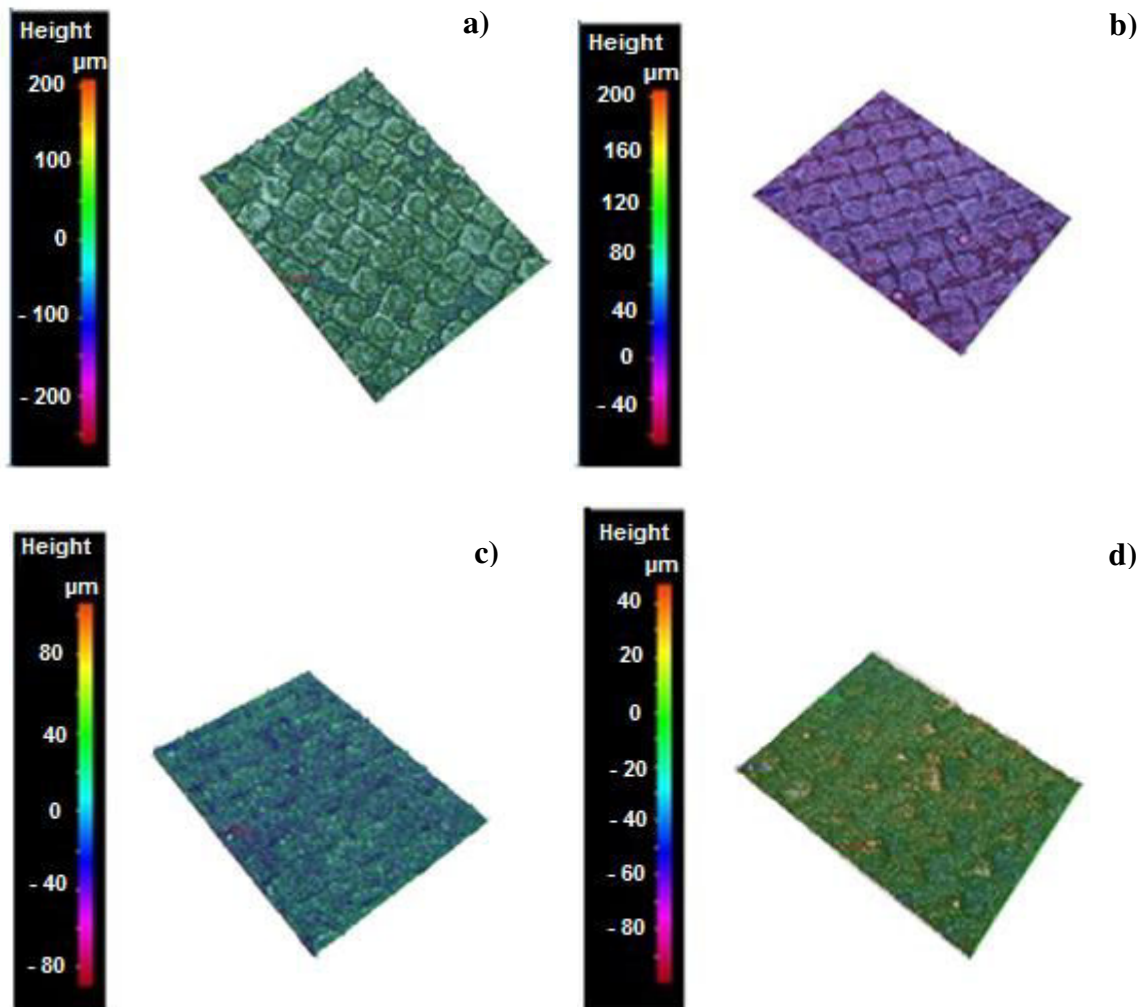


Figure 3.18. Topography image of calendered negative electrode at 1(a) - 3(b) – 33(c) and 73(d) kN/m at a magnitude of 5x.

Topography images in Figure 3.18 show surface modifications as function of the applied linear load. In Figure 3.18.a and Figure 3.18.b screen pattern is clearly observed as mentioned before in SEM images for not calendered negative electrode. For a linear load up

## Chapter 3: Development and characterization of printed anode

then 3 kN/m screen pattern is less evident and a smoother surface appears (Figure 3.18.c and Figure 3.18.d). As listed in Table 3.7, physical properties are strongly connected to calendering pressures. A continuous decrease of porosity was observed due to the compression of the electrode. A plateau in decreasing trend was observed since 3 kN/m due probably to the maximal compression of substrate. The value of porosity obtained is comparable with commercial graphite based negative electrode, as reported by Striebel et al. [158]. Electronic conductivity rises up progressively from 69 S/m to 619 S/m owing to better connection between graphite particles. As reported by Takamura et al. an excellent conductivity within the negative electrode structure leads to the formation of a uniform SEI layer [159]. Roughness values decreases when calendering pressure increases as showed before by topography images in Figure 3.18.

Table 3.7. Electrode characterization as function of calendering linear load

		<b>M<sub>s</sub> (GP_CMC_MFC) / 40(97_2_1)</b>				
		<b>Calendering linear load (kN/m)</b>				
		<b>-</b>	<b>1</b>	<b>3</b>	<b>33</b>	<b>73</b>
Coating thickness	μm	71±3	38±1	35±2	33±2	32±2
Electronic conductivity	S/m	69±19	145±54	177±45	278±77	619±57
Porosity	%	70±3	39±4	40±5	36±3	34±3
Roughness (S <sub>a</sub> )	μm	11.9±0.4	9.7±0.5	7.4±1.2	7.3±1.1	6.1±0.5

### 3.3.2 Electrochemical characterization

Electrochemical characterization of electrodes was performed to analyze the influence of calendaring process. Electrodes were cut and assembled in Swagelok<sup>®</sup> cells with Celgard<sup>®</sup> separator and 1M LiPF<sub>6</sub> in EC/DMC/PC 1:3:1 electrolyte as described before for not calendared electrode. In Figure 3.19. discharge profile at a current rate of C/10 after SEI formation is plotted. An increment of specific capacity was measured when calendaring pressure increases. In addition, if we consider the typical plateau of graphite during intercalation process at voltage lower than 0.2 V, a reduction of polarization of the electrode was observed when calendaring pressure increases. In fact, a diminution of the porosity occurs when calendared pressure increases, by reducing the electronic pathway of the electrons. In added, as described by Novak et al.[160] and by Gnanaraj et al.[161] there is a strong connection between performances and porosity of the electrodes. In Table 3.8 specific capacity values of different calendared electrodes were measured as function of current rate from C/10 value until C value current rate. An increase of specific capacity was measured for all current rates tested with a maximum value of 315 mAh/g, not far from theoretical graphite value of 372 mAh/g, at the higher calendaring pressure. Our results are in agreement with investigation performed by Shim et al. [162]. They show how graphite based electrodes exhibit an increase of rate capacity until a maximum of electrode density. In fact an increment of the electrode density corresponds to a diminution of porosity. Thus the contact between graphite particles are enhanced and electrons can flow easily from the electrode to the current collector. Nevertheless a maximum value has not be exceed otherwise a fade of capacity occurs, probably due to the limitation of lithium ion diffusion or damage of the electrode [163].

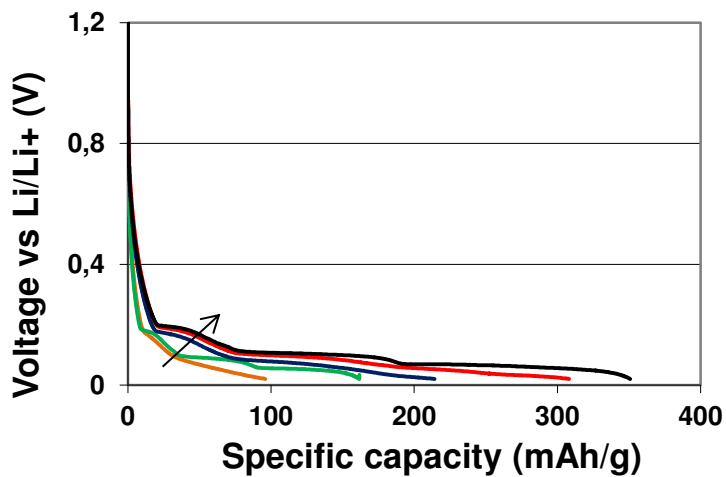


Figure 3.19. Discharge profile as function of calendaring at: 0 kN/m (-), 1 kN/m (-), 3 kN/m (-), 33 kN/m (-) and 73 kN/m (-)

Table 3.8. Specific capacity as function of calendaring linear load at different current rate

$M_s$ (GP_CMC_MFC) / 40(97_2_1)				
Specific capacity (mAh/g)				
Calendering linear load (kN/m)	C/10	C/5	C/2	C
-	93±8	58±2	20±3	5.3±0.2
1	155±3	116±4	31.9±0.1	17.0±0.4
3	208±3	180±6	57±2	20±2
33	306±4	237±7	65±6	23±2
73	315±1	297±7	129±6	44±3

Figure 3.20 shows the influence of the coulombic efficiency as function of linear load at the first cycle at a current rate corresponding to C/10. It is expressed as the ratio between charge

and discharge reaction at the first cycle. A progressive increase of the coulombic efficiency was measured when linear load is augmented. Generally this behavior can be related to the formation of the SEI layer based on reactions at the surface of the electrode [164]. By contrast, in our case the irreversible capacity related to the formation of the SEI layer didn't seem affected by the calendaring process. In fact a value of 170 mAh/g for the irreversible capacity was measured at a calendaring pressure corresponding to 73 kN/m, not far from 140 mAh/g for not calendared electrode. This value suggests that the increment of capacity is more affected by the low polarization at higher calendared pressures thanks to the reduction of the porosity and to the increment of electronic conductivity and not by the formation of the SEI layer.

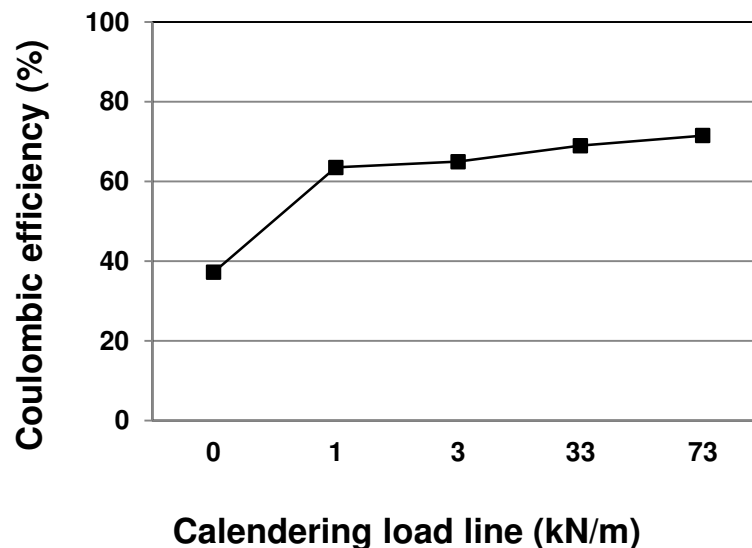


Figure 3.20. Coulombic efficiency at a first cycle during SEI formation as function of calendaring linear load.

### 3.3.3 Optimization of SEI layer

SEI layer is one of the parameter that affects graphite electrode performance, in order to print a full cell, it is crucial to optimize anode SEI layer to avoid excessive consumption of lithium ions. Two different approaches were chosen: use of additive and use of binary electrolyte without propylene carbonate (PC) solvent. The first approach consists in the introduction of additives such as mono fluoro ethylene carbonate (<sup>1</sup>FEC). It has been demonstrated that additives polymerizes on the electrode surfaces, producing a protective film that prevent

further reaction at the interface between electrolyte and electrode [165]. The second approach consists in the replacement of ternary electrolyte with a binary commercial electrolyte composed by 1 M  $\text{LiPF}_6$  in EC/DMC 1:1 wt. In fact as reported by Aurbach et al. the methyl group derived from the reduction of propylene carbonate (PC) based electrolyte, prevents the precipitation of this product in compact layer. Thus, no efficient passivation of the graphite electrode can be obtained in PC solutions if is not properly mixed with other organic solvents [35]. As showed in Figure 3.21 a considerable enhancement of specific capacity was reached by using binary electrolyte and additive with ternary electrolyte. In Table 3.9 a comparison of reversible and irreversible capacity shows how the presence of additives reduces the irreversible capacity from a value of 144 mAh/g for not calendered electrode until a value of 115mAh/g. The higher reversible capacity was obtained by using the binary electrolyte. A value of 322 mAh/g was measured. In terms of coulombic efficiency the table shows how a considerable enhancement was reached by adding an additive and using the binary electrolyte. Coulombic efficiency increased from 37% until 67 %.

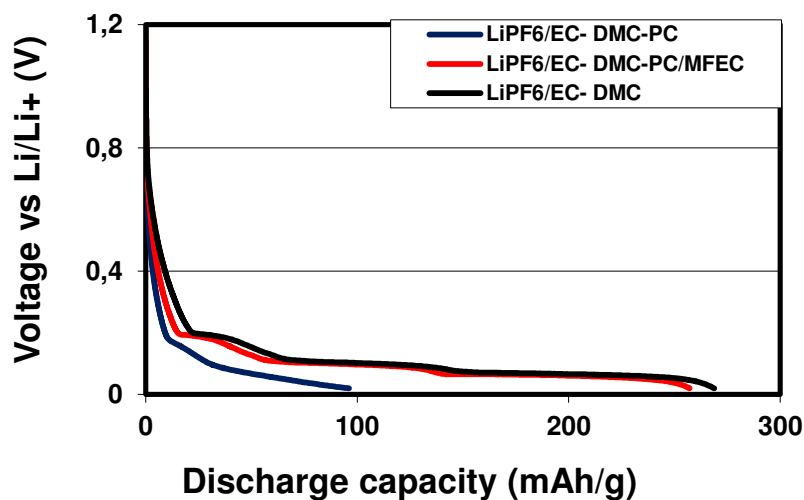


Figure 3.21. Discharge profile as function of electrolyte composition after first cycle

Table 3.9. Specific capacity and at 1<sup>st</sup> cycle at C/10, as function of electrolyte composition for not calendered electrode

	<b>Total capacity</b>	<b>Reversible capacity</b>	<b>Irreversible capacity</b>	<b>C.E.*</b>
	mAh/g	mAh/g	mAh/g	(%)
LiPF <sub>6</sub> in EC/PC/DC 1:1:3	229	85	144	37
LiPF <sub>6</sub> in EC/PC/DC 1:1:3 + 2% wt <sup>1</sup> FEC	355	239	115	67
LiPF <sub>6</sub> in EC/DMC 1:1	480	322	158	67

\* coulombic efficiency (C.E.)

### 3.4 Conclusion

In this work we demonstrated how cellulose derivatives and a conventional printing process such as screen printing, can be used in the manufacturing of negative electrodes for lithium ion batteries. As described in the introduction of this work, one of the aims was the replacement of toxic components. By using carboxy methyl cellulose (CMC) and micro fibrillated cellulose (MFC) as binder and reinforcement respectively, and water as solvent, we demonstrate the feasibility of inks adapted for screen printing process. This inks exhibit an appropriate rheology behavior for the suitable printing process, as demonstrated by steady state, oscillatory and thixotropic measurements. Electrodes were printed onto cellulose substrate and characterized by physical and electrochemical investigations. The obtained results confirm how cellulose based components and printing process can be combined to obtain environmental friendly and up scalable negative electrodes. The last part of this work was dedicated to improve results obtained by following two strategies. A Calendering process was performed in order to improve electronic conductivity and to reduce porosity of electrodes. A progressive increase of conductivity and electrochemical properties was observed for all pressures values tested. As example reversible capacity at the first cycle rises from about 100 mAh/g for not calendered electrode, to 315 mAh/g for high calendered electrode. Indeed the increase of contact between graphite particles and the reduction of

## Chapter 3: Development and characterization of printed anode

---

porosity have a predominant effect on cycling efficiency of compressed electrodes. The second strategy was to reduce the passivation layer (SEI) formed during first cycles. The first idea was to add an additive in the electrolyte in order to reduce consumption of lithium ions for SEI formation and the second one was the replacement of ternary electrolyte by a binary one, without propylene carbonate (PC) component. Results confirm how binary electrolyte and additive allow to obtain a reversible capacity and a coulombic efficiency higher respect to ternary electrolyte. In fact it seems that binary electrolyte and additive contribute to form a less resistive SEI layer, as showed by the loss capacity value, lower than ternary electrolyte.

---

# **Development and characterization of printed cathode**



## 4. Development and characterization of printed cathode

### Introduction

In this work screen printed positive electrodes are manufactured by following the same strategy used for the fabrication of negative electrodes. Inks are formulated by using as binding and reinforcing cellulose derivatives. A conductive agent is added in order to insure a good electronic conductivity. Rheological study are performed in order to find the suitable properties for the screen printed process and to investigate the influence of components. Physical and electrochemical characterizations of printed electrodes are presented and discussed and a calendaring study is proposed to enhance properties. Finally a conclusion resumes main results obtained in this work in terms of rheological, physical and electrochemical properties.

### 4.1 Ink formulation

Inks were formulated by following the same procedure used for negative inks. Different content ratio of dry matters were investigated, in order to find the best formulation processable with screen printing process,  $\text{LiFePO}_4$  (LFP) was selected as active material for positive electrode because among all active materials, it is one of the safest and environmental benign [166]. Owing to its intrinsic low electronic conductivity of about  $10^{-7} \text{ S m}^{-1}$  [167], the addition of a conductive agent such as carbon black (CB) is necessary to insure an optimal electronic conductivity [168]. Binder material content (CMC and MFC) was minimized at 3 wt % in order to maximize electrochemical and electronic properties. As a first approach inks were coated onto cellulose substrate with a conventional coating method (blade method) in order to evaluate printing quality. Figure 4.1 exemplifies the printing quality for two inks with a dry material weight ( $M_s$ ) corresponding to 40 % (Figure 4.1.a) and 60% (Figure 4.1.b) respectively. Table 4.1 reports results obtained for all tested inks.

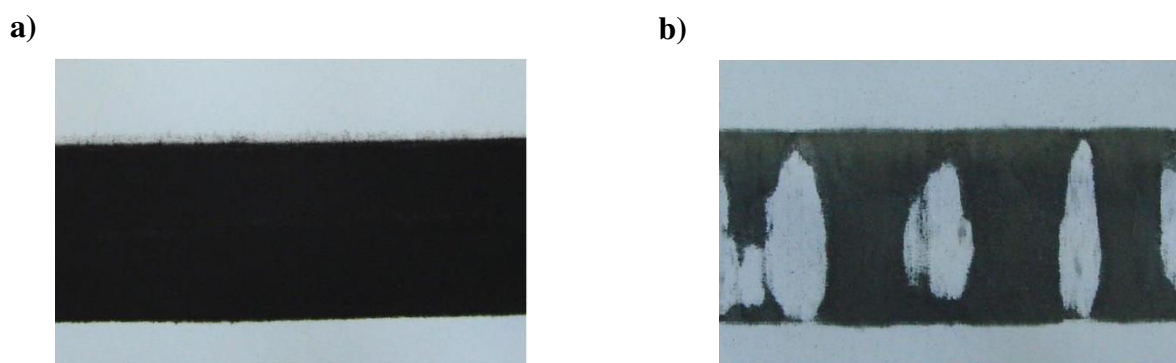


Figure 4.1. Printing quality of blade coated inks with a) 40 wt% and b) 60 wt% of dry content.

Table 4.1. Printing quality as function of ink composition. The symbol  $\checkmark$  indicates good adhesion between ink and substrate while the symbol x indicates bad printing quality

Cathode formulations						
$M_s$	LFP	CB	wt (%)			Printing quality
			CMC	MFC	H <sub>2</sub> O	
60	70	27	2	1	40	x
50	70	27	2	1	50	x
40	70	27	2	1	60	$\checkmark$
30	70	27	2	1	70	x

The best formulation for a screen printing process, analyzed by rheological experiment, is 40 % wt of dry material ( $M_s$ ) and 60 % wt of solvent. This value of dry material was fixed and an investigation in terms of component contents was performed. Cellulosic based components (MFC and CMC) were fixed at 3 % wt in order to enhance electrochemical properties. One of the most important parameter for LiFePO<sub>4</sub> based electrodes is the content of conductive agent because of intrinsic resistivity of LiFePO<sub>4</sub> [169]. In order to understand the influence of this parameter, rheological study was carried out by varying carbon black content from 7 % wt until 27 % wt as showed in Table 4.2.

### 4.1.1 Rheology characterization

Table 4.2. Composition of cathode formulated inks as function of conductive agent content from a content value of 7 % to a value of 27 %.

<b>Cathode formulations</b>					
<b>wt (%)</b>					
<b>M<sub>s</sub></b>	<b>LFP</b>	<b>CB</b>	<b>CMC</b>	<b>MFC</b>	<b>H<sub>2</sub>O</b>
40	90	7	2	1	60
40	80	17	2	1	60
40	70	27	2	1	60

#### Steady shear study

Figure 4.2 shows the evolution of apparent viscosity as function of shear rate for formulated inks at different carbon black contents: 7 wt % (filled triangles), 17 wt % (filled squares) and 27 wt % (filled circles). A dependence of apparent viscosity versus the shear rate was observed for tested inks, typical of non newtonian liquids. More precisely a thinning behavior was reported for all inks with a decrease of the apparent viscosity when shear rate increases, as observed by Dominko et al. for carbon black aqueous dispersion [170]. When shear rate increases network structure can be ruptured and therefore suspensions can flow with a typical shear thinning behavior [171]. When carbon content increases a thickening effect was observed, because of interactions between carbon black particles that form a network structure stronger when content ratio increases [171]. At low shear rate ( $< 3 \text{ s}^{-1}$ ) some differences between curves were observed. Up to 7 wt % of CB, rheological curves present a change in slope corresponding to a critical shear rate, associated to carbon black dispersions. As explained by Amari et al. carbon black particles form a network structure at lower shear rate [171]. It seems that contribution to rheological behavior becomes less influent at percentage lower than 7 wt % as showed by a continuous shear thinning behavior even at low shear rate.

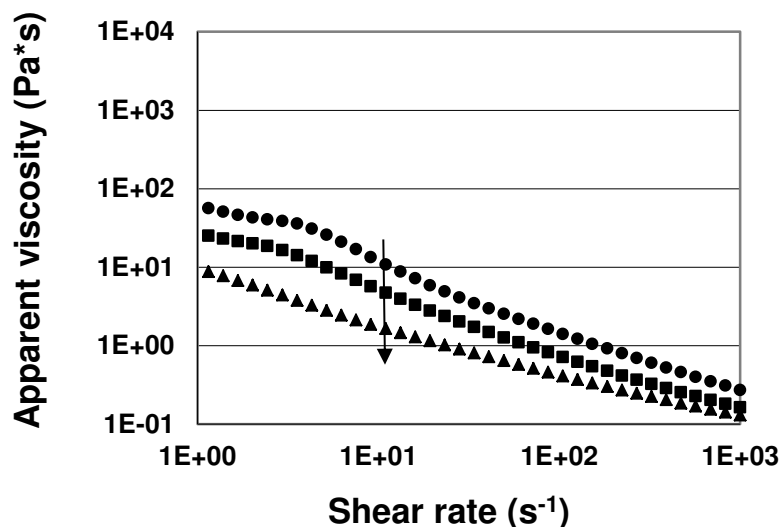


Figure 4.2. Viscosity as a function of shear rate for inks at 7 % (●), 17% (■) and 27% (▲) of carbon black content

Shear stress behavior is presented as function of shear rate in Figure 4.3. A characteristic threshold value is evident at a shear rate of  $1 \text{ s}^{-1}$  for all tested inks, as reported in Table 4.3. At this shear stress value corresponds a critical shear rate. Up to this critical value inks flow.

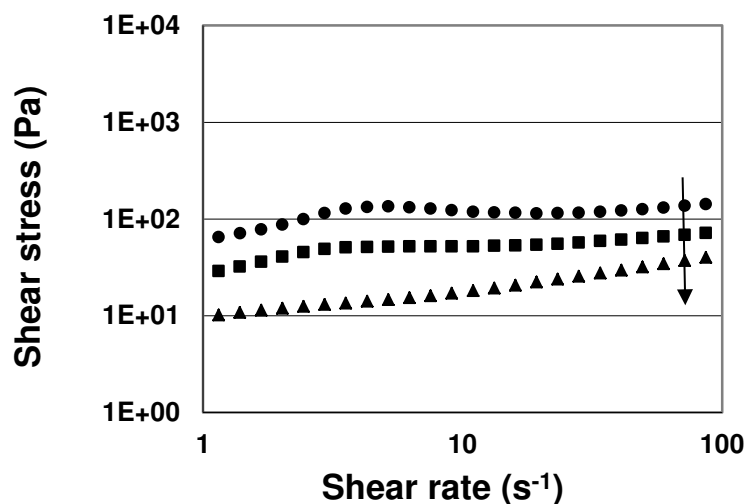


Figure 4.3. Shear stress as a function of shear rate for inks at 27 wt% (●), 17wt% (■) and 7wt% (▲) of carbon black content

Carbon black content affects strongly the electronic conductivity of the electrode. Inks were screen printed onto a paper substrate and electronic conductivity was measured by means of a

## Chapter 4: Development and characterization of printed cathode

four probe instrument, by following the same procedure for all tested inks. As showed in table 3.3 up to 17wt%, inks present an appreciable electronic conductivity that enhances with increasing the carbon black content. Bischoff et al. report the influence of carbon black additive. Electronic conductivity increases sharply in polymer matrix when fraction content increases [172]. They measured a percolation threshold value corresponding to a volumic fraction of 0.1. In our case the percolation threshold is lower than 27 % wt. The thickening role of carbon black is illustrated in Table 4.3 and Figure 4.4. Interactions between particles and CB becomes more important when carbon black content increases. This fact is associated with the consequent increase of apparent viscosity and shear stress.

Table 4.3. Rheological characteristics (viscosity and shear stress) of the formulated ink

Ink M <sub>s</sub> (LFP_CB_CMC_MFC)	Viscosity at $\dot{\gamma} = 1 \text{ s}^{-1}$	Shear stress at $\dot{\gamma} = 1 \text{ s}^{-1}$	Conductivity
	Pa·s	Pa	S/m
40(90_7_2_1)	9	10	Not measurable
40(80_17_2_1)	25	29	17±3
40(70_27_2_1)	56	64	35±2

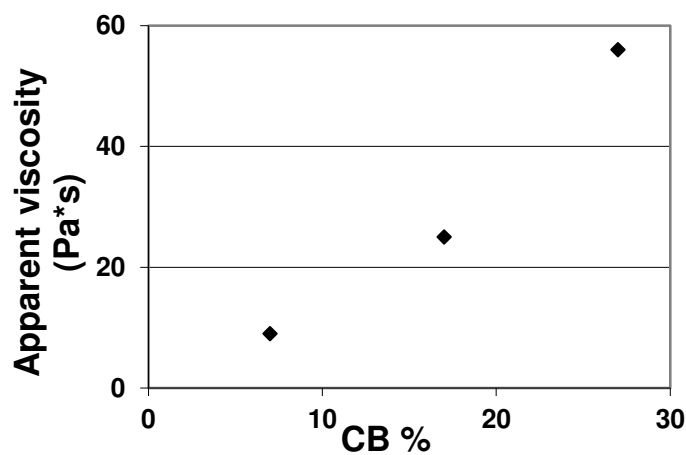


Figure 4.4. Apparent viscosity as function of CB content

The ink with 27 wt% of CB was selected as optimal formulation in order to insure an appreciable electronic conductivity and to fill the rheological requirement for the printing process selected to manufacture the electrode. Despite this value of CB content is higher than the percolation threshold for CB in the electrode, this content will allow to reduce the porosity of the electrode by triggering electrochemical properties of the printed electrode. Ink was dispersed and homogenized by following experimental procedure described in paragraph 2.2.1. Figure.4.5 shows the evolution of apparent viscosity as function of shear rate for selected ink. Two different steady shear experiments were performed in order to investigate ink rheological behavior. As explained for the negative inks, the “filled squares” curve was obtained by imposing a shear rate from 0.1 to 1000  $\text{s}^{-1}$ . By contrast “empty squares” curve was obtained by imposing a shear rate from 1000 to 0.1  $\text{s}^{-1}$ . Both curves exhibit a shear thinning behavior. As suggested by Lee et al. this behavior can be associated to the breakdown of agglomerates composed by cellulose and conductive components. The applied shear forces induce a progressive decrease of the apparent viscosity and CMC and MFC play a role of surface modifier by affecting frictions forces between particles [173]. A slight hysteresis loop was observed at a shear rate ranging between 1  $\text{s}^{-1}$  and 200  $\text{s}^{-1}$  that indicates a thixotropy behavior of the ink.

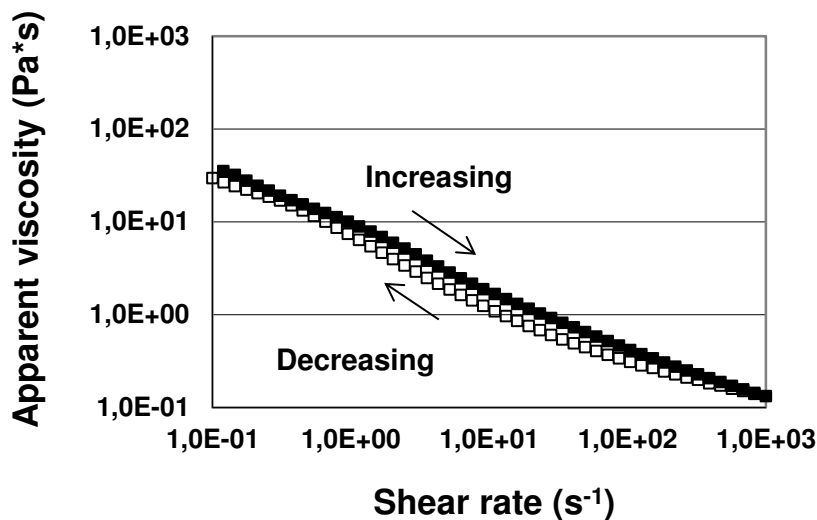


Figure.4.5. Apparent viscosity as function of increasing (□) and decreasing (■) shear rate

In Figure 4.6 shear stress as function of shear rate is illustrated. Ink exhibits a yield stress of about 4 Pa at a shear rate corresponding to  $0.1 \text{ s}^{-1}$ . As reported by different authors, CMC, MFC and CB can create a network structure at low shear rates in aqueous suspension [174-175]. Porcher et al. described how a low content of carbon black (5 wt %) and CMC (1 wt %) particles doesn't allow to clearly distinguish a yield stress [176]. In our case the addition of MFC and the higher content of CB additives, seems to affect rheological behavior at low shear rate by increasing yield stress point.

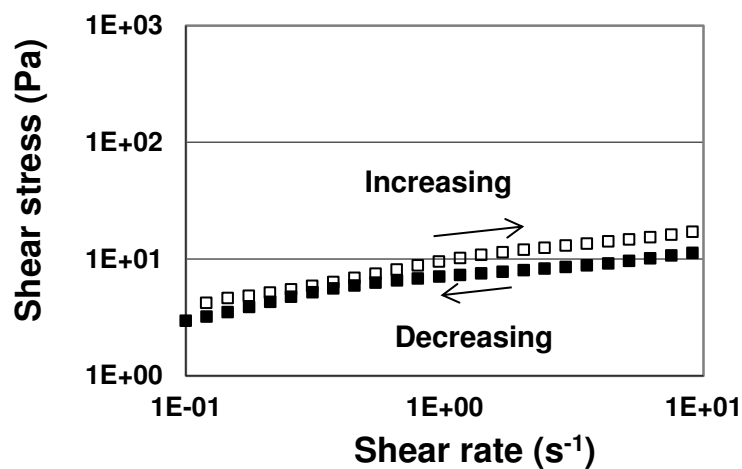


Figure 4.6. Shear stress as function of increasing ( $\square$ ) and decreasing ( $\blacksquare$ ) shear rate

### Thixotropic study

Figure 4.7 shows a thixotropy study carried out to understand the hysteresis loop observed previously. The protocol measurement is the same followed for negative electrode described in paragraph 2.2.2. A low constant shear rate is applied for a determined time and immediately after, a constant high shear rate is imposed for 5 minutes to insure the complete destructure of ink. As last step a constant shear rate is applied until stabilization of ink structure. In this study, for the last step of the experiment, five shear rates were imposed to investigate the recover ability of the ink. As illustrated in Figure 4.7, in order to evidence the recover ability of ink, only a part of the break down and the build up step of the experiment are showed. Inks recover their structure for all imposed shear rates. The transient time

necessary to stabilize structure decreases when shear rate increases. If we consider build up curves at  $0.01 \text{ s}^{-1}$  and  $100 \text{ s}^{-1}$ , an instantaneous recovering of structure can be pointed out for curve obtained at  $100 \text{ s}^{-1}$ . This phenomenon can be associated to the weak interactions between components because, at this shear rate, ink is in a flow state where floc structures are minimized [177].

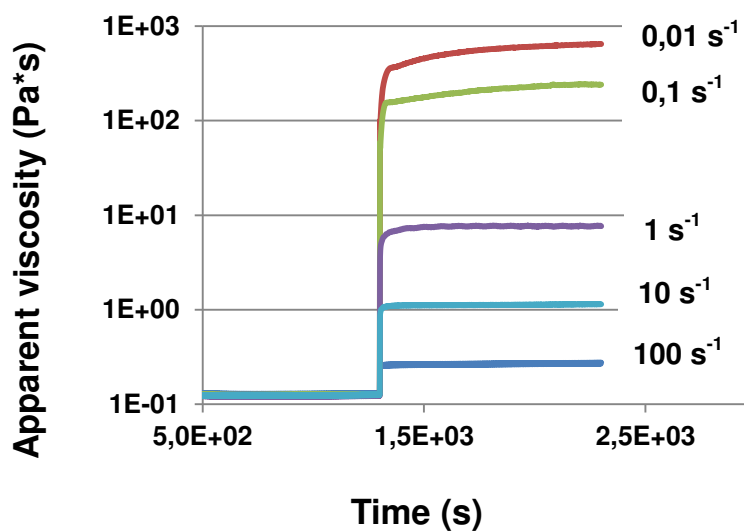


Figure 4.7. Thixotropy test at different shear rates

### Viscoelastic study

Viscoelastic properties were investigated by means of rheological study. Linear viscoelastic region (LVR) was determined by following procedure described in section 2.2.2. As showed by Figure 4.8 ink has not an extended linear region because of low content of binding. Complex modulus is constant at low shear rate before dropping off as a result of network structure breakdown. This behavior is typical for Maxwell fluids [178] as reported by Phair et al. for screen printed solid oxides for fuel cell applications [179] or by Mahendra et al. for screen printed solid oxide fuel cell [180].

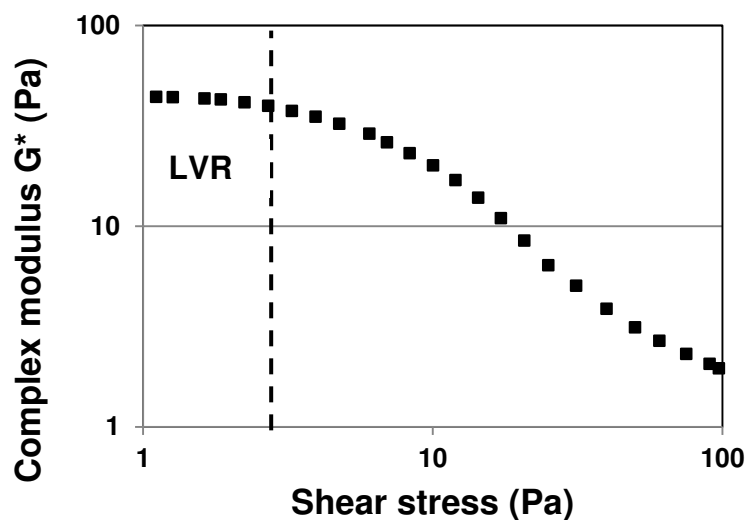


Figure 4.8. Linear Viscoelastic region (LVR) determination

Storage and loss modulus were investigated within LVR range in a frequency range from 1 to 10 Hz as described in section 2.2.2. As showed in Figure 4.9 weak frequency dependence was observed for both parameters within frequency range. Another important aspect is that storage modulus (represented by filled squares) is always higher than loss modulus (represented by empty squares) as expected for structured paste where a solid state behavior is predominant. This indicates that particles are connected between them in a network structure [181].

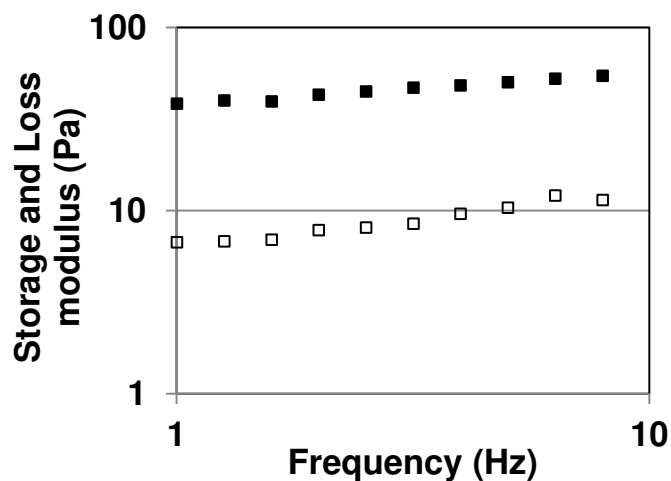


Figure 4.9. Storage (■) /loss modulus (□) as function of frequency

## 4.2 Electrode characterizations

### 4.2.1 Physical characterizations

Electrodes were printed by screen printing process by following procedure described in paragraph 2.3.1. A study of coating thickness as function of number of squeegee passages was realized. As showed in Figure 4.10 coating thickness increases linearly for 3 passages. Up to this value it doesn't seem affected by number of passages. This fact can be associated to the emulsion thickness and the open size of the screen. In fact these parameters affect the transferred volume of ink and therefore the coating thickness [182]. A linear dependence was reported by Ito et al. between number of passages and coating thickness for screen printed dye solar cells, similar to our behavior [183]. They measured a continuous increment of thickness of 2  $\mu\text{m}$  for each coating layer, from 3  $\mu\text{m}$  at 1 passage, to 19  $\mu\text{m}$  at 9 passages.

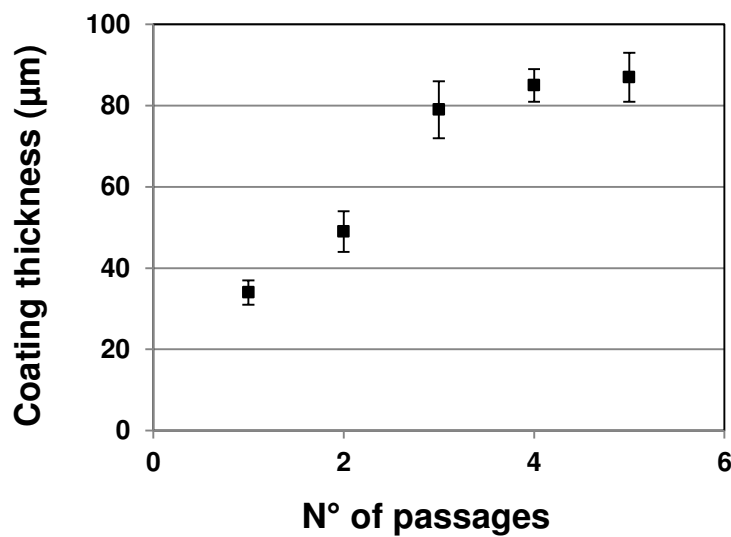


Figure 4.10. Coating thickness as number of passages

Table 4.4 lists parameters of screen printing process and screen characteristics employed in this work. The same screen and printing parameters described previously for negative electrode were employed for positive electrode, in order to ensure an optimal transfer of ink without damaging of the screen. In Figure 4.11 a picture of printed electrode is presented.

## Chapter 4: Development and characterization of printed cathode

Table 4.4. Parameters of screen printing process

Screen printing process		
Open area	%	41
Emulsion thickness of screen	$\mu\text{m}$	110
Squeegee speed	mm/s	125
Squeegee force	kg	5
Snap off distance	mm	1
Number of passages		1

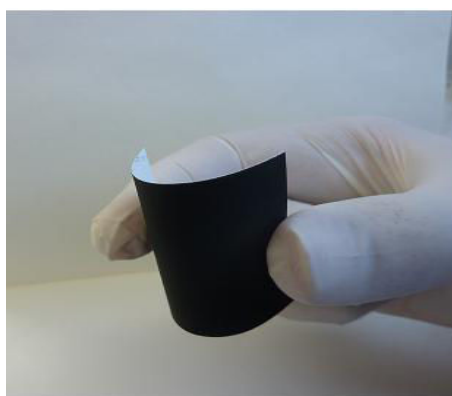


Figure 4.11. Cathode printed electrode

In Figure 4.12 SEM image shows a cross view of printed cathode where it can be distinguished active layer (on the top) and paper separator (at the bottom) with a thickness of about  $30 \mu\text{m}$ . SEM images at the interface electrode – separator didn't reveal particles of the electrode in the structure of the separator. These observations allow to exclude possible short circuits during cycling. The surface homogeneity of the printed cathode is illustrated by the Figure 4.12.b where cracking or peel off defects, typical of screen printed process [184], are not evident. Some agglomerates of  $\text{LiFePO}_4$  particles bigger than  $1 \mu\text{m}$  are visible (Figure 4.12.c). This fact is reported in literature by different authors for carbon coated  $\text{LiFePO}_4$  particles [185-186]. It is likely due to an agglomeration during synthesis process. At higher magnification, interactions between MFC indicated by red narrow and  $\text{LiFePO}_4$  particles

pointed out by blue narrow can be noticed (Figure 4.12.d). As described for negative electrodes MFCs create a network structure that enhances interactions between particles. The same structure was described by Leijonmarck et al. for nanofibrillated cellulose and  $\text{LiFePO}_4$  particles for the production of flexible nano paper positive electrodes [187].

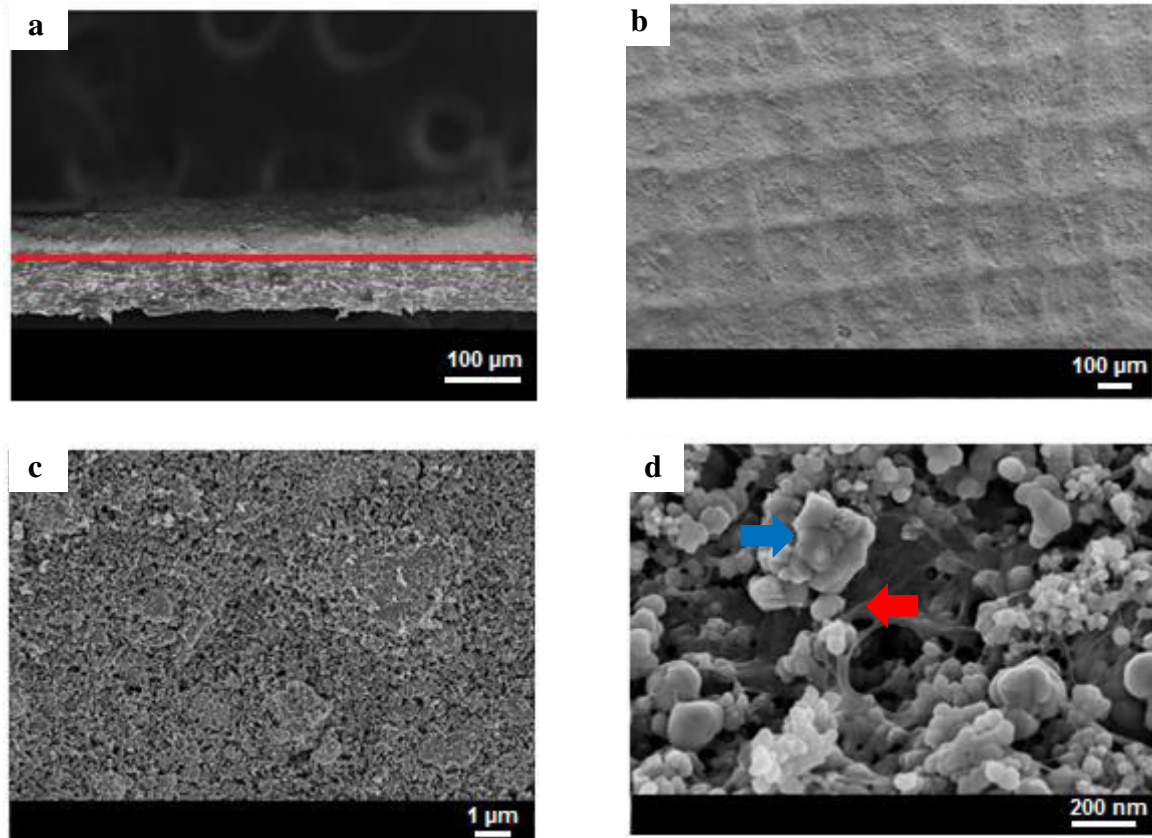


Figure 4.12. FESEM images of screen printed cathode at different level of magnitude. a) Cross section image, b-c) Surface images d) Interactions between MFC (blue arrow) and LFP (red arrow) particles.

After printing stage, electrodes were characterized in terms of active layer thickness, electronic conductivity and grammage coating by performing measurements onto electrodes with different techniques described in paragraph 2.3.2. The porosity was calculated as ratio between void volume and apparent volume of the electrode, by formula presented in section 2.3.2. Physical results are listed in Table 4.5. An electrode thickness value of  $31 \pm 3 \mu\text{m}$  was measured. This value is comparable with results obtained by Geyer et al. for screen printed lithiated oxides of about  $28 \mu\text{m}$  [98]. Measured Surface roughness is lower than value

## Chapter 4: Development and characterization of printed cathode

obtained for negative electrode. In fact a value of  $7.8 \pm 1.4$  was measured whereas for the negative electrode, a roughness of  $11.9 \pm 0.4$ . The same behavior was reported by Rouault et al. for screen printed electrodes onto aluminum current collector. In fact they measured an anode roughness value three times higher than positive electrode roughness [99]. An appreciable electronic conductivity value was measured of about  $35 \pm 2$  S/m thanks to high content of carbon black. A porosity value of 68 % is calculated, in good agreement with value reported in literature by Rouault et al. ranging between 68% and 75% for screen printed positive electrodes [99]. Topography image in Figure 4.13 shows how the structure is more homogenous compared to the surface images obtained for anode electrode.

Table 4.5. Physical characterization of the electrode in terms of coating thickness, electronic conductivity, grammage, porosity and surface roughness

<b>Ms(LFP_NC_CMC_MFC) / 40(70_27_2_1)</b>		
Coating thickness	$\mu\text{m}$	$34 \pm 3$
Electronic conductivity	S/m	$35 \pm 2$
Grammage of the coating layer	$\text{g/m}^2$	$31 \pm 3$
Porosity	%	$68 \pm 4$
Surface Roughness ( $S_a$ )	$\mu\text{m}$	$7.8 \pm 1.4$

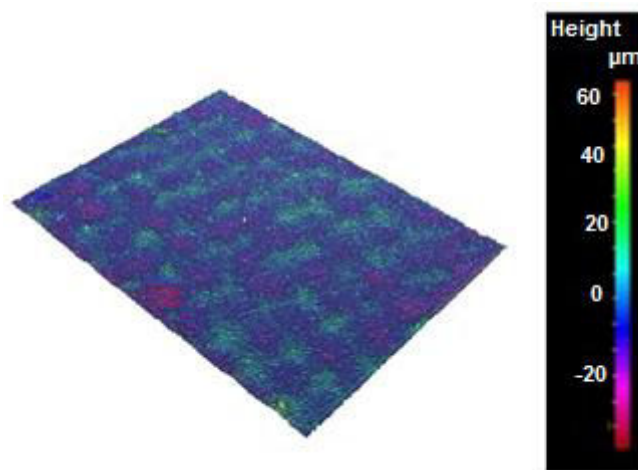


Figure 4.13. Topography image of  $\text{LiFePO}_4$  based electrode taken by a multifocal optic microscope (Alicona<sup>®</sup>)

## 4.2.2 Electrochemical characterization

### Voltammetry measurements

A voltammetry measurement at a scan rate of  $0.1 \text{ mVs}^{-1}$  was performed on printing electrode to evaluate oxidation and reduction peak of  $\text{LiFePO}_4$  by following experimental procedure described in paragraph 2.5.2. As showed in Figure 4.14, the oxidation peak corresponding to delithiation process is located at 3.6 V while the reduction peak corresponding to lithiation process at 3.2 V as well as reported in literature for carbon coated  $\text{LiFePO}_4$  [188] and  $\text{LiFePO}_4$  [189]. The measured surface below the oxidation and reduction peak, corresponding to charge and discharge capacity is  $0.10 \text{ mAhg}^{-1}$  and  $0.09 \text{ mAhg}^{-1}$ . This slight mismatch is typical of a non ideal reversible reaction as described by Yu et al. [190]. In fact generally the reaction of lithiation and delithiation is described as a two phase mechanisms between  $\text{LiFePO}_4$  and  $\text{FePO}_4$  [190]. This difference in electrochemical environment can affect diffusion process of lithium ions.

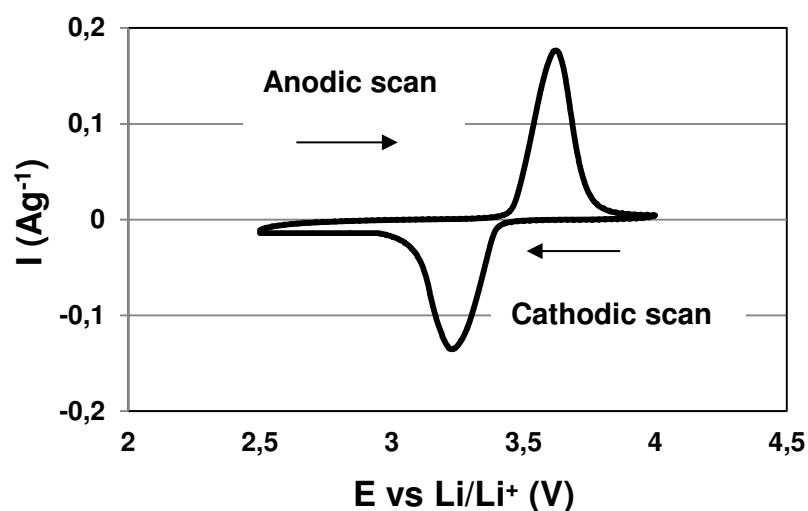


Figure 4.14. Voltammogram for cathode electrode at a scan rate of  $0.1 \text{ mVs}^{-1}$  in EC/DMC/PC (1:3:1), 1M  $\text{LiPF}_6$ .

## Chapter 4: Development and characterization of printed cathode

---

If we compare these results with those reported in literature for  $\text{LiFePO}_4$  based cathode, we can observe a substantial agreement between anodic and cathodic potential as showed in Table 4.6. The differences become more important when we considere charge and discharge capacity. As reported by Yu et al., voltammetry profiles depend on different parameters as electrode loading, electrolyte composition, scan rate and temperature [190]. These results are in good accordance with those previously reported by Yu et al..

Table 4.6. Comparison of voltammetry cycling results with values reported in literature

---

		Our sample	Yu et al. [190]	Takahashi et al. [189]	Arumugam et al. [191]
<b>Scan rate</b>	$\text{mVs}^{-1}$	0.1	0.1	0.05	0.1
<b>Anodic potential</b>	V	3.6	3.6	3.6	3.6
<b>Cathodic potential</b>	V	3.3	3.3	3.4	3.4

---

### Galvanostatic cycling

Galvanostatic cycling was performed in a potential range between 2 and 4 Volt. Figure 4.15 shows the evolution of voltage as function of specific capacity at a current rate of  $C/10$  during the first cycle. Charge profile is represented by dotted line and discharge profile by black line. A characteristic plateau in a wide voltage range was observed for both curves corresponding to lithium deinsertion / insertion process as described in literature [191]. The capacity of first cycle corresponds to 70% of the theoretical value. This value is lower than values reported in literature. Owing to the high porosity of the electrode (68%), some particles of the electrode could be not involved in the reactions of charge / discharge. In addition other parameters as the size, the synthesis strategy and the contact between particles can affect specific capacity by limiting the deinsertion and insertion of lithium ions [192].

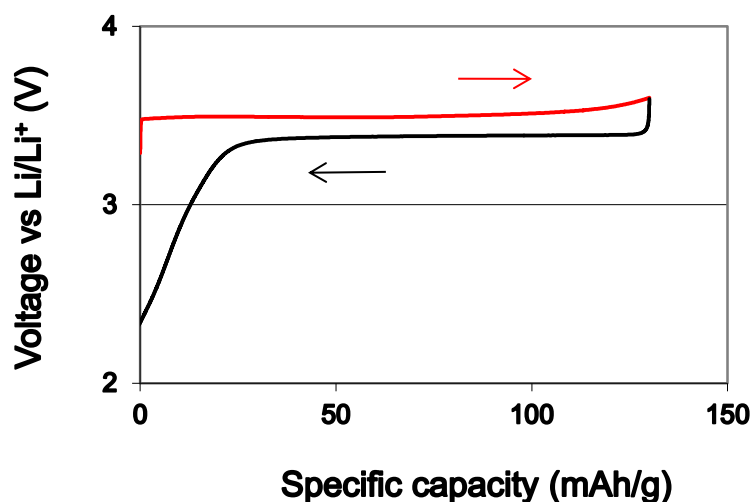


Figure 4.15. Discharge (-)/charge (-) profile as function of specific capacity at 1<sup>st</sup> cycle

Galvanostatic cycling at different current rates were performed to evaluate the performances of the electrode versus cycling. Figure 4.16 shows the capacity profile for the first 5 cycles at a constant current rate of  $C/10$ . A continuous increase of the capacity was measured ranging from 129 mAh/g at first cycle (black curve) to 143 mAh/g at fifth cycle (red curves). A stabilization of the capacity at 143 mAh/g was observed for the fourth and fifth cycle (orange and red curves). This progressive increase of the capacity may be due to a better wettability by of  $\text{LiFePO}_4$  particles by the electrolyte during cycling.

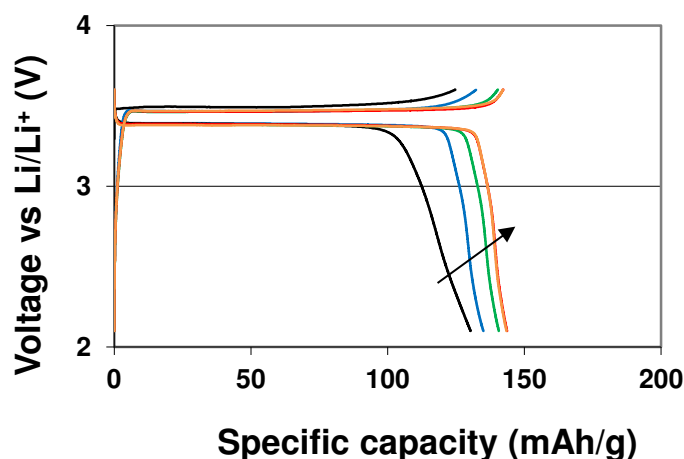


Figure 4.16. Discharge and charge profiles at a constant current rate corresponding to  $C/10$  at first (black curves), second (blue curves), third (green curves), fourth (orange curves) and fifth (red curves) cycle.

As illustrated in Figure 4.17 and Figure 4.18 when current rate increases a decrement in specific capacity was measured. This behavior is probably due to a polarization of the electrode that becomes more important at a current rate of  $C$ . In fact, an electrode with high porosity leads to an increment of the tortuosity. This affects the flow of the electrons in the electrode by increasing its resistivity. A capacity of 142 mAh/g was observed at  $C/10$  for charge and discharge curve. A slight loss of capacity was observed at  $C/5$  by measuring a value of 133 mAh/g. Specific capacity decreases sharply until a value of 106 mAh/g at  $C/2$  and 105 mAh/g at  $C$ . Analogue behavior was reported for carbon coated  $\text{LiFePO}_4$  by Jin et al. [193], at a current rate corresponding to  $C/2$  and  $C$ .

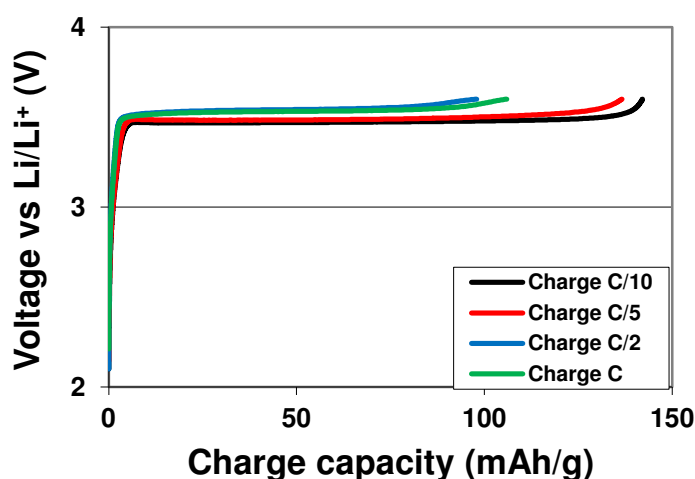


Figure 4.17. Charge profiles at different current rates.

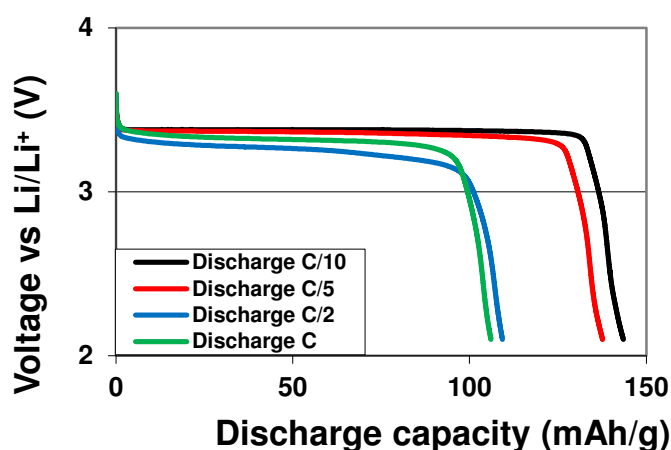


Figure 4.18. Discharge profiles at different current rates.

## Chapter 4: Development and characterization of printed cathode

---

Figure 4.19 illustrates the evolution of retention capacity as function of current rate. As showed, capacity retention decreases from 97% at C/5 until 72 % at C. A capacity retention of 72 % at C is a high value if we consider that the electrode exhibits a high porosity (68%). This behavior was in good accordance with the data reported in literature for conventional electrode, over all at C/10 and C/5 [194]. In Figure 4.20 charge ( $\square$ ) / discharge ( $\blacksquare$ ) capacity and coulombic efficiency ( $\Delta$ ) vs number of cycles are plotted. For a current rate corresponding to C/10 and C/5 a plateau can be observed. Thus performances of the electrode are not affected by cycling for the first 15 cycles. By contrast specific capacity measured at a current rate corresponding to C/2 and C respectively, doesn't follow the same behavior. When current imposed changes from C/5 to C/2 specific capacity drops from 136 mAh/g to 108 mAh/g. The decrease of capacity can be attributed to the slow diffusion of lithium ions because of elevate reaction kinetics at higher current rates and to the low electronic conductivity of the electrode [195]. When current rate is fixed at C, a progressive increment in specific capacity was observed during first cycles until a stable value of 106 mA/h. This behavior is unexpected and not reported in literature for conventional electrodes. Coulombic efficiency attains rapidly 97% and remains stable for all tested current rates. This fact confirms that there are not side reactions involved during charge/ discharge mechanism even if the porosity of the electrode is higher respect a conventional electrode. The stability of the electrode is illustrated in Figure 4.21 where charge and discharge capacity are plotted as function of cycles for a constant current rate corresponding to C/5. A constant capacity of about 120 mAh/g was measured for 150 cycles.

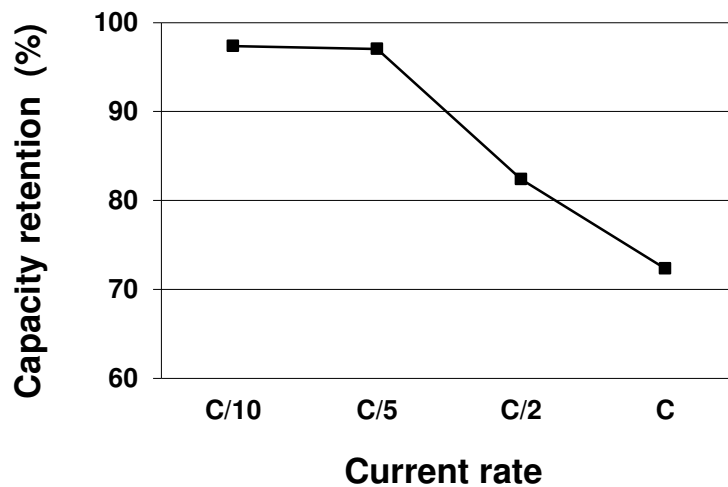


Figure 4.19. Retention capacity at different current rates.

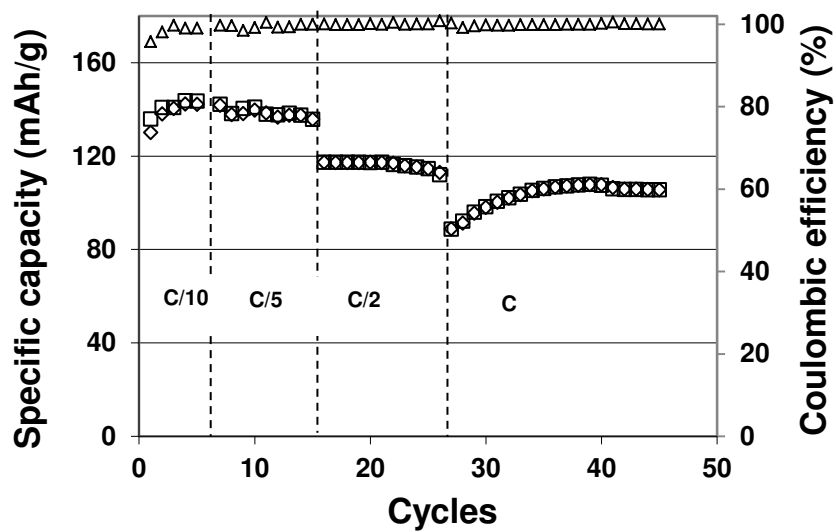


Figure 4.20. Specific Charge ( $\square$ )/Discharge ( $\blacksquare$ ) capacity and coulombic efficiency ( $\Delta$ ) as function of cycles.

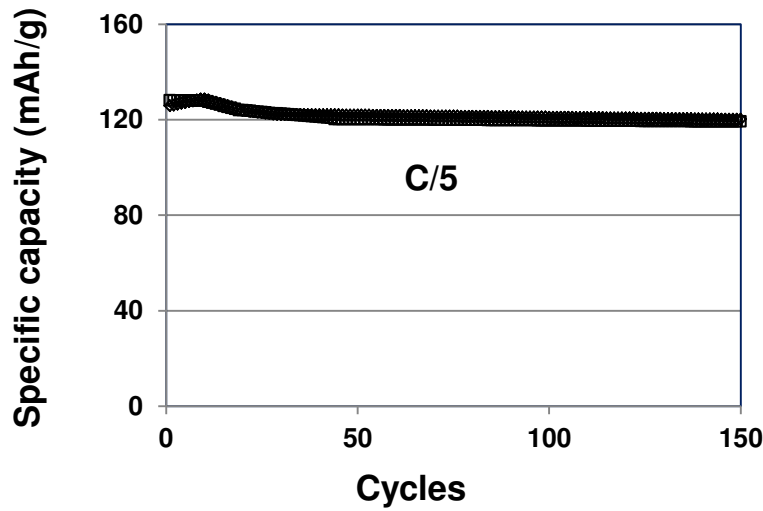


Figure 4.21. Specific Charge ( $\square$ )/Discharge ( $\blacktriangle$ ) capacity and coulombic efficiency ( $\Delta$ ) as function of cycles.  
 b) Charge ( $\square$ )/discharge ( $\blacktriangle$ ) specific capacity as function of cycles at a constant current rate of C/5

### 4.2.3 Calendering study

#### Physical characterization

A calendaring study was performed to analyze influence of calendaring process on physical and electrochemical properties. Electrodes were calendared at a linear load of 1, 3, 33 and 73 kN/m. Topography images were taken in order to investigate surface and roughness of electrodes. Images in Figure 4.22 show the evolution of surface topography as function of calendaring linear load. At 1 and 3 kN/m typical marks of printing screen is always visible. Up to 3 kN/m, surface topography changes radically as showed in Figure 4.22.c and Figure 4.22.d. Main physical properties were measured and analyzed as function of calendaring linear load and listed in Table 4.7. As showed for calendared negative electrode, electronic conductivity enhances by increasing calendaring pressures because of better interactions between carbon black particles surrounding  $\text{LiFePO}_4$  particles [196]. Topography images surface shows that roughness is strongly influenced by calendaring pressures with a continuous decrease of roughness value from 7.8  $\mu\text{m}$  at 1 kN/m to 4.9  $\mu\text{m}$  at 73 kN/m. The same behavior was observed for coated thickness with a continuous decrease of thickness

from 34  $\mu\text{m}$  to 16  $\mu\text{m}$  at 1 kN/m and 73 kN/m respectively. Porosity exhibits a continuous reduction from 69 % to 46% at 1 and 73 kN/m respectively.

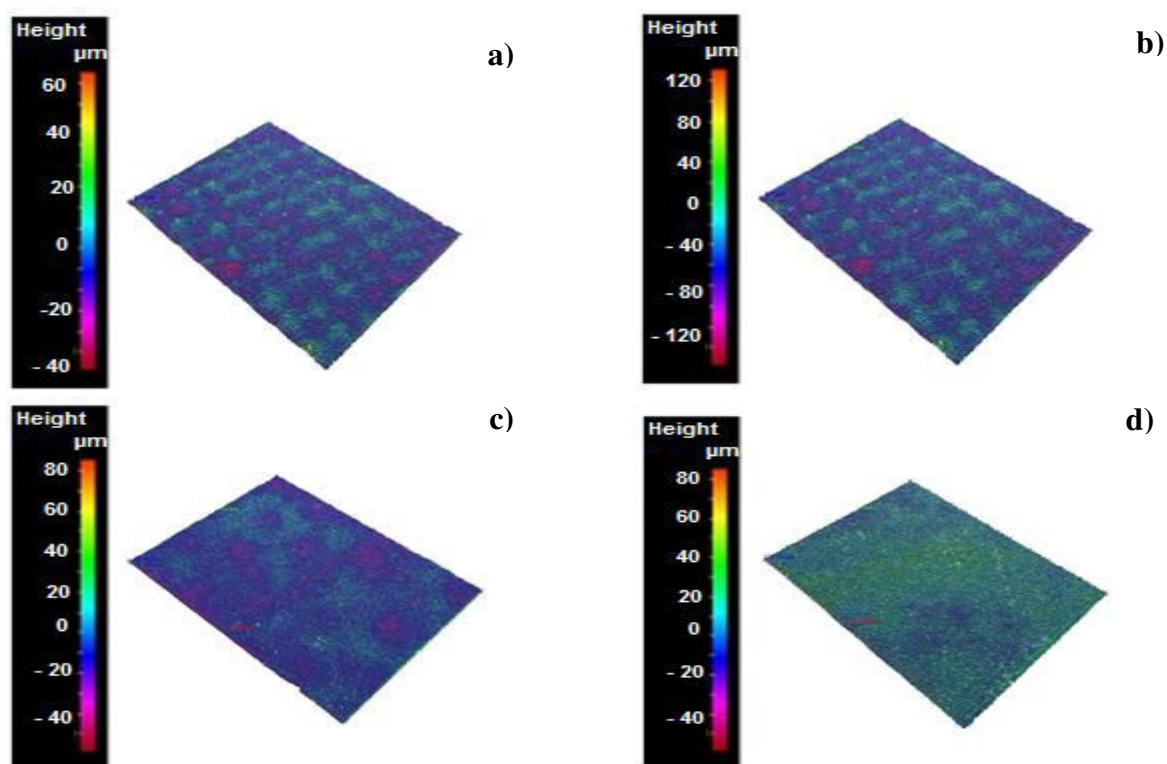


Figure 4.22. Topography images of calendared positive electrode at 1(a) - 3(b) - 33(c) and 73(d) kN/m at a magnitude of 5x.

Table 4.7. Physical characterization as function of calendaring linear load at different current rates

$M_s$ (LFP_NC_CMC_MFC) / 40(70_27_2_1)		Calendaring linear load (kN/m)				
		-	1	3	33	73
Coating thickness	$\mu\text{m}$	34 $\pm$ 3	30 $\pm$ 3	25 $\pm$ 3	19 $\pm$ 2	16 $\pm$ 2
Electronic conductivity	S/m	35 $\pm$ 2	52 $\pm$ 4	71 $\pm$ 3	92 $\pm$ 5	108 $\pm$ 13
Porosity	%	69 $\pm$ 5	65 $\pm$ 4	61 $\pm$ 3	54 $\pm$ 2	46 $\pm$ 2
Roughness ( $S_a$ )	$\mu\text{m}$	7.8 $\pm$ 1.4	6.3 $\pm$ 0.1	5.4 $\pm$ 0.4	5.3 $\pm$ 0.2	4.9 $\pm$ 0.5

### **Electrochemical characterization**

Electrochemical properties were investigated to understand the influence of calendaring pressure. The measurement protocol employed in this study is the same described before for positive electrode. Table 4.8 shows the evolution of specific capacity as function of calendaring linear load at different current rates. The values are expressed as percentage respect to the capacity at C/10. Despite an increment of the electronic conductivity of the electrode when calendaring pressure increases (see Table 4.7), a progressive diminution of the capacity was measured. In fact compared with not calendared electrode, rate capability decreases progressively. This behavior may be explained if we consider the nature of the separator. In fact the structure of the cellulosic based separator used in this study, could be influenced by the calendaring pressure. Thus some inhomogeneity in the printed layer could appear by reducing the surface of active material involved in the reactions of charge and discharge. Generally rate capability is strongly affected with increasing active material loading over all at a current rate corresponding to C/5 and C/2, as reported in literature by Yu et al. for LiFePO<sub>4</sub> based cathodes [197]. Zheng et al. measured a direct correlation between the thickness of the electrodes and the current rates. They report that electrodes can deliver the higher capacity at a small discharge rate of C/10 [198].

Table 4.8. Electrochemical properties as function of calendaring linear loads at different current rates

<b>Specific capacity</b>				
<b>Linear load (kN/m)</b>	<b>C/10</b>	<b>C/5</b>	<b>C/2</b>	<b>C</b>
	<b>mAh/g</b>	<b>% respect C/10</b>		
-	140±3	99	81	74
<b>1</b>	131±1	98	91	87
<b>3</b>	128±5	90	85	75
<b>33</b>	126±2	90	85	70
<b>73</b>	123±3	99	84	65

### 4.3 Conclusion

In this subchapter flexible positive electrodes were manufactured by screen printing technique. Firstly water and cellulosic based ink were formulated. A study to find the optimal content of carbon black was carried out. Results revealed how 27% of carbon black allows to obtain an optimal electronic conductivity of  $35\pm 2$  S/m. Rheological properties demonstrated the suitable properties of the ink to be printed with a screen printed process. The influence of components was investigated by oscillatory and thixotropy test and results confirmed how this interaction can strongly affect the flow properties of the ink. Physical characterizations were performed and revealed the characteristics of the printed cathodes in terms of porosity and roughness. As showed by topography and SEM images, a homogenous and uniform surface was obtained. Electrochemical properties revealed a good and stable cycling. A retention capacity of 70% even at medium current rate (C/2 and C) was obtained and a stability of electrochemical properties was measured for more than 150 cycles. In order to enhance properties, a calendaring strategy was proposed. Physical properties were enhanced, over all in terms of electronic conductivity and porosity by passing from a value of  $35\pm 2$  S/m and  $69\pm 5$  % for a not calendered electrode to  $108\pm 13$  S/m and  $46\pm 2$  % for a high calendered electrode. By contrast electrochemical properties were enhanced just at low calendaring pressure. In fact calendaring pressure, can damage the cellulosic made separator by affecting the homogeneity of the active layer. Thus some particles of the positive electrode can be not involved in the reaction of charge / discharge by reducing performances of the electrode. All these results have to be considered for the manufacturing of a full cell, in order to maximize electrochemical properties and performances.

---

# **Development and characterization of full cell**



## 5. Development and characterization of full cell

### Introduction

This section is focused on printing and characterization of a full printed cell. Firstly a presentation of different assembling strategies is proposed by underlining the advantages and disadvantages. A part is dedicated to expose our assembling strategy based on front / back (recto / verso) printing approach. Physical and electrochemical results are exposed and analysed in comparison with other full cells described in literature and obtained with different techniques. Finally a comparative study is performed in order to evaluate if the assembling strategies, the nature of the substrate and calendering can affect the performance of the cell.

### 5.1 Cell assembling strategy

Generally two approaches are employed for the fabrication of printed batteries: the stack or sandwich layout and the coplanar layout [69], as showed in figure 5.1. Thanks to its structure where all components are parallel between them the stack design presents a very short ion path compared with coplanar lay out and a high charge, discharge current. One drawback is the numerous printed layers necessary to assembly the full cell as showed in figure 5.1.a. By contrast coplanar layout doesn't require a large number of printed layers but performances are lower than stack design because of ions have to spread across interface between active materials and substrate (figure 5.1.b.)

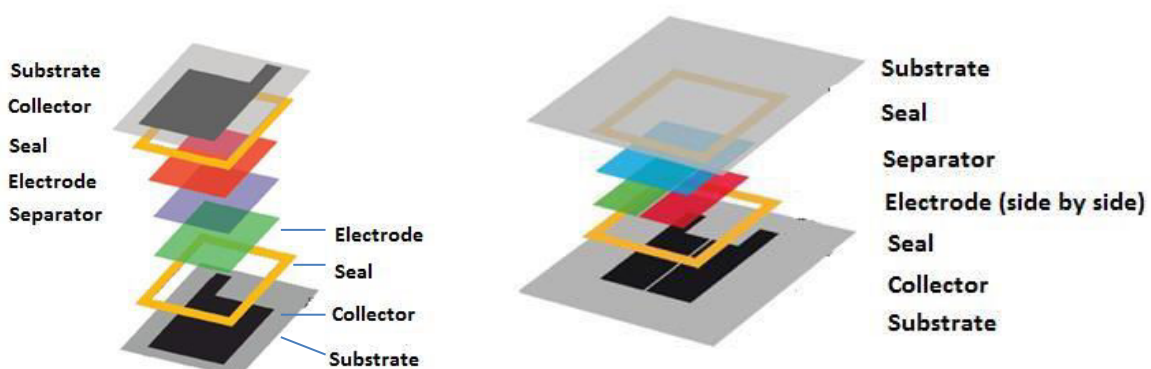


Figure 5.1 Full cell assembling strategy used in literature: a) Stack layout, b) co-planar layout [69].

In this work a new approach was employed. To overcome limitations of large number of printed layers and high mean path, a front / back printed layout was proposed. As showed in Figure 5.2 components are printed onto a substrate that acts at the same time as separator. Aluminum and copper were selected for the positive and negative electrode respectively as generally used in literature [199-200]. As reported by Zhang et al. aluminum is used for cathode electrodes because it forms spontaneously a passive layer on the surface that contributes to avoid corrosion at high potential [201]. On the other hand copper is used as current collector for negative electrodes because it is not affected by reduction reactions [202].

### **5.1.1 Front / back (recto / verso) assembling strategy**

The front / back strategy can be resumed in four points:

#### **Printing of negative electrode (anode) onto front side of substrate**

In this step one layer of negative material is printed onto the substrate by following the same procedure used for the development of the anode in chapter 3.1. Figure 5.2 illustrates the principle.

#### **1. Embedding of current collector (copper)**

A copper made current collector is fixed onto the printed pattern and another layer is printed in order to fix the current collector. This strategy allows to insure a complete adhesion between layers by “drowning” current collector in the ink matrix avoiding each problem of electron transport between negative electrode and current collector. The result is showed in Figure 5.2.b

#### **2. Printing of positive active material (cathode) onto back side of substrate**

The positive electrode is printed on the opposite side of substrate (Figure 5.2.a). Because of different specific capacities of electrodes (350 mAh/g and 170 mAh/g for the negative and positive electrodes respectively) a balance in materials is necessary in order to avoid fade of capacity during cycling and prevents overcharge or over discharge, which are detrimental to the cyclability of the cell. For this reason two or more layers of positive electrode material are

printed on the substrate. Aluminum current collector is inserted and fixed by printing a further layer of positive electrode.

### 4. Packaging

As last step the cell is packed in a polymer coated aluminum bag after incorporation of electrolyte, evacuation of Argon and sealing, inside an argon filled glove box. Figure 5.2.b and Figure 5.2.c show a picture of negative printed electrode with current collector embedded and printed full cell assembled with front / back strategy.

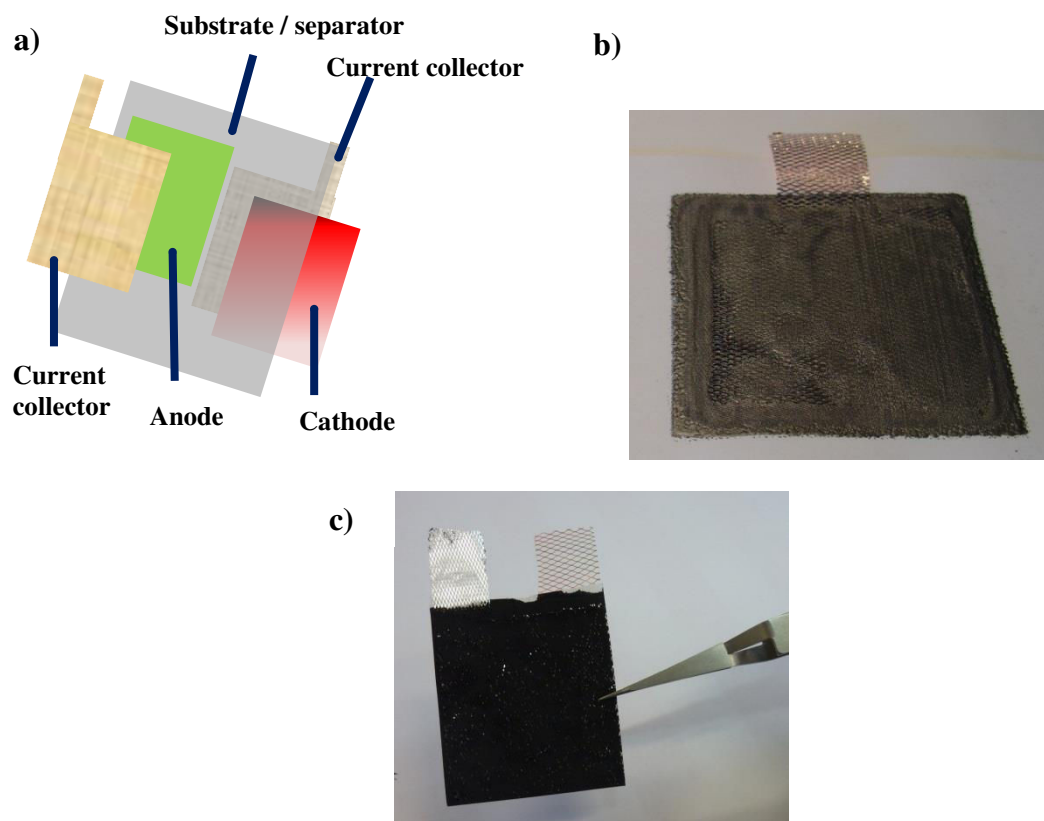


Figure 5.2. a) Full cell printing strategy: front/back lay out. b) Image of anode printed electrode with embedded current collector. c) Image of full printed cell with embedded current collectors

Comparative studies were performed by considering how the assembling strategies can influence the performances of the cell. Key parameters were considered as the dimension of

the cell, the capacity and the grammage of active layers. Cell was characterized by calculating the capacity and the energy output from the cell. The total capacity is defined as the functioning capacity of the cell divided by the total weight of the cell which includes the weight of electrolyte, separator, connectors and other components. The energy value is defined as the product of the capacity and the operating voltage. Generally an average voltage is considered. For instance for  $\text{LiFePO}_4$  the average voltage corresponds to 3.2 V. The energy output can be expressed per unit mass (gravimetric energy density), per unit surface (surface energy density) or per unit volume (volumetric energy density).

### 5.1.2 Influence of packaging strategy

First, assume a cell with a capacity of 10 Ah composed by a positive and negative layer based on graphite and  $\text{LiFePO}_4$  (LFP) with a standard dimension of 140 x 90 x 6 mm. The reversible capacity of the positive electrode is 10 Ah with no irreversible capacity. For the negative electrode we have to consider a balance of active material. In fact practical cell design requires that the capacity of electrodes be matched [203]. For the functioning of the cell the electrodes must change the same capacity in cycling. In fact the positive electrode (LFP) represents the source of lithium for the cell and there must be sufficient capacity in the negative electrode to absorb lithium ions. On the other hand, a part of the capacity of the positive electrode is consumed by the formation of the SEI layer on the negative electrode surface. The balance of remaining capacity is assumed to lithiate the negative electrode reversibly. For this calculation a theoretical SEI layer corresponding to 7 % of the reversible capacity is assumed as described by Brennet [203]. Generally one of the electrodes may be designated with more capacity than the other. In this case the positive to negative electrode capacity ratio (P/N) is assumed equal to 0.9. The aim of this choice is to provide a slight excess of capacity for the negative electrode in order to allow lithium ions to intercalate into the anode host without forming potentially hazardous metallic lithium. Table 5.1 lists characteristic of the positive and negative electrodes for a cell functioning at 10 Ah, by considering all limitations described previously.

## Chapter 5: Development and characterization of full cell

Table 5.1. Electrode active material calculation

		Positive	Negative
Reversible capacity	Ah	10	10.3
Irreversible capacity	Ah	0	0.7
Total capacity	Ah	10	11.1
Reversible Specific capacity	mAh/g	150	340
Active material	g	66.7	30.5

The other components used for the evaluation of the performances of the cell are presented in table 5.2. All these parameters have to be considered for the estimation of the performances of the battery. For this estimation the contribution of the electrolyte was neglected.

Table 5.2. Grammage and weight of components integrated in the full cell

Grammage copper current collector*	$g/cm^2$	1.6
Grammage Aluminum current collector*	$g/cm^2$	0.5
Weight positive electrode	g	82
Weight negative electrode	g	32
Grammage cellulosic separator	$g/m^2$	16
Grammage Celgard <sup>®</sup> separator	$g/m^2$	14.4

\* Current collectors are in a grid shape

Before evaluating the performance of the cell it is interesting to examine how the assembling strategies influence the volume and the total weight required to the fabrication of the cell. An estimation was performed by considering standard cell dimensions of 140 x 90 x 6 mm. Results are expressed as percentage respect to a standard assembling technique as stack layout (Table 5.3). The results show how front / back lay out allows to reduce at the same time the volume and the weight required. Because of its geometry (see Figure 5.1), coplanar lay out reduces sensibly the volume from a value of 100 % for a standard stack layer lay out to 82.9 %, by contrast the weight is not so affected. A slight reduction was calculated only for the front / back strategy. For the other techniques no increase of weight was evaluated. This

## Chapter 5: Development and characterization of full cell

behaviour can be explained if we consider that, in our estimation, the total weight of the cell is mainly affected by the weight of the electrodes and the current collectors. Thus the introduction or suppression of substrates and separators don't contribute in a ponderal way to the total weight of the cell.

Table 5.3. Influence of assembling strategy to the volume and weight necessary to manufacture a full cell. Values are expressed in percentage respect to stack lay out values

	<b>% Volume</b>	<b>% Weight</b>
Stack	100	100
Front / back	96.9	99.9
Stack with insertion of Celgard <sup>®</sup>	100	100
Coplanar	82.9	100

Typical parameters considered to evaluate the performance of the cell are the total capacity and the energy density expressed as function of the weight of the cell (gravimetric energy density), the surface (surface energy density) and the volume (volumetric energy density). Results are listed in Table 5.4. Values are comparable with standard cell with the same functioning capacity [204]. Results show how front / back strategy exhibits an increase in performances if compared with stack and coplanar layout. In fact this layout reduces the number of printed layers by increasing the gravimetric density and at the same time, it doesn't require a high surface to be manufactured. Thus, the result is high performances in terms of gravimetric and energy density.

Table 5.4. Performances of the cell in terms of capacity, total capacity (T.C.), gravimetric energy density (G.E.D), surface energy density (S.E.D) and volumetric energy density (VED).

	<b>Capacity Ah</b>	<b>T.C.<sup>1</sup> mAh/g</b>	<b>G.E.D.<sup>2</sup> mWh/g</b>	<b>S.E.D.<sup>3</sup> mWh/cm<sup>2</sup></b>	<b>V.E.D.<sup>4</sup> mWh/cm<sup>3</sup></b>
Stack	10	26	84	253	42
Front / back	10	26	84	253	43
Stack + Celgard <sup>®</sup>	10	26	84	253	42
Coplanar	10	26	84	127	51

<sup>1</sup>Total capacity, <sup>2</sup>Gravimetric energy density, <sup>3</sup>Surface energy density, <sup>4</sup>Volumetric energy density

This time we assume to reduce the volume of the cell from 140 x 90 x 6 mm to 100 x 50 x 0.725 mm, by fixing all other parameters. If we assume the same grammage of active materials, a reduction of the size of the cell leads to a diminution of active material and thus to

## Chapter 5: Development and characterization of full cell

a reduction of the functioning capacity. In fact capacity decreases from 10 Ah to 4 Ah. A slight increase of gravimetric and surface energy density was calculated even if the volume was reduced. One explanation is that the length and the width of the cell were not strongly reduced. In fact the most reduced parameter in the cell is the thickness (from 6 mm to 0,725 mm). This affects considerably the volume of the cell by increasing the volumetric energy density as showed in Table 5.5.

Table 5.5. Performances of the cell with reduced volume in terms of capacity, total capacity (T.C.), gravimetric energy density (G.E.D), surface energy density (S.E.D) and volumetric energy density (VED).

	<b>Capacity</b> Ah	<b>T.C.<sup>1</sup></b> mAh/g	<b>G.E.D.<sup>2</sup></b> mWh/g	<b>S.E.D.<sup>3</sup></b> mWh/cm <sup>2</sup>	<b>V.E.D.<sup>4</sup></b> mWh/cm <sup>3</sup>
Stack	4	27	85	254	361
Front / back	4	26	85	254	350
Stack + Celgard <sup>®</sup>	4	26	85	254	347
Coplanar	4	26	85	127	422

<sup>1</sup>Total capacity, <sup>2</sup>Gravimetric energy density, <sup>3</sup>Surface energy density, <sup>4</sup>Volumetric energy density

Another factor that can affect the performances of the cell is the grammage of active material deposited. This parameter is depending on the process used to manufacture the cell. We assume to deposit by a printing process as the screen printing a grammage of 30 g m<sup>-2</sup>. If we consider a charge of the ratio capacity (P/N) of 0.9 and a SEI layer for the negative electrode of 7 %, we can calculate an optimal grammage for the positive electrode of 78 g m<sup>-2</sup>. The functioning capacity corresponding to this value, for a given volume of the cell of 100 x 50 x 0,725 mm, is 0.03 Ah. As showed in Table 5.6 all properties of the cell are considerably affected by the low capacity.

Table 5.6. Performances of the cell with a fixed grammage in terms of capacity, total capacity (T.C.), gravimetric energy density (G.E.D), surface energy density (S.E.D) and volumetric energy density (VED).

	<b>Capacity</b> Ah	<b>T.C.<sup>1</sup></b> mAh/g	<b>G.E.D.<sup>2</sup></b> mWh/g	<b>S.E.D.<sup>3</sup></b> mWh/cm <sup>2</sup>	<b>V.E.D.<sup>4</sup></b> mWh/cm <sup>3</sup>
Stack	0.03	0.2	0.7	2.9	4.2
Front/back	0.03	0.3	1	2.9	4.1
Stack + Celgard <sup>®</sup>	0.03	0.3	1	2.9	4.1
Coplanar	0.03	0.3	1	1.5	4.9

<sup>1</sup>Total capacity, <sup>2</sup>Gravimetric energy density, <sup>3</sup>Surface energy density, <sup>4</sup>Volumetric energy density

These calculations allow to estimate properties of the cell and point out how the front / back strategy is a valid alternative to conventional assembling layout and how can affect performances of the cell. Moreover results proof how the design and the manufacturing

process affects performances of the cell. Nevertheless the accuracy of calculations depends of the electrodes. In particular changes in porosity and electrode loading can have a significant effect on the rate capability.

### 5.1.3 Physical characterization

A full cell was printed following printing strategy described before in paragraph 2.3.1. SEM image in Figure 5.3 shows an example of a cross section of active materials and substrate. As reported in Table 5.7 the full cell shows a high electronic conductivity for negative electrode component and lower conductivity for positive electrode due to higher intrinsic resistivity of  $\text{LiFePO}_4$ . The cell thickness obtained by summing components thickness is  $215 \pm 9 \mu\text{m}$ . This value is comparable with flexible batteries reported in literature obtained by different techniques. Leijonmarck et al. [104] reported a thickness of  $250 \mu\text{m}$  for a complete cell manufactured by a filtration technique. A thickness of  $300 \mu\text{m}$  was measured by Hu et al. [155] for a thin lithium ion battery manufactured by a blade method. Higher thickness was measured by Wendler et al. [69] for printed Nickel metal hydrogen (Ni-MH) battery of about  $600 \mu\text{m}$ . The measured ionic conductivity of the separator is  $5 \text{ mScm}^{-1}$ . Because of higher pore size, this value is higher than ionic conductivity of a commercial separator (about  $1 \text{ mScm}^{-1}$  [22]). A higher grammage of positive electrode was printed because of different specific capacity of the Graphite and  $\text{LiFePO}_4$ . In addition, a part of lithium ions are “sacrificed” to form the SEI layer. An excess of positive electrode balances this consumption of lithium ions. A reversible capacity of  $140 \text{ mAh/g}$  was considered for the positive electrode, whereas a capacity of  $322 \text{ mAh/g}$  for the negative electrode. The irreversible capacity considered for the formation of the SEI layer is  $158 \text{ mAh/g}$ .

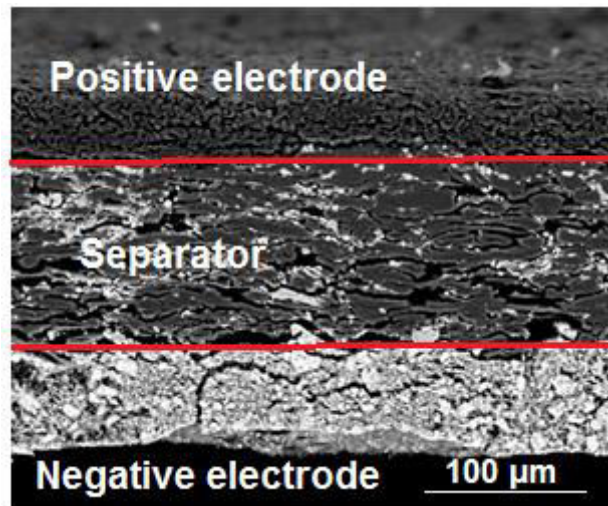


Figure 5.3. SEM image of the cross section of the full cell taken by a backscattering detector. Bright spots inside the separator represent the mineral charges of the cellulosic based separator

Table 5.7. Physical characterization of full cell components in terms of grammage, thickness and electronic conductivity

	Composition	Grammage	Thickness	Electronic Conductivity
	wt (%)	$\text{g/m}^2$	$\mu\text{m}$	S/m
<b>Negative electrode</b> $\text{M}_s(\text{GP\_CMC\_MFC})$	40(97_2_1)	$25 \pm 2$	$34 \pm 3$	$268 \pm 69$
<b>Separator</b>	cellulosic	$120 \pm 1$	$143 \pm 2$	-
<b>Positive electrode</b> $\text{M}_s(\text{LFP\_NC\_CMC\_MFC})$	40(70_27_2_1)	$70 \pm 6$	$79 \pm 7$	$37 \pm 6$

### Peel test

As explained previously, the key point of the front / back technique is the embedding of the current collector in the electrode structure. In order to quantify the cohesive energy of the multi layer structure, a peel test was performed. This test allows to quantify the energy required to remove the current collector from the electrode. In our experiment one layer of the electrode was printed onto the substrate which acts at the same time as separator. Secondly the current collector was integrated onto the printed layer and fixed by another film of the active layer (Figure 5.4.a). Depending on the energy of adhesion between the layers and the current collector we can distinguish two cases:

1. The adhesion energy between the current collector and the ink layer 1 is higher than adhesion energy between ink layer 1 substrate (Figure 5.4.b).
2. The adhesion energy between ink layer 1 and the current collector is lower than adhesion energy between ink layer 1 and substrate (Figure 5.4.c).

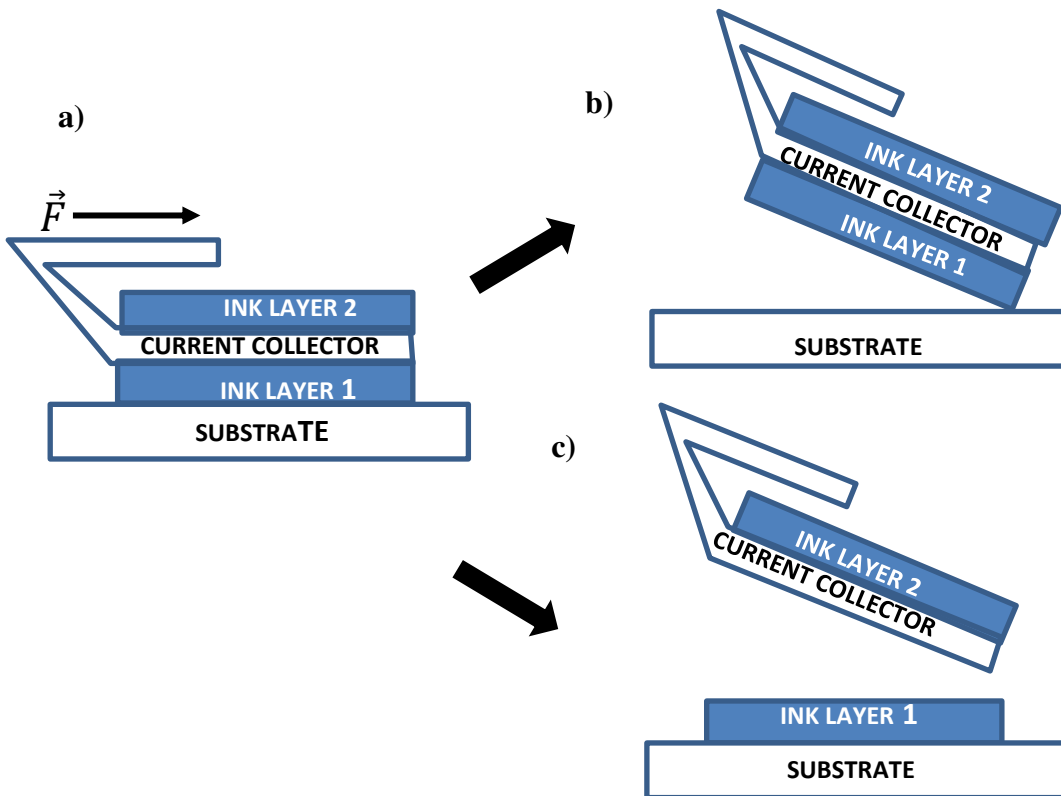


Figure 5.4. Possible configurations during peel test experiment. a) Initial configuration with a layer printed onto the substrate (layer 1) and the current collector integrated and fixed by a second layer (layer 2). b) First case of peel test with adhesion with high adhesion energy between substrate and layer 1. c) Second case of peel test with low adhesion between layer 1 and current collector

A preliminary experiment was carried out by considering a sample with a classical geometry of a current collector conventionally used in lithium ion batteries, composed by a square with the same surface of the electrode and a tab to collect electrons as showed in figure 5.5.

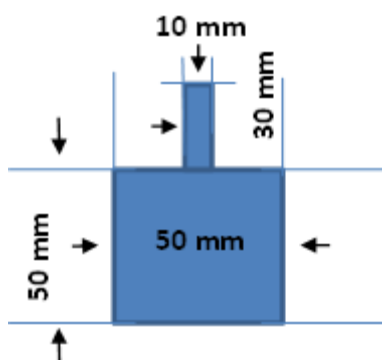


Figure 5.5. Geometry of the first sample for peel test. In this case a conventional geometry of current collectors was adopted with a surface of  $2500 \text{ mm}^2$  and a tab of  $300 \text{ mm}^2$ .

In this case the adhesion between the ink and the current collector was high enough to tear the tab during peel test. Obviously this experiment was not considered to quantify the adhesion energy but it points out how strong is the interaction between the current collector and the ink. A second experiment was performed by using samples with standard geometries in order to quantify the energy. Figure 5.6 shows four samples after testing. It is evident how the first layer is not removed from the substrate. This aspect confirms how the interaction at the interface between the first ink layer and the current collector is lower than the interaction between the substrate and the ink.

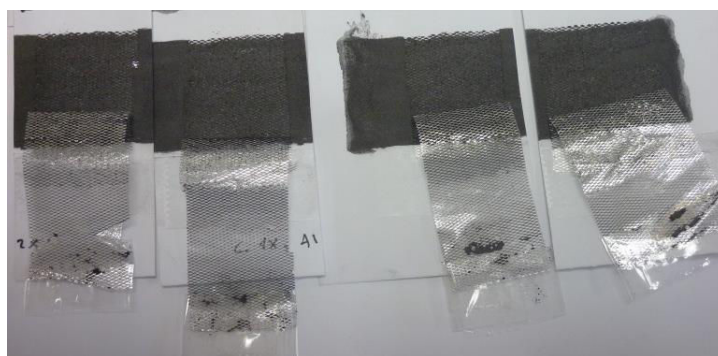


Figure 5.6 Positive electrodes after peel test.

This test allowed to quantify adhesion energy between aluminum current collector and ink. Figure 5.7.a and Figure 5.7.b show the evolution of the adhesion energy as function of the displacement for the cathode and anode ink respectively. Adhesion energy increases progressively until a plateau corresponding to the maximum adhesion energy between ink and current collectors. Cathode ink exhibits a more stable curve with an adhesion energy value corresponding to  $64 \pm 1 \text{ J/m}^2$  while for the anode ink a value of  $23 \pm 3 \text{ J/m}^2$  was measured. The

binder content inside the electrodes is the same. The difference could be related to the presence of 27 % wt of carbon black in addition to the binder, in the cathode composition. As reported by Chen et al. carbon black insures the mechanical integrity of the electrode [205]. By contrast, anode ink contains only 3 % wt of binder in order to maximize electrochemical properties. This amount of binder could be not enough to obtain adhesion performances comparable with cathode ink. The adhesion values measured for negative electrode are comparable with values reported by Chen et al.. In fact they measured an energy of 12 J/m<sup>2</sup> for silicon based electrodes.

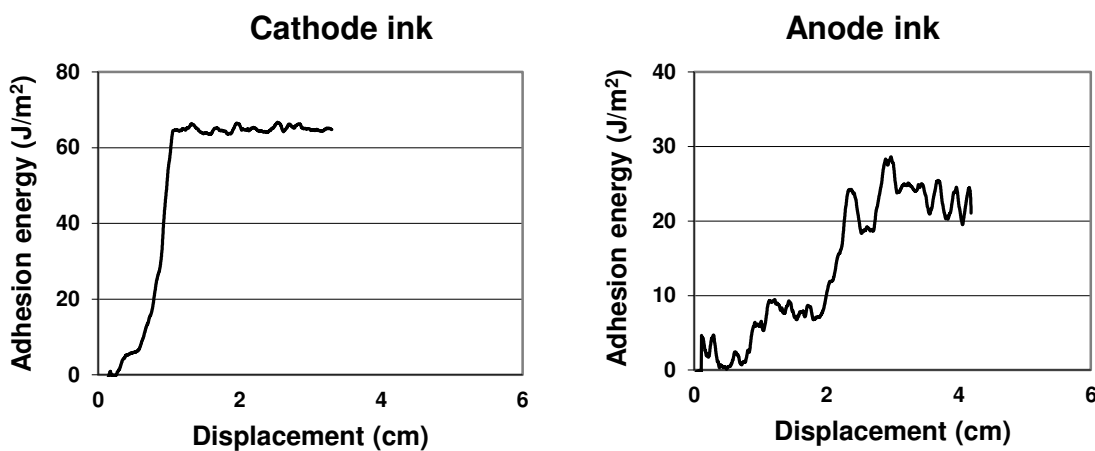


Figure 5.7. Evolution of adhesion energy as function of displacement for a) Cathode ink and b) anode ink. The results are an average of four tests.

### 5.1.4 Electrochemical characterization

An electrochemical study was performed to evaluate performance and properties of the full printed cell. As described previously for the negative electrode, electrolyte based on LiPF<sub>6</sub> 1 M in EC/DMC 1:1 insures higher capacity retention compared with ternary based electrolyte. For this reason all electrochemical experiments were performed by using this electrolyte. Chronopotentiogram in Figure 5.8 shows potential profile as function of time at different current rates. Typical charge and discharge peaks can be observed without artifacts due to side reactions caused by water contamination or electrolyte degradation.

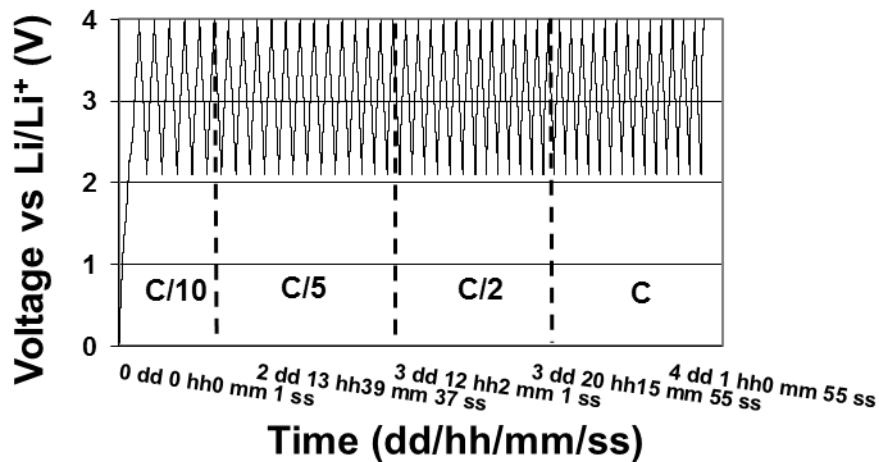


Figure 5.8. Chronopotentiogram of full cell at different current rates

Figure 5.9 shows charge and discharge profile at different current rates. As showed by graphs a continuous decrease of charge and discharge capacity was observed during cycling, from a value of about 64 mAh/g at C/10 for the first cycles to 31 mAh/g at C after 45 cycles (Figure 5.9.b)

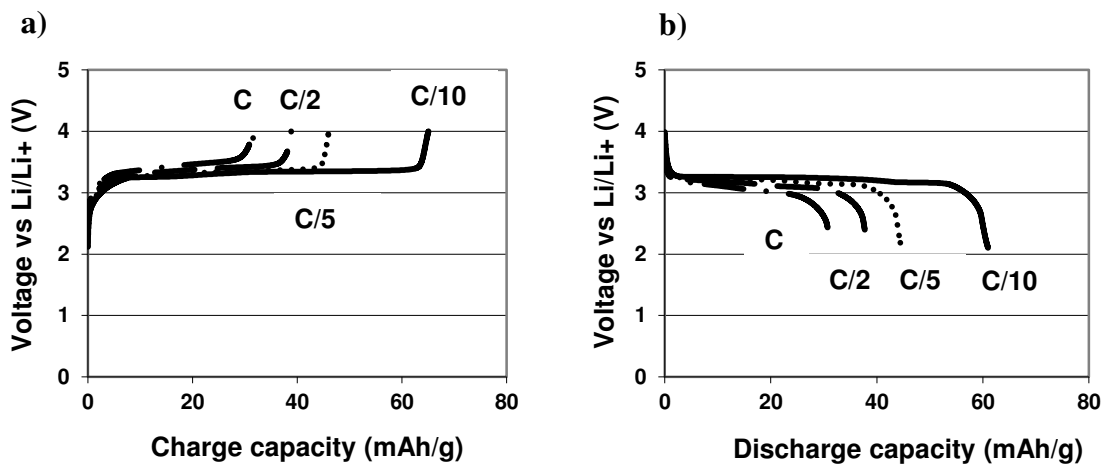


Figure 5.9.a) Voltage profile as function of charge capacity. b) Voltage profile as function of discharge capacity. Specific capacity was calculated respect to the grams of  $\text{LiFePO}_4$

The continuous decrease of specific capacity measured may be due to the different (higher) grammage of positive electrodes deposited on the substrate. As reported in Table 5.7 the balancing of the material leads to the deposition of at  $70 \text{ g/m}^2$  of positive electrode, more than grammage calculated for the development of the negative electrode ( $25 \text{ g/m}^2$ ). A thicker

printed electrode can be affected by delamination problems during cycling and has higher resistivity respect a thinner one. In addition electrodes exhibit a porosity of 70% and 68% for the negative and positive respectively. These values are higher than conventional electrodes (40 %). A high porosity can promote a delamination process in the electrodes. Coulombic efficiency shows that a part of capacity is dedicated to the formation of SEI layer. In fact coulombic efficiency increases from 38% until 96 % during first six cycles. Another important aspect is the evolution of the coulombic efficiency during cycling. Figure 5.10 shows how the cell attains a value up to 99 % after the 26th cycle. This behavior was not measured for both electrodes during investigations in half cell test, where coulombic efficiency reached more than 99 % after 9 and 3 cycles respectively. It is likely due to side reactions between lithium ions and contamination as water molecules still present in the electrodes.

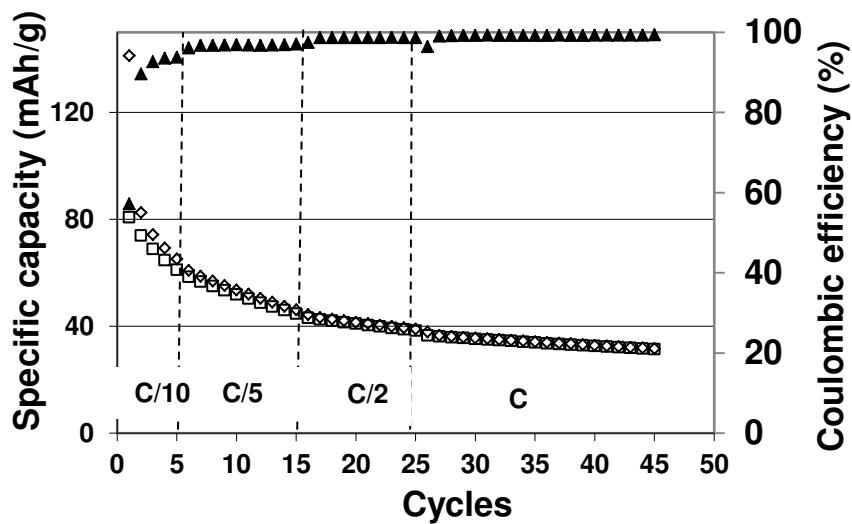


Figure 5.10. Charge ( $\diamond$ ) / discharge ( $\square$ ) specific capacity and coulombic efficiency ( $\Delta$ ) as function of number of cycles

## 5.2 Comparative study

### 5.2.1 Influence of testing strategy

As described previously one key point of the front / back strategy is the insertion of the current collector during the assembling process. We performed a comparative study by assembling a recto verso cell without current collector in a two electrodes Swagelok cell. In this configuration steel pistons act directly as current collector (Figure 5.11). Moreover pistons insure a constant pressure onto the electrodes by avoiding electrical contact problems between the cell and the current collectors.

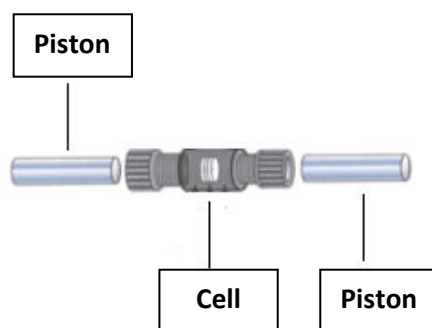


Figure 5.11. Two electrodes test cell configuration

A galvanostatic study was performed at different current rates by following the same procedure performed for the pouch cell. Figure 5.12 shows the comparison between the two assembling strategies in terms of specific capacity. The black symbols represent the pouch cell assembling strategy while the blue symbols the two electrodes test cell. A similar behavior was measured for both techniques with a progressive decrease of the specific capacity. At low current rates ( $C/10$  and  $C/5$ ) assembling strategy doesn't seem affect the performance of the cell. A slight mismatch was measured at higher current rate ( $C/2$  and  $C$ ) with a slight increase of the performance for the pouch cell. These results confirm how the Front / back assembling strategy, with embedded current collectors doesn't affect electrochemical properties of the cell. The embedding step of the current collector insures a current transport as well as steel pistons in two electrode test cell. Therefore low capacity is not related to the testing strategy but to local problems inside the electrodes.

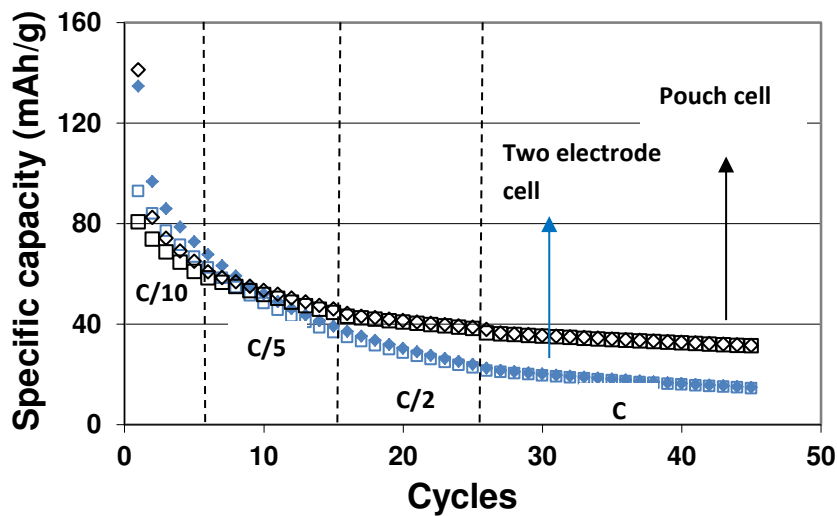


Figure 5.12. Galvanostatic cycling of two electrode cell (blue symbols) and pouch cell (black symbols)

### 5.2.2 Calendering study

In order to verify if calendering process improves the performance of the cell, a calendering step before assembling was performed at a pressure of 1 kN/m. This value of pressure was selected because, as reported in paragraph 4.2.3, it doesn't affect cathode properties while anode performances are enhanced when calendering pressure is increased as described previously in paragraph 3.3. Figure 5.13 shows the chronopotentiogram plot obtained for the calendered cell. When cell is charged from 0 V to 4 V an unexpected voltage profile was observed at the first cycle: two plateaux at about 1 and 1.5 V were measured. This behavior can be ascribed to possible short circuits in the cell when calendering step is performed. Because of calendering pressure, some particles of positive and negative electrode can flow through the separator and interact by forming local short circuit inside the cell. This process strongly affects performances of the cell. In fact a strong fade of capacity was measured at low current rate ( $C/10$ ) since first cycles. These results show how, in our case, calendering process can not be performed to enhance properties of the cell with this type of separator. The employment of a separator with tailored properties can overcome these limitations.

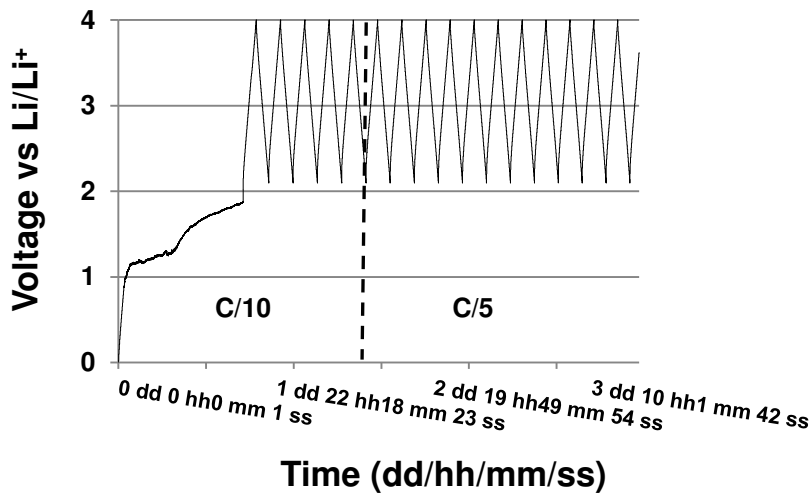


Figure 5.13. Chronopotentiogramm of calendared cell at 1 kN/m at a current rate of C/10 and C/5

### 5.2.3 Influence of substrate

In order to understand if separator can be one possible factor affecting performances of the cell, another cellulosic substrate was used as separator with physical properties more tailored for battery requirements. Two different assembling strategies were performed in order to evaluate the performance of the cell.

#### Front / back assembling strategy

All layers are printed onto one substrate. On the front side negative electrode is printed while on the reverse side positive electrode. Thanks to this approach substrate acts at the same time as substrate and separator Figure 5.14.a

#### Stack assembling strategy

This approach consists on printing each electrode onto a different substrate. Not printed face of the electrode acts as separator. Layers are then stacked to form a full cell. A commercial separator was occasionally inserted between positive and negative layers to insure a further electronic isolation between electrodes (Figure 5.14.b).

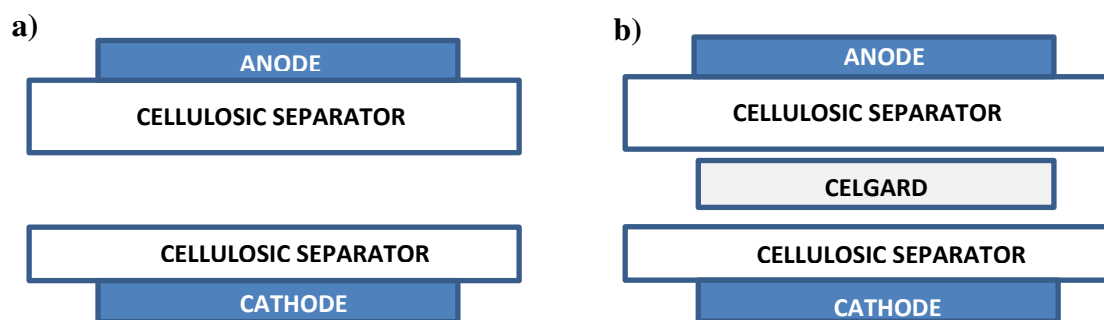


Figure 5.14. Stack layer assembling configuration. a) Cellulose separator acts as substrate for the active layer from one side and separator from the other side. b) Stack configuration with insertion of Celgard layer to enhance isolation between electrodes.

Electrochemical tests were carried out in a two electrode tests by means of Swagelok<sup>®</sup> cells and it has been employed the same electrolyte used for the previous experiments:  $\text{LiPF}_6$  1M in EC:DEC (1/1). A Celgard<sup>®</sup> separator was selected for the experiments. Table 5.8 lists parameters and principle physical characteristics of printed layers and substrate. The thickness and the grammage of active materials were balanced with an excess of  $\text{LiFePO}_4$  (LFP) in order to avoid over charge or discharge of the cell. The separator exhibits lower grammage and thickness compared to the first one used in the previous experiment but it has a higher calculated porosity corresponding to 80 %.

Table 5.8. Main physical properties of full cell printed onto a cellulosic separator

Sample	Composition	Grammage	Thickness	Electronic Conductivity
	wt (%)	$\text{g/m}^2$	$\mu\text{m}$	S/m
Negative electrode $\text{M}_s(\text{GP\_CMC\_MFC})$	40(97_2_1)	$25 \pm 2$	$21 \pm 3$	$28 \pm 9$
Separator	cellulose	$23 \pm 1$	$78 \pm 2$	-
Positive electrode $\text{M}_s(\text{LFP\_NC\_CMC\_MFC})$	40(70_27_2_1)	$65 \pm 3$	$61 \pm 3$	$18 \pm 2$

### **Front/ back full cell**

In this case the front / back layout was not the best strategy. In fact galvanostatic cycling analysis showed in each test a short circuit phenomenon since first cycles. These phenomena were likely due to a direct contact between particles during cycling because of high porosity of the separator (80%). In fact the high pore size of the separator can allow the migration of particles between electrodes. For this reasons our attention was focused on stacked assembling strategy.

### **Stacked full cell**

Figure 5.15 shows the galvanostatic study of the stacked full cell without a commercial separator among layers performed at different current rates:  $C/10 - C/5 - C/2 - C$ . As expected, a decrease of the capacity at the first cycle was measured because of the formation of SEI layer. As observed for thicker cellulosic based separator, a continuous decrement of capacity was measured when current rate increases. This fact proofs that current rates are not the predominant factor for the fade of capacity in our cell. As explained before for the thicker separator, water molecules can be adsorbed onto the surface of fiber cellulose even after drying process at 105 °C. These molecules can react with lithium ions and electrolytes by affecting performances of the cell. In this case water absorption is more important respect to the separator with high grammage. In fact this cellulosic based separator doesn't present a water resistive barrier as the first separator.

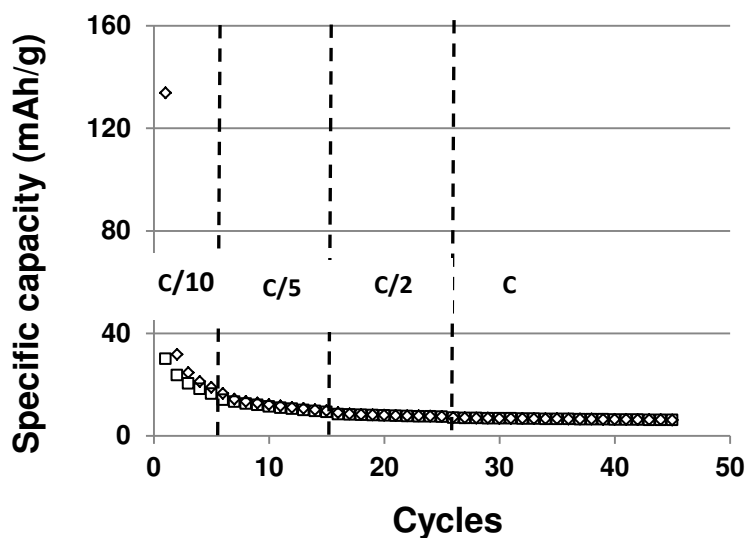


Figure 5.15. Galvanostatic cycle of a full printed cell referred to the weight of cathode material onto a cellulosic based separator with low grammage

A galvanostatic study was performed at a current rate corresponding to  $C/5$  to evaluate performances of the stacked cell with and without insertion of commercial separator between layers. In this case performances are comparable. A specific capacity of about 20 mAh/g and 14 mAh/g was measured for cells as showed in Figure 5.16 at the first cycle. The similar behavior confirms how the fade of capacity is not related to the insertion of a commercial separator between layers but to other phenomena that occur inside the electrodes. These phenomena seem to be predominant during the first cycle because a stable behavior was measured for following cycles. In fact, a part of lithium ions is “sacrificed” for the formation of the SEI layer. The cell with commercial separator exhibits a considerable loss of capacity, corresponding to 80% of lithium ions (Lis) involved in the reactions of charge and discharge. Therefore only 20 % of Lis affect performances of the cell. The same interpretation can be argued for the cell without commercial separator. In fact in this case the loss of capacity reaches 95 %.

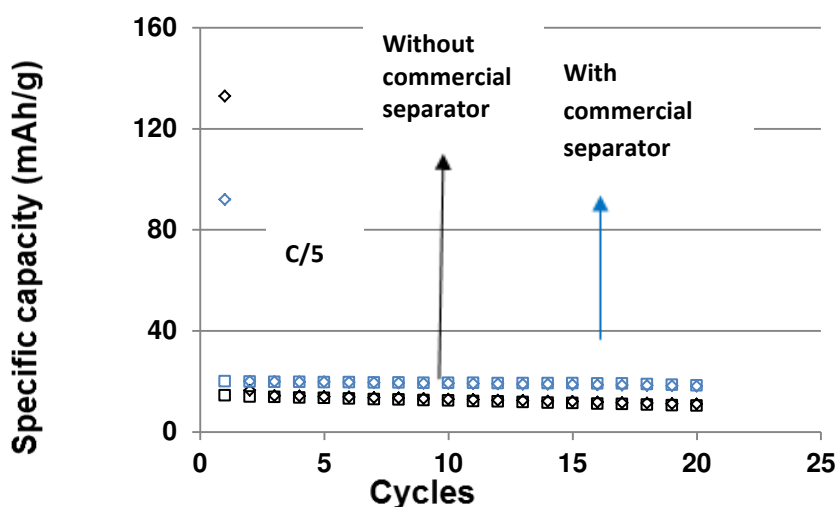


Figure 5.16 Specific capacities as function of cycles for stacked full cell with (blue symbols) and without (black symbols) additional separator layer at a constant current rate  $C/5$ .

### 5.3 Conclusion

In this chapter full printed cells were manufactured by proposing a new assembling strategy based on front / back printing of components onto a cellulosic substrate. This strategy combines the advantages of conventional assembling approaches by reducing the number of printed layers and optimizing the mean path of lithium ions inside the cell. Moreover front / back printing layout allows to enhance battery performances by reducing the volume and the mass required to the fabrication of the full cell. In fact the specific and volumetric energy density were calculated by considering a reference electrode. The values obtained were higher compared to the conventional assembling techniques. Full printed cell exhibits a thickness of  $215 \pm 9 \mu\text{m}$ , comparable with other cell reported in literatures. Electrochemical results showed how charge and discharge reactions are reversible and stable at different current rates. Galvanostatic results exhibit a progressive reduction of charge/discharge capacity when current rate increases from a value of 64 mAh/g at a current rate of  $C/10$  until 31 mAh/g at  $C$ . In term of performance a progressive reduction of specific capacity was measured as function of cycles. This progressive reduction doesn't seem affected by current rates because characteristics plateau were not evident when current rate increases. Results obtained for pouch cell was compared with a cell assembled in a classic two electrode configuration,

always in a front / back layout. Results revealed how the testing configuration doesn't affect performance of cell. In fact comparable specific capacity values were measured. This experiment shows how the fade of the capacity is likely not due to the assembling strategy but to some phenomena that occurs inside the electrodes. A second study was carried out by using this time a cellulosic separator tailored for battery requirements more porous than the first one but with a lower grammage. In this case the front / back strategy was not the best approach because of high porosity (80 %). In fact chronopotentiogram revealed some local short circuit in the battery due probably to a direct contact between positive and negative electrode. A conventional stack layout was selected to investigate the performance of the printed cell. In order to evaluate the performance a comparative study was performed by adding in one case a Celgard<sup>®</sup> separator between active layers. Galvanostatic results showed how the addition of a commercial separator doesn't affect cell performance. This fact confirms how the fade of the capacity in the battery is likely not due to the separator but to reactions involved inside the electrodes. In fact the high porosity of the electrodes (70%) doesn't insure the formation of a compact SEI layer. In addition water contaminations, due to a not complete dryness of the electrodes could consume lithium ions during cycling.

---

# **General conclusion**



---

## General conclusion

The aim of this work was the manufacturing of flexible lithium ion batteries by introducing new solutions in order to solve two critical points affecting lithium ion batteries production: 1) Replacing of toxic products commonly used (PVdF binding and NMP solvent components) . 2) Using of conventional manufacturing techniques with low cost impact and easily scalable. As showed in this dissertation these two critical points were solved by coupling the use of cellulose derivatives and water based solvent with printing techniques commonly used in printing industries. In literature review it has been showed how these two approaches were already mentioned, for example for the production of cellulose based electrodes by filtration technique [101] or for manufacturing of conventional PVdF based electrodes by printing process [98]. The new approach in this work was to combine these two strategies in order to manufacture batteries based on eco sustainable components and easy scalable and low cost production processes. In added conventional battery assembling techniques, based on ‘jelly roll’ [52] or stack lay out [69] techniques were replaced by a front / back printing technique. Firstly results show how it is possible to formulate inks based on cellulose components with tailored properties, comparable with conventional slurries based on PVdF and NMP components. These results spread potential of these inks to the fabrication of other electronic printing devices such as capacitor or printed conductive wires based on aqueous solvent and cellulosic binders. Secondly electrochemical performances obtained for printed electrodes, show how screen printing processes can be applied to replace usual deposition techniques such as blade or coating techniques to manufacture flexible electrodes. As showed in chapter 3, printing processes and calendering step can enhance electrochemical and conductive properties until reaching performance values comparable with commercial electrodes. Promising results were found by applying a calendering step as described in chapter 3 section 3.2. Electrochemical properties of substrate were triggered and this improvement contributed to improve electrode performance. Finally, the new assembling approach based on front / reverse layout is a valid alternative to classic assembling strategy. According to this new strategy, anode components were printed onto front side of substrate and cathode components onto back side. An important advantage respect to conventional strategies is the integration of the current collectors during printing stage. In fact this approach allows to reduce operational time for an up scalable manufacturing process by the integration

---

of current collector during printing of electrodes with minimal costs. This new approach avoids problems related to high number of printed layers or long ion mean path for conventional strategies. Preliminary results showed how performances are not yet comparable with commercial batteries. Different parameters were analyzed in order to understand which affects performances. Results revealed how problems are likely due to some phenomena that occur in the electrode related to not optimal contact between particles. In fact assembling strategy and substrate properties (grammage and thickness) don't seem influence in a considerable way the performance of the full cell. Calendering process was also tested. Results showed how the elevate porosity of the separator doesn't allow to enhance performance by reducing porosity and increasing electronic conductivity.

## **Perspectives**

During this work different crucial points focused our attention and the strategies we proposed to overcome them, were validated by obtained results. Obviously performance can be further improved by proposing new strategies to face problems not yet solved. As showed by calendering study, contact between particles is a crucial point to insure an optimal electronic conductivity. One solution could be the formulation of inks composed by aluminum and copper to replace current collector by printing directly onto the electrodes. This strategy avoids contact problem between solid collector (such as grid or foil) and printed electrodes. In addition, in the perspective of large area production, printing of the current collector would be totally integrated in printing process machine with minimal costs.

If we consider the substrate, the use of a multilayer structure can enhance electrochemical properties without affecting the affinity between ink and substrate. In fact a hypothetical structure with three layers with different porosity and pore size could avoid problems related to the local short circuits observed in this work during the manufacturing of the full cell.

Printing process and inks can be adapted to be printed onto other type of substrates such as membranes. A preliminary study was carried out during these three years by processing polymeric membranes based on polyethylene oxide (PEO) and MFC reinforcing. Printing tests displayed a good adhesion between ink and substrate. This different approach allows to replace liquid electrolyte by "gel polymer" electrolytes in the perspective of large area battery production.

---

## References

- [1] Dudley, G., Verniolle, J. *Secondary Lithium Batteries for Spacecraft*, European space agency, Bulletin Nr. 90, 1997.
- [2] Taylor, B. *So what makes hydrogen fuel so appealing as an energy source?*. <http://www.hydrofuelnews.com>. 2013.
- [3] *Product and Technology Elton Super Capacitors*. <http://www.elton-cap.com>.
- [4] Whittingham, M.S, Savinelli, R.F., Zawodzinsky T. *Introduction: Batteries and Fuel Cells*. Chem. Rev. 2004,104, 10, p. 4243-4244.
- [5] Winter, M., Brodd, R.J. *What are batteries, fuel cells and Supercapacitors?*. Chem. Rev. 2004, 104, p. 4245- 4269.
- [6] Martinet S. *Nouvelles génération des batteries des véhicule électriques et hybrides*. <http://www.techniques-ingenieur.fr>. 2012.
- [7] Linden, D., Reddy T. B. *Handbook of battery. Third edition*. McGraw-Hill. 2002, p. 24-25.
- [8] *Thin-film and Printed Battery Markets*. NanoMarkets. 2012.
- [9] *Recommendations on the transport of Dangerous Goods; Manual of Test and Criteria. Third revise edition*. United Nations. 2002.
- [10] Yoshio, M., Brodd, R.J., Kozawa A. *Lithium-ion batteries science and technologies*. Springer, Chapter 1. 2009.
- [11] Scrosati, B., Garche J. *Lithium batteries: Status, prospects and future*. J. Power Sources. 2010, 195, p. 2419 – 2430.
- [12] Yoshio, M., Brodd, R.J., Kozawa A. *Lithium-ion batteries science and technologies*. Springer, Chapter 2, 2009.
- [13] Linden, D., Reddy T. B. *Handbook of battery. Third edition*. McGraw-Hill. Chapter 5, 2002.
- [14] Scrosati, B., Schalkwijk, W.A. *Advances in Lithium – Ion Batteries*. Klower Academic Publisher. Chapter 9, 2002.
- [15] Cohen, E. and Guttoff, E. *Modern Coating and Drying Technology*. New York : WileyVCH, 1992.
- [16] Yoshio, M., Brodd, R.J., Kozawa A. *Lithium-ion batteries science and technologies*. Springer, Chapter 8, 2009.

- 
- [17] Tarascon, J.M., Armand, M. *Issues and challenges facing rechargeable lithium batteries*. Nature. 2001, 414, p. 359-367.
- [18] Yabuuchi, N., Ohzuku, T., *Novel lithium of  $\text{LiCo}_{1/3}\text{Ni}_{1/3}\text{Mn}_{1/3}\text{O}_2$  for advanced lithium-ion batteries* J. Power Sources. 2003, 119-121, p. 171-174
- [19] Ju, J.H., Ryu K.S., *Synthesis and electrochemical performance of  $\text{Li}(\text{Ni}_{0.8}\text{Co}_{0.15}\text{Al}_{0.05})_{0.8}(\text{Ni}_{0.5}\text{Mn}_{0.5})_{0.2}\text{O}_2$  with core-shell structure as cathode material for Li-ion batteries* J. Alloy Compd.. 2011, 509-30, p. 7995-7992
- [20] Dahn, J. R. et al. *Carbon and graphites as substitutes for the lithium anode*. Industrial Chemistry Library 5, Pistoia, G. 1994.
- [21] Thackeray, M.M, David, W.I.F., Bruce, P.G., Goodenough, J.B. *Lithium insertion into manganese spinels*. Mat. Res. Bull. 1983, 18, p. 461- 472
- [22] Kim, Y.J., Park M.S., Sohn, H.J., Lee H. *Electrochemical behaviors of SnO and Sn anodes for lithium rechargeable batteries* J. Alloy Compd.. 2011, 509-12, p. 4367-4371
- [23] Winter, M., Besenhard J.O., *Electrochemical lithiation of tin and tin-based intermetallics and composites* Electrochim. Acta. 1999, 1-2, 31-50
- [24] Arora, P., Zhang Z.J. *Battery Separators*. Chemical Review. 2004, 104, p. 4419 – 4462.
- [25] Yoshio, M., Brodd, R.J., Kozawa A. *Lithium-ion batteries science and technologies*. Springer, Chapter 19. 2009.
- [26] Song J.Y., Wang Y.Y., Wan C.C. *Review of gel-type polymer electrolytes for lithium – ion batteries*. J. Power Sources. 1999, 77, p. 183–197.
- [27] Xu X. *Non aqueous Liquid Electrolytes for Lithium-Based Rechargeable Batteries*. Chem. Rev. 2004, 104, p. 4303-4417.
- [28] Leggesse, E.G., Lin, R.T., Teng, T., Chen, C.L., Jiang, J.C. *Oxidative Decomposition of Propylene Carbonate in Lithium Ion Batteries: A DFT Study*. J. Phys. Chem. - US. 2013, A 177, p. 7959-7969.
- [29] Koxh, V.R., Goldman, J.L., Mattos, C.J., Mulvaney M.J. *Specular Lithium Deposits from Lithium Hexafluoroarsenate/DiethylEther Electrolytes*. J. Electrochem. Soc. 1982, 129, p. 1-4.
- [30] Foos, J.S., McVeigh, J. *Lithium Cycling in Polymethoxymethane Solvents*. J. Electrochem. Soc. 1983, 130, p. 628-630.
- [31] Abraham, K. M., Goldman, J. L., Natwig, D. L. *Characterization of Ether Electrolytes for Rechargeable Lithium Cells*. J. Electrochem. Soc. 1982, 129, p. 2404-2409.

- 
- [32] Moss, P.L., Au, G., Plichta, E.J., Zheng P. *Study of Capacity Fade of Lithium-Ion Polymer Rechargeable Batteries with Continuous Cycling*. J. Electrochem. Soc. 2010, 157, 1, p. 1-7.
- [33] Sankarasubramanian, S., Krishnamurthy, B. *A capacity fade model for lithium –ion batteries including diffusion and kinetics*. Electrochim. Acta. 2012, 70, p. 248 -254.
- [34] Chung, K.Y., Lee, H.S., Yoon, W.S., McBreen, J., Yang X.Q. *Studies of LiMn<sub>2</sub>O<sub>4</sub> capacity fading at elevated temperature using in situ synchrotron X-ray diffraction*. J. Electrochem. Soc. 2006, 153, 4, p. 774 –780
- [35] Eli, Y.E., Markovsky, B., Aurbach, D., Carmeli Y., *The dependence of the performance of Li-C intercalation anodes for Li-ion secondary batteries on the electrolyte solution composition*. Electrochim. Acta. 1994, 39-17, p. 2559-2569.
- [36] Guyomard, D., Tarascon, J.M. *Rechargeable Li<sub>1+x</sub>Mn<sub>2</sub>O<sub>4</sub>/Carbon Cells with a New Electrolyte Composition :Potentiostatic Studies and Application to Practical Cells*. J. Electrochem. Soc. 1993,140-11, p. 3071-3081.
- [37] Ohzuku, T., Iwakoshi, Y., Sawai K. *Formation of Lithium-Graphite Intercalation Compounds in Nonaqueous Electrolytes and Their Application as a Negative Electrode for a Lithium Ion (Shuttlecock) Cell*. J. Electrochem. Soc. 1993, 140-9, p. 2490-2498.
- [38] Tarascon, J.M., Guyomard, D. *New electrolyte compositions stable over the 0 to 5 voltage range and compatible with the Li<sub>1+x</sub>Mn<sub>2</sub>O<sub>4</sub>/carbon Li-ion cells*. Solid State Ionics. 1994, 69, p. 293-305.
- [39] Plashnitsa, L.S., Kobayashi, E., Okada, S., Yamaka J.I. *Symmetric lithium – ion cell based on lithium vanadium fluorophosphates with ionic liquid electrolyte*. Electrochim. Acta. 2011, 56, p.1344 – 1351.
- [40] Diijan, D., Alloin, F., Martinet, S., Lignier H., *Macroporous poly(vinylidene fluoride) membrane as a separator for lithium – ion batteries with high charge rate capacity*. J. Power Sources. 2009, 187, p. 575 -580.
- [41] Saunier, J., Alloin, F., Sanchez, J.Y., Barriere, B. J. Polym. Sci. Part B: Polym. Phys. 2004, 42 -3, p. 532-543.
- [42] Dahn, J. R., Sleight, A. K., Shi, H., Way, B. M., Weydanz, W. J., Reimeres, J. N., Zong, Q., Von Sacken, U. *Lithium Batteries—New Materials, Developments and Perspectives* G. Pistoia. 1994,1–97.

- 
- [43] Dudley, J. T. et al. *Conductivity of electrolytes for rechargeable lithium batteries*. J. Power Sources. 1991, 35, p. 59-82.
- [44] Peled, E. *Lithium Batteries*. J.P. Gabano. 1983, p. 43.
- [45] Peled, E., Golodnitsky, D., Ardel, G. *Advanced Model for Solid Electrolyte Interphase Electrodes in Liquid and Polymer Electrolytes*. J. Electrochem. Soc. 1997, 144, L208-L210.
- [46] Edström, K., Herstedt, M., Abraham D.P. *A new look at the solid electrolyte interphase on graphite anodes in Li-ion batteries*. J. Power Sources. 2006, 153, p. 380–384.
- [47] Chung, G.C., Zhang, X., Appleby, A.J., Chen X. *Little self discharge of secondary lithium ion graphite anodes*. J. Power Sources. 2002, 112, p. 98 -104.
- [48] Andersson, A.M., Edström, K., *Chemical Composition and Morphology of the Elevated Temperature SEI on Graphite*. J. Electrochem. Soc. 2001, 148, p. A1100-A1109.
- [49] Takahashi, T. *Silver ion conducting solid electrolytes*. . *Handbook of Solid State Batteries and Capacitors*. ed. Z. Munshi. Singapore : World Scientific. Chapter 4. 1995.
- [50] Owens, B.B. *Solid State electrolytes: overview of materials and applications during the last third of the twentieth century*. J. Power Sources. 2000, 90, p. 2–8.
- [51] Tatsuminago, M., Wakihara, M., Iwakura, C., Kohjiya S. *Solide state ionic for batteries*. Minami T. 2005.
- [52] Mercier, R., Malugani, J.-P., Fahys, B G., Robert. *Structure du Tetrathiophosphate de Lithium* Acta Crys. 1982, 38, p. 1887-1890
- [53] Kanno, R., Murayama, M. *Lithium Ionic Conductor Thio-LISICON: The  $\text{Li}_2\text{S} - \text{GeS}_2 - \text{P}_2\text{S}_5$  System*. J.Electrochem. Soc. 2001, 148, p. A742-A746.
- [54] Bohnke, O., Bohnke C., Fourquet, J.L., *Mechanism of ionic conduction and electrochemical intercalation of lithium into the perovskite lanthanum lithium*. Solid State Ionics. 1996, 91, p. 21-31.
- [55] Aono, H., Sugimoto, E., Sadaoka, Y., Imanaka, N., Adachi, G. *The Electrical Properties of Ceramic Electrolytes for  $\text{LiM}_x\text{Ti}_{2-x}(\text{PO}_4)_3 + y\text{Li}_2\text{O}$ ,  $M = \text{Ge}, \text{Sn}, \text{Hf}$ , and  $\text{Zr}$  Systems*. J. Electrochem. Soc. 1993, 140, p. 1827-1833.
- [56] Yu, X., Bates, J.B., Jellison, G.E., Hart, F. X. *A Stable Thin-Film Lithium Electrolyte: Lithium Phosphorus Oxynitride*. J. Electrochem. Soc. 1997, 144, p. 524-532.
- [57] Dias, F.B., Plomp, L., Veldhuis, J.B.J. *Trends in polymer electrolyte for secondary lithium batteries*. J. Power Sources. 2000, 88, p. 169–191.

- 
- [58] Song, J.Y., Wang, Y.Y., Wan, C.C. *Review gel-type polymer electrolytes for lithium-ion batteries*. J. Power Sources. 1999, 77, p. 183-197.
- [59] Alagmir, M., Abraham, K.M., G.Pistoia (Ed.), *Lithium Batteries: New materials, Development and perspectives*. Amsterdam: Elsevier. 1994, p. 93.
- [60] Nair, J.R., Gerbaldi, C., Meligrana, G., Bongiovanni, R., Bodoardo, S., Penazzi, N. *UV-cured polymer electrolyte membranes for Li-cells: improve mechanical properties by a novel cellulose reinforcement*. Electrochem. Commun. 2009, 11, p. 1796–1798.
- [61] Nair, J.R., Gerbaldi, C., Meligrana, G., Bongiovanni, R. *UV-cured methacrylic membranes as a novel gel polymer electrolyte for Li-ion batteries*. J. Power Sources. 2008, 178, p. 751–757.
- [62] E. A. Apps *Ink technology for printer and students*. 1963.
- [63] Kipphan, H. *Handbook of print media: Technologies and Production methods*. Springer, Chapter 1.5, 2001.
- [64] Hilali, M.M. *Understanding and development of manufacturable screen-printed contacts on high sheet-resistance emitters for low-cost silicon solar cell*. Ph.D dissertation : Georgia institute of technology, 2005.
- [65] Barbic, B., Binder, B., Voss, H., Hofer, F., Grogger, W. *Thin film Zinc/Manganese Dioxide Electrodes based on microporous polymer foil*. J. Power Sources. 1999, 79, p. 271-276.
- [66] Birke, P., Chu, W. F., Weppner, W. *Materials for lithium thin-film batteries for applications in silicon technology*. Solid State Ionic. 1996, 93, 1-2, p. 1-15.
- [67] Paloshav, R., Becker, E., Riedl, T., Johannes, H.H., Kowalsky, W. *Large Area Using Printing Methods*. Proceeding of IEE. 2005, 93-7, p. 1321-1329.
- [68] George, A., Liu, C. C., Webber, A., Feddrix, F. H. *Development and Characterization of a Thick-Film Printed Zinc-Alkaline Battery*. J. Electrochem. Soc. 2003, 150, p. A922-A927.
- [69] Wendler, M., Hübner, G., Krebs M. *Development of printed thin film and flexible batteries*. Science and technology. 2011, p. 33-41.
- [70] Hilder, M., Winther-Jensen, B., Clark, N.B. *Paper-based, printed zinc-air battery*. J. Power Sources. 2009, 194, p. 1135–1141.

- 
- [71] Gaikwad, A.M., Whiting, G.L., Steingart, D.A., Arias, A.C. *Highly flexible, printed alkaline batteries based on mesh embedded electrodes*. Adv. Mater. 2011, 23, p. 3251 – 3255.
- [72] Gaikwad, A.M., Steingart, D. A., Ng, T.N., Schwartz, D.E., Whiting G.L. *A flexible high potential printed battery for powering printed electronics*. Appl. Phys. Lett. 2013, 102, 233302.
- [73] Karpinski, A., Makovetski, B., Russell, S., Serenyi, J., Williams, D. *Silver-Zinc: status of technology and applications*. J. Power Sources. 1999, 80, p. 53–60.
- [74] Braam, K.T., Volkman, S.K., Sububramanian, V. *Characterization and optimization of a printed, primary silver–zinc battery*. J. Power Sources. 2012, 199, p. 367– 372.
- [75] Ferreira, I., Brás, B., Correia, N., Barquinha, P., Fortunato, E., Martins, R. *Self rechargeable paper thin-film batteries*. J. Disp. Technol. 2010, 6-8, p. 332-335.
- [76] Zhao, Y., Zhu, Q., Liu, L., Xu, J., Yan, M., Jiang, Z. *A novel and facile route of ink-jet printing to thin film SnO<sub>2</sub> anode for rechargeable lithium ion batteries*. Electrochim. Acta, 2006, 51, p. 2639–2645.
- [77] Ding F., Fu, Z., Zhou, M., Qin, Q. *Tin-Based Composite oxide Thin-Film Electrode Prepared by Pulsed Laser Deposition*. J. Electrochem. Soc. 1999, 146, p. 3554-3559.
- [78] Xie, J., Varadan, V.K. *Synthesis of tin oxide/carbon nanotube composite by homogeneous precipitation and characterizations*. Proceeding of SPIE. 2004, 5389, p. 210-220.
- [79] Li N., Martin, C.R., Scrosati B. *Nanomaterials based Li-ion battery electrodes*. J. Power Sources. 2001, 97–99, p. 240-243.
- [80] Park, Y.J., Park, K.S., Kima, J.G., Kim, M.K., Kim, H.G., Chung H.T. *Characterization of tin oxide/LiMn<sub>2</sub>O<sub>4</sub> thin film*. J. Power Sources. 2000, 88, p. 250-254.
- [81] Nam, S.C., Yoon, Y.S., Cho, W.I., Cho, B.W., Chun, H.S., Yun, K.S. *Reduction of irreversibility in the first charge of tin oxide thin film negative electrodes*. J. Electrochem. Soc. 2001, 148-3, p. A220-A223.
- [82] Kim, Y.-I., Yoon, C.S., Park, J.W. *Microstructural Evolution of Electrochemically Cycled Si-Doped SnO<sub>2</sub>-Lithium Thin-Film Battery*. J. Solid State Chem. 2001, 160, p. 388-393.
- [83] Brousse, T., Retouxf, R., Herterich, U., Schleich, D.M. *Thin-Film Crystalline SnO<sub>2</sub>-Lithium Electrodes*. J. Electrochem. Soc. 1998,145, p. 1-4.

- 
- [84] Brousse, T., Crosnier, O., Devaux, X., Fragnaud, P., Paillard, P., Santos-Pen, J., Schleich, D.M., *Advanced oxide and metal powders for negative electrodes in lithium-ion batteries*. Powder Technol. 2002, 128, p. 124-130.
- [85] Li, N., Martin, C.R. A *High-Rate, High-Capacity, Nanostructured Sn-Based Anode Prepared Using Sol-Gel Template Synthesis*. J. Electrochem. Soc. 2001, 148, p. A164-A170.
- [86] Ding, F., Fu, Z., Zhou, M., Qin, Q. *Tin-Based Composite Oxide Thin-Film Electrodes Prepared by Pulsed Laser Deposition*. J. Electrochem. Soc. 1999, 146-10, p. 3554-3559.
- [87] Nuli, Y., Zhao, S., Qin, Q. *Nanocrystalline tin oxides and nickel oxide film anodes for Li-ion batteries*. J. Power Sources. 2003, 114, p. 113-120.
- [88] Mohamedi, M., Lee, S.J., Takahashi, D., Nishizawa, M., Itoh, T., Uchida, I. *Amorphous tin oxide films: preparation and characterization as an anode active material for lithium ion batteries*. Electrochim. Acta. 2001, 46-8, p. 1161-1168.
- [89] Maranchi, J.P., Hepp, A.F., Kumta P.N. *LiCoO<sub>2</sub> and SnO<sub>2</sub> thin film electrodes for lithium-ion battery applications*. Mat. Sci. Eng.: B. 2005, 116, p. 327-340.
- [90] Liangbing, H., Mantia, H.F., Yang, Y., Cui, Y. *Thin flexible secondary Li-ion paper batteries*. ACSNANO. 2010, 4 -10, p. 5843–5848.
- [91] Singh, N. et al. *Paintable battery* Scientific report. 2012, 2, 481, p. 1-5.
- [92] Sun, K., Wei, T.S., Ahn, B.Y., Seo, J.Y., Dillon, S. J., Lewis, J. A. *3D Printing of Interdigitated Li-Ion Microbattery Architectures*. Adv. Mater. 2013, 25, p. 4539-4543.
- [93] Tymecki, L., Zwierkowska, E., Koncki, R. *Screen printed reference electrodes for potentiometric measurements*. Anal. Chim. Acta. 2004, 526, p. 3–11.
- [94] Dudney, N.J., Jang, Y.I. *Analysis of thin-film lithium batteries of 50 nm to 4 μm thick LiCoO<sub>2</sub>*. J. Power Sources. 2003, 119–121, p. 300.
- [95] Lee, S.T., Jeon, S.W., Yoo, B.J., Choi, S.D., Kim, H.J., Lee, S.M. *Electrochemical properties of LiCoO<sub>2</sub> thick-film cathodes prepared by screen-printing technique*. J. Power Sources. 2006, 155, p. 375–380.
- [96] Park, M.S., Hyun, S.H., Nam, S.C. *Characterization of a LiCoO<sub>2</sub> thick film by screen-printing for a lithium ion micro-battery*. J. Power Sources. 2006, 159, p. 1416–1421.
- [97] Park, M.S., Hyun, S.H., Nam, S.C. *Mechanical and electrical properties of a LiCoO<sub>2</sub> cathode prepared by screen-printing for a lithium-ion micro-battery*. Electrochim. Acta. 2007, 52, p. 7895–7902.

- 
- [98] Geyer, U., Siegel, F., Kreutzer, A., Blaudeck, T., Reinhard, R. Baumann. *Printing electrode materials for rechargeable lithium thin-film batteries*. LOPE-C. 2009, 09.
- [99] Rouault H. et al. *Development of electrodes for printed Li-ion Thin Film Batteries*. ISFOE09. 2009.
- [100] Ohta, S., Komagata, S., Seki, J., Saeki, T., Morishita, S., Asaoka, T. *All-solid-state lithium ion battery using garnet-type oxide and  $\text{Li}_3\text{BO}_3$  solid electrolytes fabricated by screen-printing*. J. Power Sources. 2013, 238, p. 53-56.
- [101] Jabbour, L., Destro, M., Gerbaldi, C., Chaussy, D., Penazzi, N., Beneventi, D. *Aqueous processing of cellulose based paper-anodes for flexible Li-ion batteries*. J. Mater. Chem. 2012, 22, p. 3227-3233.
- [102] Jabbour, L., Destro, M., Chaussy, D., Gerbaldi, C., Penazzi, N., Bodoardo, S., Beneventi, D. *Flexible cellulose/ $\text{LiFePO}_4$  paper-cathodes: toward eco-friendly all-paper Li-ion batteries*. Cellulose. 2013, 20, p. 571–582.
- [103] Jabbour, L., Gerbaldi, C., Chaussy, D., Zeno, E., Bodoardod, S., Beneventi, D. *Microfibrillated cellulose–graphite nanocomposites for highly flexible paper-like Li-ion battery electrodes*. J. Mater. Chem. 2010, 20, p. 7344-7347.
- [104] Leijonmarck, S., Cornell, A., Lindbergh, G., Wagberg, L. *Single-paper flexible Li-ion battery cells through a paper making process based on nano-fibrillated cellulose*. J. Mater. Chem. A. 2013, 1, p. 4671–4677.
- [105] Scrosati B. *Nanomaterials :Paper powers battery breakthrough*. Nat. Nanotechnol. 2007, 2-10, p. 598-599.
- [106] Pushparaj V.L. et al. *Flexible energy storage devices based on naocomposite paper*. Proceeding of the National Academy of Sciences of the United States of America. 2007, 104, p. 13574–13577.
- [107] Siro, I., Plackett, D. *Microfibrillated cellulose and new composite materials a review*. Cellulose. 2010, 17, p. 459 – 494.
- [108] Jabbour, L. *Elaboration of Li-ion batteries using cellulose fibers and papermaking techniques*. Ph.D dissertation: Grenoble. 2012.
- [109] Lee, J.H., Lee, S., Paik, U., Choi, Y.M. *Aqueous processing of natural graphite particulates for lithium-ion battery anodes and their electrochemical performance*. J. Power Sources. 2005, 147, p. 249-255.

- 
- [110] Wang, Y., He, P., Zhou, H. *Olivine LiFePO<sub>4</sub>: development and future* Energy Environ. Sci. 2011, 4, p. 805-817.
- [111] Choi, Y.M., Paik, U., Kim, K.H. *Anode composition for lithium battery and anode and lithium battery using the same*. Korean Patent Application No. P2003-0040085, 2008.
- [112] Lin, H. W., Chang, C. P., Hwu, W. H., Ger, M. D. *The rheological behaviors of screen-printing pastes*. J. Mater. Process Tech. 2008, 197, p. 284–291.
- [113] Hoornstra, J., Weeber, A.W., De Moor, H.H.C., Sinke, W. C. *The importance of paste rheology in improving fine line, thick film screen printing of front side metallization*. Netherland Energy Research Foundation. 1997.
- [114] T.A. Instrument *Rheology solutions : determining the linear viscoelastic region in polymers*. <http://www.tainst.com>.
- [115] Faddoul R. *Procèdes d'impression dédiés a la production de masse de microcomposants électroniques a base de céramique*. Ph.D dissertation : Grenoble, 2012.
- [116] Pan, J., Tonkay, G.L., Quintero, A. *Screen Printing Process of Experiments for Fine Line Printing of Thick Film Ceramic Substrates*. J. Electron. Manuf. 1999, 9, p. 203-223.
- [117] Jandel Universal Probe technical information
- [118] Kovalchick C. *Mechanics of Peelings: Cohesive Zone Law and Stability*. Ph.D Dissertation: California, 2011.
- [119] Rivlin, R.S. *The Effective work of adhesion*. J. Paint Technol. 1944, 9,p. 244.
- [120] Alicona infinite focus technical information
- [121] Iotti M., Gregersen, W., Moe, S., Lenes, M. *Rheological Studies of Microfibrillar Cellulose Water Dispersions*. J. Polym. Environ. 2011, 19, p. 137-14.
- [122] Jeffrey, D.J., Crivos, A. *The rheological properties of suspensions of rigid particles*. Aiche J. 1976, 3, p. 417-432.
- [123] Liu, W.H., Yu, T.L., Lin, H.L. *Shear thickening behavior of dilute poly(diallyl dimethyl ammonium chloride) aqueous solutions*. Polymer. 2007, 48-14, p. 4152-4165.
- [124] Clasen. C., Kulicke, W.M. *Determination of viscoelastic and rheo-optical material functions of water-soluble cellulose derivatives*. Prog. Polym. Sci. 2001, 26-9, p. 1839-1919.
- [125] Dave, E., Dunstan, K., Hill, E., Wei, Y. *Direct measurement of polymer segment orientation and distortion in shear: semi-dilute solution behavior*. Polymer. 2004, 45-4, p. 1261-1266.

- 
- [126] Benchabane A. & Bekkour K. *Rheological properties of carboxymethyl cellulose (CMC) solutions*. Colloid Polym. Sci. 2008, 286, p. 1173-1180.
- [127] Scher, J. *Rhéologie, texture et texturation des produits alimentaires*. Techniques de l'Ingénieur - F3300V2, 1998.
- [128] Russel, W.B. *Distinguishing between dynamic yielding and wall slip in a weakly flocculated colloidal dispersion*. Colloid Surf., A. 2000, 161.
- [129] Mahendra, R., Brandon, S. P., Brandon, N. P. *Rheological Studies of Nickel/Scandia-Stabilized-Zirconia Screen Printing inks for Oxide Fuel Cell Anode Fabrication*. J. Amer. Ceram. Soc. 2012, 95-4, p. 1220-1228.
- [130] Mallik, S., Schmidt, M., Bauer, R. and Ekere, N.N. *Influence of Solder Paste Components on Rheological Behaviour*. 2<sup>nd</sup> Electronics System-Integration Technology Conference IEE, 2008.
- [131] Strnadel, J., Simon, M., Machač, I. *Wall effects on terminal falling velocity of spherical particles moving in a Carreau model fluid* Chem. Pap. 2011, 65.
- [132] Németh, C., Zeke, I., Juhász, R., Friedrich, L., Bata, J., Balla, C. *Flow Properties of Processed Liquid Egg White Products*. Annu. Trans. Nord. Rheol. Soc. 2010, 18.
- [133] Ghorbel, D., Barbouche, N., Riahi, H., Braham, A., Attia H. *Influence of fat content on rheological properties of molten ice cream compound coatings and thickness of solidified products*. J. Food Process Eng. 2008.
- [134] Barns, H. A. *Thixotropy a review*. J. Non-Newton Fluid. 1997, 70, p. 1-33.
- [135] Heckroodt, R.O., Ryan, W. *Clay suspensions with "negative thixotropy"*. Trans British Ceramic Society. 1978, 77.
- [136] Kanai, H., Amari, T. *Negative thixotropy in ferric oxide suspensions*. Rheol. Acta 1995, 34, p. 303-310.
- [137] Lowys, M.P., Desbrieres, J., Rinaudo, M. *Rheological characterization of cellulosic microfibril suspensions. Role of polymeric additives*. Food Hydrocolloid. 2001, 15-1, p. 25-24.
- [138] Agoda-Tandjawa, G., Durand, S., Berot, S., Blassel, C., Gaillard, C., Garnier, C., Doublier J.L. *Rheological characterization of microfibrillated cellulose suspensions after freezing*. Carbohydr. Polym. 2010, 80-3, p. 677-686.
- [139] Buzby, D., Dobie, A. *Fine line screen printing of thick film pastes on silicon solar cells*. IMAPS, 2008.

- 
- [140] Jeong, S.S., Bockenfeld, N., Balducci, A., Winter, M., Passerini, S. *Natural cellulose as binder for lithium battery electrodes*. J. Power Sources. 2012, 199, p. 331-335.
- [141] Kim, D.Y., Lee, B.K., Choi, S.J. *Copper foil for current collector of lithium secondary battery with improved wrinkle characteristics*. US patent 2013/0108887 A1. 2013.
- [142] Hideaki, M., Sakiko T. *Negative pole material manufacturing method for lithium ion secondary battery and negative pole material for lithium ion secondary battery*. WO2013018898. 2013.
- [143] Channu, V.S., Bobba, R., Holze, R. *Graphite and graphene oxide for lithium ion batteries*. Colloid and Surfaces A: Physicochemical and Engineering Aspects. 2013, 436.
- [144] Noel, M., Suryanarayanan, V. *Role of carbon host lattice in Li-ion intercalation/de-intercalation processes*. J. Power Sources. 2002, 111, 2-23, p. 193-209.
- [145] Buqa, H., Wursig, A., Goers, D., Hardwick, L.J., Holzappel, M., Novak, P., Krumeich, F., Spahr, M.E. *Behaviour of highly crystalline graphites in lithium-ion cells with propylene carbonate containing electrolytes*. J. Power Sources. 2005, 146, 1-2, p. 134-141.
- [146] Levi, M.D., Aurbach, D. *The mechanism of lithium intercalation in graphite film electrodes in aprotic media part I*. J. Electroanal. Chem. 1997, 421, 1-2, p. 79-88.
- [147] La Mantia, F., Vetter, J., Novak, P. *Impedance spectroscopy on porous materials: A general model and application to graphite electrodes of lithium-ion batteries*. Electrochim. Acta. 2008, 53, 12, p. 4109-4121.
- [148] Aurbach, D., Markovsky, B., Weissman, I., Levi, E., Ein-Eli, Y. *On the correlation between surface chemistry and performance of graphite negative electrodes for Li ion batteries*. Electrochim. Acta. 1999, 45.
- [149] Aurbach, D., Levi, M.D., Levi, E., Teller, H., Markovsky, B., Salitra, G. *Common Electroanalytical Behavior of Li Intercalation Processes into Graphite and Transition Metal Oxides*. J. Electrochem. Soc. 1998, 145-9, p. 3024-3034.
- [150] Novak, P., Joho, F., Lanz, M., Rykart, B., Panitz, J.C., Alliata, D., Kotz, R., Haas, O. *The complex electrochemistry of graphite electrodes in lithium ion batteries*. J. Power Sources. 2001, 97-98, p. 39-46.

- 
- [151] Yoshio, M., Wang, H., Fukuda, K., Hara, Y., Adachi, Y. *Effect of Carbon Coating on Electrochemical Performance of Treated Natural Graphite as Lithium-Ion Battery Anode Material*. J. Electrochem. Soc. 2000, 147-4, p. 1245-1250.
- [152] Ghimbeu, C.M. et al. *Influence of Graphite Characteristics on the Electrochemical Performance in Alkylcarbonate LiTFSI Electrolyte for Li-Ion Capacitors and Li-Ion Batteries*. J. Electrochem. Soc. 2013, 160-10, p. A1907-A1915.
- [153] La Mantia, F. *Characterization of Electrodes for Lithium-Ion Batteries through Electrochemical Impedance Spectroscopy and Mass Spectrometry*. Ph.D dissertation, 2008.
- [154] Hu, L., Pasta, M., La Mantia, F. et al. *Stretchable, porous, and conductive energy textiles*, Nano Letter, 2010, 10-2, 708-714.
- [155] Hu, L., Wu, H., Cui, Y. *Printed energy storage devices by integration of electrodes and separators into single sheets of paper*. Appl. Phys. Lett. 2010, 96.
- [156] Lee, J.H., Paik, U., Hackley, V. A., Choi, Y.M. *Effect of Carboxymethyl Cellulose on Aqueous Processing of Natural Graphite Negative Electrodes and their Electrochemical Performance for Lithium Batteries*. J. Electrochem. Soc. 2005, 152-9, p. A1763-A1769.
- [157] Chiappone, A., Nair, J.R., Gerbaldi, C., L. Jabbour, Bongiovanni, R., Zeno, E., Beneventi, D., Penazzi, N. *Microfibrillated cellulose as reinforcement for Li-ion battery polymer electrolytes with excellent mechanical stability*. J. Power Sources. 2011, 196-23, p. 10280-10288.
- [158] Striebel, K.A., Sierra, A., Shima, J., Wang, C.-W., Sastry, A.M. *The effect of compression on natural graphite anode performance and matrix conductivity*. J. Power Sources. 2004, 134-2, p. 241-251.
- [159] Takamura, T. et al. *Charge/discharge efficiency improvement by the incorporation of conductive carbons in the carbon anode of Li-ion batteries*. J. Power Sources. 2000, 90-1, p. 45-51.
- [160] Novak, P., Sceifele, W., Winter, M., Haas, O. *Graphite electrodes with tailored porosity for rechargeable ion-transfer batteries*. J. Power Sources. 1997, 68-2, p. 267-270.
- [161] Gnanaraj, J.S., Cohen, Y.S., Levi, M.D., Aurbach, D. *The effect of pressure on the electroanalytical response of graphite anodes and LiCoO<sub>2</sub> cathodes for Li-ion batteries*. J. Electroanal. Chem. 2001, 516, 1-2, p. 89-102.

- 
- [162] Shim, J., Striebel, K.A. *Effect of electrode density on cycle performance and irreversible capacity loss for natural graphite anode in lithium-ion batteries*. J. Power Sources. 2003, 119-121, p. 934-937.
- [163] Arora P., White, R.E., Doyle, M. *Capacity Fade Mechanisms and Side Reactions in Lithium-Ion Batteries*. J. Electrochem. Soc. 1998, 145-10, p. 3647-3667.
- [164] Zaghbi, K., Brochu, F., Guerfi, A., Kinoshita K. *Effect of particle size on lithium intercalation rates in natural graphite*. J. Power Sources. 2001, 103.
- [165] McMillan, R., Slegel, H., Shu, Z.X., Wang, W. *Fluoroethylene carbonate electrolyte and its use in lithium ion batteries with graphite anodes*. J. Power Sources. 1999, 81-82, p. 20-26.
- [166] Padhi, A.K., Nanjundaswamy, K.S., Goodenough, J.B. *Phospho-olivines as Positive-Electrode Materials for Rechargeable Lithium Batteries*. J. Electrochem. Soc. 1997, 144-4, p. 1188-1194.
- [167] Wang, G., Chen, L., Mathur, G. N., Varadan, V.K. *Lithium Iron Phosphates as Cathode Materials in Lithium Ion Batteries for Electric Vehicles* Nanosensors. Biosensors and Info-Tech Sensors and Systems. 2012.
- [168] Dominko, R., Gaberscek, M., Drofenik, J., Bele, M., Jamnik, J. *Influence of carbon black distribution on performance of oxide cathodes for Li ion batteries*. Electrochim. Acta. 2003, 48-24, p. 3709-3716.
- [169] Rwei, S.P., Ku, F.H., Cheng, K.C. *Dispersion of carbon black in a continuous phase: Electrical, rheological, and morphological studies*. Colloid Polym. Sci. 2002, 280-12, p. 1110-1115.
- [170] Dominko, R., Bele, M., Gaberscek, M., Remskar, M., Hanzel, D., Pejovnik, S., Jamnik J. *Impact of the Carbon Coating Thickness on the Electrochemical Performance of LiFePO<sub>4</sub>/C Composites*. J. Electrochem. Soc. 2005, 152-3, p. A607-A610.
- [171] Amari, T., Uesugi, K., Suzui, H. *Viscoelastic properties of carbon black suspension as a flocculated percolation system*. Prog. Org. Coat. 1997, 31-1-2, p. 171-178.
- [172] Bischoff, M.H., Dolle F.E. *Electrical conductivity of carbon black-polyethylene composites Experimental evidence of the change of cluster connectivity in the PTC effect*. Carbon. 2001, 39-3, 375-382.

- 
- [173] Lee, J.H., Kim, J.S., Kim, Y.C., Zang, D.S., Paik, U. *Dispersion properties of aqueous-based LiFePO<sub>4</sub> pastes and their electrochemical performance for lithium batteries*. Ultramicroscopy. 2008, 108-10, p. 1256-1259.
- [174] Saarinen, T., Lille, M., Seppala, J. *Technical Aspects on Rheological Characterization of Microfibrillar Cellulose Water Suspensions*. Annu. Trans. Nord. Rheol. Soc. 2009, 17.
- [175] Kulichet, W.M., Kull, A.H., Kull, W., Thielking, H. *Characterization of aqueous caboxymethylcellulose solutions in terms of their molecular structure and its influence on rheological behavior*. Polymer. 1996, 37-13, p. 2723-2731.
- [176] Porcher, W., Lestriez, B., Jouanneau, S., Guyomard D. *Design of Aqueous Processed Thick LiFePO<sub>4</sub> Composite Electrodes for High-Energy Lithium Battery*. J. Electrochem. Soc. 2009, 156-3, p. A133-A144.
- [177] Agoda-Tandjawa, G., Durand, S., Berot, S., Blassel, C., Gaillard, C., Garnier, C., Doublier, J.L. *Rheological characterization of microfibrillated cellulose suspensions after freezing*. Carbohydr. Polym. 2010, 80-3, p. 677-686.
- [178] Rehage, H., Hoffman, H. *Rheological Properties of Viscoelastic Surfactant Systems*. J. Phys. Chem.- US. 1988, 92-16, p. 4712-4719.
- [179] Phair, J.W. *Rheological Analysis of Concentrated Zirconia Pastes with Ethyl Cellulose for Screen Printing SOFC Electrolyte Films*. J. Amer. Ceram. Soc. 2008, 91-7, p. 2130-2137.
- [180] Mahendra, R., Brandon, S., Brandon P. *Rheological studies of nickel/Scandia stabilized zirconia screen printing inks for solide oxide fuel cell anode fabrication*. J. Amer. Ceram. Soc. 2012, 95-4, p. 1220-1228.
- [181] Lee, G.W., Ryu, J.H., Han, W., Ahn, K.H., Oh, S.M. *Effect of slurry preparation process on electrochemical performances of LiCoO<sub>2</sub> composite electrode*. J. Power Sources. 2010, 195-18, p. 6049-6054.
- [182] Krebs, F.C. *Fabrication and processing of polymer solar cells: A review of printing and coating techniques*. Sol. Energ. Mat. Sol. C. 2009, 93, p. 394-412.
- [183] Ito, S., Chen, P., Comte, P., Nazeeruddin, M.K., Liska P., Pechy, P., Gratzel, M. *Fabrication of Screen-Printing Pastes From TiO<sub>2</sub> Powders for Dye-Sensitised Solar Cells*. Progress in Photovoltaics Research and Applications. 2007, 15-7, p. 603-612.

- 
- [184] Lee, M.Y., Park, J.E., Park, J.S., Song C.K. *A printing technology combining screen-printing with a wet-etching process for the gate electrodes of organic thin film transistors on a plastic substrate*. *Microelectron. Eng.* 2010, 87-10, p. 1922-1926.
- [185] Dominko, R., Goupil, J.M., Bele, M., Gaberscek, M., Remskar, M., Hanzel, D., Jamnik J. *Impact of LiFePO<sub>4</sub>/C Composites Porosity on Their Electrochemical Performance*. *J. Electrochem. Soc.* 2005, 152-5, p. A858-A863.
- [186] Zaghib, K., Mauger, A., Gendron, F., Julien, C.M. *Surface Effects on the Physical and Electrochemical Properties of Thin LiFePO<sub>4</sub> Particles*. *Chem. Mater.* 2008, 20-2, p. 462-469.
- [187] Leijonmarck, S., Cornell, A., Lindbergh, G., Wagberg L. *Flexible nano-paper-based positive electrodes for Li-ion batteries Preparation process and properties*. *Nano Energy*. 2013, 2-5, p. 794-800.
- [188] Kumar, A., Thomas, R., Karan, N.K., Saavedra-Arias, J.J., Singh, M.K., Majumder, S. B., Tomar, M. S., Katiyar, R. S. *Structural and Electrochemical Characterization of Pure LiFePO<sub>4</sub> and Nanocomposite C-LiFePO<sub>4</sub> Cathodes for Lithium Ion Rechargeable Batteries*. *J. Nanotechnol.* 2009, 1-10.
- [189] Takahashi, M., Tobishima, S., Takei, K., Sakurai, Y. *Reaction behavior of LiFePO<sub>4</sub> as a cathode material for rechargeable lithium batteries* *Solid state Ionics*. 2002, 148-3-4, p. 283-289.
- [190] Yu, D.Y.W., Fietzek, C., Weydanz, W., Donue, K., Inoue, T., Kurokawa, H., Fujitani, S. *Study of LiFePO<sub>4</sub> by Cyclic Voltammetry*. *J. Electrochem. Soc.* 2007, 154-4, p. A253-A257.
- [191] Ravet, N., Chouinard, Y., Magnan, J.F., Besner, S., Gauthier, M., Armand, M. *Electroactivity of natural and synthetic triphylite*. *J. Power Sources*. 2001, 97-98, p. 503-507.
- [192] Yun, N.J., Ha, H.W., Jeong, K. H., Park, H.Y., Kim, K. *Synthesis and electrochemical properties of olivine-type LiFePO<sub>4</sub>/C composite cathode material prepared from a poly(vinyl alcohol)-containing precursor*. *J. Power Sources*. 2006, 160-2, p. 1361-1368.
- [193] Jin, B., Gu, H.B., Zhang, W., Park, H., Sun G. *Effect of different carbon conductive additives on electrochemical properties of LiFePO<sub>4</sub>-C/Li batteries*. *J. Solid State Electrochem.* 2008, 12, p. 1549-1554.

- 
- [194] Liu, A., Hu, Z.H., Wen, Z.B., Lei L., An, J. *LiFePO<sub>4</sub>/C with high capacity synthesized by carbothermal reduction method*. Ionics. 2010, 16-4, p. 311-316.
- [195] Popovic, J., Cakan, R.D., Tornow J., Morcrette, D.S.Su., Schlogl, R., Antonietti, M., Titirici M.M. *LiFePO<sub>4</sub> Mesocrystals for Lithium-Ion Batteries*. Small. 2011, 7-8, p. 1127-1135.
- [196] Haselrieder, W., Ivanov, S., Christen, D. K., Bockholt, H., Kwade, A. *Impact of the Calendering Process on the Interfacial Structure and the Related Electrochemical Performance of Secondary Lithium-Ion Batteries*. J. Electrochem. Soc. 2013, 50-26, p. 59-70.
- [197] Yu, D.Y.W., Donoue, K., Inoue, T., Fujimoto, M., Fujitani, S. *Effect of Electrode Parameters on LiFePO<sub>4</sub> Cathodes*. J. Electrochem. Soc. 2006, 153-5, p. A835-A839.
- [198] Zheng, H., Li, J., Song, X., Liu, G., Battaglia, V.S. *A comprehensive understanding of electrode thickness effects on the electrochemical performances of Li-ion battery cathodes*. Electrochim. Acta. 2012, 71, p. 258-265.
- [199] Zhao, M., Lemke, F.R., Dewald, H.D. *Electrochemical Stability of Copper in Lithium Ion Battery Electrolytes*. J. Electrochem. Soc. 2000, 147-8, p. 2874-2879.
- [200] Behl, W.K., Plich E.J. *Stability of Aluminum in Low-Temperature Lithium-Ion Battery Electrolytes*. Army Research Laboratory. 1999, p. 1-17.
- [201] Zhang, S.S., Jow, T.R. *Aluminum corrosion in electrolyte of Li-ion battery*. J. Power Sources. 2002, 109, p. 458-464.
- [202] Xu, M., Dewald, H.D. *Impedance studies of copper foil and graphite-coated copper foil electrodes in lithium-ion battery electrolyte*. Electrochim. Acta. 2005, 50, p. 5473-5478.
- [203] Bennet, W.R. *Considerations for Estimating Electrode Performance in Li-Ion Cells*. Energytech 2012 IEE. 2012, 1-5, p. 29-31.
- [204] <http://www.bestgopower.com/products/battery-overview/lifepo4-pouch-cell-list.html>
- [205] Chen, Z., Christensen, L., Dahn, J.R. *Large volume-change electrodes for Li-ion batteries of amorphous alloy particles held by elastomeric tethers*. Electrochem. Commun. 2003, 5, p. 919-923.





# French extended abstract

## Introduction

Le secteur énergétique actuel basé sur les combustibles fossiles a atteint une valeur critique à cause des prix toujours plus élevés du pétrole et l'absence de ressources énergétiques renouvelables. Un autre aspect crucial correspond aux émissions de CO<sub>2</sub> qui continuent d'augmenter depuis ces dernières 30 années. Tout ceci a justifié la recherche d'énergie renouvelable qui soit en même temps aussi une source d'énergie propre sans émissions polluants. Les efforts portés dans cette direction ont été multiples dans le monde entier, spécialement dans le domaine de l'énergie solaire et éolique. Par contre ces sources nécessitent des systèmes de stockage d'énergie. Dans cette optique, les systèmes électrochimiques constituent une alternative intéressante sous réserve qu'ils présentent un impact environnemental réduit. Des systèmes comme les batteries, les piles à combustibles ou les super condensateurs peuvent jouer un rôle crucial grâce à la leur capacité à stocker et à délivrer de l'énergie sur demande.

Les batteries sont des systèmes capables de stocker de l'énergie avec un taux de conversion important en absence d'émissions nocives. En plus elles représentent l'option la plus prometteuse dans les domaines de véhicules hybrides et véhicules électriques. Plus particulièrement, les batteries rechargeables ont une importance croissante grâce à leur énergie spécifiques élevée, leur performance et leur cout de revient. Actuellement, les batteries lithium-ion (LIBs) surclassent les autres technologies alternatives grâce à leur densité d'énergie élevée. Les LIBs représentent aujourd'hui la solution idéale pour le marché d'électronique à faible puissance. En fait 63% du marché globale des batteries est constitué par les batteries lithium – ion.

Par contre la diffusion massive de LIBs est limitée par trois facteurs :

- Réduction de prix de production
- Identification des matériaux et procédés de production à faible impact environnemental
- Développement de dispositifs facilement recyclables

Une possible solution pour faire face à ces verrous dans la production des batteries lithium-ion est l'utilisation de matériaux bio-sourcées à bas coût comme les matériaux cellulosiques.

Pour cette raison la cellulose a été sélectionnée comme potentiel substrat pour la réalisation de dispositifs électroniques à faible cout de production.

En effet, la cellulose est un des matériaux le moins onéreux et le plus répandu. Un autre atout de la cellulose est son aptitude à être recyclée.

Parallèlement à cela, l'utilisation des procédés d'impression est une voie prometteuse pour la fabrication de ces dispositifs électroniques grâce aussi à la facilité de mise en œuvre de produits flexibles. Au contraire des techniques conventionnelles utilisées pour la production d'électrodes de batteries, les procédés d'impression, grâce à leur technique de production de masse peuvent permettre de réduire considérablement le prix et en assurant des cadence de production industrielles.

Les objectifs de ce travail de thèse peuvent être résumés en trois points :

- I. Substitution des liants conventionnels utilisés dans la production des batteries lithium-ion par des polymères bio-sourcées (i.e. cellulose et dérivées)
- II. Formulation d'encres aqueuses contenant les matériaux classiquement utilisés dans la fabrication des électrodes
- III. Fabrication d'électrodes et de batteries flexibles par dépôt de matières actives sur un substrat cellulosique par procédé d'impression.

Ce manuscrit est divisé en cinq chapitres :

**Chapitre 1** : Une partie bibliographique met en évidence les points clés du projet et introduit brièvement les caractéristiques générales des batteries lithium-ion. La deuxième partie est dédiée à une dissertation concernant les matériaux, le fonctionnement et le procédé de fabrication conventionnelle des batteries. Enfin une partie exhaustive est consacrée à la description de procédés de formulation des encres conductrices et aux différents procédés de fabrication des batteries lithium ion

**Chapitre 2** : Ce chapitre résume les matériels et les méthodes utilisés pendant ce travail de thèse. Les matériaux utilisés sont listés et décrits dans la première partie de cette thèse. Les principales techniques de caractérisation et le procédé d'impression sont aussi présentés en détail. La dernière partie est dédiée à la préparation des électrodes, à la technique d'assemblage et aux tests de caractérisation électrochimiques.

**Chapitre 3** : Dans ce chapitre les étapes de fabrication des électrodes négatives sont décrites en détail. Les résultats rhéologiques sont présentés pour les encres formulées, en analysant l'influence de leurs différents constituants. Après une étape d'impression les électrodes sont caractérisées d'un point de vue physique et électrochimique. La dernière partie est dédiée à

l'analyse des résultats obtenus en utilisant différentes stratégies pour améliorer les performances.

**Chapitre 4 :** L'élaboration des électrodes positives est présentée dans ce chapitre. Les encres ont été formulées en utilisant un liant et un dispersant dérivé de la cellulose et un agent conducteur pour améliorer la conductivité électronique des électrodes. Une étude rhéologique a été menée pour trouver les propriétés rhéologiques optimales pour la technique d'impression sérigraphique et l'influence des composants sur les encres formulées. Une caractérisation physique et électrochimique a été réalisée. Les résultats sont présentés en mettant en évidence les résultats obtenus après l'étape de calandrage. Enfin une conclusion résume les principaux résultats obtenus d'un point de vue rhéologique, physique et électrochimique.

**Chapitre 5 :** Ce chapitre se focalise sur l'impression et la caractérisation de la cellule complète. Différentes stratégies d'assemblages sont proposées en présentant les principaux avantages et inconvénients de chaque stratégie. Une partie est dédiée à l'exposition de la technique d'assemblage élaborée pendant ce travail de thèse, basé sur une technique d'impression recto / verso du substrat d'impression. Des analyses physiques et électrochimiques sont réalisées et les résultats sont comparés avec d'autres cellules complètes réalisées par des techniques d'assemblage conventionnelles. Certains paramètres clés comme la porosité, l'épaisseur et le grammage ont été optimisés pour améliorer les performances de la cellule assemblées.

Enfin, une conclusion générale résume les résultats les plus importants obtenus pendant ce travail de thèse.

# 1. Batteries

## 1.1 Principes électrochimiques

Les systèmes électrochimiques pour le stockage et la conversion d'énergie sont constitués par les batteries, les piles à combustible et les condensateurs électrochimiques. Même si les mécanismes de stockage et conversion d'énergies sont différents les trois systèmes en question présentent des similarités. Comme le montre la figure 1.1, les trois systèmes consistent en deux électrodes en contact direct avec une solution électrolytique.

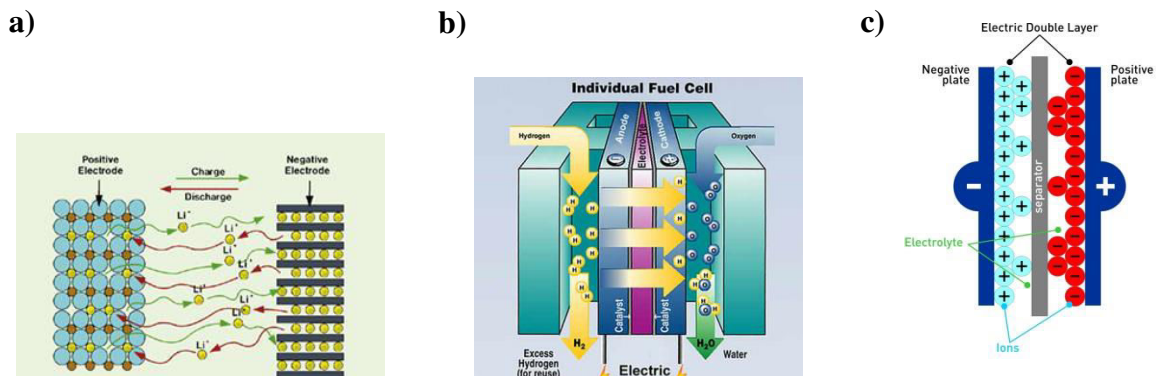


Figure 1.1.a) Batterie lithium – ion b) Pile à combustible c) Supercondensateur [1-2-3]

Les batteries et les piles à combustibles sont des systèmes qui transforment l'énergie chimique en énergie électrique par des réactions d'oxydation et de réduction au niveau des électrodes. Ces systèmes consistent en une anode dans laquelle la réaction d'oxydation a lieu et une cathode où a lieu la réaction de réduction. Enfin un électrolyte assure la conduction des ions dans le système [4]. La différence entre les batteries et les piles à combustibles est liée au système de stockage et conversion de l'énergie. Dans les super condensateurs l'énergie n'est pas délivrée par des réactions d'oxydo-réduction. Les ions à l'interface électrolyte / électrode sont formés et libérés. Cette formation continue des ions à l'interface se traduit dans un flux des électrons dans le circuit externe qui peuvent être utilisés pour alimenter un dispositif électronique. A nos jours, les batteries représentent le système de stockage d'énergie le plus répandu dans le marché. Une représentation graphique utilisée pour comparer la puissance et l'énergie de systèmes électrochimiques est le « Ragone plot ». Le Ragone plot en figure 1.2 montre que d'une part, les piles à combustibles peuvent être considérées comme des systèmes à énergie élevée (Specific energy). D'autre part, les super condensateurs sont considérés

comme des systèmes à haute puissance (Specific power). Les batteries ont des performances en termes de puissance et d'énergie intermédiaires.

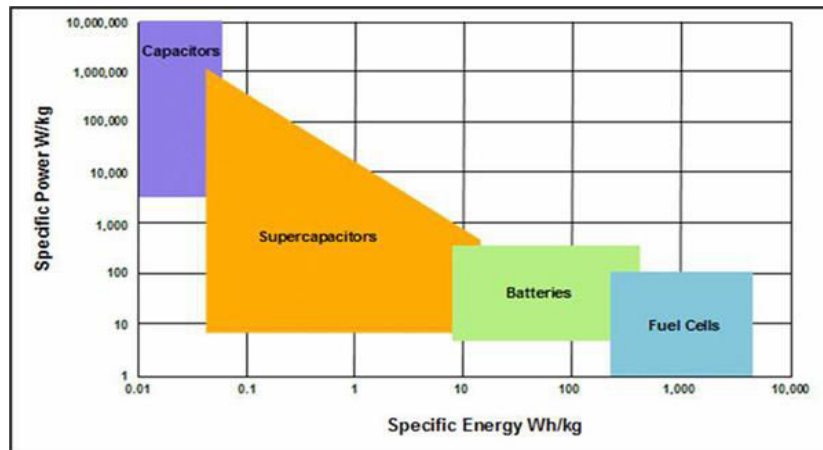


Figure 1.2. Représentation graphique de systèmes de stockage d'énergie électrochimique [5]

## 1.2 Batteries lithium – ion (LIBs)

Le lithium est le métal plus électronégatif (-3.04 V) et l'un des plus léger (poids moléculaire  $\rho = 0.53 \text{ g.cm}^{-3}$ ). Ces caractéristiques font du lithium le matériau idéal pour la production des batteries à haute densité d'énergie. La figure 1.3 montre le processus de charge et décharge dans les LIBs.

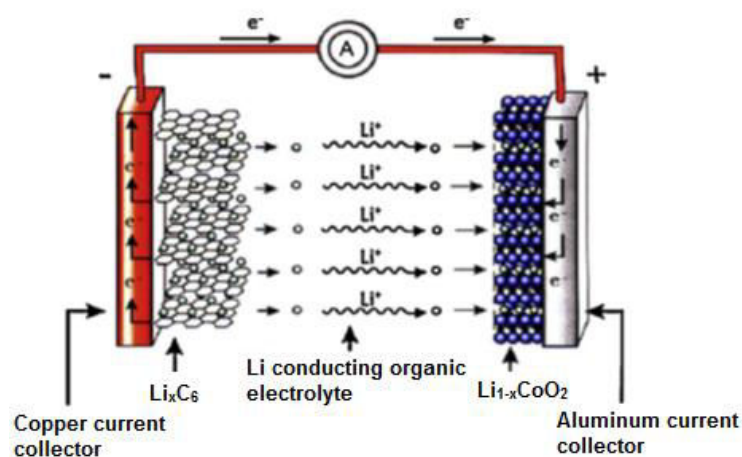


Figure 1.3. Schéma de fonctionnement d'une batterie lithium ion pendant la phase de décharge [6]

La structure classique d'une LIB est composée par une anode en graphite, une cathode formée par une structure lithium oxyde de métal et un électrolyte constitué par un sel de lithium dissous dans un mélange de solvants organiques et imbibé dans un séparateur.

### 1.2.1 Electrodes

Des efforts considérables ont été menés visant à améliorer les performances des électrodes. En fait, la nature de la matière active a une importance cruciale sur la densité d'énergie de la batterie. Le paramètre qui détermine l'énergie d'une batterie est le nombre d'électrons qui peuvent être stockés par unité de volume et de poids dans les électrodes.

#### Electrode positive

L'oxyde de lithium cobalt ( $\text{LiCoO}_2$ ) est une des électrodes positives commercialement la plus utilisée. Des problèmes de sécurité d'utilisation ont cependant limité son développement. La recherche s'est dirigée vers d'autres composants moins dangereux.

- **Stabilisation de la structure cristalline par le remplacement d'un cation :** une série de structures basées sur l'oxyde de lithium nickel manganèse (NMC) [18] ont été proposées. Ils ont une capacité spécifique d'environ 200 mAh/g pour une gamme de tension entre 2.5 et 4.6 V. Une autre structure proposée est l'oxyde de nickel, cobalt aluminium (NCA) [19] qui possède une capacité spécifique d'environ 190 mAh/g.
- **Synthèse de structures poly anioniques de type M-O-X :** une optimisation de potentiel d'oxydo-réduction peut être atteinte en changeant la nature de l'élément X. Le lithium fer phosphate est un des candidats les plus prometteurs grâce à sa capacité quasi constante de 170 mAh/g.

#### Electrode négative

Les électrodes négatives à base de carbone sont de plus en plus performantes avec une capacité spécifique de 350 mAh/g. D'autres systèmes ont été étudiés pour remplacer les électrodes à base de carbone. Les alliages de lithium en sont un exemple. Malheureusement ces alliages présentent des avantages liés à la brusque expansion volumétrique pendant le cyclage qui affecte les propriétés mécaniques ( $\text{LiSn}$  ou  $\text{LiSi}$ ) [23].

### 1.2.2 Séparateur

A partir de l'introduction de LIBs en 1990 différentes études ont été menées sur le séparateur. Les séparateurs à base d'oléfinés (polyéthylène ou polypropylène) ont été développés et sont couramment utilisés dans l'industrie.

### 1.2.3 Electrolyte

La nature et les propriétés de l'électrolyte jouent un rôle important dans les performances d'une batterie lithium ion.

- **Electrolyte liquide** : l'électrolyte liquide est composé par un sel de lithium dissout dans un mélange de solvants organiques. Différents solvants ont été élaborés pour atteindre des propriétés optimales. Généralement deux familles de solvants sont utilisées : les carbonates et les éthers. Grace à sa conductivité électrique élevée le sel  $\text{LiPF}_6$  est le plus utilisé.
- **Electrolyte solide** : Différents systèmes ont été élaborés. Même si les électrolytes solides ont une conductivité ionique très faible, leur utilisation permet de résoudre les problèmes d'électrodéposition de lithium sur les électrodes pendant le cyclage et la formation d'une surface de passivation. L'un des plus utilisés est le LIPON [26], un électrolyte solide à base d'oxidonitruure.
- **Electrolyte gel polymère** : La réalisation des électrodes gel polymère a permis de résoudre des problèmes importants comme : l'élimination de lithium électrodéposé sur les électrodes pendant le cyclage et une amélioration des propriétés mécaniques grâce à l'adaptation de l'électrolyte au changement de volume de l'électrode. Différents systèmes ont été élaborés à base d'éthylène oxyde, de propylène oxyde ou poly fluorure de vinylidene.

### 1.3 Marche batteries lithium – ion

Les batteries lithium-ion (LIBs) ont été introduites dans le marché pour la première fois en 1990. Depuis cette année le marché des LIBs a atteint le 11 milliard de dollars en 2010 et les estimations parlent de 43 milliards de dollars atteint en 2020. Les principaux producteurs mondiaux de LIBs sont situés en Asie. L'Europe et les Etats Unis ne présentent pas de producteurs majeurs dans ce secteur, même s'ils représentent une partie importante du marché des LIBS. Grace à leur potentiel d'énergie élevée les LIBs ont contribué à la croissance des marchés de dispositifs à faible puissance comme les téléphones, les ordinateurs etc. Pour cette raison, de nos jours des milliards de cellules par an sont vendues.

### 1.4 Marché des batteries minces et imprimées

Les batteries minces et imprimées ont une importance de plus en plus croissante dans le marché globale des batteries. Ce type de batteries a été développé pour répondre aux

exigences des systèmes de stockage et de conversion d'énergie flexibles. Elles trouvent leur application idéalement dans des secteurs stratégiques comme la production de « smart card » pour l'élaboration de packaging intelligent. Le marché de la radio-identification (RFID) est un autre secteur prometteur pour l'application des batteries imprimées. La figure 1.4 montre la croissance importante qu'aura le marché des batteries minces et imprimées dans les années à venir.

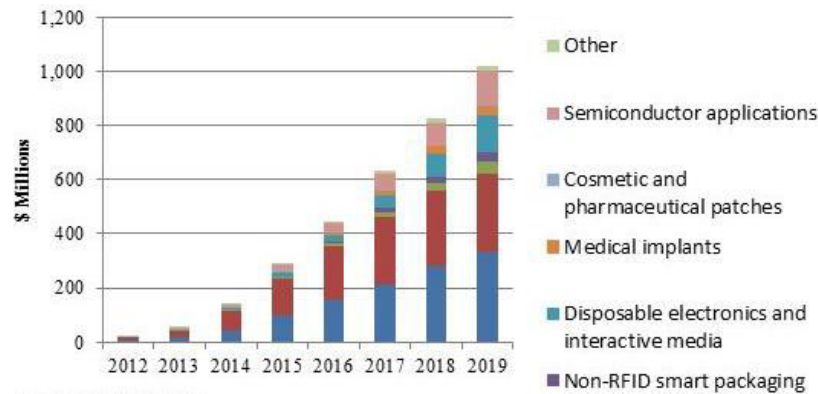


Figure 1.4. Evolution des batteries minces et imprimées [8]

## 1.5.Méthode industrielle de fabrication des batteries lithium ion

Les LIBs sont des batteries à haute énergie qui doivent être manipulées avec attention. Des contraintes mécaniques et des chocs thermiques peuvent créer des dysfonctionnements de la batterie. Pour cette raison, la méthode de production adoptée doit assurer une densité de courant homogène dans toutes les électrodes. L'utilisation de conducteurs électroniques comme le noir de carbone assure cette fonction. Le liant couramment utilisé est le polyfluorure de vinylidene (PVdF) qui permet d'avoir une cohésion entre la structure de l'électrode et le collecteur de courant. Le procédé de d'enduction du collecteur de courant est une étape importante dans la production de LIBs. Cohen et Gutoff [15] décrivent une méthodologie basée sur la rhéologie des suspensions utilisées qui permet d'optimiser la phase de déposition sur le collecteur de courant. Une fois la suspension déposée sur le collecteur de courant, le solvant présent dans la suspension est éliminé par évaporation. Le procédé d'assemblage classique d'une batterie peut être divisé en trois étapes : le bobinage des électrodes et séparateur (winding), l'isolation de la batterie et enfin l'insertion de l'électrolyte.

## 1.6 Procédures alternatives de production : techniques d'impression

Dans le domaine de l'électronique imprimée différentes techniques d'impression ont été utilisées avec des résultats prometteurs en termes de reproductibilité et qualité. La plupart des études présentées dans la littérature utilisent des techniques conventionnelles comme le jet d'encre, la sérigraphie et la flexographie.

## 1.7 Impression des batteries

Dans la dernière décennie différentes techniques ont été testées afin de concevoir une production de masse de batteries à bas coût. Une alternative concrète a été trouvée dans l'impression par sérigraphie. Cette technique assure une répétabilité optimale et une qualité comparable aux autres techniques d'élaboration des batteries conventionnelles. La potentialité de cette technique est en cours d'étude par la plupart des chercheurs, pour élaborer des batteries primaires et secondaires imprimées. Un exemple de batterie non rechargeable imprimée a été proposé par George et al. [68]. Ils ont développé une batterie zinc alcaline. Une anode contenant le Zinc et une cathode constituée par le dioxyde de manganèse ont été imprimées sur des collecteurs de courant en argent et assemblées en une cellule en utilisant un séparateur papier et un électrolyte à base d'hydroxyde de potassium (figure 1.5).

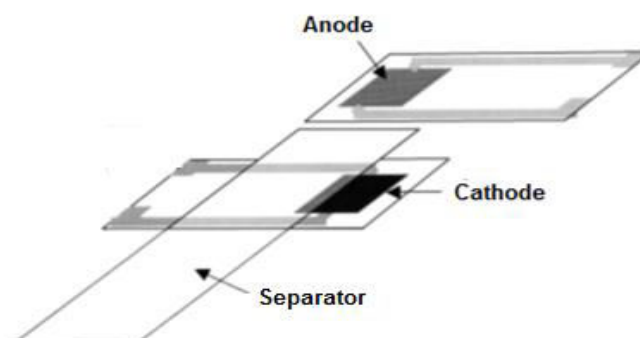


Figure 1.5. Stratégie de fabrication d'une cellule complète [68]

Le prototype développé a montré de bonnes performances correspondant à 90% de la valeur théorique lorsqu'un taux élevé de graphite est utilisé pour améliorer les propriétés électriques. En revanche la stratégie d'assemblage ne résout pas les problèmes éventuels de fuite d'électrolyte et de stress mécanique. Une batterie lithium-ion imprimée en sérigraphie a aussi été développée par Rouault et al [99]. La batterie est ainsi constituée par une cathode

ayant une structure d'oxyde métallique ( $\text{LiNi}_{1/3}\text{Mn}_{1/3}\text{Co}_{1/3}\text{O}_2$ ) et une anode en graphite. Les deux électrodes ont été imprimées sur les deux collecteurs de courant en Al et Cu respectivement (figure 1.6).

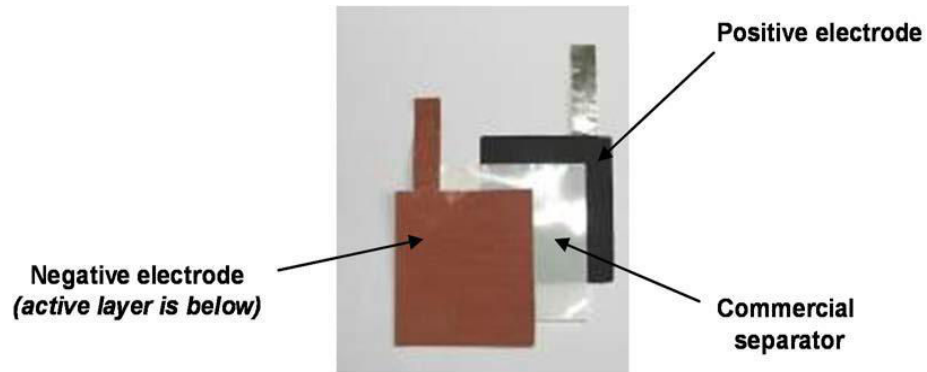


Figure 1.6. Electrode positive et négatives imprimées sur un foil en Al et Cu respectivement [99]

Les batteries imprimées ont montré des capacités spécifiques comprises entre 57.6 mAh et 64.0 mAh correspondant à environ 80- 90% de la capacité nominale.

## **2. Elaboration et caractérisation d'une électrode négative**

Ce chapitre, concerne l'élaboration de l'électrode négative. En premier lieu, des encres contenant les composants actifs ont été formulées et l'influence des différents constituants a été étudiée par une analyse rhéologique. Une deuxième étude rhéologique a été menée en faisant des tests en mode oscillatoire et thixotropique pour mieux comprendre la structure des encres formulées. Dans la deuxième partie de ce chapitre, l'élaboration et la caractérisation des électrodes sont présentées. Des mesures ont été réalisées pour caractériser la structure des électrodes imprimées et ensuite des analyses électrochimiques ont permis d'étudier les performances des électrodes. La dernière partie de ce chapitre est dédiée à la proposition de deux stratégies pour améliorer les performances des électrodes, l'une basée sur une étape de calandrage pour densifier les électrodes et l'autre, sur l'introduction d'un additif et l'utilisation d'un électrolyte binaire pour améliorer les performances.

### **2.1 Caractérisations rhéologiques**

Des encres de différentes concentrations ont été élaborées pour trouver la formulation optimale compatible avec la technique d'impression sérigraphique. La concentration des encres est exprimée en pourcentage massique de matière sèche (Ms). Les concentrations des composants sont exprimées en fonction de la matière sèche. Après une première étude rhéologique une valeur de Ms correspondant à 40 % a été sélectionnée comme concentration optimale. Une étude rhéologique a été réalisée pour approfondir l'influence des différents composants : caboxymethylcellulose (CMC), microfibrille de cellulose (MFC) et graphite (GP).

Des mesures en écoulement ont été réalisées pour étudier le comportement des encres sous l'application d'un taux de cisaillement croissant. Comme le montre la figure 2.1, les encres présentent un comportement rhéofluidifiant et la concentration des MFC influence l'évolution rhéologique des encres. Les MFC jouent un rôle d'épaississant en augmentant la viscosité apparente des encres.

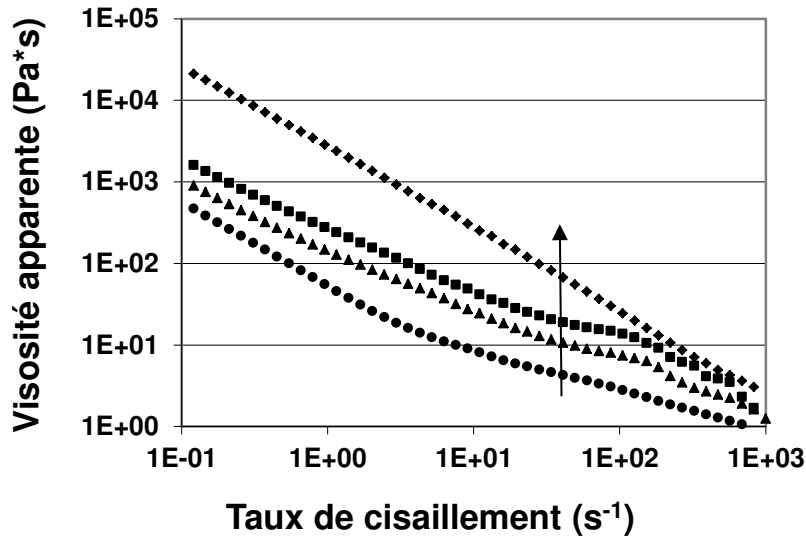


Figure 2.1. Evolution de la viscosité apparente en fonction de taux de cisaillement pour une concentration des MFC correspondant à : 0% (●), 1% (▲), 1.5% (■) et 2% (◆)

Une concentration critique correspondant à 1.5 % de MFC a été définie. Au-dessus de cette concentration les valeurs de viscosité augmentent fortement. L'encre contenant 1 % de MFC a été sélectionnée comme la formulation optimale qui répond le mieux aux contraintes rhéologique imposés par le procédé d'impression sérigraphique. Après avoir développé un protocole de dispersion et d'homogénéisation spécifique à l'encre de l'électrode négative, une étude thixotrope et oscillatoire ont été réalisées pour mieux comprendre la structure de l'encre sélectionnée. Les mesures thixotropiques ont montré une boucle d'hystérésis à des taux de cisaillement inférieur à  $10 \text{ s}^{-1}$ . Cette boucle d'hystérésis est due à la capacité de l'encre à récupérer son état initial après sa déstructuration. La concentration des MFC et CMC influence la capacité de l'encre à récupérer cet état. Les expériences réalisées ont permis aussi de trouver un taux de cisaillement correspondant à  $0.2 \text{ s}^{-1}$ . Au-dessus de cette valeur l'encre présente un comportement rhéofluidifiant. Au contraire en dessous, il devient épaississant. Le même comportement a été montré dans la littérature pour des encres sérigraphiques [129]. Des mesures en mode oscillatoire ont aussi été effectuées pour mieux comprendre les propriétés viscoélastiques de l'encre et les forces d'interaction entre les composants. Les modules élastique et visqueux ont été mesurés en fonction de la fréquence d'oscillation. Une augmentation de ces deux grandeurs a été mise en évidence lorsque la fréquence de sollicitation augmente. Cette dernière peut être associée à l'influence de la fréquence sur la formation d'un réseau entre les particules de graphite. Le module élastique présente une valeur plus grande que celle du module visqueux sur la toute la plage de

fréquences considérée. Ce comportement est typique d'une encre sérigraphique dont le caractère élastique est prédominant sur le caractère visqueux.

## 2.2 Caractérisation physique

Les encres formulées ont été imprimées par sérigraphie sur un substrat cellulosique sélectionné pour ses propriétés physiques optimales pour l'impression en sérigraphie. Pour assurer une bonne impression et une bonne répétabilité, les paramètres d'impression comme la vitesse d'impression, la force de la racle et la distance écran - substrat ont été optimisés. Les électrodes ainsi imprimées ont été caractérisées par différentes techniques. Des images MEB et FEG ont été réalisées pour analyser la structure des électrodes et les interactions entre les composants.

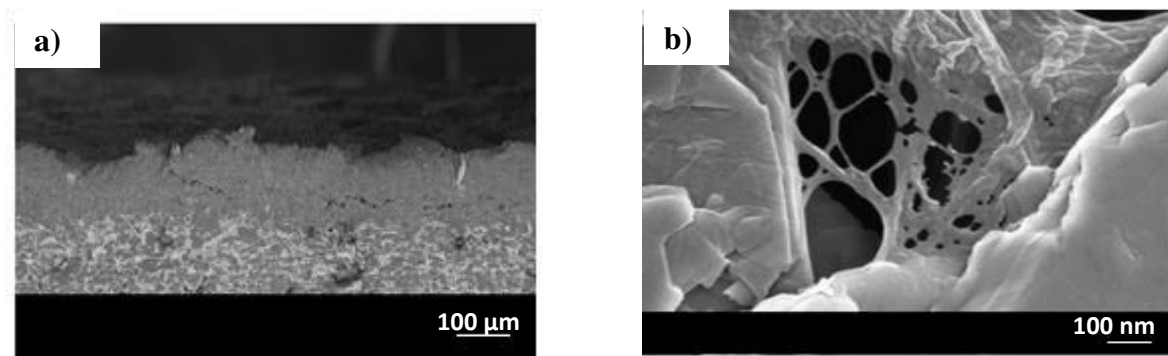


Figure 2.2. Images au FEG de l'électrode négative. a) Section transversale de l'électrode à 100X. b) Structure de l'électrode à 50 kX.

La figure 2.2. montre la section transversale de l'électrode. Deux couches sont mises en évidence : la couche inférieure représente le séparateur cellulosique et la couche supérieure au dépôt de l'électrode. La figure 2.2.b permet de visualiser les MFCs dans l'électrode imprimée. Ces derniers jouent un rôle de liant en créant des interactions entre les particules de graphite. Cette structure en « toile d'araignée » permet d'améliorer les propriétés mécaniques de l'électrode. Par la suite une série de mesures physiques et électriques a été réalisée. La porosité calculée des électrodes est de  $70 \pm 3 \%$ , cette valeur est conforme aux données de la littérature pour des électrodes imprimées par sérigraphie [98]. La conductivité électronique mesurée est de  $69 \pm 19 \text{ S/m}$  et le grammage déposé de l'électrode négative est de  $49 \pm 2 \text{ g/m}^2$ .

## 2.3 Caractérisation Electrochimiques

Des mesures voltammétrique et galvanostatique ont été réalisées pour évaluer les propriétés électrochimiques et les performances des électrodes. L'étude voltammétrique a permis de détecter à 0.43 V le pic de réduction caractéristique du graphite associé à la formation de la surface de passivation (SEI layer). Deux autres pics de réduction ont aussi été mesurés correspondant à la formation du composé  $\text{LiC}_6$  à 0.16 V. Pour ce qui concerne de l'étape d'oxydation, deux pics ont été détectés correspondant aux procédés de déintercalation du lithium. Les mesures galvanostatiques ont été réalisées entre 0.02 V et 1.2 V. L'évolution de la capacité spécifique a été étudiée en fonction de nombre de cycles (figure 2.3). Une capacité initiale de 100 mAh/g pour les 5 premiers cycles a été mesurée pour une valeur de régime de courant correspondant à C/10. Cette valeur n'est pas conforme à la valeur théorique du graphite (372 mAh/g). Une capacité irréversible de 142 mAh/g, correspondant à la formation de la couche de passivation (SEI layer), a été mesurée au premier cycle. Cette valeur est plus élevée que les valeurs rencontrées dans la littérature (entre 20 et 100 mAh/g). Ces performances en retrait peuvent être dues à une porosité trop élevée de l'électrode (70 %). En effet, cette dernière contribue à la réduction de la conductivité électronique de l'électrode, En ce qui concerne l'efficacité coulombique une augmentation progressive a été mesurée à partir de 38% au premier cycle. Cette valeur faible est due à la formation du « SEI layer » qui nécessite du temps pour former une surface stable. Pour cette raison l'efficacité coulombique n'atteint pas une valeur proche de 100 % au deuxième cycle.

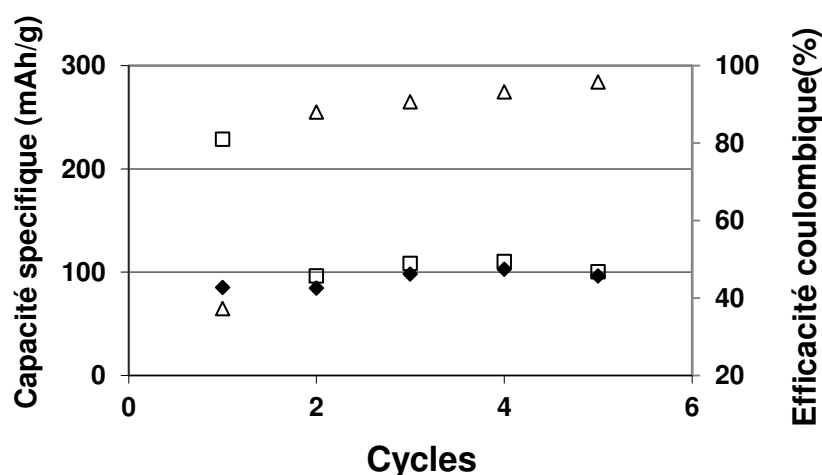


Figure 2.3. Capacité spécifique de charge (■) / décharge (□) et efficacité coulombique (Δ) en fonction de nombre de cycles

## 2.4 Stratégies d'amélioration

### 2.4.1 Calandrage

Comme expliqué dans le paragraphe 2.4 une porosité trop élevée peut affecter la conductivité électronique et les performances des électrodes. Pour cette raison une étape de calandrage a été proposée pour améliorer les résultats obtenus. Les électrodes ont été calandrées à quatre charges linéiques différentes: 1 – 3 – 33 et 73 kN/m et les propriétés physiques et électrochimiques ont été analysées. Comme le montre le tableau 2.1 une diminution progressive de la porosité a été observée lors de la compression de l'électrode. L'évolution de la porosité se stabilise à partir d'une charge linéique de 3 kN/m. Le calandrage permet ainsi d'améliorer le contact entre les particules. Cela se traduit par une augmentation de la conductivité électronique de 69 S/m jusqu'à 619 S/m. La rugosité de surface et l'épaisseur sont aussi fortement réduites par l'étape de calandrage.

Table 2.1 Caractérisation physique des électrodes calandrées en fonction de la charge linéique

		<b>M<sub>s</sub> (GP_CMC_MFC) / 40(97_2_1)</b>				
		<b>Charge linéique (kN/m)</b>				
		<b>-</b>	<b>1</b>	<b>3</b>	<b>33</b>	<b>73</b>
Épaisseur couche déposée	μm	71±3	38±1	35±2	33±2	32±2
Conductivité électronique	S/m	69±19	145±54	177±45	278±77	619±57
Porosité	%	70±3	39±4	40±5	36±3	34±3
Rugosité de surface (S <sub>a</sub> )	μm	11.9±0.4	9.7±0.5	7.4±1.2	7.3±1.1	6.1±0.5

Des analyses électrochimiques ont été réalisées pour évaluer l'effet du calandrage sur les propriétés des électrodes pendant le cyclage. Une augmentation de la capacité spécifique a été mesurée avec la charge linéique imposée. La valeur maximale est atteinte pour la charge linéique de 73 kN/m. La capacité spécifique mesurée est de 315 mAh/g. Comme indiqué dans la figure 2.4, une réduction de la polarisation de l'électrode est mise en évidence pour un

potentiel inférieur à 0.2 V, correspondant à la phase d'intercalation. En fait l'amélioration des contacts entre les particules de graphites permet de réduire les problèmes de polarisation.

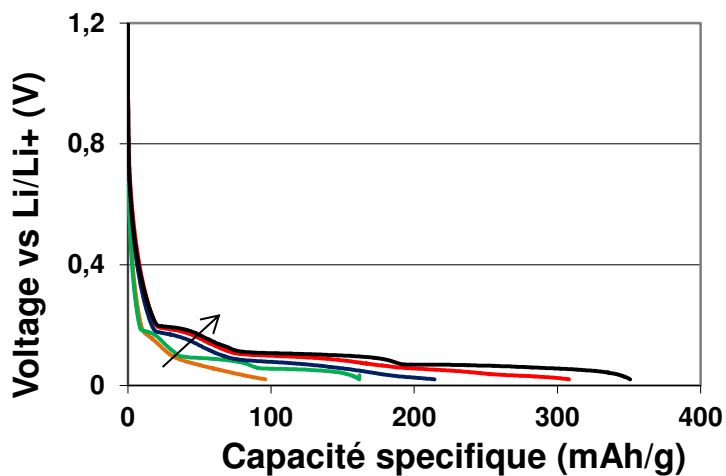


Figure 2.4. Profil de décharge en fonction de la charge linéique : 0 kN/m (-), 1 kN/m (-), 3 kN/m (-), 33 kN/m (-) and 73 kN/m (-)

#### 2.4.2 Optimisation de SEI layer

La couche de passivation (SEI layer) est un des phénomènes qui affecte les performances de l'électrode négative. Ce paramètre devient plus important lorsqu'une cellule complète est élaborée. Dans ce cas une couche de passivation trop épaisse introduit une consommation excessive des ions lithium qui pénalise les performances de la batterie. Dans cette étude deux stratégies ont été proposées :

- 1) L'utilisation d'un électrolyte binaire qui ne contient pas de propylène carbonate (PC) : Eli et al. [35] ont montré comment le groupe méthylène dérivé de la dégradation du PC sur la surface du graphite empêche la formation d'une surface de passivation stable.
- 2) L'introduction d'un additif comme le mono fluore éthylène carbonate (<sup>1</sup>FEC) : ce dernier polymérise sur la surface du graphite, en formant une couche protectrice qui empêche d'éventuelles réactions entre électrolyte et l'électrode [165].

La figure 2.5 montre les profils de décharge obtenus après formation de la couche de passivation. Une amélioration de la capacité spécifique a été obtenue avec l'utilisation d'un électrolyte binaire et après introduction du <sup>1</sup>FEC. La valeur maximale de 322 mAh/g a été mesurée pour l'électrolyte binaire, correspondant à une augmentation de l'efficacité coulombique au premier cycle de 67%.

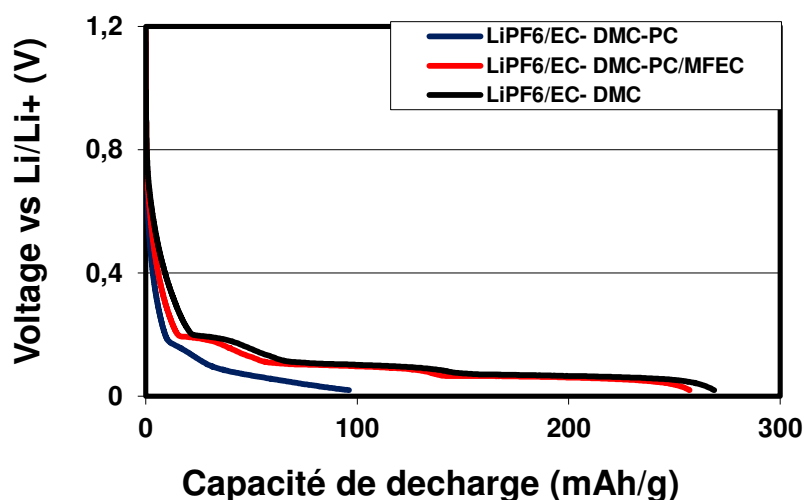


Figure 2.5. Profil de décharge en fonction de la composition de l'électrolyte après le 1er cycle

### 3. Elaboration et caractérisation d'une électrode positive

Dans ce chapitre des électrodes positives ont été élaborées en suivant la même procédure décrite pour l'électrode négative. Des encres contenant des dérivées de la cellulose (MFC et CMC) ont été formulées. Un agent conducteur a été ajouté pour améliorer la conductivité électronique de la matière active. Une étude rhéologique a été menée afin de trouver une formulation optimisée pour le procédé d'impression sérigraphique et pour déterminer l'influence des différents composants. Comme pour l'électrode négative, l'utilisation du procédé de calandrage a été proposée pour améliorer les résultats obtenus.

#### 3.1 Caractérisation rhéologique

Une première étude rhéologique a été faite en modifiant le pourcentage de matière sèche afin de définir une formulation adaptée au procédé d'impression sérigraphique. Le lithium fer phosphate a été sélectionné comme matière active pour ces propriétés en termes de sécurité pendant la phase d'utilisation et sa stabilité pendant le cyclage. L'ajout de noir de carbone (CB) est nécessaire pour améliorer ses propriétés électroniques. Les agents cellulosiques liant et dispersant (CMC et MFC) ont été fixés à 3 % pour maximiser le contenu de matière active et d'agent conducteur. L'étude rhéologique a permis de choisir la concentration de 40 % en Ms comme valeur optimale pour la méthode d'impression sérigraphique. Une fois fixée la

concentration de matière sèche, une deuxième étude a été réalisée pour analyser l'impact de l'agent conducteur sur les propriétés électrochimiques et rhéologiques des encres formulées. Comme indiqué dans le tableau 3.1 les encres formulées présentent une conductivité électronique appréciable au-dessus de 17 % de CB introduit. D'un point de vue rhéologique, le noir de carbone joue un rôle d'épaississant en augmentant la viscosité apparente et la contrainte de cisaillement. Ce fait peut être expliqué par une modification des interactions entre les particules et le noir de carbone lorsque la concentration de CB est augmentée.

Table 3.1 Influence de CB sur les propriétés rhéologiques (viscosité et contrainte de cisaillement) des encres formulées

<b>Ink</b> <b>M<sub>s</sub>(LFP_CB_CMC_MFC)</b>	<b>Viscosité</b> <b>à <math>\dot{\gamma} = 1 \text{ s}^{-1}</math></b>	<b>Contrainte</b> <b>at <math>\dot{\gamma} = 1 \text{ s}^{-1}</math></b>	<b>Conductivité</b> <b>électronique</b>
	Pa·s	Pa	S/m
40(90_7_2_1)	9	10	pas mesurable
40(80_17_2_1)	25	29	17±3
40(70_27_2_1)	56	64	35±2

L'encre contenant 27% de CB a été choisie car elle assure une bonne conductivité électronique et satisfait aux contraintes rhéologiques imposées par la méthode d'impression sérigraphique. Une étude rhéologique en écoulement a été réalisée en suivant le même protocole utilisé pour l'électrode négative. Les résultats obtenus montrent un comportement rheo-fluidifiant qui peut être associé à une déstructuration des agglomérats composés par les MFC, CMC et CB.

Une étude thixotropique a aussi été réalisée. Tout d'abord, un taux de cisaillement faible est imposé pour un temps fixé afin d'homogénéiser l'encre. En suite un taux de cisaillement élevé est imposé pendant 5 minutes pour assurer la déstructuration totale de l'encre. Enfin, une dernière étape à taux de cisaillement constant est appliqué jusqu'à la récupération totale de la structure de l'encre. Dans cette expérience cinq taux de cisaillement ont été choisis pour cette dernière étape afin d'étudier le comportement rhéologique de l'encre pendant la phase de récupération de la structure sous différentes conditions. La figure 3.1 montre les résultats obtenus. Une récupération de la structure de l'encre a été observée à différents taux de cisaillement. Cette récupération est plus rapide lorsque l'on augmente le taux de cisaillement imposé mais dans tous les cas la récupération de la structure est toujours très rapide. Ce

phénomène peut être associé aux faibles interactions entre les composants à cause de l'état rhéofluidifiant de l'encre dans la plage des taux de cisaillement sélectionnés.

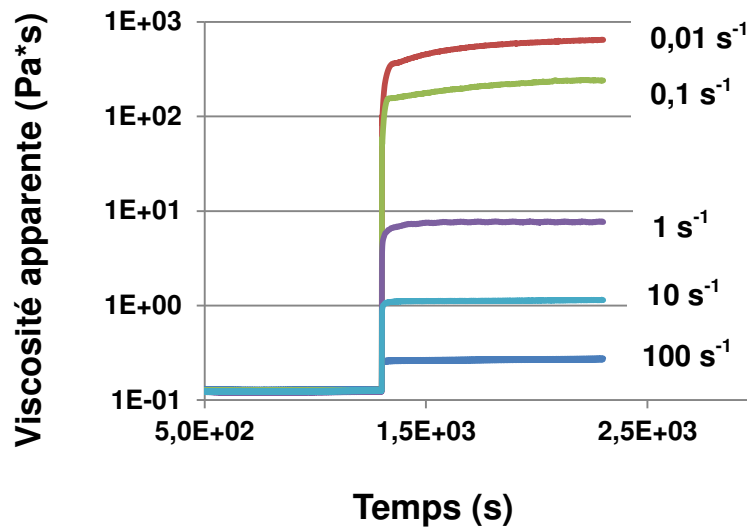


Figure 3.1. Test thixotropique à différents taux de cisaillement

Les mesures en mode oscillatoire ont montré une dépendance du module élastique et visqueux en fonction de la fréquence avec un comportement typique de ces encres dont le caractère élastique est prédominant par rapport au caractère visqueux.

### 3.2 Caractérisation physique

Les encres formulées ont été imprimées par sérigraphie. Une étude présente l'évolution de l'épaisseur de la couche imprimée déposée en fonction du nombre d'impressions réalisées (impression multicouche). L'épaisseur atteint une valeur maximale de 80  $\mu\text{m}$  après 3 passages. Cette valeur maximale est directement liée aux paramètres d'impression comme l'épaisseur de l'émulsion appliquée sur l'écran ou sa porosité. Dans ce cas aussi des images MEB et FEG ont été réalisées pour visualiser la surface des électrodes et les interactions entre les composants. La figure 3.2.a montre la flexibilité de l'électrode imprimée. La figure 3.2.b montre le rôle de liant assuré par les MFCs. Les particules de LFP sont connectées entre elles par l'intermédiaire d'un réseau créé par les MFCs (flèche rouge). Les particules plus claires représentent le noir de carbone qui entoure les particules de LFP (flèche bleu).

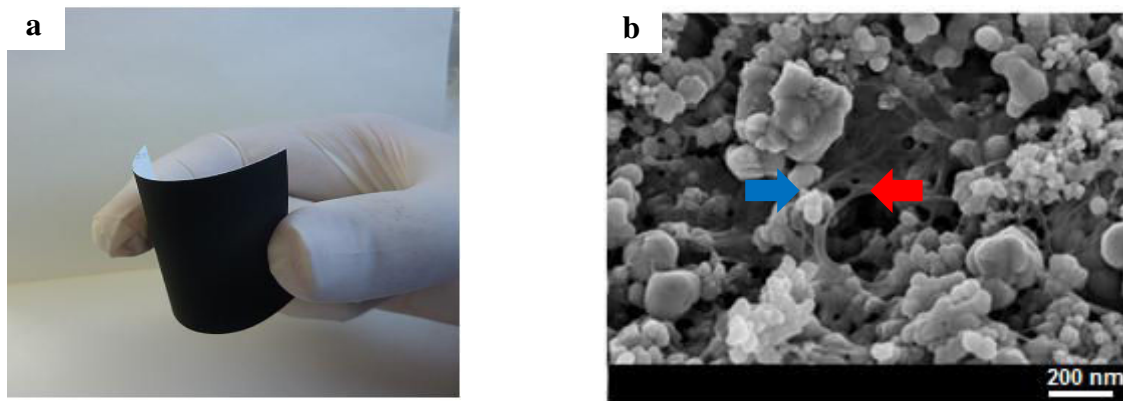


Figure 3.2.a) Electrode imprimée flexible. b) Images FEG : Interactions entre MFC et LFP (flèche rouge), et interactions entre CB et LFP (flèche bleu)

Les électrodes ont été ensuite caractérisées par différentes techniques afin d'évaluer l'épaisseur de la couche imprimée, la porosité, la conductivité électronique et la rugosité de surface. L'électrode présente une épaisseur de la couche imprimée de  $31 \pm 3 \mu\text{m}$ . Grâce à l'ajout de 27 % de noir de carbone, l'électrode présente une conductivité électronique appréciable de  $35 \pm 2 \text{ S/m}$ .

### 3.3 Caractérisation électrochimique

Des mesures de voltammétrie ont été faites pour évaluer les pics d'oxydation et de réduction du LFP. Les résultats obtenus sont comparables aux données reportées dans la littérature. Ils sont caractérisés par un pic d'oxydation, correspondant au procédé d'extraction des ions lithium à 3.6 V et par un pic de réduction correspondant au procédé d'insertion des ions lithium à 3.2 V [188]. Des tests galvanostatiques ont ensuite été réalisés à différents régimes de courants. Les résultats montrent que l'électrode présente une capacité spécifique de 143 mAh/g à faible régime de courant ( $C/10$ ). Cette valeur est cohérente avec la capacité nominale du LFP (150 mAh/g). La rétention de la capacité est aussi performante puisqu'une valeur de 70 % a été obtenue à un régime de courant de  $C$  (figure 3.3). Pour ce qui concerne la stabilité aux cyclages, des tests galvanostatiques ont été réalisés à un régime de courant constant de  $C/5$ . Les électrodes montrent une capacité spécifique quasi constante de 120 mAh/g pour plus de 100 cycles.

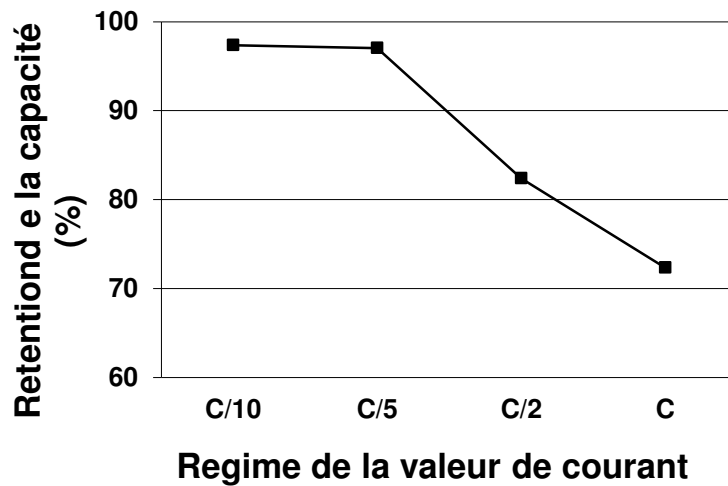


Figure 3.3. Rétention de la capacité à différents régimes de la valeur de courant

### 3.4 Calandrage

Une étape de calandrage a aussi été envisagée pour améliorer les performances de l'électrode comme dans le cas de l'électrode négative (la même procédure a été réalisée). Les résultats montrent que, dans ce cas l'étape de calandrage, peut affecter les performances de l'électrode pendant le cyclage, surtout à des charges linéiques élevées. Par exemple à C/10 la capacité spécifique mesurée pour une charge linéique de 73 kN/m est passé à 120 mAh/g. Cette valeur correspond à une diminution de 15 % de la capacité comparée à la valeur de l'électrode non calandree. Cette perte de capacité peut être due à l'endommagement du substrat lors de la mise en pression de l'électrode pendant la phase de calandrage.

## **4. Elaboration et caractérisation d'une cellule complète**

Cette partie est dédiée à la réalisation d'une cellule complète en partant des résultats obtenus pour les électrodes. La première partie est focalisée sur l'élaboration d'une stratégie d'assemblage basé sur l'impression recto / verso du séparateur cellulosique. Dans la deuxième partie une caractérisation physique et électrochimique ont été réalisées pour valider la stratégie proposée. Les résultats obtenus ont été ensuite comparés avec les données obtenues pour des cellules élaborées de manière conventionnelle.

### **4.1 Stratégies D'assemblage**

Dans la littérature, deux stratégies sont proposées pour l'élaboration de batteries imprimées : une stratégie par empilement et une stratégie coplanaire. La stratégie par empilement consiste dans l'empilement de plusieurs couches constituant la batterie. Cette approche permet de réduire la distance de transport moyen d'ions lithium dans la batterie mais elle comporte l'impression d'un nombre élevé de couches. Pour ce qui concerne la stratégie d'assemblage coplanaire, l'impression de couches est fortement réduite mais la distance de transport moyen est plus élevée. La solution proposée dans ce travail cherche de combiner les avantages des deux techniques. Elle consiste en l'impression recto / verso du séparateur cellulosique. Sur la face recto les éléments constituant l'électrode négative sont imprimés et par simple retournement du séparateur les éléments constituant l'électrode positive peuvent être à leur tour imprimés sur la face opposé. Cette stratégie permet de réduire le nombre de couches imprimées car le substrat d'impression est utilisé en même temps comme séparateur. En plus l'impression de deux faces assure une distance de transport moyen réduite comme dans le cas de l'assemblage par empilement. Une étape d'intégration des collecteur de courant pendant la phase d'impression a aussi été proposée pour réduire les temps de production (figure 4.1)

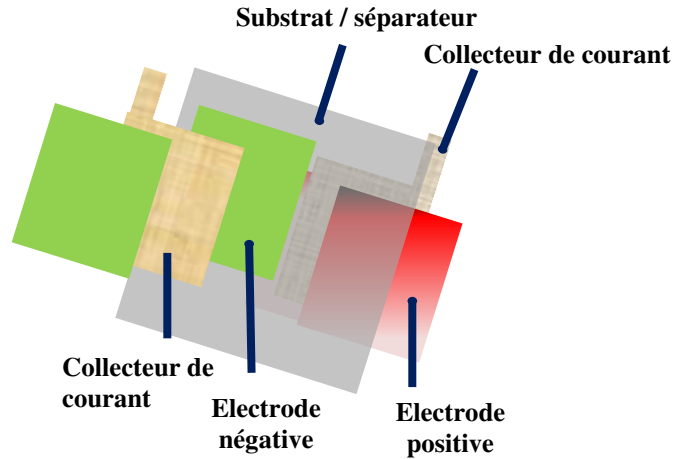


Figure 4.1. Technique d'impression recto / verso avec collecteurs de courants intégrés

Une cellule complète a été réalisée selon la stratégie décrite. Le contenu des matières actives a été optimisé afin de compenser la différence de capacité spécifique entre la GP et le LFP. La cellule fabriquée a une épaisseur totale de  $215 \pm 9 \mu\text{m}$ . Le séparateur cellulosique utilisé a un grammage de  $120 \text{ g/m}^2$  et une épaisseur de  $143 \pm 2 \mu\text{m}$  pour assurer une bonne isolation entre l'électrode positive et négative. Des mesures d'arrachage ont été réalisées pour évaluer la force d'adhésion entre les électrodes et les collecteurs de courant. Les résultats trouvés sont comparables aux données de la littérature. Une force d'adhésion de  $64 \pm 1 \text{ J/m}^2$  a été mesurée pour l'électrode positive. Cette valeur est environ trois fois plus grande que celle mesurée pour l'électrode négative. La raison de cette différence peut être expliquée par l'ajout de noir de carbone dans l'électrode positive. En fait le CB forme des interactions avec les particules de LFP en augmentant la force d'adhésion [205].

## 4.2 Caractérisation électrochimique

Une étude électrochimique a été réalisée pour évaluer les performances de la cellule complète. L'électrolyte binaire testé pour l'élaboration de l'électrode négative a été utilisé aussi dans ce cas car il assure une rétention de la capacité plus élevée comparé à l'électrolyte ternaire. Les résultats obtenus ont montré une stabilité des pics d'oxydation et de réduction dans le temps à différents régimes de valeurs de courant. Une capacité spécifique de  $80 \text{ mAh/g}$  a été mesurée au première cycle à  $C/10$ . La figure 4.2 montre l'évolution de la capacité en fonction de nombre de cycle à  $C/10$ . Une réduction progressive de la capacité spécifique a été observée, due probablement à la porosité élevée des électrodes.

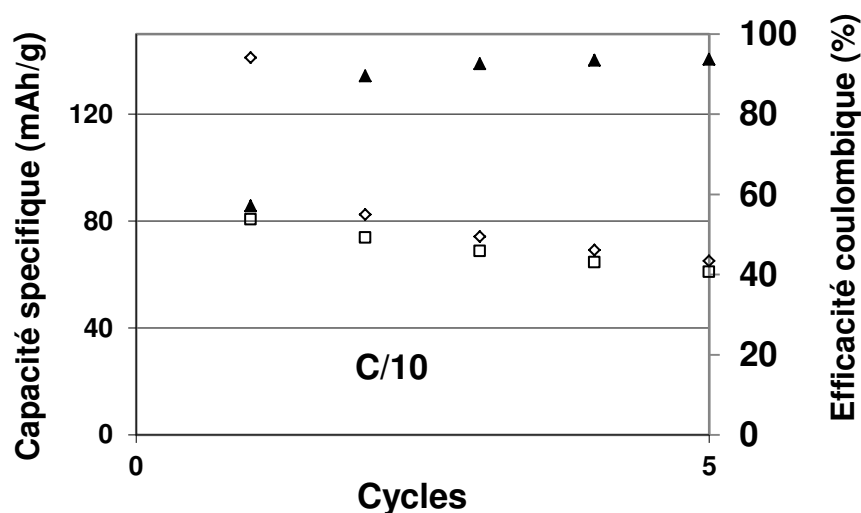


Figure 4.2. Capacité spécifique de charge (◇) et décharge (□) et efficacité coulombique (△) en fonction de nombre de cycle à C/10

### 4.3 Etude comparative

Des études ont été réalisées pour comparer les résultats obtenus pour l'impression recto / verso avec des techniques d'assemblage plus conventionnelles. Différents paramètres ont été modifiés pour vérifier leur impact sur les performances de la cellule. La première étude réalisée a eu comme objectif la mise en relation de la configuration de mesure utilisée et les performances de la cellule. Deux type de cellules ont été assemblés, l'une selon une configuration « Swagelok® » et l'autre « pouch cell ». Les résultats trouvés sont comparables. Cela montre qu'il n'y a pas de dépendance de la configuration de mesure sur les performances de la cellule. Une étape de calandrage a été proposée pour densifier les électrodes. Les résultats obtenus ont montré que la pression appliquée affecte fortement les performances. Des particules de GP peuvent migrer à travers le séparateur vers l'électrode positive en produisant des courts circuits locaux qui affectent les performances de la cellule. Enfin un séparateur cellulosique à plus faible grammage a été utilisé pour vérifier si la nature du séparateur peut modifier les performances. Vu la porosité élevée (80%) du séparateur, deux techniques d'assemblage ont été utilisés. Dans le premier cas, l'électrode positive et négative ont été imprimées sur deux substrats et empilées pour avoir une cellule complète (figure 4.3.a). Dans le deuxième cas, la même technique a été utilisée mais un séparateur commercial (Celgard®) a été ajouté pour assurer une isolation électrique optimale entre les électrodes (figure 4.3.b)

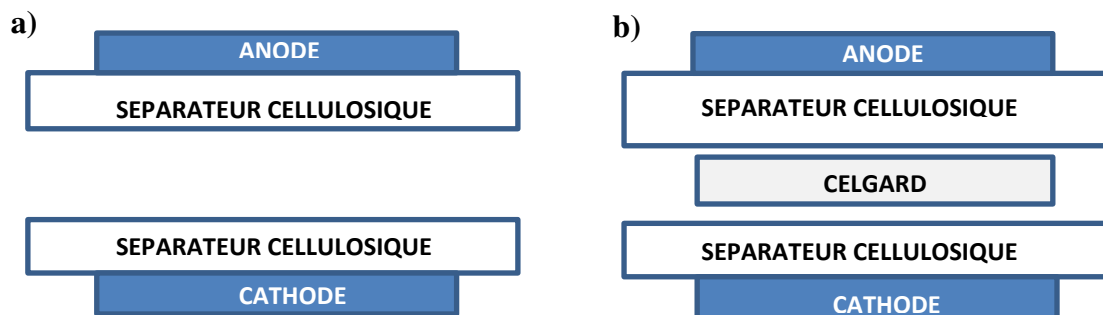


Figure 4.3. Configuration d'assemblage par empilement. a) Le séparateur cellulosique joue le rôle de substrat d'impression de l'électrode et en même temps il a le rôle de séparateur de la cellule. b) Assemblage par empilement avec insertion d'un séparateur Celgard® pour améliorer l'isolation électrique entre les électrodes.

Une étude galvanostatique a été réalisée pour évaluer les performances des deux stratégies d'assemblage à une valeur de régime de courant correspondant à  $C/5$ . Une capacité spécifique de 14 et 20 mAh/g a été mesurée pour les deux stratégies d'assemblages proposées. Ces valeurs montrent que la perte de capacité n'est pas reliée à l'insertion d'un séparateur mais à des phénomènes locaux à l'intérieur des électrodes qui influencent les performances de la batterie. Ces phénomènes semblent être prédominants au 1<sup>er</sup> cycle car une perte de capacité significative a été mesurée.

## 5. Conclusion

L'objectif de ce travail a été la fabrication de batteries lithium-ion en proposant de nouvelles solutions pour résoudre deux aspects critiques qui affectent la production des batteries lithium-ion : 1) La substitution des produits toxiques couramment utilisés (polyfluorure de vinylidene (liant) et le N-méthyl-2-pyrrolidone (solvant)). 2) L'utilisation des techniques de production de masse et à bas coût. La stratégie proposée pour faire face à ces deux aspects a été la combinaison de deux solutions différentes : l'utilisation de produits bio-sourcés avec des bases aqueuses et la fabrication avec des techniques d'impression conventionnelles. L'idée innovante de ce travail réside dans le couplage de ces deux techniques pour fabriquer des batteries lithium-ion composées par des constituants non toxiques et produits à partir d'une technique d'impression comme la sérigraphie. La deuxième innovation dans ce travail a été le remplacement de la technique conventionnelle d'assemblage par une technique d'impression recto / verso avec intégration des collecteurs de courant. Pour mener à bien cette étude, il a été nécessaire de développer un protocole de formulation d'encres à base aqueuse constituées de dérivées de cellulose, compatibles avec le procédé d'impression sérigraphique et présentant

des propriétés optimales pour la production de batteries lithium-ions. Pour chaque électrode de la batterie une encre a été spécifiquement formulée et caractérisée d'un point de vue rhéologique. Ces encres ont ensuite été imprimées sur un séparateur cellulosique et ont permis l'obtention d'électrodes imprimées et flexibles. Ces électrodes ont été caractérisées d'un point de vue physique et électrochimique. Les résultats ont démontré que la technique d'impression par sérigraphie pouvait être utilisée pour remplacer les techniques d'enduction classique comme le « blade coating ». Deux stratégies ont été proposées pour améliorer les performances des électrodes fabriquées. La première consiste en une étude sur les effets du calandrage avec l'objectif d'améliorer la conductivité électronique des électrodes. Ceci s'est traduit par une réduction de la porosité de 70 à 40%. Les résultats ont montré que cette étape de calandrage est fondamentale pour améliorer les performances, spécialement celles de l'électrode négative. En effet, il a été possible d'augmenter la capacité spécifique de 90 à 315 mAh/g. Cette valeur n'est pas éloignée de la valeur théorique du graphite (350 mAh/g). La deuxième stratégie étudiée a été l'introduction d'additifs dans l'électrolyte et l'utilisation d'électrolytes binaires pour résoudre le phénomène d'exfoliation qui affecte l'électrode négative à base de graphite, ceci a permis d'améliorer sensiblement les performances des électrodes. La dernière étape de ce travail a été la fabrication d'une batterie lithium-ions imprimée en utilisant la stratégie d'impression recto / verso du séparateur avec l'intégration des collecteurs de courant pendant la phase d'impression. Cette nouvelle technique permet de réduire le nombre des impressions nécessaires en diminuant ainsi la masse totale et le volume occupé par la batterie. Ces deux paramètres sont fondamentaux pour maximiser la densité d'énergie spécifique et volumique de la batterie. Les résultats obtenus ont permis de valider cette nouvelle technique d'assemblage des batteries lithium-ions.



## **Résumé**

Le travail présenté dans ce mémoire concerne la réalisation des batteries souples au lithium sur papier par procédé d'impression. Il a comme objective le développement de nouveaux procédés comme l'impression par sérigraphie pour la fabrication de batteries et le remplacement des polymères issus de la chimie de synthèse par des matériaux bio-sources utilisables en milieu aqueux. Les premières résultats obtenus, ont montré qu'il est possible formuler des encres à base de dérivées de la cellulose, adaptable aux technologies d'impression en ayant des propriétés compatible avec le comportement requis pour le fonctionnement de la batterie. Les électrodes ainsi fabriquées ont été testées et caractérisées soit d'un point de vue physique que électrochimique et deux stratégies différents ont été proposées pour améliorer les performances. Enfin, en considérant les résultats obtenus pour les électrodes, une cellule complète a été fabriquée en proposant une nouvelle stratégie d'assemblage basée sur l'impression recto/verso du séparateur et intégration de collecteur de courant pendant la phase d'impression. Les cellules ont été enfin caractérisées et comparées avec des autres obtenues par des techniques classiques d'assemblage.

## **Abstract**

The work presented in this manuscript describes the manufacturing of lithium-ion batteries on paper substrates by printing technique. Its aim is the development of new up scalable and large area techniques as screen printing for the fabrication of lithium-ion batteries and the replacement of conventional toxic components by bio-sourced one and water based solvent. First results shows how it is possible to formulate cellulose based ink tailored for screen printing technology with suitable properties for lithium-ion batteries requirements. Electrodes were manufactured and tested from a physical and electrochemical point of view and two strategies were proposed to enhance performances. Finally, by considering results obtained for the electrodes, a full cell was manufactured with a new assembling strategy based on: front / back printing approach and the embedding of the current collectors during printing stage. As a final point cells were characterized and compared with others obtained by conventional assembling strategies.